INVESTIGATION OF MICROPLASMA GENERATION IN DENSE MEDIUM

A Dissertation

by

PENG XIAO

Submitted to the Office of Graduate and Professional Studies of
Texas A&M University
in partial fulfillment of the requirements for the degree of

DOCTOR OF PHILOSOPHY

Chair of Committee,	David Staack
Committee Members,	Tim Jacobs
	Sy-Bor Wen
	Rodney Bowersox
Head of Department,	Andreas A. Polycarpou

August 2015

Major Subject: Mechanical Engineering

ABSTRACT

This dissertation presents the experimental studies of low energy microplasma discharges in liquid and the model studies of microdischarge-generated microbubbles in liquid. The main focus is to determine the properties of the microbubble and relate them to the initiation and dynamics of the observed microplasma. Microplasma in liquid began to draw researchers' attention in recent decades because of its low energy input, micron scale size and nanosecond scale duration. The understanding of plasma discharges in gases has been well established; however, the mechanism of plasma initiation in liquid is still unclear. Several theories were proposed to provide different explanations of this mechanism, but none of them have been proven exclusively correct. Results here show that the generation of a microplasma needs higher energy than the generation of a microbubble from the same discharges. This supports the theory that during the microplasma initiation a lower density gaseous site is generated before the microplasma and the microplasma exists inside a microbubble. The typical form of a plasma and bubbles in liquid reported in literature are branch-like structures. Here we report spherical microplasma and microbubble afforded by relatively lower energy input, and it was found that for branched bubbles increasing the ambient pressure was able to reduce the microbubble size and eliminate its branches. The dynamics of the spherical bubbles could be modeled with a customized Rayleigh-Plesset model considering both

condensable and incondensable gases in the bubble, the initial neutral temperature and neutral pressure were estimated to be as high as 550 K and 1.2 GPa.

ACKNOWLEDGEMENTS

First and foremost, I would like to express my deepest gratitude to Dr. David Staack for everything he has given me. I was very fortunate to be able to work closely with him. His work ethic has always served as the highest model for my own. His clarify of thought, encyclopedic knowledge, and uncompromising stance on quality have been a constant source of inspiration. It is truly an honor to pursue my doctoral degree under his supervision. I could not have wished for a better mentor.

I am also grateful to Dr. Rodney Bowersox, Dr. Tim Jacobs, and Dr. Sy-Bor Wen, for serving on my committee and for giving me valuable comments on both my research and an earlier draft of this dissertation. Besides my committee members, I would like to express my gratitude to Dr. Waruna Kulatilaka for being part of my final defense.

The work reported in this dissertation benefited a great deal from the research project led by Dr. Staack under the auspices of the National Science Foundation (PHY-1057175). In addition, I really appreciate the professional assistance and technical support I have received from the administrative staff at Texas A&M University. This research would never have been possible without the use of SEM, Raman spectroscopy and clean room. Thus I would like to extend my indebtedness to TAMU Materials Characterization Facility for their friendly cooperation. Since parts of this work have been presented at various conferences, I would like to thank the respective audiences for their valuable comments.

I was very fortunate to be a member of the Plasma Engineering and Diagnostics Lab (PEDL), which proved to be a very fruitful environment to work in. Many thanks to the other members of PEDL (listed in alphabetical order), Andrew, Cliff, Dani, Harica, Ilan, John, Kalisa, Kenneth, Kenton, Kunpeng, Matthew, Michael, Patricia, Robert, Stephen and William for their help and support, and for being the pleasant colleagues that everyone has wished for. Chapter VI of this dissertation sprang from the collaborated work with Andrew Nelson. I thank him for being a great collaborator.

Last but not least, I feel grateful to my Wife Vera Zu for completing me, filling me with unconditional love and sacrificing so much in order to be with me. Her caring, patience and understanding support means a lot to me, and her unshakable and unyielding faith made me believe in love. My grateful thanks surely go to my parents for always having faith in me and allowing me great freedom to do what my interests lie in. This dissertation is dedicated to them.

TABLE OF CONTENTS

Page

ABSTRACT ii

ACKNOWLEDGEMENTS iv

TABLE OF CONTENTS vi

LIST OF FIGURES ix

LIST OF TABLES xvii

CHAPTER I INTRODUCTION 1

1.1 Background 1
1.2 Motivation 2
1.3 Dissertation Statement 6
1.4 Dissertation Overview 6

CHAPTER II PREREQUISITE KNOWLEDGE AND LITERATURE REVIEWS 10

2.1 Prerequisite Knowledge of Experimental Equipment 10
2.1.1 Prerequisite Knowledge of Plasmas 10
2.1.2 Plasma Generation and Diagnostic Techniques 32
2.2 Literature Review 39
2.2.1 Plasma Discharges with Liquid 39
2.2.2 Micro Scale Plasma Discharges in Water 53

CHAPTER III MICROPLASMA LIGHT EMISSION IN LIQUID 61

3.1 Section Overview 61
3.2 Experimental Setup 62
3.2.1 Reduction of EMI for PMT Measurement 65
3.2.2 Energy Inputs to Liquid for Microdischarges 67
3.2.3 PMT Signals for Discharges after Shielding of EMI 70
3.3 Analysis and Discussion of Experimental Results 73
3.3.1 Light Emission by Microsecond Discharges Recorded by ICCD and PMT 74
3.3.2 Thresholds Concerning Microbubbles and Microplasma Light Emission by Nanosecond Discharges 76

3.4 Discussion of Thresholds from Perspective of Energy and Electrical Field 84
3.5 Summary 87

CHAPTER IV MICRODISCHARGE GENERATED MICROPLASMA AND SPHERICAL MICROBUBBLES 89

4.1 Section Overview 89
4.2 Mechanism and Initiation Rate of Microdischarge Generated Microbubbles 90
4.3 Experimental Setup 97
4.3.1 Microelectrode Fabrication 99
4.3.2 Experimental Layout 102
4.3.3 Image Acquisition Equipment 106
4.4 Experimental Results and Discussion 107
4.4.1 Microplasma Initiation and Nanosecond Duration 107
4.4.2 Microplasma Generated Microbubble 109
4.5 Rayleigh-Plesset Model of Microplasma Generated Microbubble 115
4.6 Uncertainty Study of Best-fitting Parameter 135
4.7 Summary 143

CHAPTER V DYNAMICS OF MICRODISCHARGE GENERATED SPHERICAL MICROBUBBLE UNDER VARIOUS AMBIENT PRESSURES 146

5.1 Section Overview 146
5.2 Experimental Setup 147
5.2.1 Image Acquisition Toolset 148
5.2.2 Experimental Layout 151
5.2.3 Fabrication of Pressure Vessel 154
5.2.4 Algorithm of MATLAB for Boundary Identification 158
5.3 Experimental Results and Discussion 167
5.3.1 Parametric Design 168
5.3.2 Uncertainty of Microbubble's Dynamics under Different Parameters 170
5.3.3 Changes of Microbubble's Dynamics 176
5.4 Rayleigh-Plesset Model with Varied Ambient Pressures 183
5.4.1 Best Fitting of Microbubble's Dynamics under Different Parameters 184
5.4.2 Thermodynamic Properties of Microbubbles under Different Ambient Pressures 190
5.5 Summary 194

CHAPTER VI MICRODISCHARGE GENERATED ASPHERICAL MICROBUBBLES IN LIQUID 196

6.1 Section Overview 196
6.2 Experimental Setup 197
6.2.1 Experimental Design 197
6.2.2 Energy Input and Conductivity 198
6.3 Experimental Results 199
6.3.1 Branched Microbubble in Conductivity Controlled Liquid 201
6.3.2 Suppression of Branched Microbubble in Pressure Controlled Environment 207
6.4 Summary 213

CHAPTER VII CONCLUSION AND FUTURE WORK 214

7.1 Conclusion 214
7.2 Future Work 219
7.2.1 Short Term Plans 219
7.2.2 Long Term Plans 221

REFERENCES 222

APPENDIX 239

LIST OF FIGURES

Page

Figure 1. Different Forms of Plasma in Universe [3](Copyright © 1996 Contemporary Physics Education Project (CPEP) – CPEPweb.org) 2

Figure 2. Microdischarge on One Onion Cell 5

Figure 3. Inside View of JET Tokamak [22](Copyright © EFDA-JET) 14

Figure 4. Dielectric Barrier Discharge (DBD) on Person's Forehead [23] (Copyright © PEDL TAMU) 14

Figure 5. Schematic Energy Distribution of Equilibrium Plasma (Yellow Region Indicates Ion and Red Region Indicates Electron) 16

Figure 6. Schematic Energy Distribution of Non-equilibrium Plasma (Yellow Region Indicates Ion and Gas, and Red Region Indicates Electron) 17

Figure 7. Voltage and Current Relationship of DC Discharge in Vacuum Tube [24] 19

Figure 8. Paschen Curves for Different Gases [26] 22

Figure 9. Illustration of Increasing Number Density of Neutrals Requiring Higher Breakdown Voltage 23

Figure 10. Illustration of Reducing Distance between Electrodes Requiring Higher Breakdown Voltage 25

Figure 11. Illustration of Reducing Mean Free Path by Increasing Pressure 27

Figure 12. TEM Images of (a) Ag Nanoparticles Synthesized from Anodic Dissolution of Ag Foil and Microplasma Reduction, (b) Au Nanoparticles Synthesized from Anodic Dissolution of Au Foil and Microplasma Reduction, (c) Ag Nanoparticles Synthesized from Microplasma Reduction of Aqueous $AgNO_3$ Soution, (d) Au Nanoparticles Synthesized from Microplasma Reduction of Aqueous $HAuCl_4$ [30] 30

Figure 13. The Shock Wave Generator by Plasma Discharge in Water for Medical Application [48] (Copyright © Institute of Plasma Physics AS CR) 32

Figure 14. CMOS (Copyright © Photron FASTCAM SA5) and ICCD (Copyright © Stanford Computer Optics) High Speed Camera [49] 36

Figure 15. PMT with 28 mm Dia., Side-on Type, Multialkali Photocathode (Effective Area: 8 x 24 mm and Spectral Response: 185 to 900 nm) [50] (Copyright © Hamamatsu Photonics).....37

Figure 16. Working Principle of PMT 38

Figure 17. Fabrication of Pin Electrode for Discharges in Liquid [51] [52].....40

Figure 18. Schematic of Pin to Plane Discharge: (a) Streamer Discharge, (b) Spark with Streamer, (c) Spark Discharge [38].....41

Figure 19. Discharge in Liquid and Long Time Exposure for Multiple Discharge Channels [23](Copyright © PEDL).....43

Figure 20. Typical Electrode Configurations for Three Different Types of Discharges with Liquids (a) Direct Liquid Phase Discharge Reactor [57], (b) Gas Phase Discharge Reactor with Liquid Electrode [58], (c) Example of Bubble Discharge Reactor [59]. 46

Figure 21. Overview of Different Electrode Configurations Used to Study Electrical Breakdown of Bubbles in Liquid [60].....46

Figure 22. Experimental Setups Developed for Discharges in Bubbles, (a) Bubble Corona Discharge Reactor [60], (b) Capillary Gas Flow Bubbling Reactor [61], (c) Volume Pulsed Discharges Bubbling Reactor [62], (d) Bubble Surface Discharge Reactor [63], (e) Discharge Reactor with Submerged Liquid Jet, (f) DC Arc Discharge Reactor in Gas Channel with Liquid Wall [58, 64-68] 47

Figure 23. Different Electrode Configurations Used to Study Electrical Discharges with Liquid, (a) Discharge Reactor between Two Liquid Electrodes, (b) Setup to Study Discharges between Two Droplets, (c) Water Surface Discharge Setup, (d) Gliding Arc Reactor with Active Water Electrode [71], (e) Gliding Arc Reactor with Passive Water Electrode, (f) Hybrid Reactor [72].....49

Figure 24. Illustration of Electrical Holes Formation by Electrostatic Stress in Liquid[73] 51

Figure 25. Illustration of Formation of Localized High Electrical Field at Spark Tips [73] 52

Figure 26. Schematic Illustration Mechanism of Microplasma Generation in Liquid, (a) Direct Electron Avalanche in Liquid, (b) Joule Heat Generated Microbubble, (c) Electrostatic Cracking Theory, (d) Pre-existing Microbubble 55

Figure 27. 3D Drawing of Microelectrode Tip Immersing in Water with Microplasma and Microbubble Generation 64

Figure 28. Schematic Drawing of Experimental Setup. 65

Figure 29. Output Signals of PMT Affected by EMI; a) Prior to Shielding, b) After Shielding and Isolation Measures. Flat Cut at First 2 μs of (a) Caused by Limitation of Oscilloscope's Range 66

Figure 30. Energy Input to Liquid with Different APVs of Nanosecond Discharges in Liquid 70

Figure 31. Successive PMT Signals of (a) Microsecond Discharges and (b) Nanosecond Discharges 72

Figure 32. Time Scheme of Light Transmission and EMI Transmission 73

Figure 33. Light Emission Signals Collected from PMT and ICCD (Dots on Green Line Representing Maximum Intensity of Plasma Light Emission on Each ICCD Photo. APVs = -4 kV and Conductivity of Liquid for Discharge =1990 μs/Cm) 75

Figure 34. Light Emission and Microbubble from Microsecond Discharge (Delay Time (td)=200 ns, Exposure Time=20 ns, Liquid Conductivity=1990 μS/cm and APV=-2 kV). 76

Figure 35. Light Emission and Microbubble from Nanosecond Discharge (Delay Time (td)=20 ns and 200 ns, Exposure Time=200 ns, Liquid Conductivity=17600 μS/cm and APV=-2 kV). 77

Figure 36. Plasma Light Emission and Microbubble from Tip Size of 3 μm 81

Figure 37. Plasma Light Emission and Total Energy Corresponding to Applied Peak Voltage from Tip Size of 3 μm 82

Figure 38. Plasma Light Emission and Microbubble from Tip Size of 5 μm 83

Figure 39. Plasma Light Emission and Total Energy Corresponding to Applied Peak Voltage from Tip Size of 5 μm 84

Figure 40. (a) PMT Peak Signals vs. Applied Peak Voltage of 3 μm and 5 μm Microelectrode Tips; (b) PMT Peak Outputs vs. Electrical Field at Microelectrode Tips; (c) PMT Peak Outputs vs. Energy Input to Liquid of Two Microelectrode Tips. 86

Figure 41. Electrode Geometry 91

Figure 42. Time Constants for Low Density Bubble Formation vs. Bubble Size 97

Figure 43. 3D Drawing of Microelectrode Tip Immersing in Water with Microplasma and Microbubble Generation Illustrated....98

Figure 44. (a) Microelectrode Tip Fabricated by Electrolysis, (b) Microelectrode Covered by Epoxy....100

Figure 45. (a) SEM Photos for Microelectrode Tip before Discharges, (b) SEM Photos for the Same Microelectrode Tip after 200 Discharges....101

Figure 46. Schematic Illustration of Experimental Layout with Double- and Single-Spark-Gap Switching 103

Figure 47. Voltage and Current Variation vs. Time of Single-Spark-Gap Microsecond Pulse Discharge....104

Figure 48. Voltage and Current Variation vs. Time of Double-Spark-Gap Nanosecond Pulse Discharge....104

Figure 49. Nanosecond Pulsed Microplasma without Background Light with 10 ns Exposure Time at t=70 ns. (a) Single Microplasma Light Emission Captured by ICCD Camera, (b) Integrated Images of 20 Pulses Averaged by ICCD Camera....108

Figure 50. Time-Sequence Photos of Microplasma and Microbubble Initiations at the Microelectrode Tip Generated by Nanosecond Discharges with Consideration of Internal Delay of ICCD Camera. Top Row with Backlit and Bottom Row within Dark Environment 109

Figure 51. Microbubble Initiated by Microplasma in Water, t=16.5 μs after Discharge Event....110

Figure 52. Time-Sequence Photos of Microplasma Generated Microbubble's Life Cycle by High Speed CMOS Camera with 300000 fps....111

Figure 53. Time-Sequence Photos of Nanosecond Discharge Microplasma Generated Microbubble's Life Cycle by High Speed CMOS Camera with 300000 fps 113

Figure 54. Comparison of Time Dependent Radius Change between Microsecond and Nanosecond Discharges with Error Bars. 114

Figure 55. Comparison of Experimental Results with RP Model Results for Both Microsecond and Nanosecond Discharged Microbubbles 120

Figure 56. Comparisons of Pressure (a, e), Temperature (b, f), Mass (c, g) and Internal Energy (d, h) of Microsecond Discharged Microbubble and Nanosecond Discharged Microbubble Predicted by RP Model. 123

Figure 57. Possible Energy Dissipation in Liquid 127

Figure 58. Sensitivity Study of Best-Fitting Parameters in RP Model 138

Figure 59. Neutral Density Filters 150

Figure 60. Schematic Diagram of Experimental Setup Using Pressure Vessel 153

Figure 61. Experimental Setup with Different Components Corresponding to the Diagram in Figure 60 154

Figure 62. Cross Section View of Pressure Vessel Using SolidWorks Illustration 158

Figure 63. Microbubble Together with Microplasma Recorded by CMOS Camera 160

Figure 64. Microelectrode Tip in Liquid without Discharges 161

Figure 65. Boundary Identification Using "canny" Algorithm 162

Figure 66. Boundary Identification of Microelectrode Tip 163

Figure 67. Distance between Each Point on Circles to Microelectrode Tip 163

Figure 68. Microbubble Boundary after Microplasma Boundary Elimination 164

Figure 69. Big Portion of Microbubble Boundary in Image 165

Figure 70. Small Portion of Microbubble Boundary in Image 165

Figure 71. Identification of Left and Right Side of Microbubble 166

Figure 72. Perfect Circle to Represent Microbubble in Image 166

Figure 73. Radius Changes vs. Time Collected by Program 167

Figure 74. Voltage Rising from -2 kV to -12 kV for Microdischarges.....168

Figure 75. Energy Input to Liquid (a) Nanosecond Discharges and (b) Microsecond Discharges.....169

Figure 76. Microdischarges Generated Microbubbles by Microsecond Discharges at -9 kV under Ambient Pressures Ranging from 0 psig to 80 psig.....173

Figure 77. Mean Maximum Radius of 4 Different Conditions with Standard Deviation vs. Ambient Pressures. 174

Figure 78. Microdischarges Generated Microbubbles by Microsecond Discharges at -7 kV under Ambient Pressures Ranging from 0 psig to 80 psig.....175

Figure 79. Images of Radius Change vs. Time for -9 kV, µs Discharge with Ambient Pressures at 0 psig, 40 psig and 80 psig.....178

Figure 80. Radius vs. Time for -9 kV, µs Discharge in DI Water with Surface Tension of 35 mN/m and Ambient Pressure Ranging from 0 psig to 80 psig.....180

Figure 81. Discharges with Same Parameters Presented in Figure 80 except Surface Tension (Surface Tension = 71 mN/m) 181

Figure 82. Discharges with Same Parameters Presented in Figure 80 except Applied Peak Voltage (Applied Peak Voltage = -7 kV) 182

Figure 83. Comparison between Experimental Results and Rayleigh-Plesset Model Study (Discharge Condition at -9 kV APV, µs Duration and 35 mN/m Surface Tension).....185

Figure 84. Equilibrium Radius vs. Ambient Pressure (Discharge Condition at -9 kV APV, µs Duration and 35 mN/m Surface Tension).....186

Figure 85. Initial Radius vs. Ambient Pressure (Discharge Condition at -9 kV APV, µs Duration and 35 mN/m Surface Tension).....187

Figure 86. Initial Velocity vs. Ambient Pressure (Discharge Condition at -9 kV APV, µs Duration and 35 mN/m Surface Tension).....187

Figure 87. Saturation Temperature and Equilibrium Temperature vs. Ambient Pressure (Discharge Condition at -9 kV APV, μs Duration and 35 mN/m Surface Tension).....188

Figure 88. Polytropic Index vs. Ambient Pressure (Discharge Condition at -9 kV APV, μs Duration and 35 mN/m Surface Tension).....188

Figure 89. Thermodynamic Properties of Microbubbles under Different Pressures (Discharge Condition at -9 kV APV, μs Duration and 35 mN/m Surface Tension).....191

Figure 90. Variation of Maximum Total Mass and Maximum Total Energy of Microbubbles vs. Ambient Pressures (Linear Fitting Presenting General Trend).....192

Figure 91. Internal Pressure of Microbubbles at 50 ns after Initiation under Different Ambient Pressures Based on RP model.....192

Figure 92. Water Phase Change Diagram [117] (Copyright © Wikipedia) (Thermodynamic Properties of Microplasma Initiation in Red Box Region) 193

Figure 93. Microbubble Images with 0.5 μs Delay, 0.5 μs Exposure Time 202

Figure 94. Bubble Images with 0.1% Mass Concentration of NaCl and Exposure Time of 0.5 μs in Dark and Illuminated Environment 203

Figure 95. Bubble Images with (a) 1.5 us Delay, 0.5 us Exposure Time, (b) 4.5 us Delay, 0.5 us Exposure Time, (c) 9.5 us Delay, 0.5 us Exposure Time.....205

Figure 96. Integrated Energy for First 100 ns vs. Input Voltage. Bubble Shape Determined from 0.5 μs and Indicated by X=Branched Bubble Δ= Non-Spherical Bubble O=Spherical Bubble. Lines Connecting Conditions of Same Conductivity. 206

Figure 97. Development of Instabilities of Microbubble on Three Dimensions (Applied Voltages, Mass Concentration of NaCl and Time of Development) 207

Figure 98. Branched Microbubbles with Low Conductivities (0.05% Mass Concentration of NaCl, 5 μs FWHM Discharge, td=3 μs and te=50 ns) Captured by ICCD Camera.....208

Figure 99. Branches of Microbubbles Suppressed by Ambient Pressures.....209

Figure 100. Statistical Study of Microbubbles with and without Branches under Different Ambient Pressures 211

Figure 101. Length of Longest Branch and Radius of Core Bubble.....212

Figure 102. Radius Change of Branched Microbubble and Length of Longest Branch Change vs. Different Ambient Pressures 212

LIST OF TABLES

Page

Table 1. Examples of Ionization, Excitation, Dissociation and Light Emission Caused by Discharges in Water 29

Table 2. Legend of Variables Used for Estimating Proportionality Constants 92

Table 3. Values Used for Comparing the Relative Rates for Each Mechanism 96

Table 4. Estimated Energy Dissipations in Microplasma Discharges 128

Table 5. Estimation Equations of Energy Dissipation 134

Table 6. Variation of Best-Fitting Parameters with Rzero as a Controlled Input 139

Table 7. Variation of Best-Fitting Parameters with Vzero as a Controlled Input 140

Table 8. Variation of Best-Fitting Parameters with Teq as a Controlled Input 141

Table 9. Variation of Best-Fitting Parameters with Req as a Controlled Input 142

Table 10. Variation of Best-Fitting Parameters with k as a Controlled Input 143

CHAPTER I

INTRODUCTION

1.1 Background

Plasma, as the fourth state of matter, plays a very important role in our universe. As suggested in the book “Physics of the Plasma Universe” [1], the plasma composes 99.999% of the known matter in universe. Why is the plasma so common in our universe, but pretty rare on earth? The answer to this question can be very complicated. In general, plasma is widely spread in the outer space, and is one of the main constituent of it. Langmuir firstly defined the plasma as a partially or fully ionized gas containing a collection of randomly moving charged particles [2].

Different from the other three states of matter, the research on the plasmas has not been a long time. From application perspective, however, the plasma based industrial products have been widely used in many areas such as semiconductor industry, water treatment industry, chemical analysis industry, surface treatment industry, nuclear industry, etc. Without the plasma based etching technique, a CPU based on vacuum tube transistors is probably still as big as a room. On the other hand from fundamental understanding perspective, there left many unknown properties of plasma and microplasma waiting us to explore.

The research objective of this dissertation is to investigate microplasma generation and microdischarge generated microbubbles in liquid. The plasma generation in different gases have been investigated for decades, but the microplasma in liquid with

low energy input only drew attentions in recent decades. Non-equilibrium transient plasma with the duration in nanosecond scale and the size in micron scale was used to explore the mechanism of microplasma generation in liquid in this work. The investigation of general background concerning the plasma, the non-equilibrium (non-thermal) plasma, the hypothesis of mechanism of plasma and microbubble generation in liquid, and some observational techniques is introduced in the following sections.

1.2 Motivation

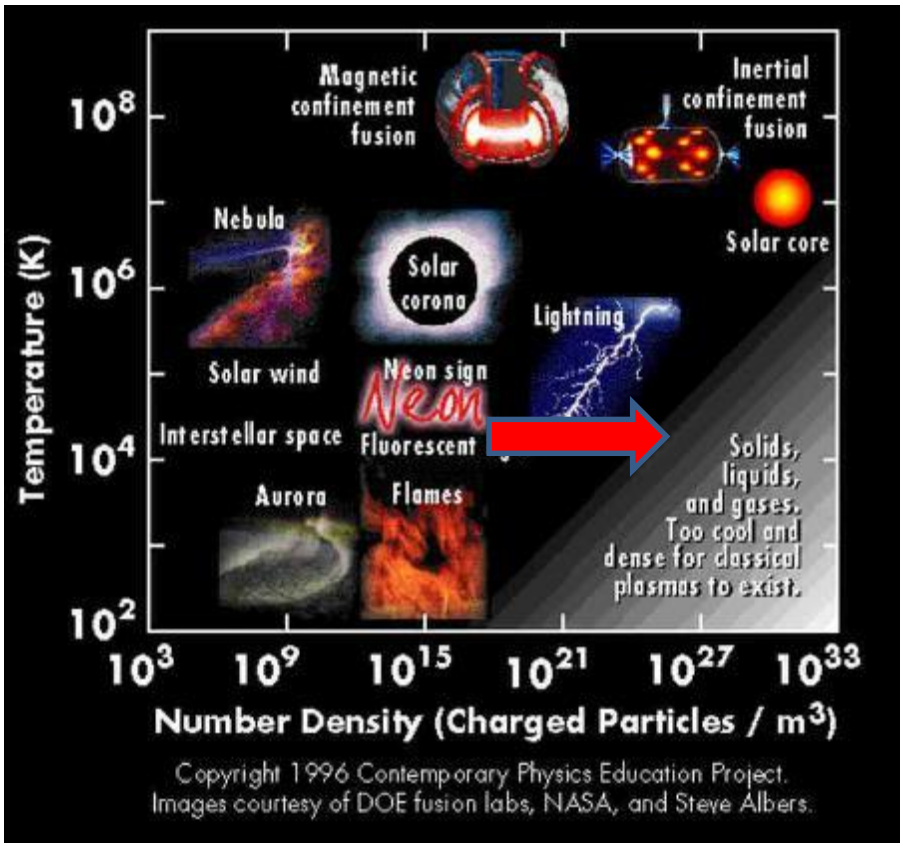

Figure 1. Different Forms of Plasma in Universe [3](Copyright © 1996 Contemporary Physics Education Project (CPEP) – CPEPweb.org)

Diversified forms of plasmas exist in our universe as presented in Figure 1. High vacuum and high energy sites in the universe provide them the stage, whereas only can the lightning and flames be seen on our earth. In Figure 1, there is a gradient grey area which marks as “Solids, liquids and gases. Too cold and dense for classical plasma to exist”. The description of this region actually answers the reason why the natural plasma is not very common on the earth. That is due to the “cold” (but being suitable for lives) temperature. Right above this grey area is the nuclear fusion application, which implies that this no-classical-plasma-existence area has its similarities (high number density) to some thermal nuclear traditional plasmas. The investigation of the plasma generation in this grey area has its potential for the exploration of the nuclear fusion. The general motivation of this research is to push the plasma research boundary into that grey region.

As briefly introduced in previous subsections, plasma as the fourth state of matter has many unique characteristics. Fundamental research wise, there are many unknowns concerning the microplasma generation in liquids. The discharges in liquid, also called plasma discharges in liquid, have been investigated for a long time. But due to the limitation on the control of energy inputs, the fabrication of microstructure electrodes, the control of the discharge duration, and the observational and analysis equipment, the investigation of microplasma generation in liquid was not practical even 20 years ago. Macro scale discharges in liquid were studied and will be introduced in the next chapter. The generation of plasma in liquid, the streamers following the plasma discharges, the generation of a large number of bubbles, the generation of many branch like channels, complicates the generation mechanism of plasma in liquid. Many phenomena occurring

at the same time makes it hard to distinguish them and identify the cause for each of them.

Thanks to the development of the high voltage power supply, the high speed switch (e.g. spark gap), the microfabrication techniques for micro structure in micron scale, the high speed cameras with shutter speed up to nanosecond scale and the GHz data acquisition oscilloscope, the experimental research of microplasma in liquid becomes possible. Since the energy input for the microplasma is in milli joule scale, there is only one plasma spot generated at the tip of the electrode. Without the distractions created by high energy discharges described above, the observation of the initiation mechanism of microbubble and microplasma can become much clearer.

The duration of microplasma is in nanosecond scale. Current experimental research on the microplasma by using the nanosecond gated ICCD camera and the nanosecond response timed photomultiplier tube still has its limitation. The research of the microbubble generated with the plasma provides a different path for the study of the microplasam generation. The microbubble was observed to coexist with the microplasma at the first 100 ns, and the duration of the microbubble can be as long as in microsecond scale. The data and image acquisition for microsecond events is easier than the nanosecond events. In the first 100 ns, the microplasma and microbubble coexisted, and the research of the microbubble in first 100 ns can benefit our understanding of the nanosecond duration microplasma in liquid. The objective of the study of micro discharge generated microbubble is to investigate the thermodynamic properties of microplasma.

Besides the intrigues of fundamental understanding of plasma discharges in gas and liquid, there still have many industrial applications. A microplasma discharge on an onion cell is presented in the Figure 2. The idea to use microplasma discharge in liquid for the cancer cell treatment as introduced in the previous subsection is the most updated research. Liquid consists of 60% to 70% percent of human body, and the discharges being operatable in aqueous environment is critical in this research.

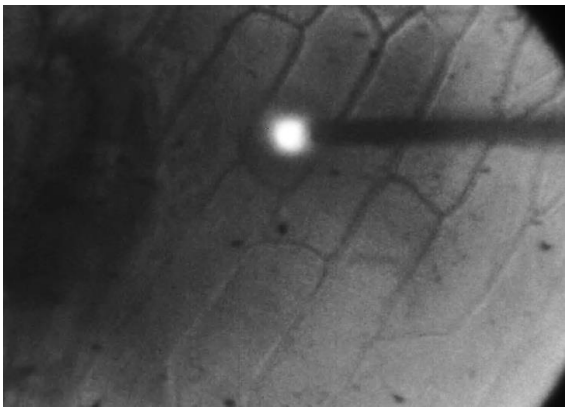

Figure 2. Microdischarge on One Onion Cell

1.3 Dissertation Statement

The goal of this dissertation is to establish the knowledge and techniques necessary to investigate the low energy microplasma discharge in liquid. The study addresses issues such as

- the time-resolved light emission from the microplasma discharge in liquid,
- the dynamics of a spherical microbubble generated by a micro discharge in liquid under atmospheric pressure,
- the dynamics of a spherical microbubble generated by a micro discharge in liquid under different ambient pressures,
- the transition from an aspherical microbubble generated by a micro discharge in liquid to a spherical microbubble.

To accomplish this goal, microplasma discharges in liquid with different energy inputs, different applied peak voltages, different size of microelectrode tips, different conductivities of liquid, different surface tensions and different ambient pressures were all employed in this research for a parametric study of the initiation and evolution of the microplasma and the microdischarge generated microbubbles in liquid.

1.4 Dissertation Overview

This dissertation contains 7 chapters. Chapter I briefly introduces the general background of plasmas, the motivation of this research, the dissertation statement and overview.

Chapter II narrows the scope to the background of natural plasma and artificial plasma, the identification of 'hot' plasma and 'cold' plasma, the plasma discharge in gas, and the plasma discharge in liquid. In addition, the equipment usage and literature review very related to the research are covered in this dissertation.

The experimental setups are introduced individually in each chapter from Chapter III to Chapter VI. With the background introduction and the literature review, one research topic of microplasma light emission in liquid begins to commence in Chapter III. In Chapter III, the microplasma light emission is detailed studied of the duration, the initiation timing, the rising time and the interaction between the microplasma light emission and microdischarge generated microbubble. One significant finding covered in this chapter is that from the energy perspective it was found the microdischarge generated microbubble requires lower energy to generate than the microplasma with all conditions same. Experimentally, it was proved that the microbubble can be generated prior to the initiation of miroplasma, and the microbubble provides an ideal inception site for the microplasma generation.

In addition to the knowledge of the coexistent of the microplasma and the microbubble at the first 100 ns, a thorough investigation of microdischarge generated microbubble is presented in Chapter IV. In Chapter IV, the radius change of microbubble versus time was accurately recorded. Based on the experimental data of the radius change, the Rayleigh-Plesset model was then used to calculate and estimate the thermodynamic properties of the microbubble. It was estimated that the microbubble

share a high temperature and pressure environment with the microplasma during the first fraction of a microsecond when they coexist.

The dynamics of the microdischarge generated microbubble was driven by the pressure difference between the pressure inside of the bubble and the pressure outside of the bubble. In Chapter V, a parametric study of microbubble's dynamics in a pressure controlled environment was investigated. It was found that the ambient pressure can significantly change the duration and the maximum radius of the microbubble. Furthermore, it was found that the microbubble's dynamics presented more uncertainty with high ambient pressures.

Most microbubbles presented in this dissertation are spherical bubbles. With state of the art experimental equipment, the energy input was reduced to microjoule and the electrical field was increased to GV/m scale at the microelectrode tip. In most plasma generation in liquid research, bubbles were either branch like or aspherical which were all addressed in Chapter II. In Chapter VI, the mechanism of the aspherical microbubble was studied experimentally, and a transition from spherical bubbles to aspherical bubbles were found experimentally as well. The findings for the transition from branched microbubbles to spherical microbubbles were used to further our understandings and techniques to create high energy density areas, control the size of microplasma and test the ambient pressure sensitivity of microplasma initiation.

A conclusion for this dissertation and the future work for this research is described in Chapter VII.

It should be mentioned that one journal paper “Microbubble Generation by Microplasma in Liquid” [4], two conferences paper “Thresholds for Microbubble & Microplasma Generation in Liquid”, “PMT & ICCD Investigation of Light Emission from Microplasma Generated in Liquid” [5, 6], and one presentation “Experimental & Modeling Analysis of the Single Micro Bubble Generation by Micro Plasma in Water” [7] have been generated from this research. In addition, two journal papers “Thresholds of Low Density Region & Light Emission by Microdischarges in Liquid” and “Transition from Aspherical to Spherical Microbubble Generated by Microplasma in Liquid” are about to submit, and one conference paper “Hydrodynamic study of plasma generation in liquid” has been accepted.

CHAPTER II

PREREQUISITE KNOWLEDGE AND LITERATURE REVIEWS

2.1 Prerequisite Knowledge of Experimental Equipment

Before the investigation of microplasma generation in liquid, prerequisite knowledge and some technical equipment are introduced first. They have been well established, so they do not belong to the research part in this dissertation. But they are all important for the experimental setup and the data acquisition and analysis.

2.1.1 Prerequisite Knowledge of Plasmas

2.1.1.1 Introduction to Plasma

From the energy perspective of atoms or molecules, the solid state has the lowest energy and the plasma has the highest energy. With the addition of energy, the solid state can be changed into the liquid state. Furthermore, more energy addition into liquid state can vaporize the liquid into the gas state. These three states of matter are the most common three phases on our earth. Beyond the gas state with more energy, the gas can be ionized, and eventually forms the plasma. In this case, the collisions between particles are so severe that some electrons cannot stay in their orbits, so the neutral atoms or molecules are ionized into two groups, one of which consists of the negative charges such as free electrons, and the other one of which consists of the positive charges such as free ions. The matters in general on earth do not have that much of energy to form

plasma. Some transient natural plasma can be observed e.g. lightning, but the stable natural plasma can only be observed in the outer space.

Plasma presents itself in various forms artificially or naturally. In Figure 1 different plasmas are presented in terms of electron number density and electron temperature. In most cases the electron temperature of plasma can range from 10^3 K to 10^9 K, and the number density of electron can range from 10^5 #/m^3 to 10^{32} #/m^3. The detailed explanation of electron temperature will be in the next subsection. For the case of the aurora which occurs on the most outside layer of atmosphere when rarified air molecules collide with solar wind, it has relatively low electron number density and electron temperature because of its nature of formation. For the case of nebula, the electron temperature is 4 orders of magnitude higher than the aurora, though the electron number density has similar value. They both exist in outer space environment, so the number density of electron of both cases is diluted by high vacuum. Since the nebula has higher ionization degree, it has higher electron temperature. Different from the aurora and nebula, the solar core is confined in the center of a nuclear fusion. Due the enormous mass, the gravity in the core of sun creates a site with high electron number density and high temperature. Besides some examples of plasma in universe, there is a grey area in Figure 1 presenting a “solids, liquids and gases” region where it is too cold or too dense that classical plasma is impossible to exist. The general objective of the research covered in this dissertation is to push the research boundary of plasma into that grey area.

The natural plasma on the earth is not as common as in the universe, but some transient plasma can also be seen in our life easily. As mentioned in previous paragraphs, lightning is a very common plasma discharge on earth. It normally involved high energy releasing and high electron temperature. The plasma generated by the lightning can create a lot of chemical reactions such as the production of ozone [8], NO_X [9, 10], etc. On the contrary, the majority of the plasma people deal with every day especially in industry is artificial plasma, and the most common one is fluorescent light. The pressure in the light tube is normally in 0.2 Torr. Mercury is excited by electrical field in the fluorescent light, and the light emission is the product after the free electrons from the mercury collides the phosphorus on the inside wall of the tube. In industry, the plasma has already been widely used in the plasma based deposition, e.g., carbon film [11], TiO_2 particles [12], atomic layer deposition of Co [13], SiO_X [14], etc., the plasma based etching, e.g., carbon fiber [15], silicon wafer [16], GaN pattern [17], etc., and the plasma based sterilization in water processing industry [18-21].

As presented in Figure 1, most electron temperature in plasma is higher than 10^3 ~ 10^4 K, so how is such high temperature used in industry? Can they destroy all the manufacturing equipment? With these two questions non-equilibrium plasma, also called non-thermal plasma, will be introduced in the following subsection.

2.1.1.2 Equilibrium (Thermal) and Non-equilibrium (Non-thermal) Plasma

Before the detailed introduction of the plasma research in this dissertation, one important definition which characterizes the internal energy of plasma is introduced

here. Plasma is categorized into the equilibrium plasma and the non-equilibrium plasma according to its thermodynamic equilibrium state, which can also be called “hot” plasma and “cold” plasma respectively according to its gas temperature.

The definition of plasma, as mentioned in previous paragraphs, is ionized gas which presents collective behaviors. In order to ionized gas or achieve different ionization degree, different methods have been employed. In the Figure 3, an inside view of Tokamak nuclear fusion presented by Joint European Torus is shown. The plasma created by nuclear fusion is regarded as the equilibrium or the “hot” plasma. The gas temperature in the nuclear fusion can be above 10^5 K and very high percentage of the atoms are ionized within the devise. On the contrary, in Figure 4 the dielectric barrier discharge based plasma jet is used on a person’s forehead for the purpose of sterilization. The pink plasma jet can be easily identified in the figure, and it can safely touch people’s skin without causing any discomfort or burning. The temperature for this plasma is just the same as the room temperature.

Figure 3. Inside View of JET Tokamak [22](Copyright © EFDA-JET)

Figure 4. Dielectric Barrier Discharge (DBD) on Person's Forehead [23] (Copyright © PEDL TAMU)

Why can the plasma show such different characteristics? From the energy perspective, the temperature of different species in a plasma needs to be clarified.

Different from the other three states of matter, species in the plasma is the mixture of the electrons, neutrals, ions and radicals. Because of their different electrical polarity, mass, size, etc, each of the species in plasma has its own energy characteristic. Using a simplified example with an assumption that the plasma only consists of electrons, ions and neutrals, an energy distribution for the equilibrium and non-equilibrium plasma is presented in Figure 5 and Figure 6.

For the case of the equilibrium plasma, the ionization degree of plasma is very high. It indicates that most of the atoms or molecules in the plasma are ionized. The energy for the high degree ionization needs to be sufficient enough to allow the electrons and the ions have same high energy distribution, which requires not only to move electrons at high speed but ions as well. To move electrons at high speed does not required a lot of energy due to their small mass, but to move ions at high speed needs a lot energy due to their much bigger mass. The energy required to achieve the equilibrium is so high that the electrons and the ions have the same thermodynamic equilibrium states. In Figure 5, a schematic illustration of energy distribution of electrons and ions is presented. Because the electrons and the ions both stay at high energy levels, the plasma temperature which is dominated by the ion temperature is at least 10000 K.

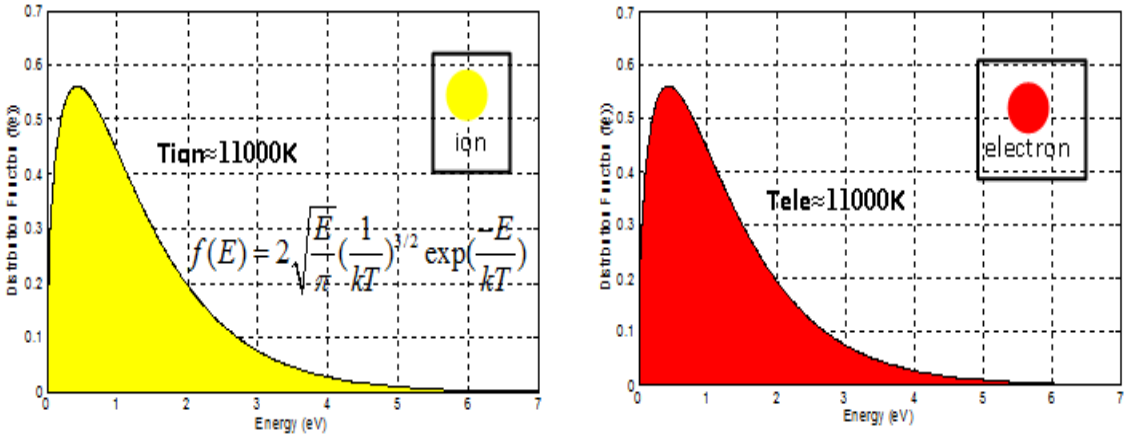

Figure 5. Schematic Energy Distribution of Equilibrium Plasma (Yellow Region Indicates Ion and Red Region Indicates Electron)

For the case of the non-equilibrium plasma, the ionization degree of plasma is very low. The ionization degree of the atoms or molecules in the plasma can be lower than 0.01%. The energy for the low ionization degree does not need to be sufficient to allow the electrons and the ions have same energy distribution. In addition, the ionization of non-equilibrium plasma only requires to excite a very small portion of atoms or molecules and to move the free electrons. In Figure 6, a schematic illustration of energy distribution of electrons and ions of non-equilibrium plasma is presented to compare with the Figure 5. In order to sustain the plasma state, the electrons have high temperature energy distribution which gives them the capability to ionize other atoms. However, the ions, due to their mass, cannot acquire enough kinetic energy to move in non-equilibrium plasma. As presented in Figure 6, the majority of electrons stays at high

energy levels, but the majority of ions stay at low energy levels. Because of the weak ionization degree for non-equilibrium plasma and the low temperature energy distribution of ions, the non-equilibrium plasma presents relatively low temperature. The low temperature plasma is a relative concept to the high temperature plasma. Their temperature is normally room temperature or a little bit higher than room temperature (300 K ~ 500 K). The low temperature plasma as mentioned in previous subsection is widely used in industry. The gas temperature of plasma is in room temperature, so most of the equipment can handle this temperature. At the same time, it still has many unique characteristics of plasma.

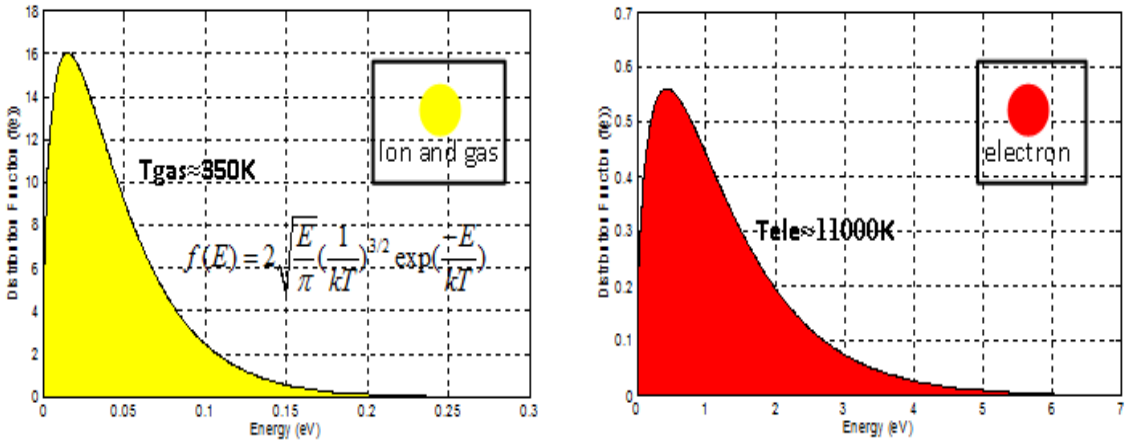

Figure 6. Schematic Energy Distribution of Non-equilibrium Plasma (Yellow Region Indicates Ion and Gas, and Red Region Indicates Electron)

2.1.1.3 Gas Discharge and Paschen's Law

The most common way to excite the non-equilibrium plasma is to use an electrical field to accelerate the collision and to enhance the ionization. As mentioned in previous section, the fluorescent light is probably the most common plasma discharge in our daily lives. The voltage and current characteristics presented in Figure 7 describes a voltage and current relationship for a glow discharge in a vacuum tube. The current in the vacuum tube is carried by electrons and ions. The detailed description of the voltage and current relationship can be found in "Gas Discharge Physics" authored by Yuri Raizer. Assuming there is a vacuum tube with argon (2 Torr) filled in with two parallel plate electrodes on each side. With an electrical potential on the anode and a ground on the cathode, the current in the tube stays at an extremely low value before the voltage gets to 600 V. At this stage, there is very limited ionization caused by cosmic rays or other sources of ionizing radiation. As the voltage increases, the free electrons are able to carry more energy to cause further ionization. When the electrons have enough energy to ionize and free another electrons in the gas, a process called electron avalanche happens. The process, also called Townsend discharge, can accelerate the generation of electrons in the gas. When the electron avalanche occurs, the current changes from 10^{-15} A to 10^{-5} A. The end of the Townsend discharge is that the secondary electron emission (SEE) can sustain this process without a high electrical field. In the Figure 7, point "D" marks the separation of Townsend discharge and self-sustained discharge. At the beginning of the self-sustained, a corona discharge appears with a drop of voltage. The corona discharge is an inefficient discharge since the current delivery is not high enough

and it only occurs in some local high electrical field places such as sharp corner of an electrode. Since the size of the sharp tips or corners normally very small, the idea of corona is used in our research to create microplasma in liquid. The corona discharge can develop into the glow discharge which is the discharge in fluorescent light or neon light. With increasing the voltage after the glow discharge, the plasma can develop into the arc discharge. The point "I" marks this transition. The mechanism of plasma changes from secondary electron emission (low temperature plasma) to thermionic emission (high temperature plasma). To be noted here, the arc plasma is beyond the scope of this dissertation.

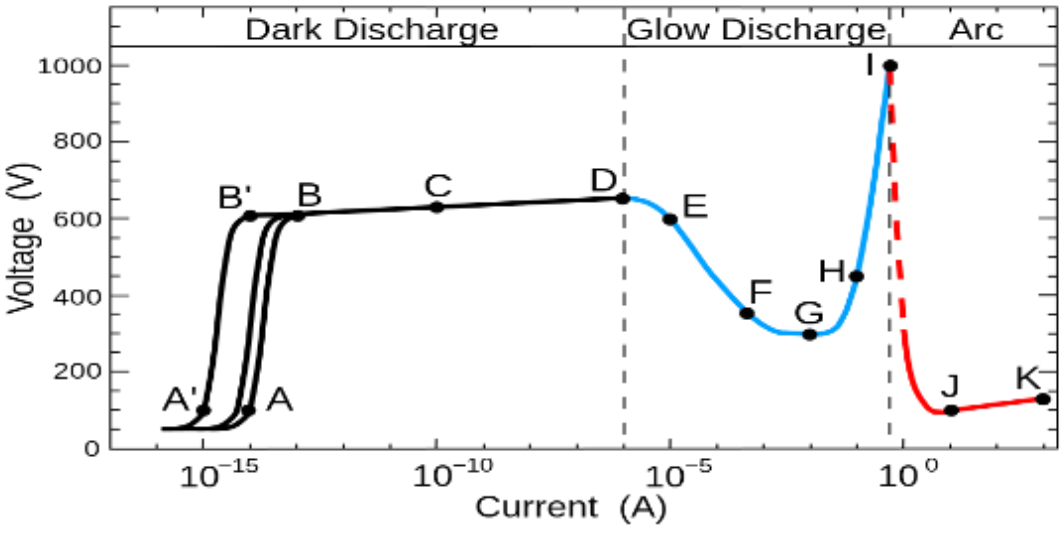

Figure 7. Voltage and Current Relationship of DC Discharge in Vacuum Tube [24]

The voltage and current relationship in Figure 7 was measured under the constant pressure. But since the plasma is generally regarded as a high energy gas, what does the pressure of the plasma can influence the generation of it?

In an electrical field, the generation of plasma depends on the electrical potential across the field. The minimum voltage required to initiate a plasma is called breakdown voltage or strike voltage. In Figure 8, different gases present different curves of breakdown voltages. These breakdown voltages vary corresponding to the change of the product of pressures (P) and the distance between electrodes (d). The patterns, however, are very similar. This pattern named after Prof. Paschen is called Paschen's Law [25]. There is a minimum breakdown voltage for each gas, and the breakdown voltages increase dramatically on both sides of this minimum value. The relationship presented in Paschen's curves can be expressed in Equation 1. The breakdown voltage of a specific gas is a function of the product of the pressure and the distance between the electrodes. For the non-equilibrium plasma, the pressure of the gas can be expressed in terms of the number density of the neutrals in the gas. So the relationship evolves from the product of the pressure and the distance between electrodes to the number density of neutrals and the distance between electrodes.

$$V_{Breakdown} = f(\mathrm{Pd}) = f(\mathrm{n}_o \mathrm{d}) \qquad \text{Equation 1}$$

In order to acquire enough energy for an electron to ionize the other atoms or molecules, it needs a clear path to accelerate in an electrical field before the collision which causes the ionization and energy losing. The energy an electron can acquire

between collisions can be expressed in Equation 2, where ‘e’ is the charge of an electron, ‘E’ is the electrical field and ‘λ_{MFP}’ is the mean free path for an electron.

$$\varepsilon = eE\lambda_{MFP} \qquad \text{Equation 2}$$

In addition, the mean free path can be express in the Equation 3, where ‘n_o’ is the number density of neutrals in the gas and ‘σ’ is the cross section of the atoms waiting for the collision with the free electrons. The cross section is one physical property of a specific gas, it does not depend on the experimental parameters.

$$\lambda_{MFP} = \frac{1}{n_o\sigma} \qquad \text{Equation 3}$$

Thanks to the Equation 2 and Equation 3, the mechanism of Paschen’s law can be unveiled according to how electrons acquire energy in gas. The explanation of Paschen’s Law is illustration in Figure 9, Figure 10 and Figure 11.

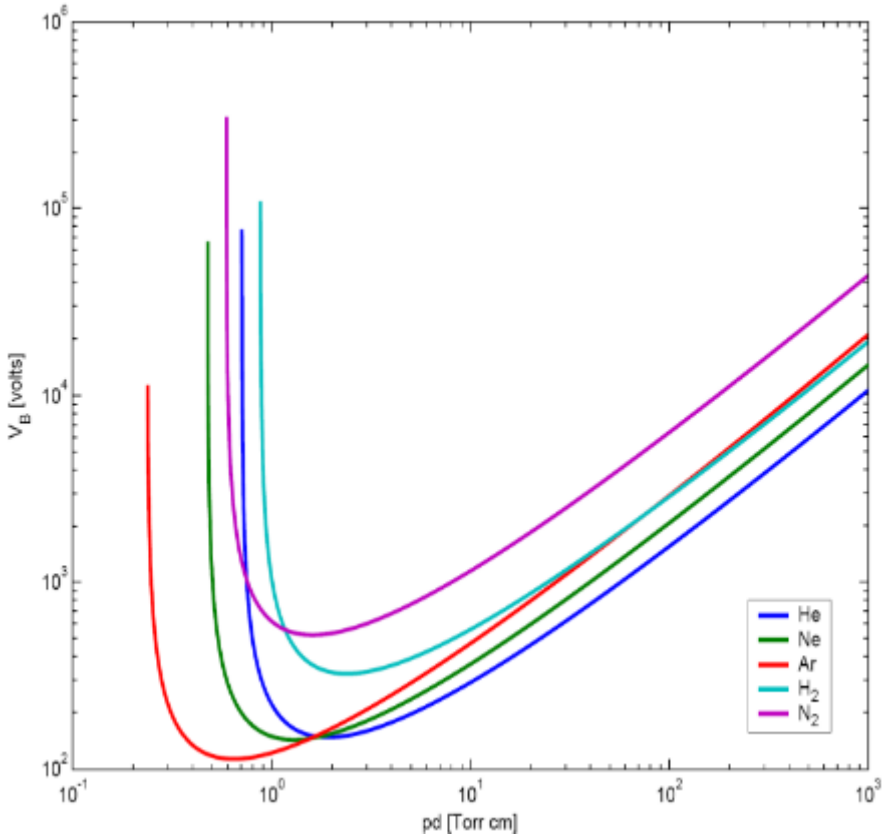

Figure 8. Paschen Curves for Different Gases [26]

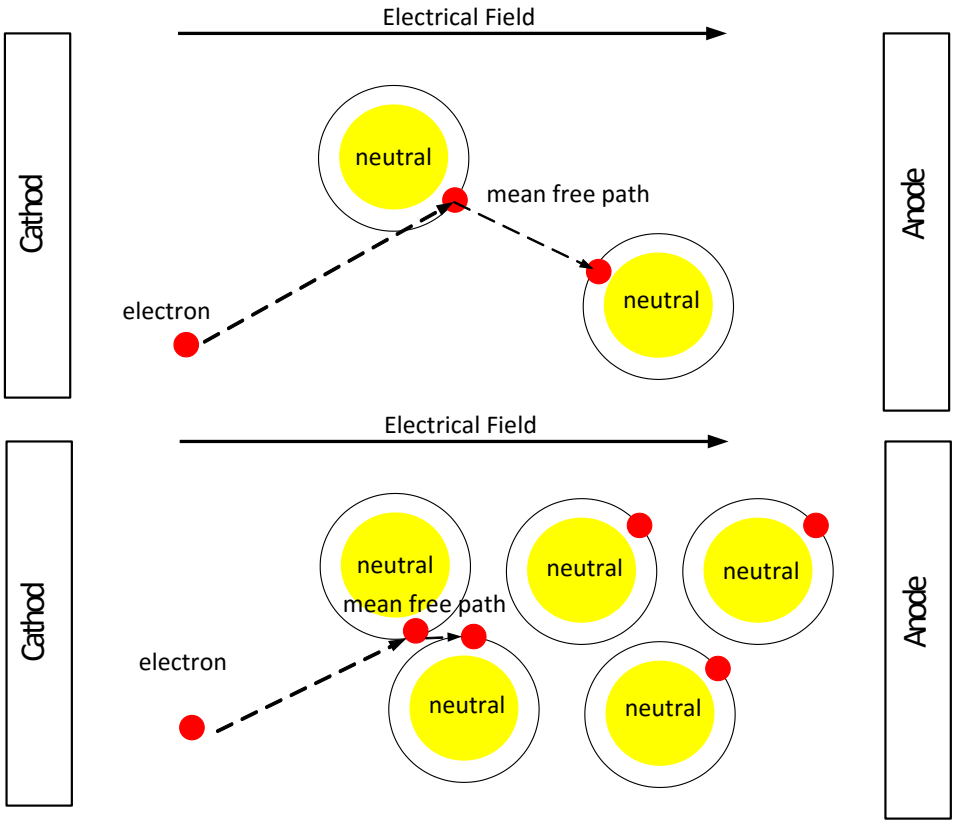

Figure 9. Illustration of Increasing Number Density of Neutrals Requiring Higher Breakdown Voltage

On the right hand side of the minimum breakdown voltage on Paschen's curves as presented in Figure 8, the breakdown voltage increases with the increment of the 'Pd'. Pressure "P" or the distance between electrodes "d" are then treated as a constant respectively for the explanation of Paschen curves. Assuming the pressure 'P' is constant in a 1D system, increasing of the distant between electrodes does need a higher breakdown voltage to maintain the electrical field between electrodes in pre-plasma

stage (E=V/d), which is the reason that the breakdown voltage needs to be changed linearly with the change of the distance between electrodes. On the other hand, assuming the distance between electrodes is constant, the increasing of the pressure or the number density of the neutrals does need a higher breakdown voltage as well. As presented in Figure 9, when the number density of neutrals increases, the mean free path between the collisions of the free electron and atoms become shorter. The ionization energy for a specific gas is constant, but a shorter mean free paths indicates that the electrons need to be provided a higher electrical field to acquire equivalent energy to the longer mean free paths cases, as suggested in the Equation 2. So when the number density of gas increases in electrode-distance-fixed system, the breakdown voltages linearly increases with the increasing of “Pd”.

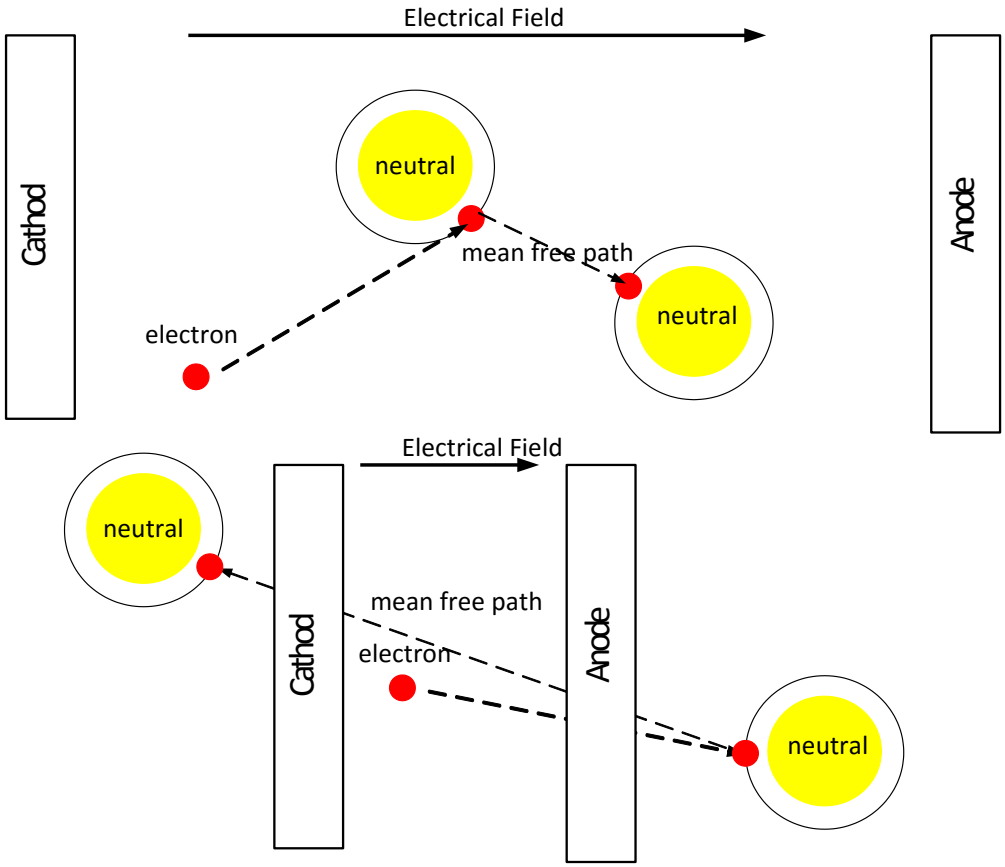

Figure 10. Illustration of Reducing Distance between Electrodes Requiring Higher Breakdown Voltage

On the left hand side of the minimum breakdown voltage on Paschen curves with the assumption of a constant distance between two electrodes, the number density of neutrals is fairly small, but the breakdown voltage does not reduce with the decreasing of the pressure "P", as explained for the right hand side of the Paschen curve. Figure 10 explains the reason why the parabolic shape of Paschen curve on the left hand side.

When the neutral number density is reduced or the mean free path is increased so significantly that the average collision distance between atoms is longer than the distance between electrodes as presented in Figure 10, an electrical field to send an electron from one electrode to the other electrode is not enough. A higher voltage is necessary to move the electrons to find atoms to ionize. The energy needs to be high enough to let the electrons run pass the electrodes.

From the Paschen's curve, the size of plasma presented in previous cases regarded as the distance between two electrodes is a function of the mean free path. The idea that can be inherited from the Paschen's curve is that by maneuvering the number density of neutrals or the pressure in the system, the size of the plasma can be controlled accordingly.

The Paschen's law and the relationship between the mean free path and the size of the plasma it represents are employed to design and direct our research of microplasma generation. As suggested, the microplasma needs a high number density of neutral to confine and restrict the size of plasma, as presented in Figure 11. A high number density of neutral is able to limit the mean free path and make the breakdown voltage back to its minimum value shown in the Paschen's curves. In order to provide a high neutral number density environment, two measures can be employed. The first one is to generate the plasma in a high pressure gas environment. The high pressure is able to reduce the mean free path of the collision, but it is not an easy job to achieve a super high pressure. The other one measure is to generate the plasma in liquid environment. The number density of molecules in the liquid is intrinsically high. Under one

atmospheric pressure, the number density of molecules in water is a thousand times higher than that in vapor under same atmospheric pressure. The vapor water can only achieve the same molecules number density of liquid water with thermodynamic state at or above the critical condition. Thanks to the high number density of molecules of liquid, the microplasma can be achieved in low ambient pressure environment.

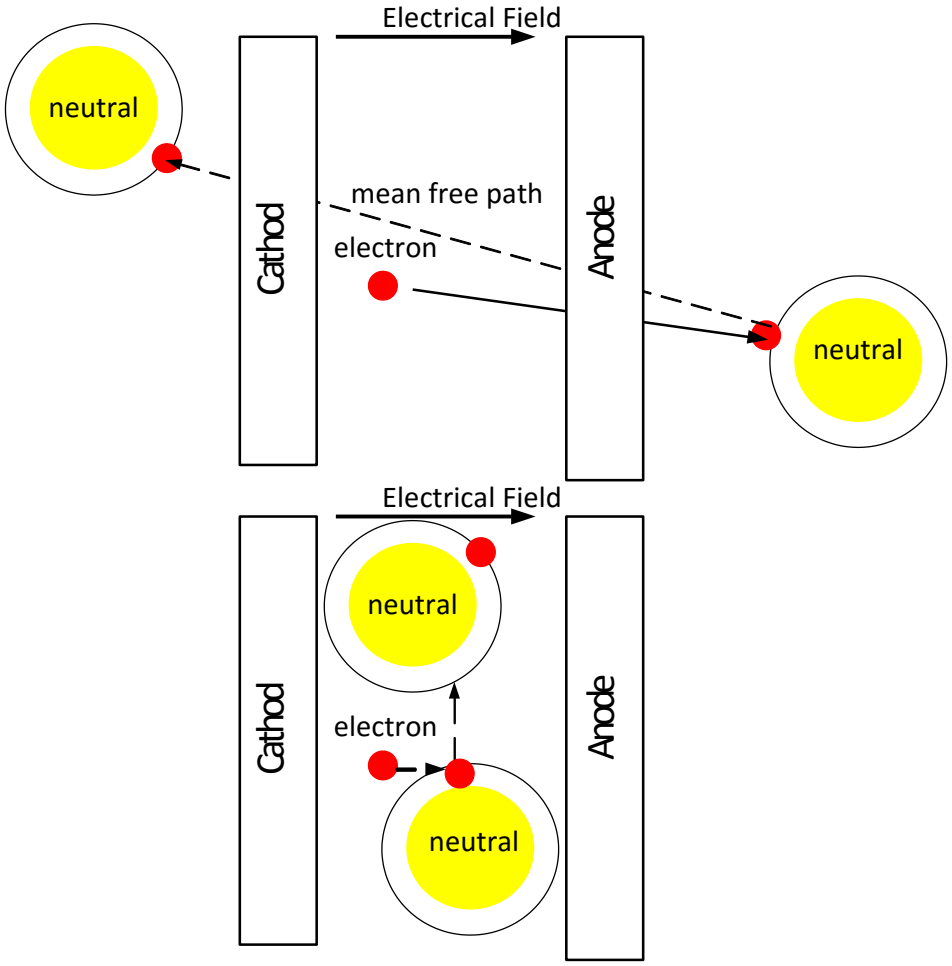

Figure 11. Illustration of Reducing Mean Free Path by Increasing Pressure

2.1.1.4 Applications of Plasma Discharge in Liquid

Discharges in liquids have been investigated for a very long time. It was studied as spark gaps for pulsed power to replace the discharge in gas [27], high voltage insulations [28, 29], material synthesis [30, 31], water treatment [32, 33], plasma surgery [34, 35], cancer therapies [36, 37], UV light emission [38, 39] and shock wave generation [40-42].

The dielectric properties of liquid is better for the purpose of insulation than the gas under atmospheric pressure. Liquids can also be used as the dielectric material for the spark gaps for pulsed power systems. Pulsed power supply needs a switch system which needs to be robust and can handle high voltage, high current and high frequency with stable repeatability. It is the same objective as using air as the dielectric material for the spark gap. The advantages of using liquid is to provide a more stable on/off switch characteristic. Before the breakdown, the liquid functions as the off switch between the electrodes. The system stays at the open-circuit state. After the breakdown occurs in the liquid, the voltage is able to rise within nanosecond or microsecond to desired values. After the breakdown, there would be many gas channels in the liquid for the plasma formation. The recovery time is limited by the quenching of the gas channel by the liquid flow or by its hydrodynamic collapse [43-45]. The electrode configuration is also very important for the discharges in the liquid. A detailed literature review will be given in the next chapter. Electrical transformers in industry are mostly used with organic liquid such as castor oil or mineral oil as the insulating liquid [46]. The bubble generation in the liquid caused by the discharge is able to add impurity into the liquid.

Those bubbles can change the breakdown voltage in the liquid, and cause the early failure for the high voltage power transformers. The generation of bubble or microbubble will also be introduced in the next chapter. By investigating the generation mechanism of the discharge based bubbles is able to benefit us knowing how to avoid their generation and the equipment failure.

Plasma discharge in liquid have been used for material synthesis as well. Plasma is able to create many chemical reactions in the liquid. In Table 1, examples of ionization, excitation, dissociation and light emission caused by the plasma in water are presented. High energy density, high production of radicals and high electrical field can all be used for the material synthesis. Figure 12 presents the gold nanoparticle and silver nanomaterial synthesis by using microplasma in liquid.

Table 1. Examples of Ionization, Excitation, Dissociation and Light Emission Caused by Discharges in Water

Ionization	$e^- + H_2O \rightarrow H_2O^+ + 2e^-$ $e^- + O_2 \rightarrow O^+ + O + 2e^-$ $e^- + H_2O \rightarrow OH^+ + H^* + 2e^-$
Excitation	$e^- + H_2O \rightarrow H_2O^* + e^-$ $e^- + H_2O \rightarrow \frac{1}{2}O_2{}^* + H_2 + e^-$ $e^- + H_2O \rightarrow \frac{1}{2}O_2 + H_2{}^* + e^-$
Dissociation	$e^- + H_2O \rightarrow \frac{1}{2}O_2 + H_2 + e^-$
Light Emission	$OH^* \rightarrow OH + h\nu$ $e^- + Na^+ \rightarrow Na + h\nu$

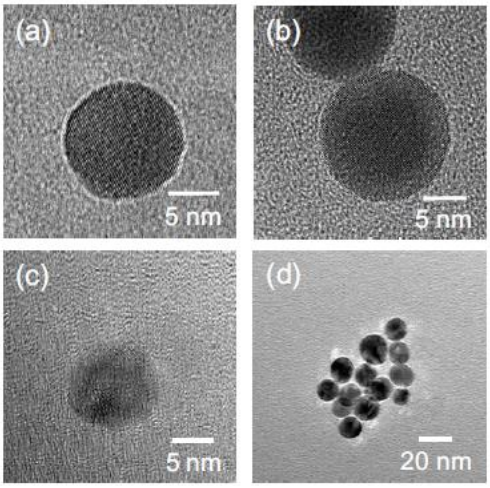

Figure 12. TEM Images of (a) Ag Nanoparticles Synthesized from Anodic Dissolution of Ag Foil and Microplasma Reduction, (b) Au Nanoparticles Synthesized from Anodic Dissolution of Au Foil and Microplasma Reduction, (c) Ag Nanoparticles Synthesized from Microplasma Reduction of Aqueous $AgNO_3$ Soution, (d) Au Nanoparticles Synthesized from Microplasma Reduction of Aqueous $HAuCl_4$ [30]

Scaled up plasma based water treatment devises can be found in water plants. They are widely used for the water pollution treatment and water pollution control. As mentioned in Table 1, the high energy electrons generated in the non-equilibrium plasma can dissociate water molecules and produce OH, H and O radicals. In addition, the relaxation of excited atoms or molecules can emit very strong UV light. These radicals are able to diffuse into the water surrounding the plasma generation sites. Radicals are generally very excited and only have micro second life time. They can quickly remove dissolved organic compound in the water. They function as oxidizers to turn any organic molecules into inorganic carbon dioxide in the water [39, 47]. The chemical reactions

caused by the plasma in the liquid is very like the plasma induced reaction in gas. The liquid molecules can be treated as the gas medium and the collision between the electrons and the water molecules to form new species or new radicals is very similar to the collision between the electrons to the gas molecules. Also in most of plasma discharge in liquid cases, there are gas channels formed in the liquid. Those gas channels function as the transition site between pure gases to pure liquids. In addition, the hydroxyl formed in the plasma discharge in liquid has much stronger oxidization characteristic, and it can also combine with water to form the hydrogen peroxide which is a very strong oxidizer. To sum up, the plasma due to its capability to form high volume of radicals and emit strong UV light has been widely used in water pollution treatment.

Plasma discharges in liquid have also been used for the research of plasma based surgery and plasma based cancer therapies. Chemically, the oxidative properties of plasma in liquid indicates it is capable of killing the biological cells. The excited radicals are able to etch the membrane of cell walls, which is able to disarm the protection layer of bacteria. Physically, the plasma discharges in liquid are able to generate very strong shock waves. The shock waves generated by high energy discharges have already been used to crash the kidney stone in human body, as presented in the Figure 13.

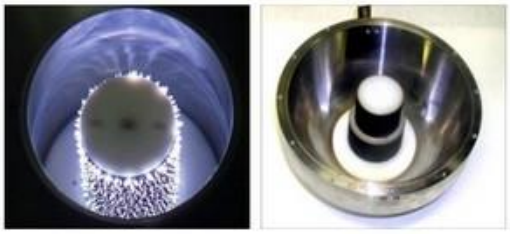

Figure 13. The Shock Wave Generator by Plasma Discharge in Water for Medical Application [48] (Copyright © Institute of Plasma Physics AS CR)

2.1.2 Plasma Generation and Diagnostic Techniques

In this research, microplasma is generated in the liquid at the microelectrode tips. The configuration of the microelectrode tips and the dielectric layer setup are a little different in each research, but the general idea that a tungsten microelectrode tip with diameter around 3 μm is covered by high dielectric epoxy is very same.

The duration of microplasma can be as short as in nanosecond scale and the duration of a microdischarge generated microbubble can be as short as in microsecond scale. In addition, the microplasma light emission generated by a low energy input can be so dim that human eyes cannot detect its existence. Two high speed cameras and one photon detection tool were all employed for the data acquisition.

2.1.2.1 Electrolysis of Microelectrode Tips

The microelectrode tip was used as the microplasma initiation site in the liquid. The size of microelectrode tip was very important. It needed to be as small as possible in micron scale, so a high electrical field can be generated at the tip.

Electrolysis was used for the microelectrode tip fabrication. A tungsten wire with the diameter of 50 μm was purchased first. The thin tungsten wire was cut into a small piece with length of 1 cm. The 1 cm tungsten wire was then soldered with a copper wire with diameter of 1 mm. The copper wire was covered with plastic coating. The solder needs to be well done so that the connection between a 50 μm tungsten wire and a 1 mm copper wire is firm enough. The soldered wire then was fixed on a stage vertically with one side dipping in NaOH solution and the other side connect to a DC power supply. A grounded tungsten plate was also placed in the NaOH solution. The solder wire was connected with the anode of the power supply and the ground was connected with the cathode of the power supply. As mentioned that the length of the tungsten wire was only 1 cm, one half of the tungsten was dipped in the solution with the rest of the soldered wire suspended in the air. The voltage used was around 30 V and gas bubbles could be observed in the solution as the electrolysis carried on. The whole half of the tungsten wire in the solution was etched, but the interface where the solution, the air, the tungsten wire contacted each other was etched much more quickly. When a notch was observed at that interface, the voltage was then reduced a little. The notch became bigger and bigger, and then the tungsten wire dipping in the solution was cut at the interface. When the dipping part of the tungsten wire began to drop in the solution, the power was cut

immediately. There was a sharp tip formed at the cutting interface with the rest of the soldered wire suspended in the air. The size of this tip was around 3 μm in our research.

The tip needed to be carefully stored since any unnoticeable contact was able to bent or damage the tip. Then the tungsten wire with solder and the exposed part (without plastic coating) of copper wire was covered by a glass tube with diameter of 2 mm. Only the electrode tip was exposed to the open air with the rest of the soldered wire was covered by a dielectric material already. After the glass tube functioned as a sleeve covered the soldered electrode, high dielectric epoxy was used to fill in the glass tube. The purpose of the high dielectric epoxy was to increase dielectric property between the tungsten tip and the liquid potentially surrounding it, and also working as a glue to hold the glass tube there permanently.

2.1.2.2 High Speed Intensified Charge Coupled Devise (Nanosecond Photo Based ICCD) and High Speed Charge Coupled Devise (Microsecond Video Based CMOS)

The duration of microdischarges and microplasmas was in nanosecond scale, and the duration of microbubbles lasted around 200 microsecond (μs) in our tests, so different high speed cameras were demanded to capture and record microplama and microbubbles. The microplasma discharge was recorded with a nanosecond gated ICCD camera, and the initiation, growth, collapse and rebound of a microbubble was recorded by a million fps CMOS video camera as presented in the Figure 14. The micropalsma was captured with a minimum exposure time of 10ns by the ICCD camera and the growth and collapse of the microbubble was recorded with the frame speed of 1180000

fps by the CMOS camera. The main differences between two cameras are that the ICCD camera could take a single photo with a nanosecond scaled exposure time, the CMOS camera however was able to take videos with a microsecond scale exposure time. Actual experimental layouts with the CMOS high speed camera mounted on the microscope are presented in the specific experimental layout section. The duration of a microplasma initiation made it impossible to be captured by the high speed CMOS camera. Even if 1 million fps was employed, it still left around 1 μs informational gap between a microplasma discharge and a microbubble formation captured by CMOS camera. Although the microplasma discharge was the only possible way to generate microbubble since there was no other sources to provide energy for phase change, videos of microbubbles by the high speed CMOS camera was still not solid enough. In order to understand more about the relationship between the microplasma and the microplasma based microbubble, an ICCD camera with nanosecond gate was used together with the CMOS camera. Both of the cameras could be trigger by the electromagnetic interference emitted from the plasma discharges or by a trigger signal sent out from a function generator or an oscilloscope. It provided much more flexibility to integrate the high speed cameras into the whole system.

Figure 14. CMOS (Copyright © Photron FASTCAM SA5) and ICCD (Copyright © Stanford Computer Optics) High Speed Camera [49]

2.1.2.3 Photomultiplier Tube Detector (Hamamatsu R928)

The light emission from the microplasma could be very dim, and the duration for such light emission could be as short as in nanosecond scale. The ICCD camera was used for the light emission detection, but the ICCD had an internal delay of 65 ns. In order to corroborate the ICCD camera, and also to compensate the first 65 ns that the ICCD camera missed, a photomultiplier tube (PMT) was used to capture the light emission from microplasma as presented in the Figure 15.

In theory, a PMT can be sensitive to a single photon emitted from a light source. The working mechanism of a PMT is presented in the Figure 16. When one photon arrives at the collection window of the PMT, an electron is excited from the

photocathode. The material chosen for the photocathode has low work function and the PMT used in our tests was made of Multialkali (Na-K-Sb-Cs) material. After the electron leaves the photocathode, it goes into a vacuum tube with 10 to 12 dynodes. The secondary electron emission is then excited from each dynode. An electrical field exists in the vacuum tube to accelerate the electron to collide with the each dynode to free more electrodes. Assuming the secondary electron emission ratio is 5 which means that one electron is able to free 5 additional free electrons. With 10 dynodes in the vacuum tube, one electron initially excited from one photon can free 6^{10} electrons. Due to this geometrical amplification in the PMT, the PMT is very sensitive and useful for weak light detection.

Figure 15. PMT with 28mm Dia., Side-on Type, Multialkali Photocathode (Effective Area: 8 x 24 mm and Spectral Response : 185 to 900 nm) [50] (Copyright © Hamamatsu Photonics)

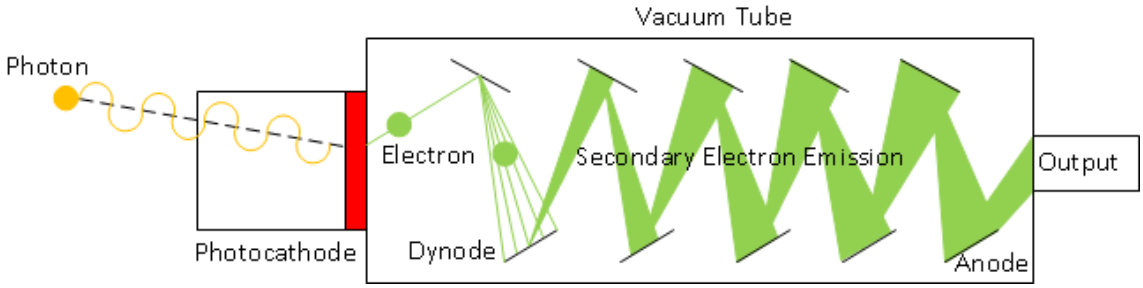

Figure 16. Working Principle of PMT

2.1.2.4 Voltage and Current Measurement

A negative DC high voltage supply (Glassman Series EH), capable of -20kV and 5mA DC, provided the initial energy for the microplasma discharge. The energy from the voltage supply charged a capacitor through a resistor, and was released to the load.

The voltage and current from the spark gap were recorded using an oscilloscope, with both a voltage probe (Lecroy S/N: 2524) and current transformer (Bergoz CT-D1.0-B) attached to the electrode. The voltage probe that was used has a maximum voltage and frequency of 20 kV and 100 MHZ. The current probe that was used had a specified rising time of 0.7 ns. For the experiments conducted the spark gap circuit consisted of a 20 MOhm resistor and 1nF capacitor. The current was set such that the pulse repetition was sufficiently low that only a single discharge occurred. Prior to discharge events, no preexisting microbubbles were observed on the probe tip. Voltage was seen to rise

rapidly, at approximately 500 V/ns, due to the rapidity of the spark gap switch. Currents and voltages reached their peaks within 10 ns and decayed to within 10% of the max values within 1-2 μs.

2.2 Literature Review

The applications of the plasma discharge in liquid has been introduced in previous chapters. Due to its unique characteristics on energy transfer, chemical activation, UV light emission, shove wave generation, etc., the plasma or discharges in liquid have been widely used to solve practical problems in real world. Fundamentally, there have been decades of research on the plasma mechanism, plasma mode, plasma discharge type, liquid properties for discharges, etc. In this subsection, a literature review concerning some key findings of the plasma discharge in liquid in past decades and the most recent microplasma generation in liquid research are presented. Many of those outstanding and thorough investigations of discharges with liquid have been inspiring our research in microplasma initiation and microdischarge generated microbubbles. This literature review is divided into plasma discharges with liquid and micro scale plasma discharges in liquid.

2.2.1 Plasma Discharges with Liquid

The research about the physical mechanism of conventional plasma discharges with liquid has focused on two topics mainly. They are electrode configuration of plasma discharges with liquid and bubble generations by discharges.

2.2.1.1 Electrode Configuration of Plasma Discharges with Water

There have been many researches on the topic of electrode configuration of plasma discharges with water. Depending on the electrode configuration and the experimental setup, different plasma discharges can be observed in water. In the Figure 17, the fabrication of a pin electrode is presented. In general, in order to create a corona discharge in liquid, only small portion of the electrode pin can expose in liquid. In the figure below, it is clear that only the tip of the electrode is not covered by the dielectric insulator. Most of the body of the electrode is covered by several layers of the insulator. It is very important to provide a high electrical field to initiate the plasma discharge in liquid. In the later chapters, the microelectrodes which were used to create microplasma with size in micron scale also employed the same idea that the most of the electrode body was covered by dielectric material except the tip.

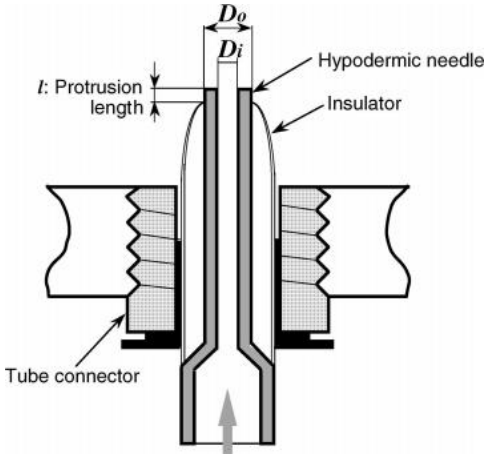

Figure 17. Fabrication of Pin Electrode for Discharges in Liquid [51] [52]

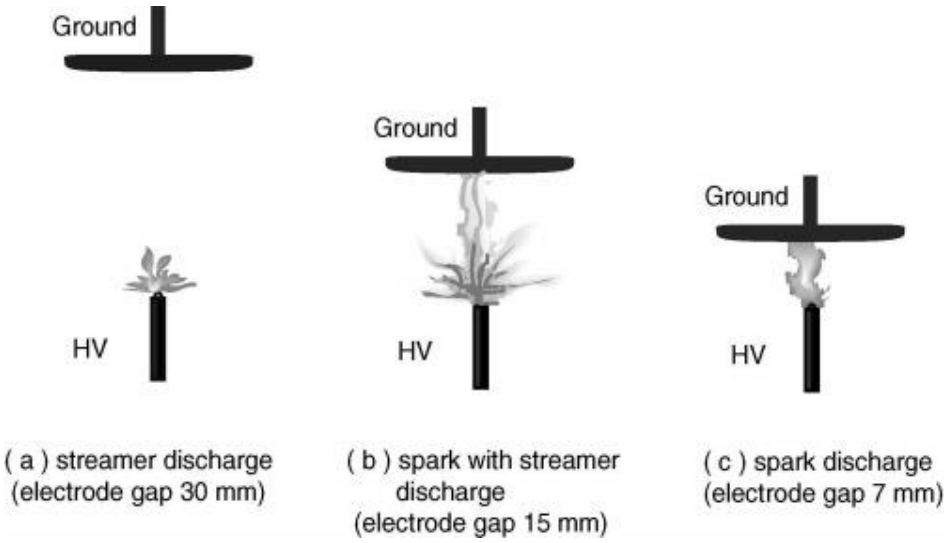

Figure 18. Schematic of Pin to Plane Discharge: (a) Streamer Discharge, (b) Spark with Streamer, (c) Spark Discharge [38].

The generation and the growth of plasma discharges in water can be a partial or a full discharge. The head of a discharge or the head of a streamer starts from one of the electrode, and may contact the other electrode directly or just extend to somewhere between two electrodes. If the head of the streamer as presented in the Figure 18(a) only extends to a very close distance, this type of discharge is regarded as a streamer or corona like discharge. The corona discharge was mentioned in the previous chapter with the gas discharge. The initiation of corona discharge in gas needs a breakdown voltage and the current for the corona discharge is very small. The corona discharge normally occurs at local high electrical field which is the reason that the corona discharge only extends to very limited distance. The streamer discharge in liquid is called corona like

discharge or sometimes corona discharge, because the discharge initiation is very similar to the corona discharge in gas. Due to the ultrashort mean free path in liquid, the mechanism of the streamer discharge in liquid is still under investigation. In addition, if the head of the discharge is able to reach the other electrode, the discharge is regarded as the spark or the arc as presented in the Figure 18(b) and (c). A conductive bridge is able to be formed between two electrodes when a spark or an arc discharge happens. The difference between a spark and an arc is not very obvious. The spark discharge is more transient, and has lower energy transfer comparing with the arc discharge. When an arc plasma is created, the electron creation mechanism is thermionic emission and the plasma is turned into thermal plasma.

The comparison between the discharges in gas and the discharges in liquid presented in the Figure 19 is that the glow discharge (homogeneous discharge) is able to be created in gas as the transition between the corona to arc, but only the spark (inhomogeneous discharge) is able to be generated between the corona to arc in liquid. A most common setup of parallel plates for plasma generation in gas environment can barely initiate a plasma in liquid. Due to the unique characteristics of discharging in liquid, various electrode configurations have been designed to generate the discharges. Most of the setups for discharges in liquid are like the pin to plane setup that provides a typical inhomogeneous electrical field. The local electrical field is provided by a high voltage and a sharp electrode.

Figure 19. Discharge in Liquid and Long Time Exposure for Multiple Discharge Channels [23](Copyright © PEDL).

Many researches have been done on the configuration of the electrodes for the discharges with liquid. In the Figure 20, three main ideas of the discharges with liquid including two electrodes immersing in liquid, only ground in the liquid with high voltage pin electrode above the liquid surface and the plasma generation in artificial pre-exist gas bubbles, are presented [29, 53-55]. The most common discharge methods for the immersed pin to plane setup (Figure 20(a)) is the discharging with a capacitor with a spark gap as a trigger. Discharges with the high voltage electrode above the gas surface and the ground in liquid is a semi-liquid discharge setup (Figure 20(b)). The discharge for this setup only occurs above the liquid surface, but since the air above the surface is probably saturated with vapor and the ground is the liquid, this setup is still regarded as

the discharges with liquid. It is well known that a DC excited atmospheric pressure glow discharge (in air) between metal electrodes tends to be unstable to radial constriction leading to arc or spark. With water electrodes it is possible to obtain diffused atmospheric pressure glow discharges in air [56]. Discharges in artificial bubble in liquid is a very interesting phenomena as well. Since the mean free path in the bubbles is much longer than the mean free path in liquid, striking voltage for the breakdown in the bubble is much lower than that for surrounding liquid. When gas sites are provided in the liquid environment, the plasma is initiated in the bubbles. The idea of creating discharge in liquid surrounding gas bubbles can be extended into the Figure 21. In Figure 21(a), the electrodes setup is like the pin to plane discharge except that the high voltage discharge is directly in a big pre-exist bubble [57]. In Figure 21(b), it is still a pin to plane discharge, but the high voltage electrode is on the same side of the ground plate. In addition, the artificial bubbles are continuously blown into the liquid. The discharge actually happens in different bubbles [58]. In Figure 21(c), one bubble is blown into a capillary, and the electrodes is a plate to plate setup. Since the location of the capillary and the electrode plate are fixed, the plasma discharges in the bubble is due to the high electrical field in the liquid [59]. The discharge in a single bubble trapped in a capillary is very same to the discharge in the Figure 20(c). In a pin to plate liquid streamer setup the pin electrode has often a needle and is used to inject gas bubbles into the reactor to increase radical formation in the Figure 22(a) [60]. A similar setup with a capillary electrode surrounded by a ceramic tube is presented in the Figure 22(b) [61]. A DC voltage is used to generate the discharge in a gas flow through the capillary. Continuous

bubbles flowing between two metal electrodes is also employed for the discharge in the artificial bubbles in the Figure 22(c) [62]. Even when the bubbles are not in contact with the electrodes, discharges can also be generated in the bubbles due to the big density difference between the gas and surrounding liquid. In the Figure 22(d), the gas film is used to function as a gas layer for discharges. The gas layer is separated from the ground electrode by a water. Due to gravity, the gas layer can only touch the upper electrode [63]. The discharges are found to be streamer and to propagate along the bubble surface.

DC discharges induced bubbles in capillaries have been investigated by many groups [58, 64-68]. In the Figure 22(e), a submerged liquid jet is used to generate a plasma shell at the jet boundary. Threshold breakdown voltages are reduced considerably when stream velocity of 30m/s is employed because of the formation of the cavity bubbles [69]. Discharges in a gas channel with a liquid wall between electrodes was presented in the Figure 22(f). The configuration consists of two tubes with the metal electrodes inserted and a gas flow is applied to both. These gas flows merge into each other and form a stable gas channel [70]. It is an arc discharge that is cooled by the water wall.

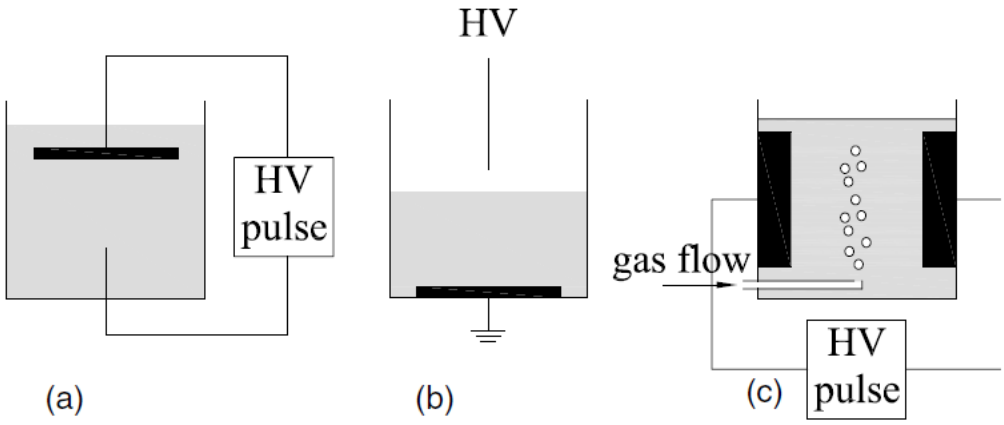

Figure 20. Typical Electrode Configurations for Three Different Types of Discharges with Liquids (a) Direct Liquid Phase Discharge Reactor [57], (b) Gas Phase Discharge Reactor with Liquid Electrode [58], (c) Example of Bubble Discharge Reactor [59].

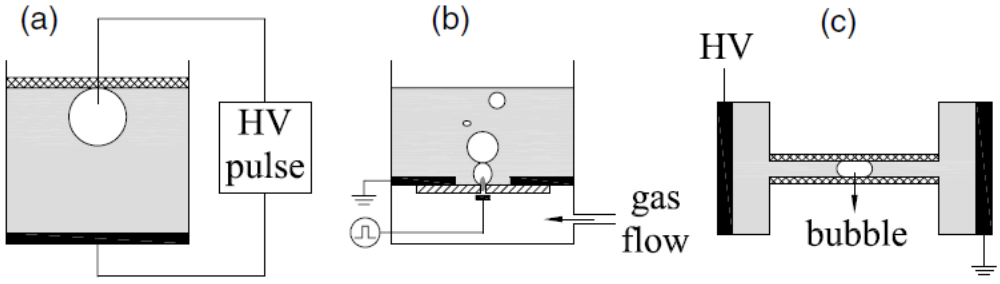

Figure 21. Overview of Different Electrode Configurations Used to Study Electrical Breakdown of Bubbles in Liquid [60].

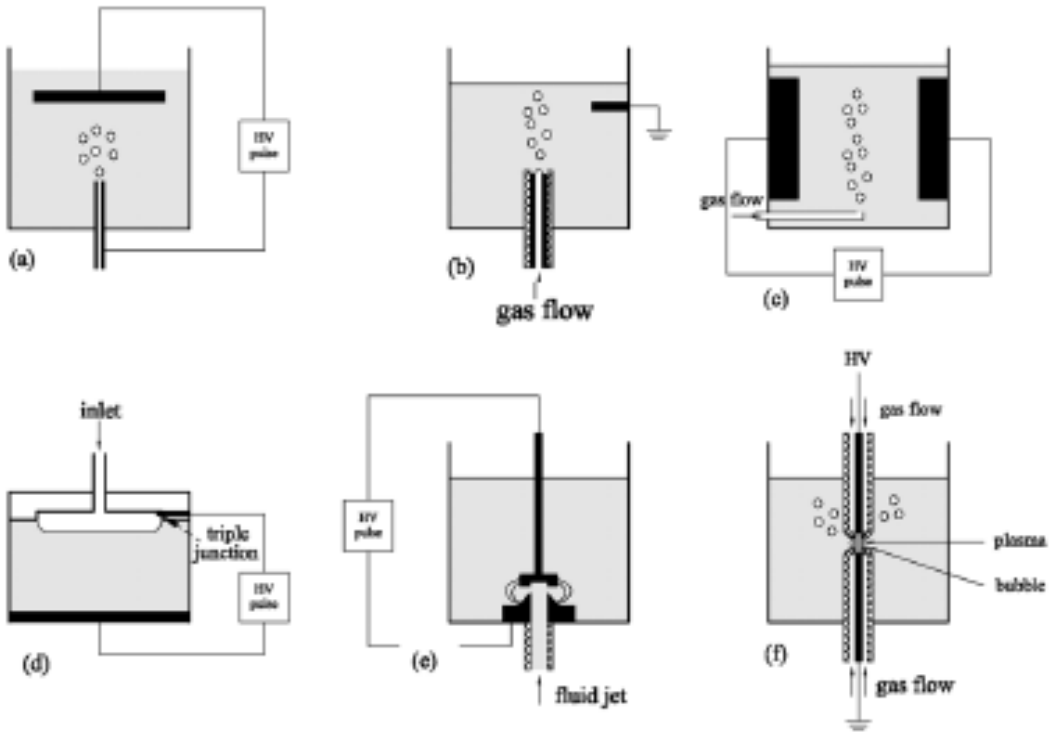

Figure 22. Experimental Setups Developed for Discharges in Bubbles, (a) Bubble Corona Discharge Reactor [60], (b) Capillary Gas Flow Bubbling Reactor [61], (c) Volume Pulsed Discharges Bubbling Reactor [62], (d) Bubble Surface Discharge Reactor [63], (e) Discharge Reactor with Submerged Liquid Jet, (f) DC Arc Discharge Reactor in Gas Channel with Liquid Wall [58, 64-68]

Most of the electrode configurations of the plasma discharges with water are pin to plate or plate to plate discharges. The major differences are where to place the high voltage electrode tip for some cases or where to place the artificial bubbles if there is any. Twelve different setups have been presented in previous paragraphs. As mentioned early, only small portion of research on discharges with liquid was directly on the full discharges in liquid. Since the low energy input discharge is not an easy mission, when a

discharge is initiated the streamer propagated in branches. The important finding of these researches is to provide us ideas to fabricate our micron scale microelectrodes in experiments. Briefly speaking, the electrode configuration used in our tests is a typical pin to plate setup except that the size of the pin is around 3 μm and only corona discharges have drawn us attention.

There are still some other electrode configurations which were mentioned in different papers. They were not used very common, so a brief introduction of their application is presented here. In the Figure 23(a), water film instead of bubble film is used to flow on the electrodes. The discharge electrodes functions also as the structure to support the whole reactor. The flow of liquid can cool down the system when an arc discharge is initiated. In the Figure 23(b), droplets of water are used to cover the electrodes. It can be treated as the setup in (a) with an open angle of 180^{o} and no flow. The setup in Figure 23(c) has been used more commonly than those in (a) and (b). The idea of high voltage pulse is to control the energy and to initiate corona discharge. But the high voltage electrode is still above the liquid not immerses in. The setups in Figure 23(d), (e), (f) are designed for the liquid treatment on dissociation or sterilization purpose. The air blow or the liquid flow caused by gravity can cool down the electrodes. In addition, the unconventional design of the electrode shape is to accommodate this application.

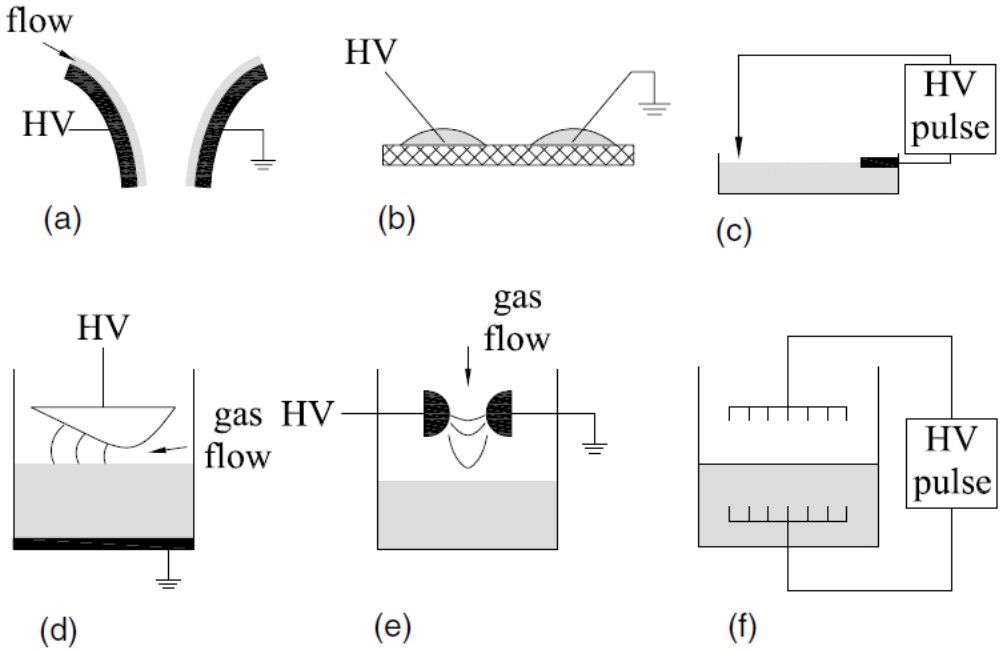

Figure 23. Different Electrode Configurations Used to Study Electrical Discharges with Liquid, (a) Discharge Reactor between Two Liquid Electrodes, (b) Setup to Study Discharges between Two Droplets, (c) Water Surface Discharge Setup, (d) Gliding Arc Reactor with Active Water Electrode [71], (e) Gliding Arc Reactor with Passive Water Electrode, (f) Hybrid Reactor [72].

2.2.1.2 Bubbles Generation

The generation of bubbles by discharges is still not very clear. Several possible mechanisms can explain the generation. Since the discharge generated bubbles are created in a complicated environment, none of the possible mechanism is exclusively conclusive. Two main hypotheses are electrostatic crack mechanism and the joule heating mechanism.

2.2.1.2.1 Electrostatic Crack Mechanism

Within a short timescale, the liquid can be treated as a solid due to its incompressible characteristic in short time scale. A crack that normally occurs to solid is able to be formed in liquid with the similar mechanism under electrostatic stress. Such crack is able to explain the propagation of the branched streamers and the bubble formation along the streamers in liquid. The electrostatic crack mechanism includes two main steps [73], small molecular vacancy which is thermoelectrically induced and a crack formation by electrostatic stress.

The idea for the initiation of small molecular vacancy is similar to the initiation of crack on solid. The concept of the defects in solid is borrowed here to describe those imperfect spots in liquid which can be later used to create the initiation site for the cracks. The criteria for a crack formation can be lowered by an electrically enhanced hole. The theory to describe such electrically enhanced imperfect is called Lippman Effect. The potential difference across an interface is balanced by a mechanical tension on the interface (surface tension). The surface tension can be significantly affected by the potential differences at the liquid to solid interface. When a high local electrical field is formed, the surface tension which limits the propagation of the crack from tearing the liquid can be reduced, as illustrated in the Figure 24. When the local surface tension is so low that the imperfect spot can develop from a molecular scale spot to a mesoscale crack, the preparation of bubble generation is finalized. The localized high electrical field (MV/cm) is normally formally in places with high curvature such as a spike or a needle tip, as presented in Figure 25.

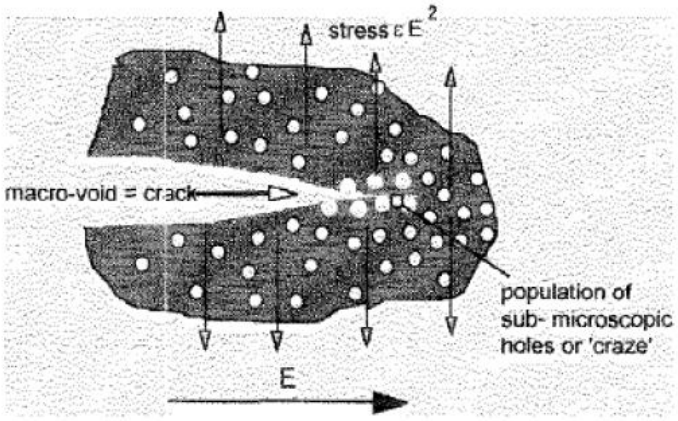

Figure 24. Illustration of Electrical Holes Formation by Electrostatic Stress in Liquid[73]

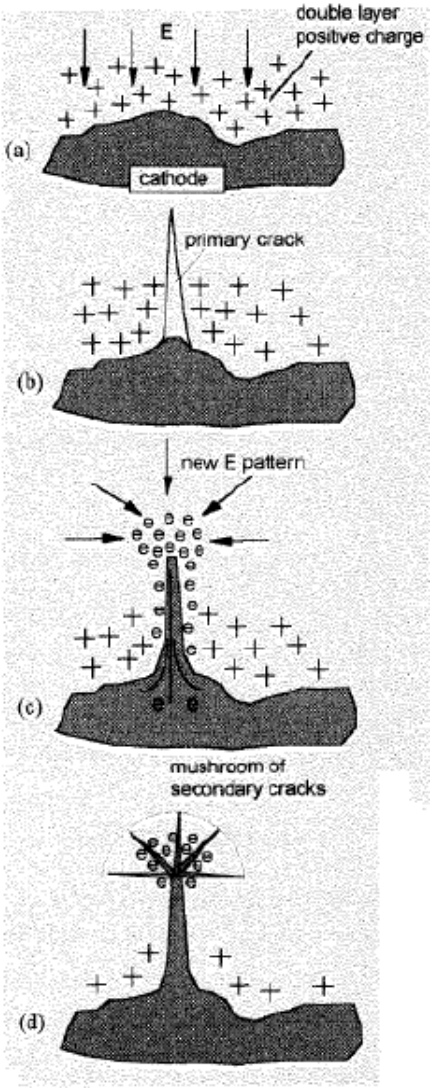

Figure 25. Illustration of Formation of Localized High Electrical Field at Spark Tips [73]

2.2.1.2.2 Joule Heating Mechanism

The joule heating mechanism is rather easily to understand. The discharge in liquid is initiated by a high voltage, and when the discharge is formed the current is transmitted in the liquid. The current is determined by the electrical impedance of the liquids and the applied voltages. The impedance passed by current is able to generate joule heat. When the joule heat is sufficient to initiate a local phase change, a bubble can be formed in the liquid.

2.2.2 Micro Scale Plasma Discharges in Water

The conventional mesoscale plasma discharges in liquid and the bubble formation caused by discharges in liquid have been discussed in previous subsections. The microscale plasma and microscale bubble began to draw our attention in the recent decade. Due to the small size and the short duration, the experimental investigation of the microplasma and microbubbles has been proved to be a challenge in this field.

2.2.2.1 Four Theories of Mechanism of Microplasma Initiation

Four different theories of the mechanism of microplasma initiation have been proposed in literatures. As same as the mechanism of discharge generated bubbles, these four theories are not exclusively correct either. One of the objective of the research covered in this dissertation is to experimentally and theoretically prove which theory has more grounds. Two mechanisms of the electrostatic cracking theory and the Joule heating theory have been introduced for the bubble formation in previous section. The

unclearness of the mechanism of microplasma or plasma generation in liquid actually is very similar to the mechanism of the discharge generated bubbles. Moreover, the main disagreement is whether the plasma is directly generated in liquid, or a microbubble is formed picoseconds or even shorter than picoseconds prior to the generation of the plasma.

As for the former opinion, the idea is that the Townsend avalanche and the secondary emission actually directly happen in liquid without the presence of any gases as showed in the Figure 26 (a). The disadvantage of this theory is that electrons seem to be hard to acquire that much energy to ionize atom or molecules in liquid. The mean free path between collisions in liquid is much smaller than that in gas (>1000 times smaller), and within such short mean free path the breakdown needs to be on order of 10^6V (deduction from Paschen's Curve) to strike a breakdown in liquid. The experimental results, however, proves that much lower voltages of 10^3 V were able to strike a breakdown.

As for the latter opinion, the idea is a low density region (gas bubble) is somehow formed very quickly prior to the generation of microplasma, as presented in the Figure 26(b), (c) and (d). The gas-phase sites in liquid becomes the inception site for the plasma. The fundamental difference of this idea from previous one is that this idea supports the generation of plasma being from a gas phase, even if the gas-phase site is very small and formed only picoseconds before the plasma. The gas bubble here is not actually a traditional concept of bubble. It is actually a low density region surrounded by

high density liquid. Furthermore, this low density region is crucial for a longer mean free path and a higher possibility for secondary electron emission.

One more theory of the origination of microbubbles is added to the other two theories proposed in previous subsections. Other than the electrostatic cracking mechanism and Joule heating mechanism to form a bubble initially, a third mechanism is that nanometer gas bubbles that already exist in liquid provide the site for plasma generation. One of these nanobubbles happens to be in front of the local high electrical field during a discharge created by the microelectrode tip, and the nanobubble then functions as the inception site for the bubble generation.

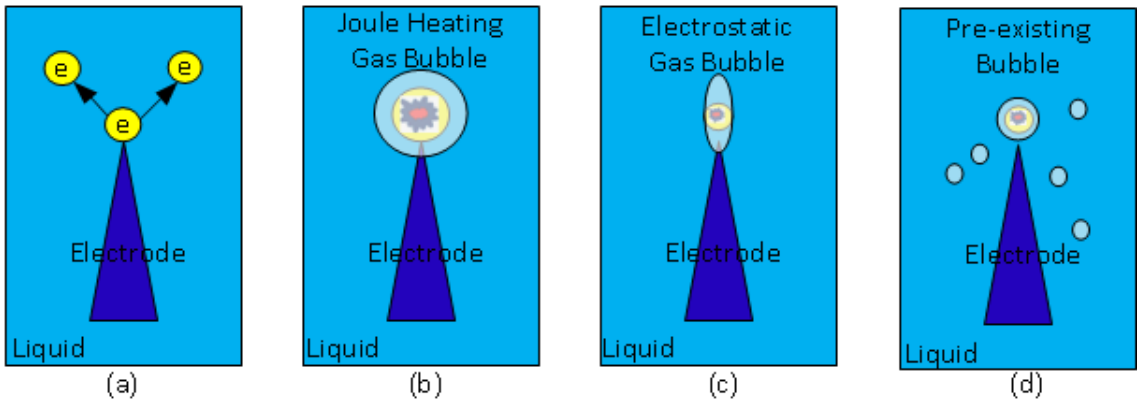

Figure 26. Schematic Illustration Mechanism of Microplasma Generation in Liquid, (a) Direct Electron Avalanche in Liquid, (b) Joule Heat Generated Microbubble, (c) Electrostatic Cracking Theory, (d) Pre-existing Microbubble

2.2.2.2 Microbubble Generation by Microdischarge in Water

Applications of microplasmas in liquid [74-78] for spectroscopy and nano-material synthesis were reported within last decade and are generally similar to those of macroscale plasmas in liquids but with added benefits of spatial localization, lower energy, and more non-equilibrium chemistry. One of advantages of microplasmas generation in liquid is that the bulk of the liquid remains at ambient conditions. Also ambient aqueous media are of biological interests [79, 80]. As live tissues, organs, and certain sensitive substrates cannot survive high energy meso-scale plasma in liquids, and liquid plays major part of biological systems, microplasmas in liquids can be applied to many biological applications such as plasma surgeries[81, 82], cancer therapies, bacteria sterilization, water treatment, etc [83-85].

In this work we investigate plasmas with maximum size less than 30μm, generated without any preexisting bubbles, but apparently existing inside a microbubble generated commensurate with the plasma. It is presented that for around one hundred nanoseconds that microplasma and microbubble coexist, after which only the bubble is present. We first reported these types of low energy discharges in applications as unique non-equilibrium systems [86]. Our long term goal is to understand the initiation mechanism and time dependent state of the microplasma: neutral density, plasma density, and temperatures. Here we focus on one aspect, the dynamics of these microscale plasmas in liquids and the micro-bubbles they generate. The dynamics of the bubble are measured, and through a Rayleigh-Plesset model, the time dependent state of the gas in the bubble is determined. This tells us the environment in which the plasma

was created, and also indirectly with some assumptions regarding mass and energy transfer some bounds on the energy and mass associated with the plasma.

This work complements and relies upon ongoing research in this area. In studies of mesoscale plasmas in liquids, without pre-existing bubbles, a transient microplasma and microbubble [87] with diameter around 500μm was captured with primary and secondary coronas, and evolves into a macroscale discharge. The properties of such microplasma in liquid are significantly different, being higher energy, than those studied here; however, some aspects of the transient primary negative streamer, namely its symmetry are similar to the discharges observed here. Microdischarges in pre-existing gas bubbles in liquid have also been studied [88-90]. In those papers, the bubbles 1-3cm in size were injected into liquid and the mechanism of microplasma initiation occurred in gases. Properties of the gases in preexisting bubbles are near ambient pressure and the sizes of the bubbles are typically noticeably larger than the plasma. While the sizes are different, there are probably direct, Paschen scaled [91], similarities between these microdischarges and those we create in smaller bubbles at higher internal pressures. However, due to the small size of our systems the propagation of the plasma within the bubble cannot be observed.

The principal mechanisms of microplasmas initiation in liquid are still under study [28, 40, 92-94], and are beyond the scope of a single paper to answer. In general the generation of microplasmas in liquid is similar to generating a corona in air. It requires atoms or molecules being ionized in an electrical field. The number density in liquid is significantly higher than that in gases. The effective pressure which reflects the

mean free path is considered in Paschen's Law [91]. In Paschen's law ($nd = \text{Constant}$), with the same breakdown voltage, in order to decrease the dimension 'd', the number density 'n' has to be increased correspondingly [95, 96]. For plasma in liquid, sharp and tiny tips were employed to create a high electrical field to maintain the reduced electrical field (E/n) for corona discharges. Also these electric fields are rapidly applied, at rates of around 500 V/ns to reduce electrochemical energy losses and dissipation. During the time of the application of the electric field, when or if a low density region (here-after referred to as a bubble) is generated the reduced electric field rises in that region facilitating breakdown. While slightly lower in density than the liquid, the initial bubble may be very high pressure, even sufficiently high pressure to be supercritical, with no clear interface with the liquid. In such a sense microplasmas in liquids are similar to discharges in a high pressure gas environment. The necessity and existence of a bubble is a point of contention [97]. It is our direct observation, in this paper, that a bubble is present in the liquid both at the same time as, and after the plasma. This contradicts some of the work of Dobrynin [20], but conditions are sufficiently different here (namely negative polarity and conducting solutions) to leave the general question as to the conditions for the presence of bubbles still open.

As already alluded to in our review of prior works, in this paper microplasmas based microbubbles are studied experimentally and theoretically. In our experiments, a single microbubble was observed with the microplasma initiation. The microbubble formation and the corresponding phase change are induced by energy release during the discharge. It was observed that the microbubbles were generated very rapidly. The

precise mechanism of the microbubble generation, however, is beyond the scope of this paper. This paper focuses on the microbubbles' dynamics within the first 40~50μs. With two sophisticated high speed cameras which can take million fps videos and nanosecond photos respectively and a 2GHz oscilloscope, the detailed study on energy inputs and images of microplasma and microbubble at the initiation stage are given in this paper. For the first around 100ns, the microplasma and microbubble coexisted together, with the microplasma observed to be inside of the microbubble. After around 100ns, the plasma disappears. The microbubble keeps on growing eventually oscillating in size with discharge energy dependent amplitude and frequency. The decaying oscillation of the microbubble's beyond about 50μs generally compare well with prior hydrodynamic studies and are not the focus of this paper. The microbubbles studied in this paper are spherical in shape for their first cycle. No branches were observed from microplasma's and microbubble's initiation. Conditions for aspherical and branched bubble could be attained but are not the focus of this dissertation. These spherical bubble conditions are unique to the low energy plasmas studied, and greatly facilitate analysis of the bubble dynamics. Established studies of vapor based microbubbles in liquid from boiling and cavitation literature [98] are used to describe the hydrodynamics of the bubble. The investigation of a microbubble at the very beginning stage assists our understanding of microplasmas. In the theoretical study of the microbubbles' dynamics in this paper, a Rayleigh-Plesset model is used to establish a momentum balance of a spherical bubble. For the first 40~50μs after plasma disappearance, still within the first cycle of bubble oscillation, there is no significant mass and energy transfer from the bubble allowing us

to estimate the conditions of the gas inside the bubble. The radius change calculated by the RP model matched well with experimental results, and the thermodynamics properties and initiation energies are estimated based on model results.

CHAPTER III

MICROPLASMA LIGHT EMISSION IN LIQUID

3.1 Section Overview

A low density region, here-after referred to as a microbubble, and light emission can be generated from a microdischarge in liquid. Several physical mechanisms of the formation of bubbles and plasmas are possible. This paper shows that a microbubble can be initiated before a microplasma during a microdischarge in liquid. Energy inputs to liquid were adjusted by changing the magnitude of the pulsing voltages, here-after referred to as applied peak voltages (APVs), the duration of discharges, the conductivities of liquid, and the size of microelectrodes. A DC power supply and spark gaps were used together as a nanosecond rise time pulsed power source. The pulsing power can output repeatable microsecond or nanosecond pulses with APVs from -2kV to -12kV. Deionized water with NaCl of two conductivities, 1990μS/cm and 17600μS/cm, and two microelectrode tips with diameter of 3μm and 5μm were tested. Visual images of microbubbles and microplasma light emission were captured by a nanosecond gated intensified CMOS camera (ICCD). The light emission from microdischarges could also be detected by an opto-isolated photomultiplier tube (PMT), which was used to provide continuous monitoring. For the microsecond duration discharges, the generation of microbubbles and microplasma light emission was observed in all tests. However, for the nanosecond discharges, there were specific thresholds for light and bubble generation affected by the conductivity of liquid and the size of microelectrodes. With

the high conductivity (17600μS/cm), the plasma light emission was always generated with a microbubble. With the low conductivity (1990μS/cm), on the other hand, three different phenomena were observed sequentially by changing the APV from -2kV to -12kV. These phenomena included 1) No bubble formation and no detection of microplasma light emission, 2) Bubble formation but no detection of microplasma light emission, and 3) Bubble formation and the detection of microplasma light emission. The three phenomena and two thresholds of APVs separating them were verified by using two microelectrode tips of different sizes. The results show that for ns-rise time discharges only at low energy can the generation of microbubbles and microplasma light emissions be distinguished, and only at lowest energy (~ 0.5 mJ) microbubbles can be initiated before a microplasma. The APV thresholds for two tips were different, but the electrical field at the tip for these thresholds was consistent at ~1.1GV/m for the microbubble generation, and at ~1.4GV/m for microplasma light emissions. From our observation, a microbubble can be initiated at lower energy and before the generation of a microplasma during a microdischarge in liquid.

3.2 Experimental Setup

Microbubbles and microplasmas were generated at a microelectrode tip in liquid. A 3D drawing of a microdischarge in liquid is presented in Figure 27. The electrical conductivity of liquid was controlled by adjusting the mass concentration of NaCl in DI water (1990μS/cm and 17600μS/cm are two conductivities reported in this paper). Tungsten (W) microelectrode tips were made through electrolysis and the tip diameters

in this research were around 5 μm. In order to reduce electrical leaking, epoxy (Loctite Hysol Adhesives) and a glass tube (OD: 1mm) were both used as an electrical insulation layer. The home-made pulsing circuit could output pulses with APVs ranging from -2kV to -12kV. The circuit consists of a DC high voltage power and spark gaps, and it could output microsecond or nanosecond duration high voltage pulses. Microsecond and nanosecond discharges, due to their different discharge durations, were employed to achieve different energy inputs to liquid. The schematic diagram of the pulsing power is presented in Figure 28. This circuit is the same as used previously [99]. An ICCD camera (Standford Computer Optics Inc. 4 Picos ICCD camera) was used to detect the microplasma light emission and record the formation of microbubbles. Electromagnetic interference (EMI) from the pulsing power was used as the trigger for the ICCD camera. The observation of the microbubble and microplasma was through a microscope with a gooseneck lamp as back lighting and without any lighting or ambient light. The PMT and compatible circuits were a Hamamatsu R928 & C6270 coupling with a 50 Ω resistor. The experimental results reported in this paper were all from the highest gain setting (1200V) of the PMT. The PMT has a response time of 1.2ns, and the output voltages of PMT are proportional to the intensity of the light inputs.

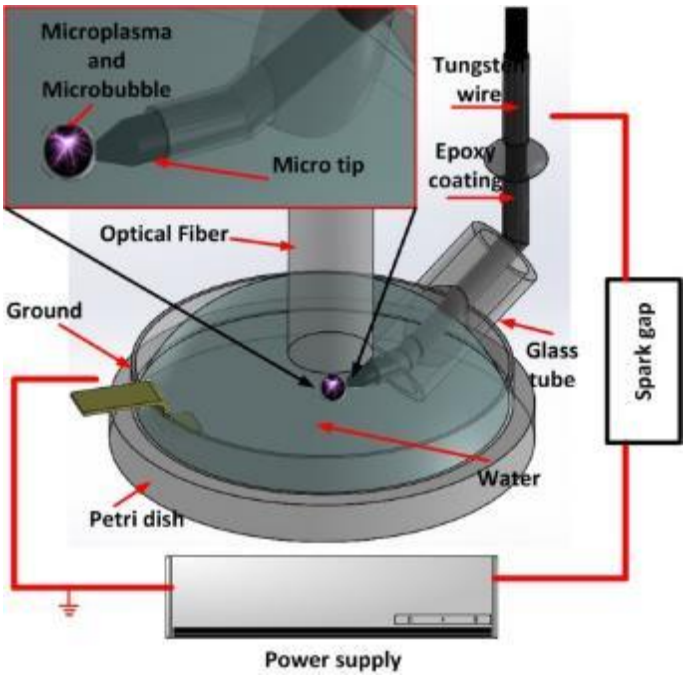

Figure 27. 3D Drawing of Microelectrode Tip Immersing in Water with Microplasma and Microbubble Generation

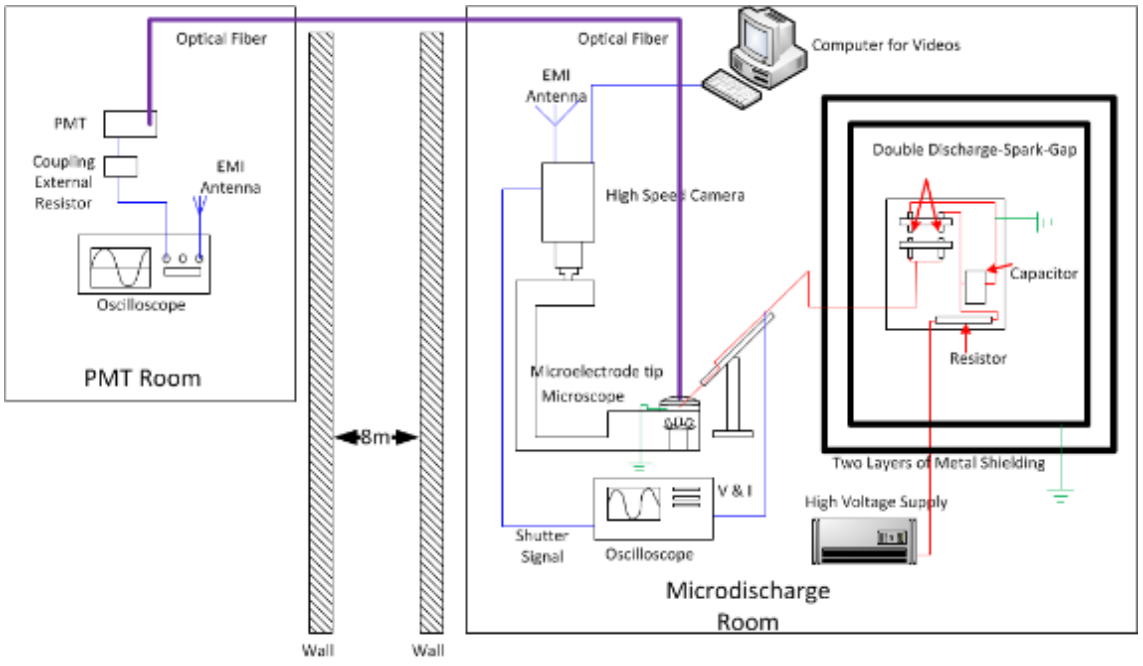

Figure 28. Schematic Drawing of Experimental Setup.

3.2.1 Reduction of EMI for PMT Measurement

EMI could be emitted by the pulsing power and transmission circuits, which significantly deteriorate the performance of the PMT. The light emission from microplasmas could be extremely dim, and the PMT output could be very low correspondingly. EMI created from discharges, hence, was able to overshadow the weak PMT output due to the low level of light from the discharge. Likely for this reason, PMT results for pulsing microdischarges in liquid are difficult to find in literature. Prior to specifically addressing various EMI issues, the PMT outputs were severely

compromised by EMI, as presented in Figure 29(a). The interference was so strong for the first several microseconds after the initiation that it was even beyond the detectable limits of our oscilloscope, and such interference lasted around 6μs to 7μs, far longer than the duration of a discharge.

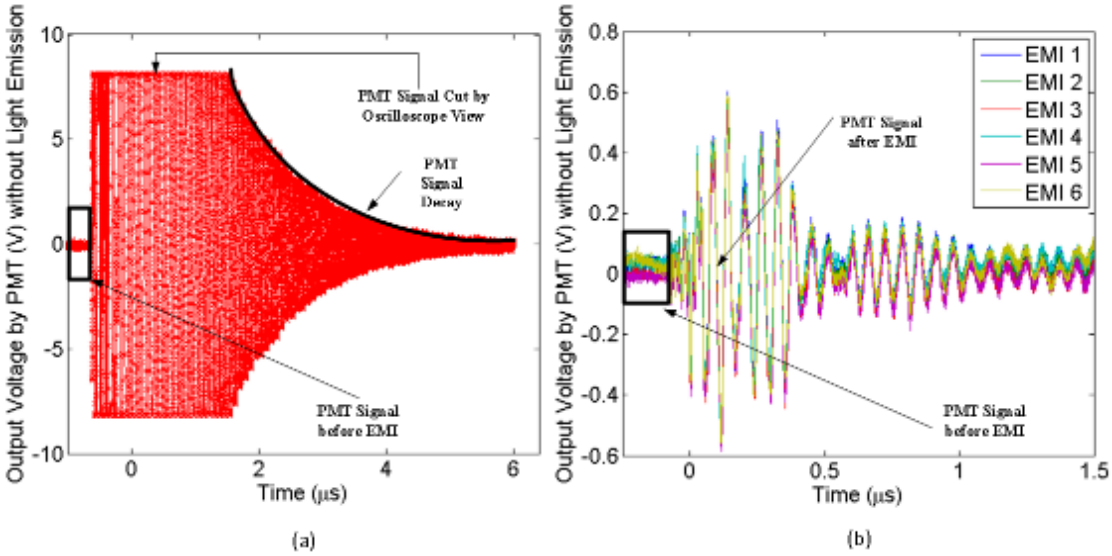

Figure 29. Output Signals of PMT Affected by EMI; a) Prior to Shielding, b) After Shielding and Isolation Measures. Flat Cut at First 2 μs of (a) Caused by Limitation of Oscilloscope's Range

To isolate the PMT from EMI, shields for switching circuit, shielded twisted pair wirings for the pulsing transmission and an optical isolation were all employed. In

Figure 28, a schematic experimental layout is presented. Two grounded metallic boxes were used to cover the spark gaps as the first barrier of EMI. Then a 12-meter optical fiber going through two sheetrock walls transmitted light emission from microdischarges to the PMT, which functioned as an optical isolator of EMI. This setup not only provided a certain physical distance between the EMI source and the EMI antenna (PMT), but also provided some barriers between them. One end of the optical fiber was placed 0.5 mm above the microelectrode tip and the other end was placed on the PMT collection window. It turned out that the Faraday cage firstly made for the PMT to isolate EMI increased EMI as it acted as a pickup antenna. The PMT was then assembled in a plastic box to reduce the pickup of EMI. The same discharges presented in Figure 29(a) were then performed with all measures of EMI isolation, and it is clear that the EMI was significantly reduced on both of the magnitude (reduction to ~1.5%) and the duration (reduction to ~21%), as presented in Figure 29(b). As a result, the electrical noises caused by EMI were low enough, and the PMT output became quite distinguishable. Moreover, six successive EMI signals, as presented in Figure 29(b), showed that the EMIs are highly consistent under the same discharge conditions. The consistency of the EMI from the discharges would be used in the later section to separate the real light signals from the EMI.

3.2.2 Energy Inputs to Liquid for Microdischarges

There are three energies to be considered in these systems. First the energy stored on the capacitor, E_C, second the energy transferred to the liquid, E_L, and third the energy

which is dissipated in the plasma discharge, E_P. Since there are two spark gap configurations, the single spark gap and the double spark gap, the energy stored on the capacitor is not the most relevant. For the single spark gap the energy input into the liquid is roughly the energy stored on the capacitor, E_L/E_C ~ 90%. For the double spark gap the energy input is significantly less since there is energy flow through the second gap, E_{SG2}, and typically E_L/E_C ~ 5%, though it can vary significantly with immersed electrode conditions. The energy transferred to the liquid, E_L, is calculable from the measured voltage and current traces. The energy transferred to the plasma is more difficult to determine since there may be parasitic losses such as those resulting from the fluids conductivity. Such differences of energy input to liquid and energy observed to pass through the plasma were addressed in previous research [5]. E_P/E_L ranged from 0.01% to 80% and was significantly smaller for single spark gap configurations such that E_P/E_C always ranged from 1% to 5%.

Considering the energy transferred from the circuit to the liquid, in practice it is a function of the APVs, the duration of discharges, the size of microelectrode tips and the conductivities of liquid. In this paper, APVs were varied systematically, it was found that while keeping the APV and discharge duration constant, the energy input from the circuit to the liquid was further determined by the conductivity of liquid. We observed that E_L increased with increased conductivity at the same APV. Explanation of this is not so straight forward. A simple consideration to explain this might be to consider the plasma and water resistance in series. In which case high conductivity would increase

energy input. However this may be an over simplification considering short time scales and double layers in conductive liquids.

Other than the electrical conductivity of the liquid, the size of microelectrode tips was also able to change the fraction of the energy which is input to liquid. In Figure 30, energy input to liquid vs. APVs from two microelectrode tips (around 3μm and 5μm) is presented respectively for nanosecond discharges. These results suggest that for a smaller tip E_L/E_C is higher. This is likely due to the higher fields and thus more rapid breakdown for the smaller tip, which apparently has a smaller impedance relative to the second spark gap than the breakdown for the large tip relative to the second spark gap. Smaller tips create a higher local electrical field (E~V/R) which can contribute in several ways to facilitate generation of a bubble. First they can reduce the surface tension through the Lippman Effect [73]. This lower surface tension makes a microbubble initiation a lower energy process. Electron field emission can also be initiated at around 1 GV/m. Injections of electrons into the liquid creates electro-hydrodynamic forces (EHF) which can generate forces and crack the liquid. Field emission and EHF could occur without light emission. A high field also increases electron avalanche and ionization processes (however these will typically be visible by increased electronic excitation processes and light emission). The inception of microbubble and the initiation of the plasma reduce the electrical resistance in liquid, which draws more energy that is diverged from E_C to E_{SG2}. On the other hand, for longer duration discharges, the microsecond discharges (single spark gap), always show both microbubble and microplasma initiation because of their higher energy input to liquid. Since threshold for

plasma initiation were only observed for the nanosecond discharges (double spark gap), they are the focus of this study.

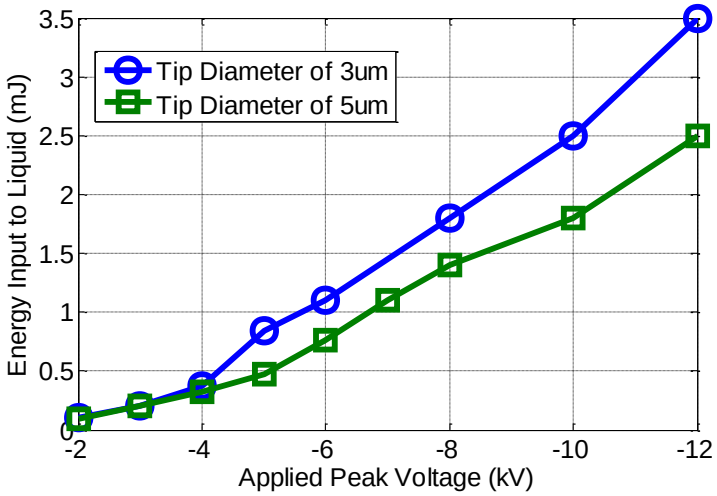

Figure 30. Energy Input to Liquid with Different APVs of Nanosecond Discharges in Liquid

3.2.3 PMT Signals for Discharges after Shielding of EMI

The PMT outputs of microsecond and nanosecond discharges are presented in Figure 31. In Figure 31(a), light emission from nine successive microsecond discharges were shown, and in Figure 31(b), light emission from ten successive nanosecond discharges were presented as well. The APVs for the microsecond and nanosecond discharges in Figure 31 were both -8kV. The PMT outputs a voltage signal that is

proportional to the light intensity it collects. The peak outputs for microsecond discharges are around 4V and the peak outputs for nanosecond discharges are around 0.8V. The microsecond discharge, due to its high energy input to liquid, not only creates a longer plasma light emission, but also makes the light emission brighter than the nanosecond discharge. The patterns of light emission presented highly repeatable characteristic, which verified the accuracy of using the multiple-gated accumulation (MGA) from successive discharge events with the ICCD camera. In addition, they show a pattern of the variation of light emission. The rising time of light emission is around 40ns in both cases. The jitter time of the standard PMT is ~1.1 ns, so such a small jitter time does not affect much on the rising time (~40 ns) of both microsecond and nanosecond discharges. However, due to the RLC effect in the circuit, i.e., the decay tail of each line, the estimation of the duration of light emission may not be accurate to the nanosecond scale. Furthermore, there is an inconsistent zone at around 1 μs with duration about 100 ns of microsecond discharges. Unlike the multiple-gated accumulation with using the ICCD, one of the advantages of PMT data collection is that each data line represents a continuous signal from a single discharge. This inconsistent intensity variation region suggests that the multiple-gated accumulation of the ICCD should be inaccurate to represent this small zone of microsecond discharges. In addition, the electrical signals and the light signals are checked independently to verify the setup. The signals of EMI sent out from the spark gas and the light signals from the discharges travelled different paths and were recorded on a same oscilloscope in the Figure 32. 63 ns time delay was found between these two signals. The individual EMI was measured

independently which needed 21 ns from its source to oscilloscope, and the light signals through many instrument was measured independently as well which needed 84±2 ns to travel. These independent measurement results matched with the time delay measured by oscilloscope, which corroborated the signals collected from oscilloscope were true signals.

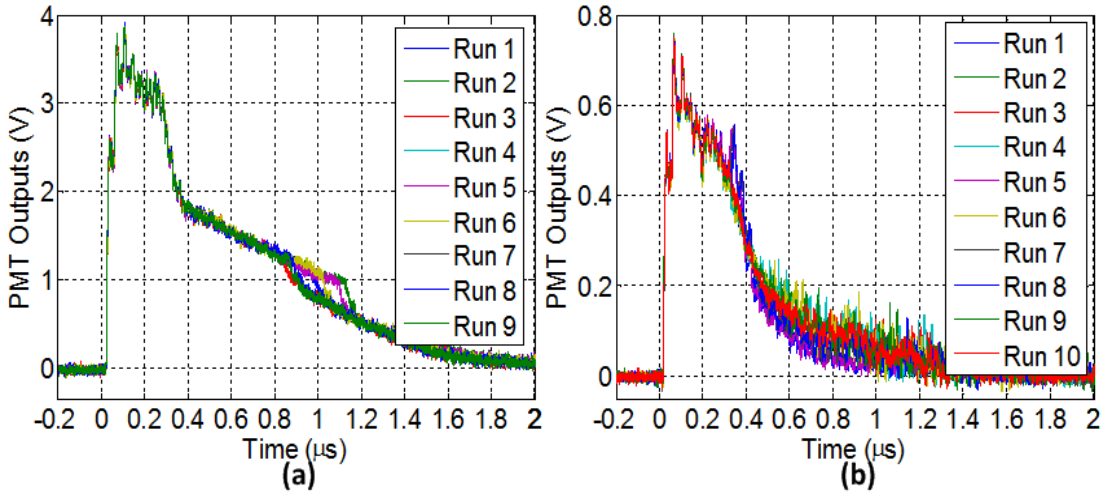

Figure 31. Successive PMT Signals of (a) Microsecond Discharges and (b) Nanosecond Discharges

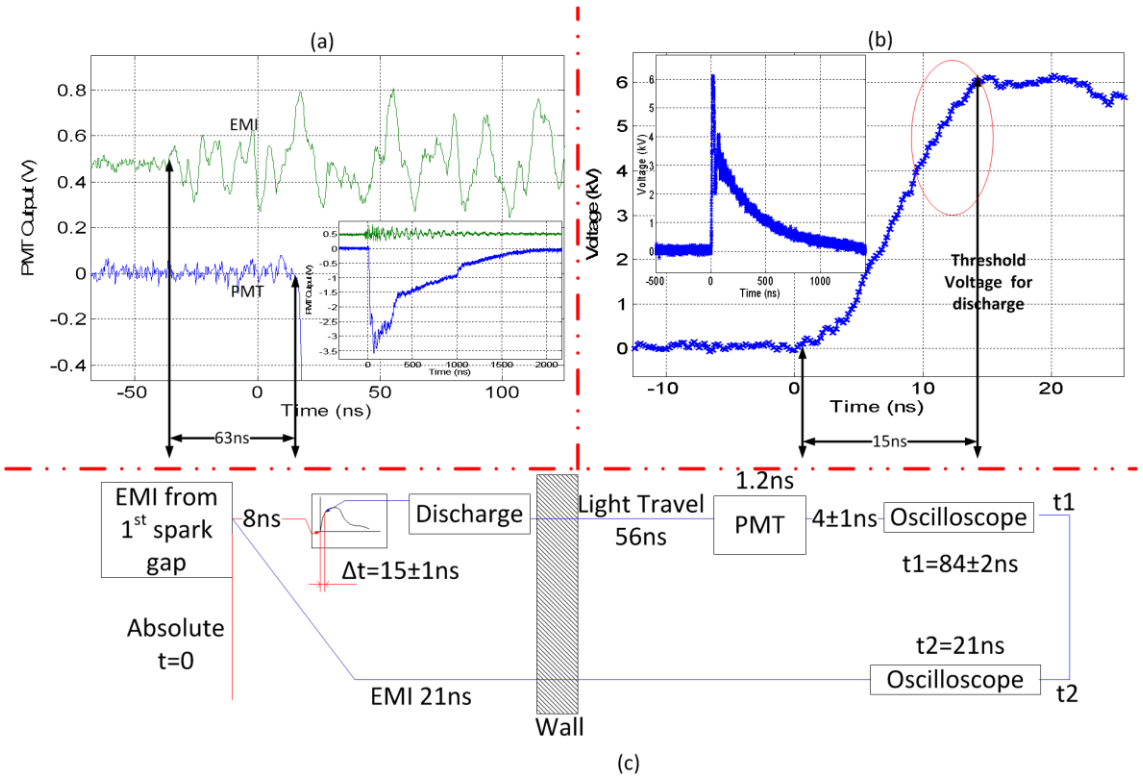

Figure 32. Time Scheme of Light Transmission and EMI Transmission

3.3 Analysis and Discussion of Experimental Results

The detection of light emission by the PMT and the ICCD were both presented and compared in this section. As the high efficient photon detection tools with fast response time, the PMT and the ICCD were used together for the detection of microplasma light emissions. As presented in Figure 33, the data line collected from the PMT of one single discharge was normalized and plotted. To compare with it, ICCD

images were taken with different delay time under the same discharge condition as well. The maximum intensity of each ICCD image was then collected, normalized and plotted in Figure 33. These dimensionless normalized plots are used to present the change of the microplasma light intensity.

3.3.1 Light Emission by Microsecond Discharges Recorded by ICCD and PMT

The light emission lasting around 1.5 μs from a microsecond discharge was clearly detected and recorded by the ICCD and the PMT, as presented in Figure 33. Each of the inset photos was captured by the ICCD camera with 10ns exposure time, different delay time and 10 multiple-gated accumulation (MGA). Since there was a time delay between the trigger and the shutter of the ICCD camera (58~63 ns), the very beginning stage of microplasma light emission was not able to be recorded by the ICCD. There was, however, no such problem of the PMT which continuously recorded the change of light intensity. A 40ns rising time of light emission to its maximum value was observed by the PMT. The results from the PMT more comprehensively revealed the variation of the light intensity of microplasmas. The dots on green line in Figure 33 were the maximum light intensity corresponding to each inset photo, and the blue line represents the evolution of a microplasma light emission recorded by the PMT. These two patterns of the PMT and the ICCD compare well. They both depicted the similar trend of the change of light intensity. The APV for the microplasma presented in Figure 33 was -4kV, and the conductivity of liquid was 1990μS/cm. From our observation, the microplasma light emission and microbubble could both be created by microsecond

discharges in all tests. The microplasma light emission captured in dark environment and the microbubble captured with ambient light on are presented in Figure 34. The delay time of ICCD camera for both images was 200ns, the exposure time was 20ns, the electrical conductivity of the liquid was 1990µS/cm, and the APV for this discharge was -2kV.

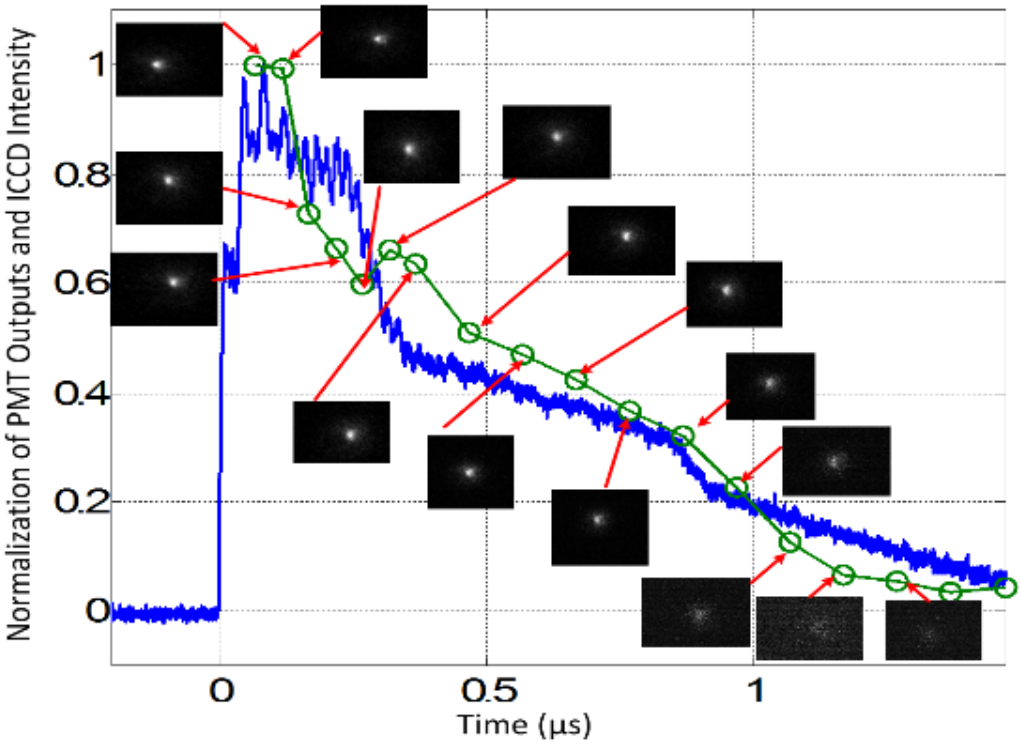

Figure 33. Light Emission Signals Collected from PMT and ICCD (Dots on Green Line Representing Maximum Intensity of Plasma Light Emission on Each ICCD Photo. APVs = -4 kV and Conductivity of Liquid for Discharge =1990µs/Cm)

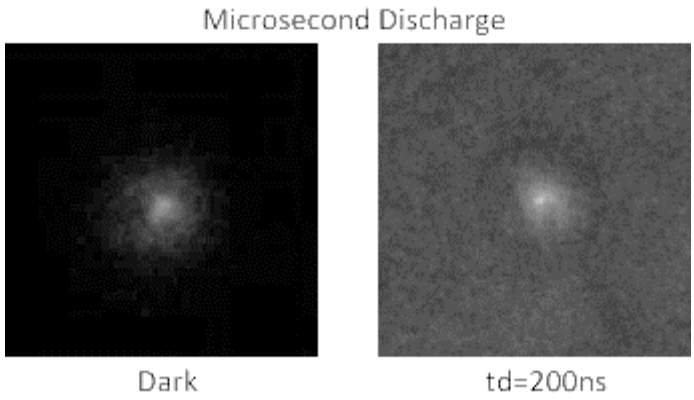

Figure 34. Light Emission and Microbubble from Microsecond Discharge (Delay Time (td)=200ns, Exposure Time=20ns, Liquid Conductivity=1990μS/cm and APV=-2kV).

3.3.2 Thresholds Concerning Microbubbles and Microplasma Light Emission by Nanosecond Discharges

The microbubble generation and microplasma light emission could always be observed with microsecond discharges in all tests. The nanosecond discharges, however, tell a different story. One advantage of nanosecond discharge is that the energy input to liquid can be significantly reduced [5]. Within using the nanosecond discharges, the electrical conductivity of liquid still can vary the energy input to liquid. The microplasma light emission and the microbubble were both captured with using nanosecond discharges in Figure 35. The electrical conductivity was 17600μS/cm, the delay time was 20ns and 200ns respectively, the exposure time was 200ns, and the APV was -2kV as well.

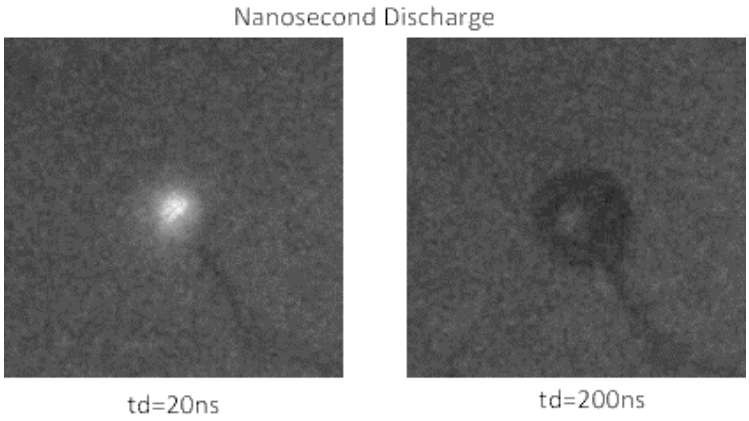

Figure 35. Light Emission and Microbubble from Nanosecond Discharge (Delay Time (td)=20ns and 200ns, Exposure Time=200ns, Liquid Conductivity=17600µS/cm and APV=-2kV).

An even lower energy inputs to liquid in this research were achieved by using nanosecond discharges and a lower conductivity (1990µS/cm). As the microbubble generation and microplasma light emission both needed energy to initiate and sustain, low energy input to liquid which might not be sufficient for both of them were expected to bring useful information about the initiation mechanism. With limited energy, the experimental results suggested that a preference exist for the initiation of microbubbles to the initiation of microplasmas. Their generation and evolution with the microelectrode of 3µm are depicted in Figure 36. In Figure 36, the first photo of each row was captured without any ambient light. The delay time was for all of the pictures was 0 ns and the exposure time of ICCD was a constant 1000 ns. They are used to identify the microplasma light emission. The rest were all taken with the ambient light for the

identification of microbubble generation with different delay times and an exposure time of 200ns. Different phenomenon concerning the initiation of microbubbles and microplasmas are revealed in Figure 36. As the discharge duration is in nanosecond scale, the exposure time of 1000 ns is believed to be long enough to detect any possible light emissions. On the other hand, for the microbubble generation, the exposure time of 200 ns together with different delay time was employed to record a microbubble's growth. When the APVs were -2 kV and -3 kV, there was no light emission detected by the ICCD camera. Neither was the generation of microbubble at the microelectrode tip detected. The first threshold dividing 1) No bubble formation and no detection of microplasma light emission and 2) Bubble formation but no detection of microplasma light emission, occurred between the APV of -3 kV and -4 kV. When the APV was -4 kV, no plasma light emission was detected by the ICCD camera as same as previous tests. The generation of microbubble, however, was observed. With the delay time of 600 ns, a tiny microbubble with the diameter around 7 μm was captured. It quickly disappeared, as no trace of microbubble was left in the image with the delay time of 1200 ns. This interesting threshold might suggest that with the APV around -4 kV of nanosecond discharges, the energy output from the pulsing power is sufficient enough to initiate a microbubble but not enough to initiate microplasma light emission. Microbubble and microplasma were both observed by using microsecond discharge with APVs from -2 kV to -12 kV with the same tip. The second threshold dividing 2) Bubble formation but no detection of microplasma light emission and 3) Bubble formation and the detection of microplasma light emission, was discovered with the APV between -4

kV and -5 kV. When the APV was -5 kV, a very weak light emission was captured in no-ambient-light photo. The weak light spot could be found in the centre of the photo in Figure 36 (APV: -5kV). Furthermore, the duration of microbubble became longer, as a microbubble was recorded when the delay time was 3000ns. The bubble disappeared between 3000ns and 5600ns. The APVs were then changed to -12kV stepwise. The microplasma light emission became brighter, and the maximum diameter of microbubbles became bigger as well. Eventually the microplasma light emissions became very bright with the APV of -12 kV. A grey scale bar was attached to the last plasma light emission figure to present the intensity differences.

The first two phenomenon were very distinguishable, since the appearance of a microbubble was clearly recorded by the ICCD camera. However, the evidence of second threshold (light emission) presented in Figure 36 was not solid enough, since the noise levels on the ICCD are too high to rule out faint light emission on the photos with the APVs of -4 kV and -5 kV. The PMT, as an alternative for the photon detection, was then used to verify the microplasma light emission, or lack thereof. In Figure 37, the normalized PMT outputs and the energy inputs to liquid, E_L, were both plotted corresponding to each APV. It is clear that the energy input to liquid presents a linear relationship with the APV. On the contrary, when the APVs were -2 kV and -3 kV, the PMT signals were both at the background (EMI) level. A rise of the PMT output was observed with the APV of -5 kV. Then the PMT outputs basically followed the same trend of the energy change. This PMT result comes to the same conclusion as the ICCD images that there exists a threshold of the microplasma light emission. In addition, the

discovery by using a PMT illustrates that the results from the ICCD and the PMT are very consistent.

As presented in Figure 36, the initiation of microbubble and microplasma light emissions was re-tested by using a different microelectrode tip with diameter of 5 μm. The size of microelectrode tip also affect the energy input to liquid. In this set of photos, the first of each row was captured without any ambient light. The delay time was all 0ns and the exposure time was all 1000 ns. The second one of each row was taken with ambient light, the same delay time of 0ns and the same exposure time of 100 ns. The first threshold concerning the microbubble generation was discovered between the APV of -5 kV and -6 kV. A microbubble was recorded with the diameter around 7 μm at the microelectrode tip, as presented in Figure 38 (APV= -6 kV). The second threshold concerning the microplasma light emission was discovered between the APV of -6 kV and -7 kV. A light spot was detected by the ICCD camera, as presented in Figure 38 (APV= -7 kV). As the APV increased, the brightness of microplasma light emission and the size of microbubble were increased correspondingly. The PMT was used as well for the microplasma light emission. The energy input to liquid and the normalized PMT outputs were also plotted together in Figure 39. The energy input to liquid shows a linear relationship versus APVs. The PMT outputs, one the other hand, presents a threshold existing in this case as well, before which the PMT signals stayed at the background level, and after which the PMT signals follows a similar linear tread of the energy input to liquid.

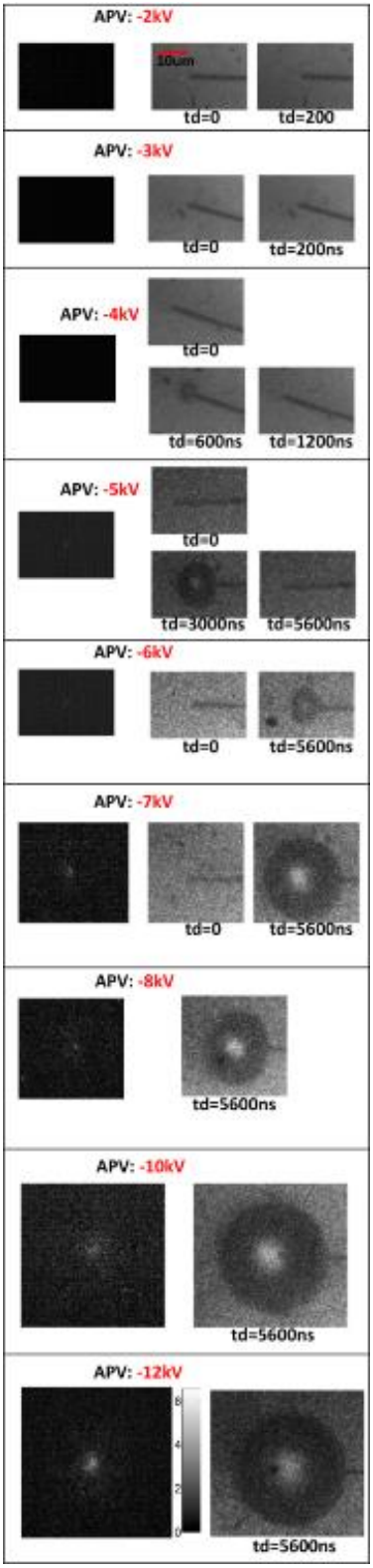

Figure 36. Plasma Light Emission and Microbubble from Tip Size of 3 μm

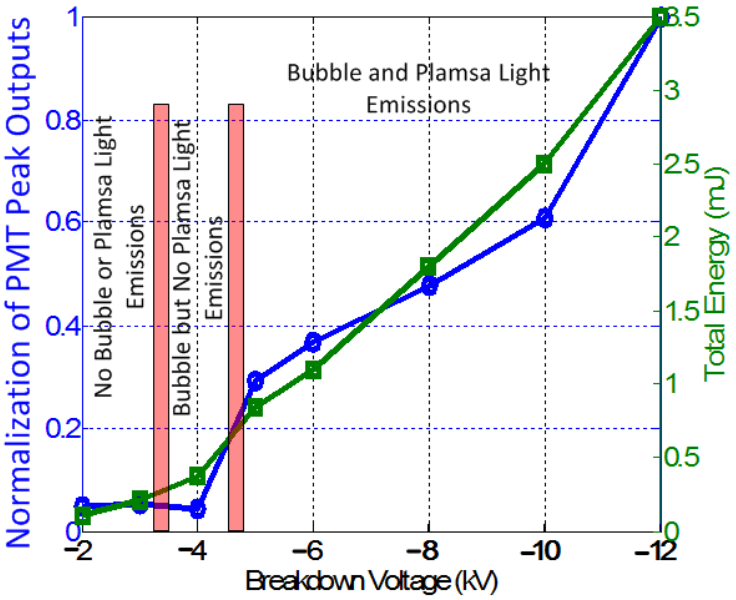

Figure 37. Plasma Light Emission and Total Energy Corresponding to Applied Peak Voltage from Tip Size of 3 µm

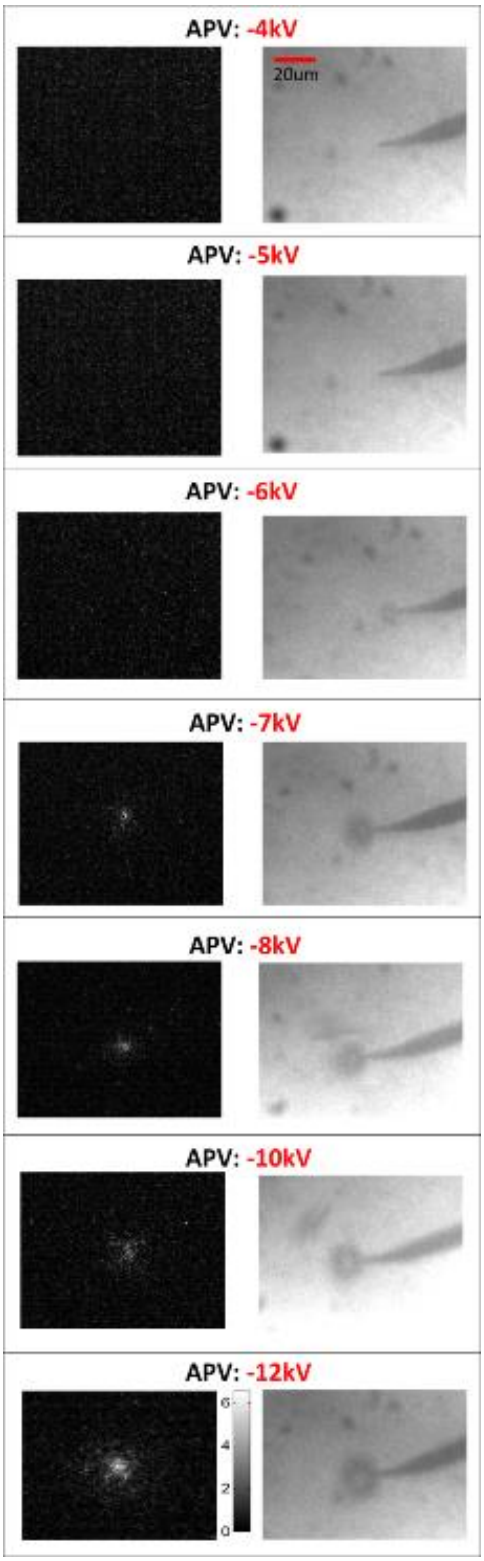

Figure 38. Plasma Light Emission and Microbubble from Tip Size of 5 µm

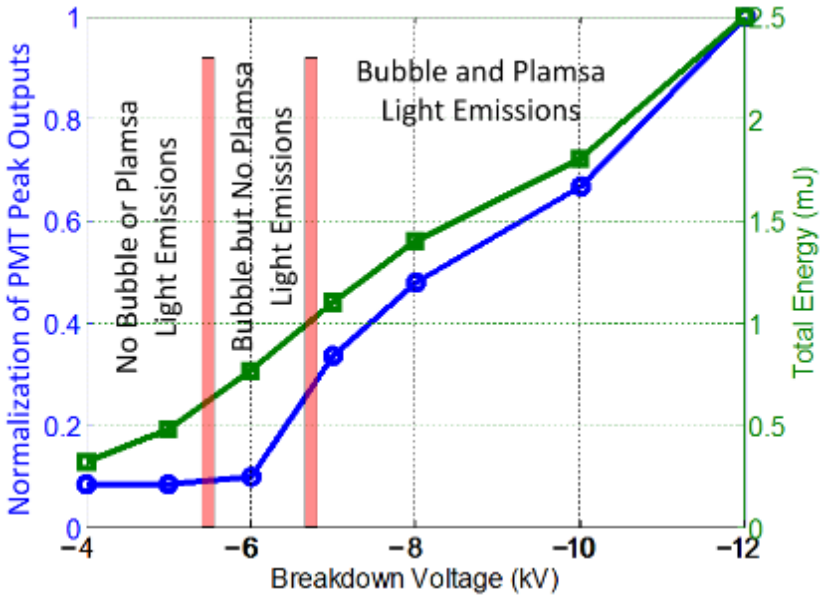

Figure 39. Plasma Light Emission and Total Energy Corresponding to Applied Peak Voltage from Tip Size of 5 µm

3.4 Discussion of Thresholds from Perspective of Energy and Electrical Field

For two different microelectrode tips using nanosecond discharges, separate thresholds for the initiation of microbubbles and microplasma light emissions were discovered. The APVs were used as the controlled parameter with other parameters as constant for each set of tests and the thresholds were only observed in nanosecond discharges. Although APV was the control parameter analysis reveals that energy input may actually be the real parameter determining these thresholds. Furthermore, a smaller tip being able to output a higher energy at each APV explained the shift of the

thresholds. As presented in Figure 40(a), the lower energy not only shifted the thresholds of APV for the microplasma initiation, but also reduced the light intensity as also illustrated. At the same APV, the light intensity from the 3 μm tip was stronger than the 5 μm tip. As the microbubble was created using the lower APV than the microplasma in each case, it seemed that phase change needs lower energy to initiate than the microplasmas. In addition to the knowledge of energy input to liquid, the electrical field at both tips was analyzed as well. With consideration of both the APVs and the size of microelectrode tips, electrical fields at the tip vs. PMT outputs are plotted in Figure 40(b). It turns out that the electrical field at the tips for the first threshold is of the same quantity at around 1.0 GV/m, and for the second threshold is at around 1.3-1.4 GV/m. To conclude, with the similar amount of energy, the electrical field at the microelectrode tip for the initiation of microbubble or microplasma light emissions was pretty consistent. Moreover, energy input to liquid vs. PMT peak output was plotted in Figure 40(c) as well. The light intensity collected by PMT should reflect the amount of energy used for plasma generation, E_P, but the energy input to liquid, E_L, conceivably can not 100% be converted into plasma generation. The conversion efficiency E_P/E_L is quite difficult to estimate and also beyond the scope of this paper. As presented in Figure 40(c), the shift between the PMT peak output of 3 μm and 5 μm illustrates that with same amount of the energy input to liquid, due to the different configuration of microelectrode tip (size difference), the energy used for plasma looks rather different.

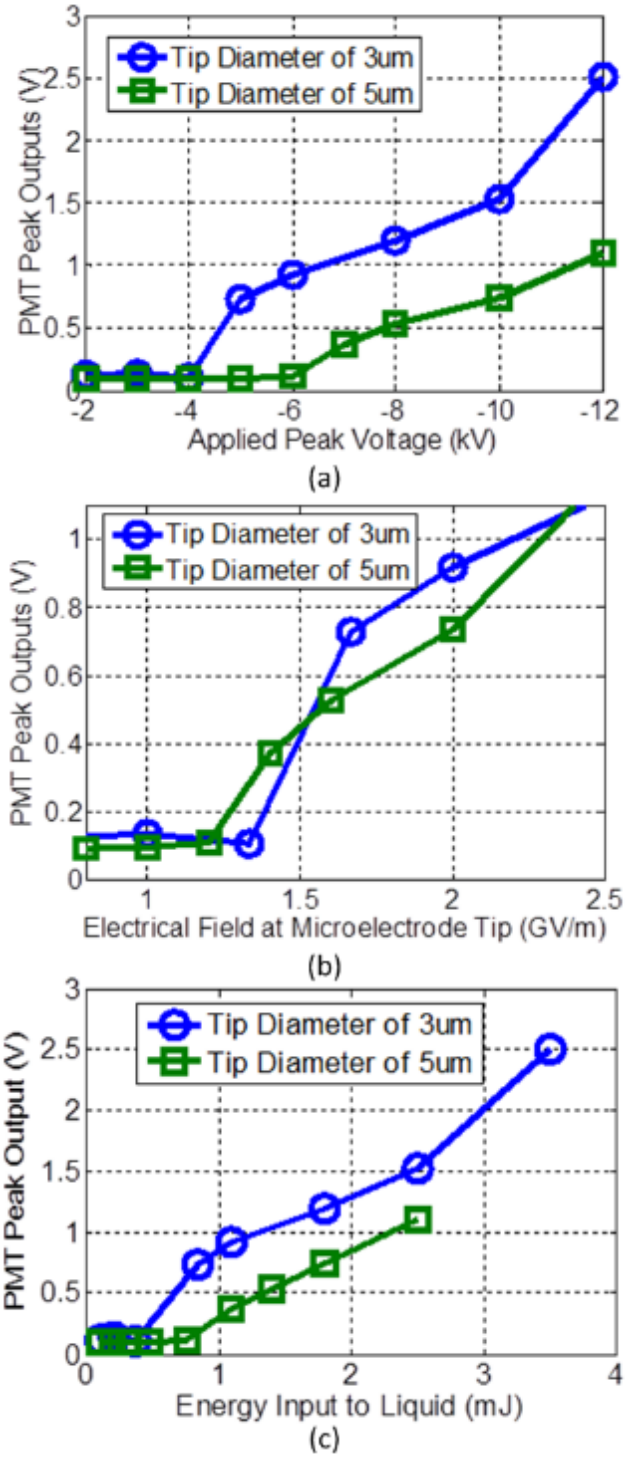

Figure 40. (a) PMT Peak Signals vs. Applied Peak Voltage of 3µm and 5µm Microelectrode Tips; (b) PMT Peak Outputs vs. Electrical Field at Microelectrode Tips; (c) PMT Peak Outputs vs. Energy Input to Liquid of Two Microelectrode Tips.

3.5 Summary

Several possible physical mechanisms of bubble and plasma formation are discussed, and systematic experiments were conducted in this research. Different applied peak voltages, duration of discharges, conductivities of liquid and size of microelectrode tips were used to explore the initiation of microbubbles and microplasma light emissions. The ICCD camera was used to record the microbubble generation and detect the microplasma light emission, and the PMT was used as an indirect visualization means for the continuous detection of microplasma light emission. Their results were used to corroborate each other. The variation of light intensities acquired from the ICCD photos matched consistently with that from the PMT. Due to the internal delay of the ICCD camera, the fact that microplasma light emission experienced a very short rising time around 40ns to their peak values was only collected by the PMT. With the same APV, the nanosecond discharge was able to output much less energy than that from microsecond discharge. The generation of microbubble and microplasma light emission were observed together in all microsecond discharges and in nanosecond discharges with the high electrical conductivity liquid. Two thresholds of APVs were discovered by using the nanosecond discharges in the low electrical conductivity liquid. One threshold was between 1) No bubble formation and no detection of microplasma light emission and 2) Bubble formation but no detection of microplasma light emission. And the other one was between 2) Bubble formation but no detection of microplasma light emission and 3) Bubble formation and the detection of microplasma light emission. The three phenomenon suggest that a certain energy input be able to initiate a phase change in

liquid without causing plasma generations. Under the same conditions, e.g., same APV, conductivity of liquid and energy input, the size of microelectrode tips shifted the thresholds from our observations. After the microplasma light emissions were initiated, their intensities showed similar linear trends as the energy input to liquid. The lower energy not only shifted the thresholds of APV for the microplasma initiation, but also reduced the light intensity. At the same APV, the light intensity from the small tip was stronger than the big tip. As the microbubble was created using the lower APV than the microplasma in each case, it seemed that phase change needs lower energy to initiate than the microplasmas. When there existed thresholds, the electrical field for microbubble generation was around 1.1 GV/m and for microplasma light emission was around 1.3-1.4 GV/m for both microelectrode tips. From energy perspective, the criteria for the initiation of microbubble seems lower than that for the initiation of microplasma. For energy provided to plasma, however, there is some uncertainty as the EP/EL is unknown. Time wise it is still unknown whether the inception of microbubble is earlier than the microplasma, even if the energy for initiation of the former is easier to meet than the latter. Determination of this would require continuous monitoring of bubble presence perhaps by a laser scattering technique.

CHAPTER IV

MICRODISCHARGE GENERATED MICROPLASMA AND SPHERICAL MICROBUBBLES

4.1 Section Overview

A microscale plasma and a spherical microscale bubble were generated by the application of a single pulsed discharge in water with no pre-existing bubble. The microscale corona discharges were created at the tip of a microelectrode by applying a voltage at around -11 kV with the rise time of around 20 ns. The energy inputs for a microplasma generation were controlled by varying the durations of discharges from nanoseconds to microseconds. Two different energy inputs 103 mJ and 0.5 mJ were studied in detail and the differences in the microplasma generated microbubbles, such as the maximum radii, the numbers of oscillation and the durations of a bubble were observed. These microbubbles were visualized using a microscope based optical system with two different high speed cameras. Images of the discharges were captured by a

*Reprinted with permission from "Microbubble generation by microplasma in water" by P. Xiao and D. Staack, 2014. *Journal of Physics D: Applied Physics,* vol. 47, p. 355203, Copyright [2014] by Institute of Physics.

nanosecond gated intensified CCD camera (ICCD), and the microbubbles' dynamics were recorded by a million-frame-per-second (Mfps) CMOS video camera. A Rayleigh-Plesset (RP) model considering both condensable (water vapor) and incondensable (H_2 and O_2) gases in the microbubble predicts the bubbles' dynamics accurately. Comparisons of the experimental results and the RP models allow estimation of the thermodynamic states of microplasmas and microbubbles. The energies in the microbubbles are analyzed quantitatively from the model and rough approximations for energy dissipation and the energy of the microplasma are made. The microplasma energy can be significantly less than the applied energy input. Such low initiation energy is the reason that the size of microplasmas is in micron scale and all microplasmas are confined in a spherical microbubble. All the microbubbles reported in this paper are spherical. The low energy also provides conditions for non-equilibrium plasmas in liquid.

4.2 Mechanism and Initiation Rate of Microdischarge Generated Microbubbles

Two similar theories are espoused by A) Lewis [100, 101], B) Kunhardt [102] and Shoenbach [97, 103] which differ on one main point. Lewis believes that the water essentially cracks under the high dielectricphoretic stresses, leaving a void due to electric fields and space charge to form bubbles according to the Lippmann Effect. Shoenbach refers to heating of the liquid to vaporization to form bubble. There is yet another theory involving pre-existing bubbles so called 'bubbstons' (bubble, stabilized by Ions) [104, 105] but it has not been widely referred to in literature. From our research, Lewis' theory

is more closed to what were observed in tests. The forces on such interfaces could be modeled using electro-hydrodynamics. The experimental verification of these theories has mainly been studying variation of breakdown with conductivity, hydrostatic pressure, and polarity. Shoenbach [97] has attempted Direct Simulation Monte Carlo (DSMC) modeling of the discharge initiation but assumes high current (fast discharge formation) and neglects the Lippmann effect. Experimentally, there are no conclusive evidences to prove what the microbubble initiation mechanism is [76, 106].

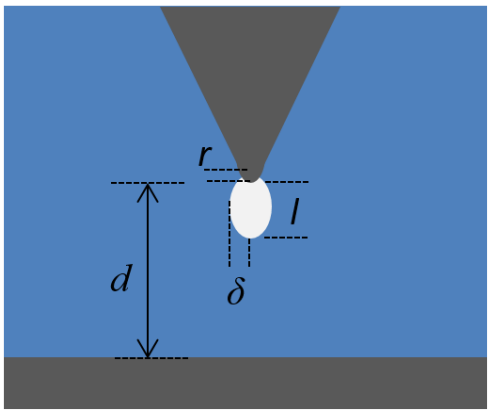

Figure 41. Electrode Geometry

In general when a voltage is applied across a solid-liquid interface several processes can occur. Three possible processes include electrolysis, local heating, and cavitation. For the case of a short transient pulse voltage the relative importance of these

processes depends largely on how rapidly the voltage is applied; therefore the characteristic times of these processes are important. Estimates for these characteristic times will be considered. The general setup is as shown in Figure 41 where a pointed electrode, with tip radius 'r', is a distance 'd', away from the other electrode and a small bubble is forming having a radius 'δ' which will be the free variable for this analysis. It will be approximated that the bubble growth away from the electrode grows with a cylindrical geometry having a constant cross sectional area; in this was the bubble grows a distance 'l' away from the electrode. In general we seek a time for the bubble will grow to some length 'l' as predicted by the different mechanisms; as will be seen these estimations will that the general form of Equation 4, where 'C_i' is a constant to be determined which is associated with a particular mechanism.

$$\tau_i = C_i l \qquad \text{Equation 4}$$

In order to make determine these constants of proportionality for each mechanism the variables in table Table 2 will be used.

Table 2. Legend of Variables Used for Estimating Proportionality Constants

Property	Variable	Units
Density	ρ	$\left[\frac{kg}{m^3}\right]$
Electric Field	E	$\left[\frac{V}{m}\right]$

Table 2 Continued

Property	Variable	Units
Enthalpy of Vaporization	h_v	$\left[\frac{kJ}{kg}\right]$
Mobility	μ_i , $(i \stackrel{\text{def}}{=} species)$	$\left[\frac{m^2}{V * s}\right]$
Number Density	n_i , $(i \stackrel{\text{def}}{=} species)$	$[m^{-3}]$
Specific Heat	$c_{p,i}$, $(i \stackrel{\text{def}}{=} species)$	$\left[\frac{kJ}{kg * K}\right]$
Voltage	V	$[V]$
Yield Strength	Y	$\left[\frac{N}{m^2}\right]$

Electrolysis requires the presence of mobile ions in the liquid in order to transfer charge; therefore if there is no ion concentration in the liquid electrolysis will not occur. However if electrolysis is possible it will tend to be a very slow process due to the relatively low mobility of the ions. A characteristic timescale for electrolysis can be estimated using Faraday's Law of Electrolysis, Equation 5 & Equation 6, where 'F' is the Faraday constant.

$$\frac{dN}{dt} = \frac{I}{F} \qquad \text{Equation 5}$$

$$N = \frac{1}{F}\int_0^{\tau} I\,dt \qquad \text{Equation 6}$$

Equation 5 can be rewritten in terms of number density using the assumption that the bubble is a cylindrical volume Equation 6.

$$n\left(\frac{\pi\delta^2 l}{N_a}\right) = \frac{1}{F}\int_0^{\tau} I\,dt \qquad \text{Equation 7}$$

The current for a specific charged species (i) can be expressed in terms of the mobility, charge, and electric field as in Equation 7.

$$I_i = en_i\mu_i EA \qquad \text{Equation 8}$$

If any of these variables change with time then they must be considered within the above integral, however for a simplified initial case it can be assumed that each one of these variables are constant. Making the constant current assumption and choosing the cross sectional area for the current to have a radius of 'δ' can be combined and solved for time; also note that the Faraday constant is simply the product of the fundamental charge of an electron and Avogadro's number, which provides the constant of proportionality for the electrolysis mechanism.

$$\tau_e = \left[\frac{n_{H2}}{n_i\mu_i E}\right] l \qquad \text{Equation 9}$$

A characteristic timescale can be estimated for boiling by considering a simple energy balance at the solid-liquid interface.

$$m\left(c_{p,H2}\Delta T + h_v\right) = VI\tau_b \qquad \text{Equation 10}$$

In order to be consistent, the voltage will be converted to the electric field, this required a further assumption for the electric field. It will be assumed that the geometry

shown in Figure 41 can be approximated as a parabolic tip above a plane. Furthermore it will be assumed that the maximum electric field will determine that current flow; this is reasonable since it is the area of the highest stress. The maximum electric field is approximated.

$$E = \frac{2V}{r \ln \frac{2d}{r}} \qquad \text{Equation 11}$$

$$\tau_b = \left[\frac{2\rho_{H2}\left(c_{p,H2}\Delta T + h_v\right)}{E^2 r \ln \frac{2d}{r} e n_e \mu_e} \right] l \qquad \text{Equation 12}$$

In order for cavitation to occur the voltage must be strong enough to overcome the yield strength of the liquid; this is equivalent to pushing the interface apart leading to the creation of a low density region. To estimate the characteristic time for this process the Yield strength of the liquid is balanced with the applied power.

$$Y \pi \delta^2 l = VI\tau_c \qquad \text{Equation 13}$$

Just as before the electric field will be related to the voltage, the current will be given. And when combined, time can be solved.

$$\tau_c = \left[\frac{2Y}{E^2 r \ln \frac{2d}{r} e n_e \mu_e} \right] l \qquad \text{Equation 14}$$

The proportionality constants for the three different mechanisms have been obtained and can now be compared by plugging in actual numbers and plotting. To create this plot the number used are shown in Table 3.

Table 3. Values Used for Comparing the Relative Rates for Each Mechanism

Variable	Value	Unit
ρ_{H2}	89.9	g/m^3
n_{H2}	2.71e25	m^{-3}
$c_{p,H2O}$	1670	J/kg*K
$h_{v,H2O}$	4.24e4	J/kg*K
n_{Na}	1.06e22	m^{-3}
μ_{Na}	5.19e-8	$m^2/(V*s)$
E	6.68e8	V/m
r	5e-6	M
d	1e-3	M
n_e	1e12	m_{-3}
μ_e	1.80e-4	$m^2/(V*s)$
Y	45e5	N/m^2

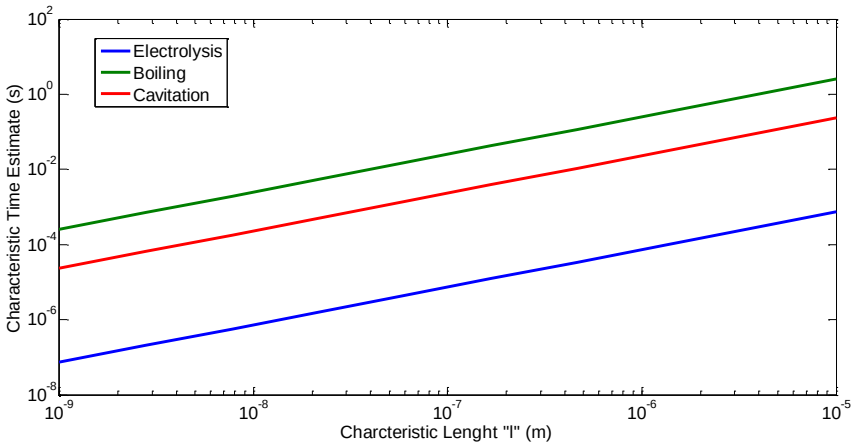

Figure 42. Time Constants for Low Density Bubble Formation vs. Bubble Size

4.3 Experimental Setup

The microplasmas in our tests were generated at a microelectrode tip. A 3D schematic drawing of microplasma in liquid is presented in Figure 43. The microelectrode tip is immersed in a petri dish containing water and a grounded metal tab is placed in the water. By using a high voltage power supply (maximum -20 kV) and a spark gap, short rise-time pulses microplasmas were able to be initiated in liquid. The size of microplasma is related to: the size of microelectrode tip, the applied electrical field, and the input energy. A small electrode tip is necessary, because it allows for a localized discharge and an attaining breakdown field with lower applied voltage and energy. The ground in not sharp and no discharge occur there. The sharp electrode tips were fabricated through electrolysis. The distance between electrodes was always around

1cm. When the two electrodes are too close (<0.5 mm depending on voltage), a spark discharge (extending the distance between the electrode) instead of a corona discharge occurs. Only corona discharges are covered in this paper. If the ground electrode is sharp, an opposite polarity discharge occurs there. To prevent electrical leaking, epoxy was used to cover the body of microelectrode except for the tip. The liquid used was a mixture of deionized water and sodium chloride (NaCl) salt with a conductivity as 9120 µS/cm, and was consistent for all our tests. The water depth was about 3 mm and the water surface was at ambient pressure. The bubble dynamics are sensitive to solution conductivity and ambient pressure, the plasma is also affected by these. A parametric study of changing the properties of liquid is ongoing work.

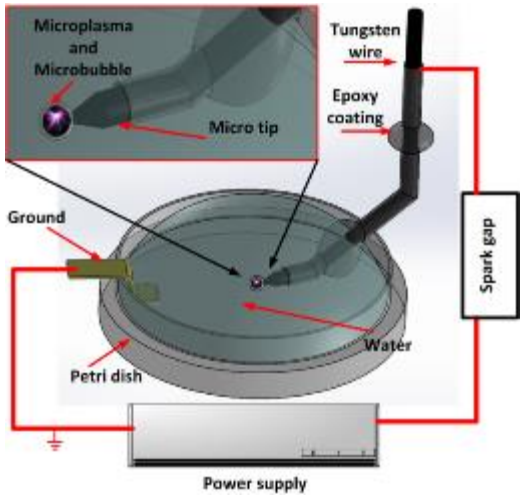

Figure 43. 3D Drawing of Microelectrode Tip Immersing in Water with Microplasma and Microbubble Generation Illustrated

4.3.1 Microelectrode Fabrication

The size of microelectrode tip is a key parameter assisting to determine the energy density of microplasma. To fabricate the micro tip, a tungsten micro wire (OD: 50μm) was suspended with one end immersed in NaOH solution and the other end connected to the anode of a DC power supply [107]. The microelectrode tip was sharpened by electrolysis at the interface of solution and air. Micro tips in our tests were around 1 μm to 3 μm presented in Figure 44(a). They were used to create a localized high electrical field to induce a breakdown. After a tungsten microelectrode tip was finished, the surface of tungsten microelectrodes would be covered by high dielectric epoxy as an insulator. Due to capillary forces, the epoxy on the surface of microelectrode formed some beads presented in Figure 44(b). It is most important to provide dielectric insulation at the water/air/electrode interface and this was done by locating the thick epoxy bead area at the interface.

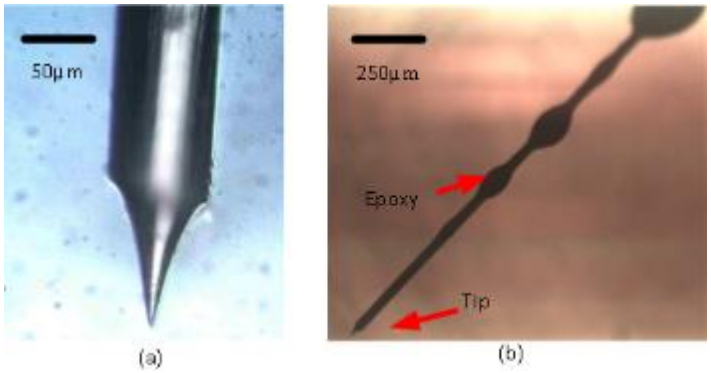

Figure 44. (a) Microelectrode Tip Fabricated by Electrolysis; (b) Microelectrode Covered by Epoxy

The surface of microelectrode tip was very smooth after electrolysis, as presented in a SEM photo in Figure 45(a). The diameter of the tip was around 1.5 µm. After about 3 discharges of 4 µs duration and 200 discharges of 200 ns duration (discharges details are described later), the tip was reshaped, likely by melting during the first several discharges of plasma as presented in Figure 45(b). The rest of microelectrode looked intact. The diameter of the tip became around 3µm to 4µm and did not change further. This was only 2 to 3 times bigger than its initial diameter. The comparisons of SEM photos show that the change to the electrode, likely melting, by the microplasma only occurred at the tip. The size of melting areas matched with the size we observed for the microplasma in Figure 45. Based upon the specific and latent heats of tungsten and the observed volume, the energy required to cause this area to melt is less than 4 µJ. Energy well in excess of this is provided during the discharge. The melting, we believe, is

caused by the plasma generation particularly during the microsecond pulsed discharges (probably less so during the ns pulsed discharges). This melting would indicate temperature in excess of 3695 K. The dark region in Figure 45(a) was caused by the accumulation of electrons on nonconductive impurities visible by the SEM. So that region appears blurred. The impurities might be due to some likely dust or un-rinsed NaOH or salts from the tip as artifact of the etching process used to fabricate the tip.

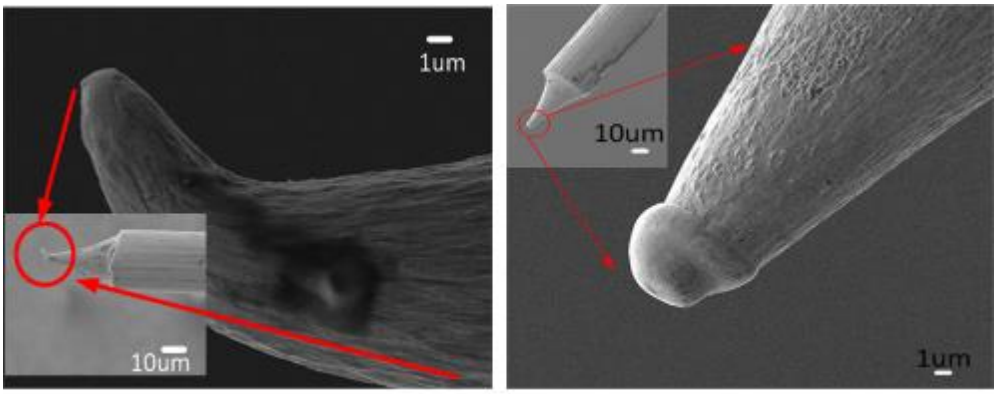

Figure 45. (a) SEM Photos for Microelectrode Tip before Discharges, (b) SEM Photos for the Same Microelectrode Tip after 200 Discharges

4.3.2 Experimental Layout

The maximum radius of microplasma and microplasma generated microbubbles in our tests were both in micron scale, so an inverted optical microscope was used to observe them. One of the outputs of a fiber optical white light source (AMScope, 150 W optical gooseneck microscope illuminator) was placed directly above the liquid container at full power to illuminate the microscopic field of view. This background lighting is similar to shadowgraph, making the density differences between the gases in a microbubble and the liquid surrounding it more distinguishable. Those shadow graphic images were used to estimate the radius variation of a microbubble. A reference object with known dimension was used under microscope with high speed cameras to calibrate the image resolution (length/pixel). The resolution was used later to calculate the diameter of microbubble based on the number of pixels. The resolution for CMOS camera is around 1 μm (1 μm/pixel) and the error for ICCD camera is around 200~300 nm (200~300 nm/pixel). The ICCD camera has better image resolution than the CMOS camera. Due to image blurring and motion during the exposures the minimum feature sizes observable were about 6 μm and 2 μm for the CMOS and ICCD respectively. A schematic illustration of experimental layout including the microscope setup, cameras, data acquisition, power supply and switching circuit is presented in Figure 46.

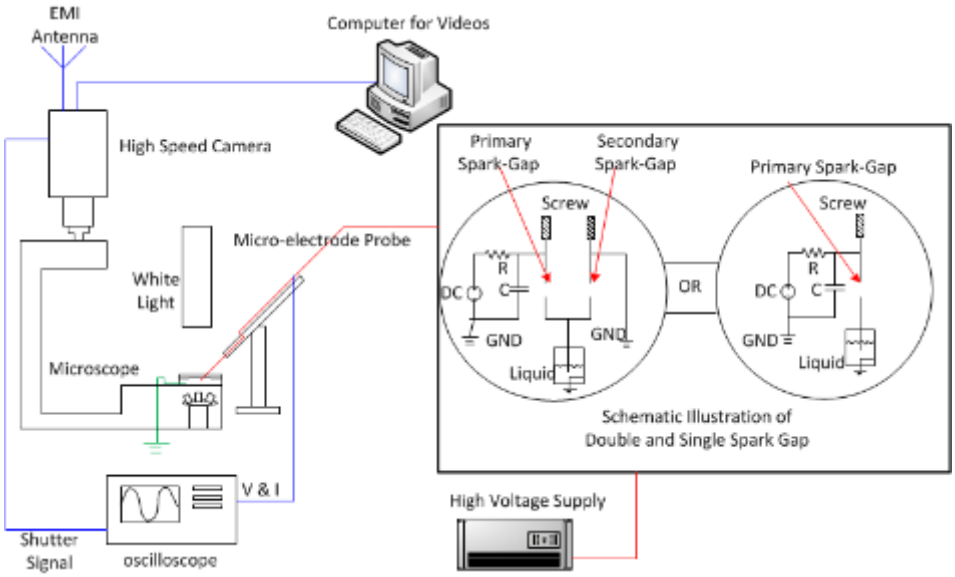

Figure 46. Schematic Illustration of Experimental Layout with Double- and Single-Spark-Gap Switching

Pulsed switching circuit employing spark gaps were used to control energy inputs for the plasma generations. The single spark gap configuration was used to provide microsecond duration discharges, while the double spark gap configuration was used to provide nanosecond duration discharges. They both worked with a 20 MΩ resistor and a 2 nF capacitor charging circuit. By adjusting the gap distances using a position screw of the primary spark gap, applied voltages to initiate microplasmas were able to be controlled. In Figure 47 and Figure 48, voltage & current vs. time from a single spark gap and a double spark gap are both presented with the same applied peak voltage (-11 kV).

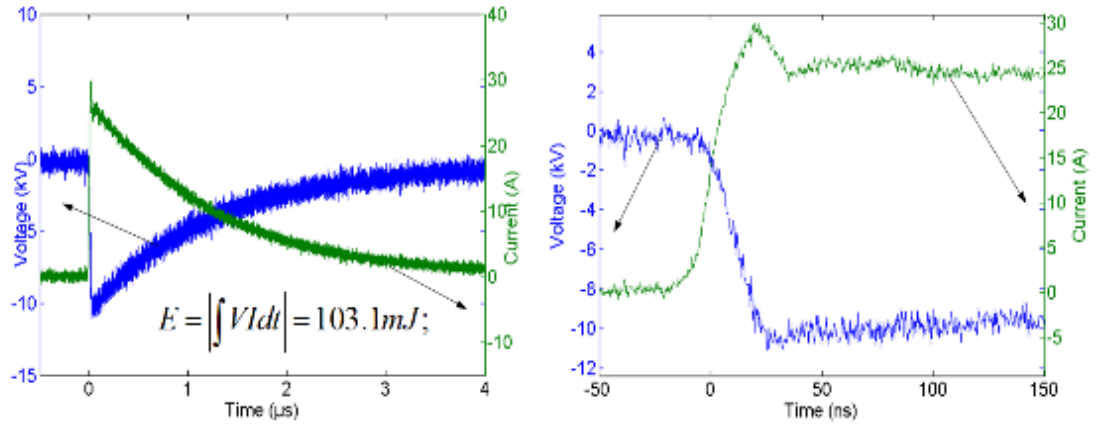

Figure 47. Voltage and Current Variation vs. Time of Single-Spark-Gap Microsecond Pulse Discharge

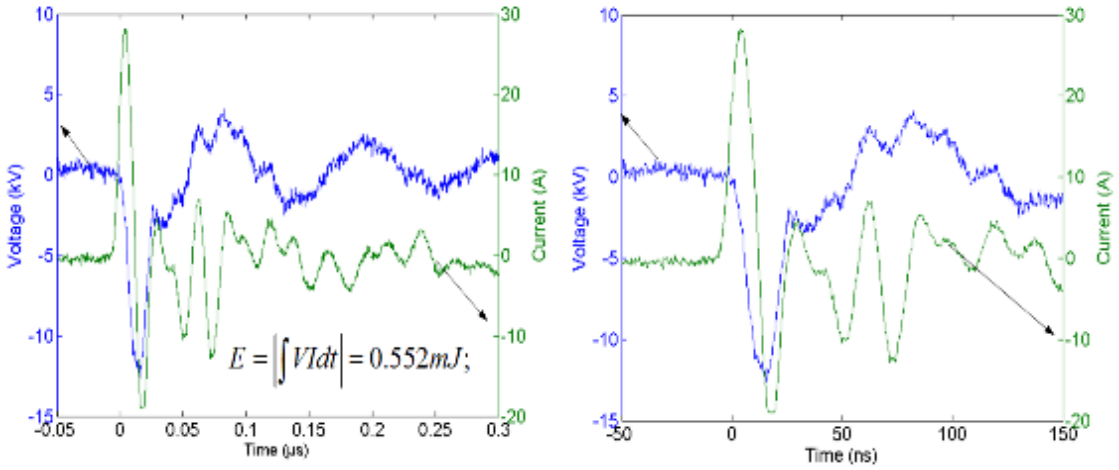

Figure 48. Voltage and Current Variation vs. Time of Double-Spark-Gap Nanosecond Pulse Discharge

For the single spark gap configuration, the total energy stored in the capacitor before breakdown is released into the load mostly. The load is the electrode immersed in the liquid when properly insulated. For the double spark gap configuration, however, the secondary spark gap connected to ground fires shortly (several nanoseconds) after the primary spark fires. In this case, the primary spark gap initially still releases the energy stored in the capacitor to the load, but the secondary spark gap interrupts this releasing and conducts the remainder of energy to ground. So the energy released into load is significantly reduced. The timing of the second spark gap firing can be adjusted by changing its gap length and wiring. In Figure 47 and Figure 48, voltages and currents take around 4.5 μs for the single spark gap and 0.2 μs for the double spark to decay to zero with some ringing. In this paper, the configuration using only one spark gap is referred to as the microsecond pulse and the configuration using double spark gap is referred to as the nanosecond pulse. Only one set of conditions for each pulse duration was studied in detail. The applied peak voltage on the voltage waveform was the same (-11 kV) for both cases. The total energy consumption in Figure 47 of microsecond pulse was around 103mJ and in Figure 48 of the nanosecond pulse was around 0.55 mJ, determined by integrating the product of the voltage and current. The total energy stored in the capacitor of our circuit is 121 mJ ($1/2CV^2$), so the energy released into load from microsecond discharge took 85% and from nanosecond discharge took 0.4%.

4.3.3 Image Acquisition Equipment

A single nanosecond pulsed discharge is able to create a microplasma in the liquid which emits light for only around 100 nanoseconds. But the microbubble generated with the microplasma lasts from tens to hundreds of microseconds. Two different high speed cameras targeting different time scales were used to capture the microplasmas and microbubbles respectively. The microplasma discharges were recorded by a nanosecond gated ICCD camera (Standford Computer Optics Inc. 4 Picos ICCD camera), and the initiation, the growth, the collapse and the oscillation of the microbubble were recorded by a CDD camera capable of million fps (Photron, FASTCAM SA5). One of the main differences between two cameras are that the ICCD camera can take a single triggered photo with nanosecond delay and nanosecond exposure time; whereas the CMOS camera can take continuous videos with microseconds interval between two frames. In all our tests, 10 ns exposure time and an average of 20 accumulations were used for the ICCD camera, and 300000 fps was used for the CMOS video camera. Due to an internal circuit delay in the ICCD camera, the shutter opened around 70 ns after it was triggered. Electromagnetic interference (EMI) from the primary spark gap was used to trigger the ICCD. The jitter of the ICCD camera is specified as <0.02 ns, and the EMI was measured to be a repeatable trigger relative to the voltage measurement within 0.5ns. The timing uncertainty is thus about 0.5 ns for the ICCD and it should not affect our accuracy with exposure time of 10 ns. All times from ICCD camera referred to in this paper are relative to this repeatable EMI signal. For the CMOS the timing uncertainty is 3.3 μs (the inverse of the frame rate).

4.4 Experimental Results and Discussion

4.4.1 Microplasma Initiation and Nanosecond Duration

The light emission due to the plasma at the probe tip for a nanosecond pulsed discharge is presented in Figure 49. Applied peak voltages for discharges were around -11 kV corresponding to Figure 48. Figure 49(a) shows the image for a single exposure of the microplasma light emission and Figure 49(b) shows the averaging of 20 exposures. In both cases, the light emission from the discharges is visible and about 15μm in diameter. Figure 50 shows the time dependent microplasma and microbubble dynamics as captured by the ICCD for the first 120ns. In these images the microelectrode is seen coming up from the bottom of the image and the discharge and bubble are at the tip of the microelectrode. The first row presents the shadowgraphic visualization of the microbubbles at the tip of microelectrode with the light source on, while the second row presents light emission from the microplasmas without any ambient light. The arrows highlight the light emission regions. To reiterate the EMI emission from the spark gap is used as the reference t=0, the first photo begins at 70 ns delay due to the internal timing of the ICCD camera. The exposure time for all photos in Figure 50 is 10 ns. In the first row of photos, the microbubble grows from around 20 μm to around 30 μm in diameter. The tip and the microbubble itself are very clear in the images. The light emissions from the plasma can also be observed to be contained inside of the microbubbles. The second row of photos presents the plasma emission under same discharge conditions without any external light sources. The maximum intensity of light emission occurred at t=80 ns.

After that, it gradually dims. After around 110 ns, the light emission of the microplasma disappears, while the microbubble surrounding the microplasma is still present and growing. Detailed study of plasma light intensity recorded by the ICCD camera was also pursued [6] and investigations of initiation mechanism are ongoing. Considering the applied peak electric field on the order of 3.5 GV/m (-11 kV, 3 μm), observed high temperature (evidence by tungsten tip melting) and secondary electron emission processes possible routes of discharge initiation are field emission, thermionic emission and Townsend breakdown. The mechanism and timing of the bubble formation is also unanswered. What is very clear from these results is that a bubble is generated in less than 70 ns and the plasma discharge is confined inside of the bubble. A reason that the plasma is micro-scale is that it is confined inside of a microscale bubble. Inside the bubble the density is lower and ionization processes are easier and more prevalent.

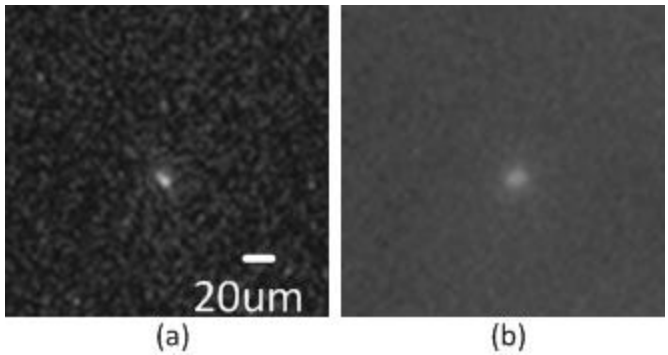

Figure 49. Nanosecond Pulsed Microplasma without Background Light with 10ns Exposure Time at t=70ns. (a) Single Microplasma Light Emission Captured by ICCD Camera, (b) Integrated Images of 20 Pulses Averaged by ICCD Camera.

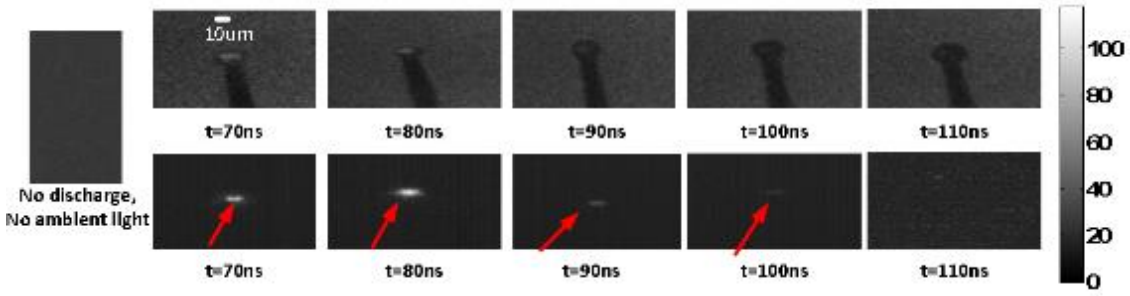

Figure 50. Time-Sequence Photos of Microplasma and Microbubble Initiations at the Microelectrode Tip Generated by Nanosecond Discharges with Consideration of Internal Delay of ICCD Camera. Top Row with Backlit and Bottom Row within Dark Environment

4.4.2 Microplasma Generated Microbubble

The time scale of bubble growth is significantly longer than the discharge events and to some approximation the discharge can be considered as a nearly constant volume energy addition. After a discharge, the volume expansion of a microbubble is visible. A single pulsed discharge is able to create a microplasma in the liquid which emits light for around 100 ns. But the microbubble generated with the microplasma lasts from tens to hundreds of microseconds. The time evolution of single microbubbles was analyzed from videos recorded by the high speed CMOS camera. In Figure 51, a single frame from the video of a microplasma generated microbubble is presented. The radius of this microbubble was around 130μm and the microelectrode tip can still be seen in the center of the microbubble. The bubble's edges are clearly distinct from the background, and a

focusing of the light is seen in the middle of the bubble due to the refraction at the bubble interface. This brightness is not plasma emission.

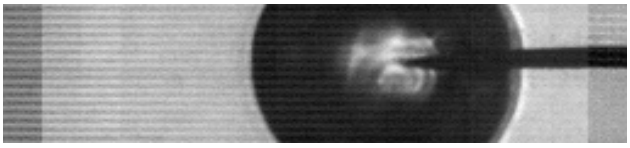

Figure 51. Microbubble Initiated by Microplasma in Water, t=16.5 μs after Discharge Event

4.4.2.1 Microplasma Generated Microbubble by High Energy Input (Microsecond Discharge)

Figure 52 shows a sequence of 49 frames from the video corresponding to the bubble generated by the microsecond discharge with voltage and current as given in Figure 47 (103 mJ). The bubble is seen to grow, reaching a maximum diameter after around 3 3 μs, collapse to a minimum diameter at around 50 μs, and continue to grow and collapse in several decaying oscillations. The whole process of oscillations takes around 170 μs from the initiation of the microbubble to its disappearance. The maximum diameter during its evolution was around 260 μm. The bubble's radius in each video frame was measured and shown as a function of time in Figure 52. Frames before the discharge with no bubble are assigned zero radii. Error bars which represented the

accuracy of radius in Figure 52 become larger as the bubble's edge blurred. The blurriness of bubbles edge may be due to: the aspherical shape of bubble, the faster speed at smaller radius, the reflection of bubble off the electrode, and the possibility of supercritical vapor in process of collapse. In the last 10 μs of frames, microbubble researches an equilibrium radius without any motion, and eventually it disappears due to dissolving/condensation or rises due to buoyance out of the view. The dissolving and condensation, and the buoyance force estimated from the volume of bubble are both able to move the bubble out of view of microscope in hundreds of microseconds.

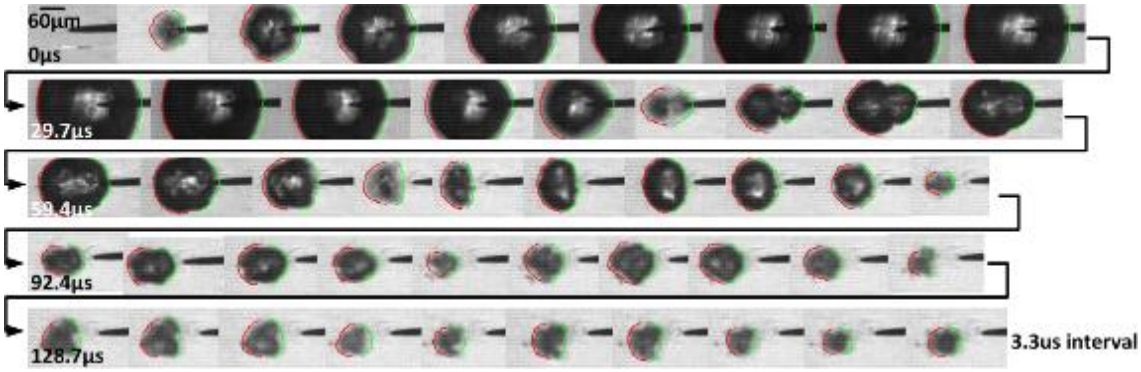

Figure 52. Time-Sequence Photos of Microplasma Generated Microbubble's Life Cycle by High Speed CMOS Camera with 300000fps

Due to a sudden increase of temperature and pressure at the tip caused by the plasma generation, the microbubble expands quickly passing its equilibrium radius to the maximum radius. With the expansion of volume, its temperature and pressure drops. The

microbubbles' dynamics are dictated by the surface tension, the inertia, and the pressure differences between the vapor and gases in the bubble and the liquid outside the bubble. When the internal pressure of microbubble is higher than its surface tension and hydrostatic pressure, the growth of microbubble accelerates and its radius is smaller than the equilibrium radius, and when the internal pressure of microbubble is lower than its surface tension and hydrostatic pressure, the growth of microbubble decelerates and its radius is bigger than the equilibrium radius. Because of the energy transfer due to temperature difference, and mass transfer due to the vapor condensation and the gas dissolving, the total energy and the maximum radius of each cycle decrease. The oscillations of bubbles have been well described by the Rayleigh-Plesse (RP) model [98], it will be analyzed in details in section IV.

4.4.2.2 Microplasma Generated Microbubble by Low Energy Input (Nanosecond Discharge)

On the other hand, for the nanosecond discharge, 0.4% of the energy stored in the capacitor of spark gap circuit was released to initiate microplasma. In Figure 53 and Figure 54 , the radius variations are presented in photos and measurements. They correspond to the voltage and current diagram in Figure 48. The maximum radius was around 88 μm, the period of the first oscillation is 25 μs, and it only oscillated twice before reaching an equilibrium radius, and remained at this radius for about 8μs before rising out of the view.

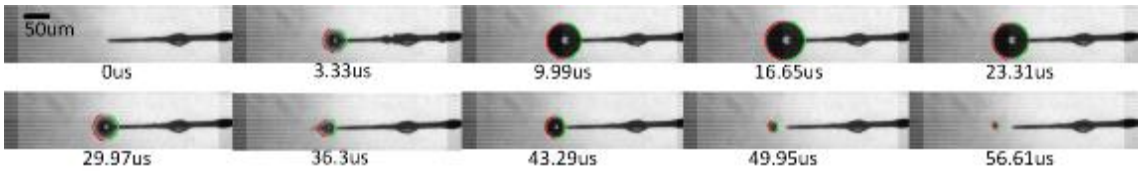

Figure 53. Time-Sequence Photos of Nanosecond Discharge Microplasma Generated Microbubble's Life Cycle by High Speed CMOS Camera with 300000 fps

4.4.2.3 Comparison between Microbubble Created by Microsecond/Nanosecond Discharge

After the first cycle, the sphericity of microbubble was changed. It is also the reason RP model was not applied for any cycle with non-spherical bubbles in this paper. The shape influence to the electrical field was not investigated in this paper. Comparing the microbubbles' dynamics in Figure 54 for the microsecond and nanosecond discharged microbubbles, the energy initiating the microbubble dissipated through heat and mass transfer. The error bars of the radius for both cases are ±2 μm for most of the first cycle, which is important for the comparison to the bubble model. The maximum radius, the oscillation period and the number of oscillations are important indicators to distinguish energy inputs. The microbubble oscillated 7 times created by the microsecond discharge and 2 times by the nanoseocnd discharge with same applied peak voltage (-11 kV). The maximum radius from the microsecond discharge was 120 μm and from the nanosecond discharge was 88μm. After oscillations, the microbubble did not

disappear immediately. On the contrary, they slowly rise due to buoyancy in liquid at a steady state equilibrium radius. It is believed that the incondensable gases, most likely O_2 and H_2, and the condensable gas such as water vapor both existed in the microbubble. The bubble might float up to the liquid surface after it departed the microelectrode. The energy input for the microsecond discharge was higher than nanosecond discharge, so the microsecond discharged microbubble oscillated more cycles than nanosecond discharged microbubble. This is the reason that the microsecond discharged microbubble took 150 μs and nanosecond microbubble took 60 μs to complete their oscillations.

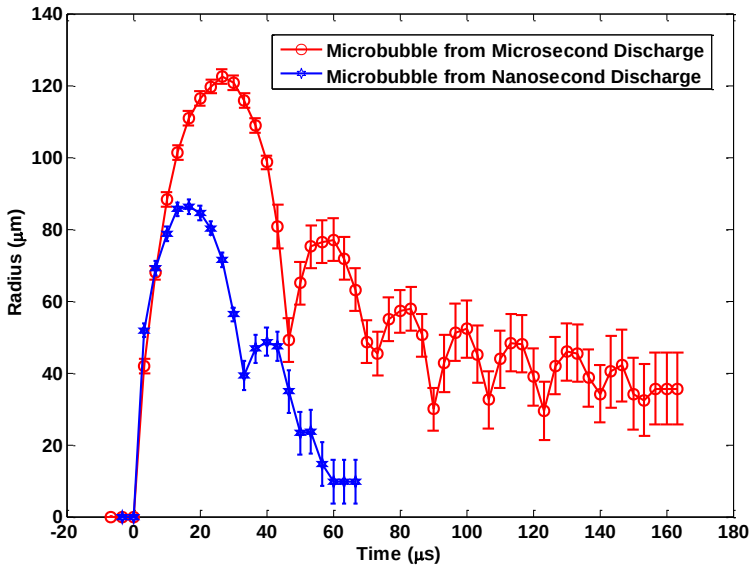

Figure 54. Comparison of Time Dependent Radius Change between Microsecond and Nanosecond Discharges with Error Bars.

4.5 Rayleigh-Plesset Model of Microplasma Generated Microbubble

The experimental study of the microplasma generated microbubbles has been introduced. From ICCD photos in Figure 52, the light emission lasted only about 120ns. The microplasma was confined in the microbubble and the microbubble kept on growing after the microplasma disappeared. The oscillation of the spherical microbubble is studied using a one-dimensional Rayleigh-Plesset (RP) model. In a simplified RP model, a void is formed in a liquid and the liquid is drawn into the void. Lord Rayleigh described how the void collapsed mathematically based on the conservation of momentum and mass [108], and Dr. Plesset supplemented the model to include a compressible gas inside the bubble which allows for collapse, growth and oscillations as well [109]. Based on prior studies of cavitation, two different RP models [98] were considered as options to analyze the experimentally observed microbubbles' dynamics as presented in Figure 52, Figure 53 and Figure 54. One is the 'thermal bubble model' which assumes energy transfer by thermal effects, i.e., the temperature difference between the gases in the bubble and the liquid outside the bubble, significantly affects the bubble's growth and collapse. The other is the 'inertia bubble model' which assumes inertia is the main driving force dominating oscillations of the bubble. The dynamics of bubble are not affected by temperature differences across boundaries in this case. The inertia model was selected with initial and boundary conditions provided from the measurements of the microbubbles. Discounting the time period of energy addition by the microplasma, the RP model is similar to the dynamics observed in the plasma generated microbubble. As shown in Figure 50, after the first 120 ns energy input, the

bubbles' dynamics are independent of energy addition. For simplicity, we modeled the first cycle of oscillation after the discharge with the assumption of no significant energy or mass transfer in the momentum balance. A fraction of the discharge energy supports the microbubble oscillations. Because of the short duration of microplasma compared to the microbubble, we assume the energy for the microbubble's oscillations was all deposited into the microbubble instantaneously at the very beginning. The gravitational effect towards pressures in the RP model is constant. Microplasma generated microbubbles under micro or zero gravity is not in the scope of this paper.

In the 'inertial bubble model' presented by Brennen [98], the dynamic force balance is given by the Equation15, Equation 16 and Equation 17 define the bubble pressure, P_b, which includes both incondensable gases pressure, P_{gas}, and water vapor pressure P_v. P_{gas} is related to the equilibrium gas pressure, P_{g-eq}, and the equilibrium radius, R_{eq}, of microbubble described by Equation 18 through a polytropic constant n. P_v is determined assuming a saturated vapor at a temperature equal to the incondensable gas temperature, T_b, as given by ideal gas and polytropic process defined in Equation 19 from equilibrium gas temperature, T_{b-eq}. The content of microbubble being the mixture of vapor and some other incondensable gases such as H_2 and O_2 has been explained based on experimental observation. It is assumed that the incondensable gases are considered to consist of 1/3 oxygen and 2/3 hydrogen by mole fraction based on H_2O dissociation. In equation 1, the first term in brackets represents the dynamic component of the boundary, the second one represents the surface tension component on the

boundary, the third one represents the internal force which includes pressures both from incondensable and condensable gases, and the last one represents ambient hydrostatic pressure.

$$[R\frac{d^2R}{dt^2}+\frac{3}{2}(\frac{dR}{dt})^2+4\frac{\nu_L}{R}(\frac{dR}{dt})]+[\frac{2S}{\rho_L R}]+[-\frac{P_b}{\rho_L}]+[\frac{P_\infty}{\rho_L}]=0; \quad \text{Equation15}$$

$$P_b = P_v + P_{gas}; \quad \text{Equation 16}$$

$$P_{gas} = P_{g-eq}(\frac{R_{eq}}{R})^{3n}; \quad \text{Equation 17}$$

$$R_{eq} = \frac{2S}{P_v + P_{g-eq} - P_\infty}; \quad \text{Equation 18}$$

$$T_b = T_{b-eq}(\frac{P_{gas}}{P_{g-eq}})^{\frac{n-1}{n}}; \quad \text{Equation 19}$$

In these equations, R is the time dependent radius of microbubble, ν_L is the kinematic viscosity, ρ_L is the density of liquid, S is the surface tension of liquid, and P_∞ is the ambient pressure. S, ν_L, P_∞, T_∞, and ρ_L are constants for the ambient water at a saturation temperature of 373K (75 mN/m, 0.801×10^{-6} m^2/s, 1.025×10^5 Pa, 300 K, 1×10^3 kg/m^3, respectively). These equations were solved for R as a function of time using a built in ordinary differential equation solver (ode23t) in Matlab. The numerical solutions were checked for time step convergence and energy conservation by calculating the solutions for many cycles and verifying that the amplitude of oscillations is constant. Initial radius R_0 and initial velocity $\dot{R}_0$ as well as n, T_{b-eq} and R_{eq} were used as fitting parameters to compare the model to experiment. These five fitting parameters are used

to achieve best fitting using least square error comparing the simulations to the experimental data for bubble radius as a function of time in the first cycle of oscillation. The initial conditions for the bubble (R_0 and $\dot{R}_0$) determine the energy available for the oscillation of the bubble. Experimentally, the initial conditions, R_0 and $\dot{R}_0$ of microbubble in our model study are estimated to be around 10μm, and 100m/s respectively, based on images in Figure 54. These values after best fitting of R_0 and $\dot{R}_0$ should be comparable. Bubble temperature and radius at equilibrium (T_{b-eq} and R_{eq}) determine the equilibrium gas pressure. And the polytropic constant (n) determines the dynamics of internal & kinetic energy transfer, and should be bounded between 1 (isothermal) and 1.4 (isentropic diatomic gas). After a best fitting solution is found, the values can be used to determine the thermodynamic state in the bubble, including pressure, temperature, vapor fraction, mass and internal energy. Based on our model results, the maximum temperature is about 390 K and the minimum temperature of microbubble is around 37 0K. This supports the assumption that heat transfer is not the main driving force over the range of radius change discussed in this paper. Including both water vapor and incondensable gases (H_2 and O_2) in the RP model is important. If water vapor is neglected, the best fitting procedure gives a polytropic index n of 0.101 which is non-physical because it requires heat flow along a positive temperature gradient. On the other hand, if only vapor existed in a microbubble, the bubble pressure is not able to provide a sufficient mechanism for oscillations in the model. So both of the

incondensable and the condensable gases are needed to make the microbubble have enough resilience to bounce.

The radius changes from the experimental observation and from the best fitting of RP model with microsecond and nanosecond discharges are both presented as comparisons in Figure 55. Experimental results and theoretical model match well for the first cycle. Fitting parameters for microsecond discharged microbubble are R_0 =10±2 μm, $\dot{R}_0$ =99±5 m/s, n =1.011±0.005, T_{b-eq} =371±2 K and R_{eq} =71.58±10 μm, and for nanosecond discharged microbubble are R_0 =10±2 μm, $\dot{R}_0$ =79±5 m/s, n =1.015±0.005, T_{b-eq} =371±2 K and R_{eq} =49.65±10 μm. The best fitting solutions were analyzed around their minima to determine the sensitivity to the fitting parameters. Ranges for the fitting parameters, as given above, were determined by comparing the experimental uncertainty in radius (determined to be around ±2μm in Figure 55 in first cycle) to the root mean square errors.

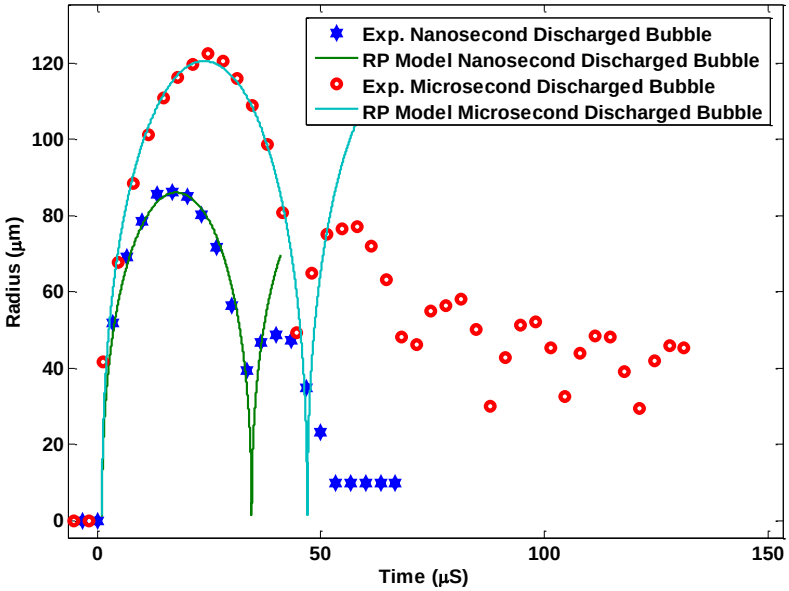

Figure 55. Comparison of Experimental Results with RP Model Results for Both Microsecond and Nanosecond Discharged Microbubbles

At the end of the first collapse, the model predicts there is what is described in the literature as a singularity, where the radii of microbubbles collapse to smaller than 1μm for both cases, as presented in Figure 56. This tiny radius would occur between two experimentally observed radii and was not recorded by the high speed CMOS camera. There are two possible reasons, one is that the camera speed is not fast enough to capture this fast variation of radius, and the other is that our inertia model does not take significant mass and energy transfer into consideration. If the formation of vapor and the heat transfer is huge, presumably, the microbubble will not be able to collapse to such a small radius before bouncing back. At the time when the radii were smaller than 10μm, a

thermal bubble model may be more appropriate than the inertia bubble model. Such models have been used for sonoluminescence bubbles [110], where similar bubble oscillation patterns and singularities are observed. But those model only covered a single species of incondensable gas in the bubble [111, 112]. Most sonoluminescence research operates at conditions without significant phase change in order to observe a sharp singularity (noble gases and specific liquids are typically used). In the research of sonoluminescence bubble, singularities which correspond to light emission and plasma generation are observed at each minimum radius during oscillations. In our microplasma generated microbubble tests, singularity and microplasma is observed at initiation only. In future work, a thermal model will be used to describe the dynamics of a microplasma generated microbubble for the small radii at initiation.

The pressure, the temperature, the mass and the internal energy of the water vapor, the incondensable gases (H_2 and O_2) and the combination of vapor and gases, based on model calculation, are presented in Figure 56. The thermodynamic properties of microsecond discharged microbubble are depicted in the first row, and those of nanosecond discharged microbubble are in the second row. The pressure drop is very fast at the beginning of the bubble's growth. At around 2 μs after the initiation, the internal pressures of microbubble are around 1 MPa for both cases. The pressure in the microbubble is mainly dictated by the vapor pressure which is relatively constant. In the figures of pressure variations, the incondensable gases' pressure changes significantly at small radius. The pressure in the microsecond discharged microbubble (1.2 MPa) is higher than that in the nanosecond discharged microbubble (0.6 MPa) at initial radius.

The temperature of the microbubble stays at around 370K except when the microbubbble is small (<3μm). From the Figure 56(b) and (f), the temperature in the microbubble is around 370K±5 K during the growth period except when the time is within the first 0.1~0.2 μs. From Figure 54, the 3 μm is estimated when the time is in the range of 0.1~0.2 μs. The internal temperatures of different species are assumed to be same. The mass of the microbubble are about 16 picogram and 5 picogram for the two conditions and they change by ~20% due to the evaporation and condensation of the water vapor. This mass transfer due to evaporation and condensation (~10 picogram) has little influence on the momentum transfer described in RP model. The momentum transfer in RP model is effectively for the mass and the motion of the liquid surrounding the microbubble. The ratio of the mass transfer of vapor (~10picogram) and the mass of liquid with same volume of microbubble (~7 μg) is around 2.5×10^{-6}. So the mass transfer in terms of evaporation and condensation in our cases affect the momentum balance very little. With consideration of both the pressure variation and mass transfer, the oscillation of microbubble can be divided into two different mechanisms. The incondensable gases play the role of providing the amplitude of the oscillations, whereas the water vapor buffers the oscillation by means of the mass transfer. The mass in the microsecond discharged microbubble is 4 times higher than that in the nanosecond discharged microbubble.

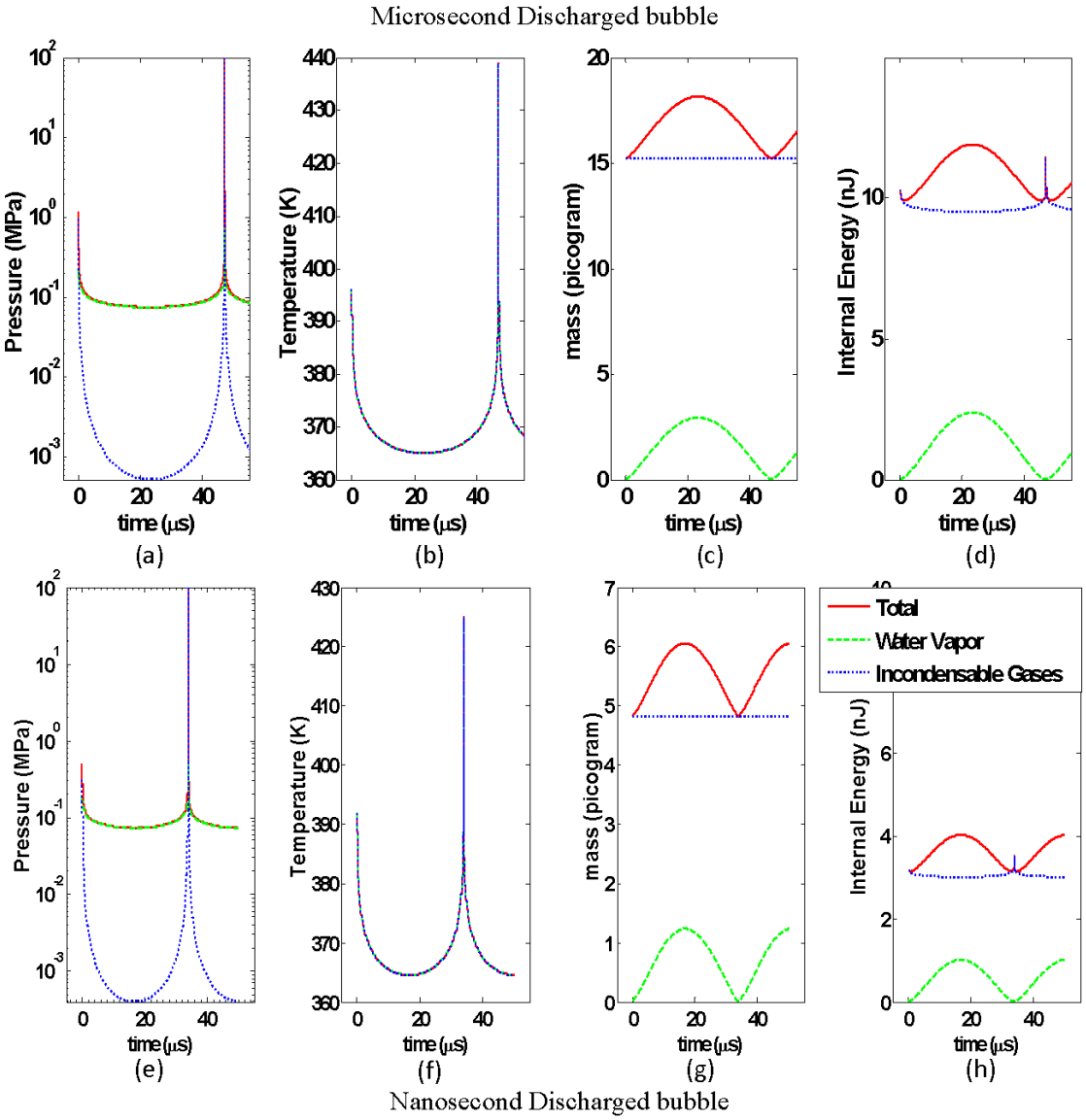

Figure 56. Comparisons of Pressure (a, e), Temperature (b, f), Mass (c, g) and Internal Energy (d, h) of Microsecond Discharged Microbubble and Nanosecond Discharged Microbubble Predicted by RP Model.

These modeling results provide parameters useful for estimating energy dissipation in the microplasma and microbubble presented in Figure 57. Several means of energy storage and dissipation from microplasmas have been considered. Considered energy associated with microplasmas from microsecond and nanosecond discharges includes 1: the internal energy of microbubble (~11 nJ and ~4 nJ), 2: the heat conduction from the hot plasma for heating and melting of the microelectrode tip (~4 μJ for both, with melting volume estimated), 3: the heat conduction from hot plasma to the microelectrode (~710 μJ and ~160 μJ with assumptions of temperature difference between plasma to far-away microelectrode as 4000 K, heat penetration time of 4μs and 200 ns respectively, and using thermal diffusivity of tungsten at 4000 K), 4: the heat conduction from hot plasma to ambient liquid (~35 μJ and ~8 μJ with assumptions of temperature difference between plasma to ambient liquid as 5000 K, heat penetration time of 4 μs and 200 ns respectively, and using thermal diffusivity of liquid water), 5: the heat conduction from the microbubble to the microelectrode (193 μJ and 170 μJ with assumptions of temperature difference between the microbubble and ambient liquid as 100 K, heat penetration time of 45 μs and 35 μs, and using thermal diffusivity of tungsten at 400 K (the time here is for the first cycle of microbubble oscillation)), and 6: the heat conduction from the microbubble to the surrounding liquid (~38 μJ and ~33 μJ with assumptions of temperature difference between the microbubble and ambient liquid as 100 K, heat penetration time of 45 μs and 35 μs, and using thermal diffusivity of liquid water). The summation at these energies represents an upper bound on the amount of energy in the plasma. The energies of microplasmas are estimated as ~980 μJ and

~375 μJ respectively. The energy input to the microelectrode for microplasma generation for both cases is in millijoule scale by circuit measurement (103 mJ and 0.5 mJ). Quantitative analysis of different energy dissipations as well as the estimated formulas is presented to illustrate that majority of energy from spark gap actually is not used for plasma generation. The energy consumptions in Table 4 are rough estimations to show the orders of the energy each means consumes for both microsecond and nanosecond discharged microbubble. Details concerning of means of energy dissipation, the formulas used for each calculation and the estimated energy consumption for both of microsecond and nanosecond discharges are described in appendix.

An important finding is that the energy for the plasma generation can be significantly less than the applied energy input. The energy used for microplasma generations is less than 1% of the input for the microsecond discharge and 65% of the input energy for the nanosecond discharge. Some of the energy supplied from spark gap is consumed through other parasitic means such as electrolysis (mainly for the microsecond discharge), inductance induced energy consumption (emitted as EMI), double layer formed capacitances along microelectrode, Joule heating from microelectrode to ambient liquid, etc., which will be addressed in detail in future work. The parasitic effects are more prominent in the microsecond discharge than the nanosecond discharges. Joule heating and electrolysis do not appear sufficient, at most ~100 μJ and ~50 μJ, for the energy not into microplasma (99% of input) for the microsecond discharge. The capacitance of the double layer is large and can store all of the missing energy at low voltage and release it over long time. However, the dynamics

of double layer at such high voltage (-11 kV) have not been studied and are difficult to estimate, leaving a proper account of 99% of applied energy in microsecond discharge as future work. This low energy process while inefficient allows for a more non-equilibrium plasma. Pulsing high voltage power supplies with energy per pulse for plasma initiation less than 1mJ are uncommon. The low energy makes the size of plasma small and it leads to discharges and microbubbles which are spherical in shape and different from other non-spherical microbubbles produced by high energy plasma discharge in liquid [113]. Processes such as the localized synthesis of nanoparticle by microplasma [74] and nanoscale corona based nanosecond optical emission spectroscopy [75] are allowed only with such low energy non-equilibrium plasmas.

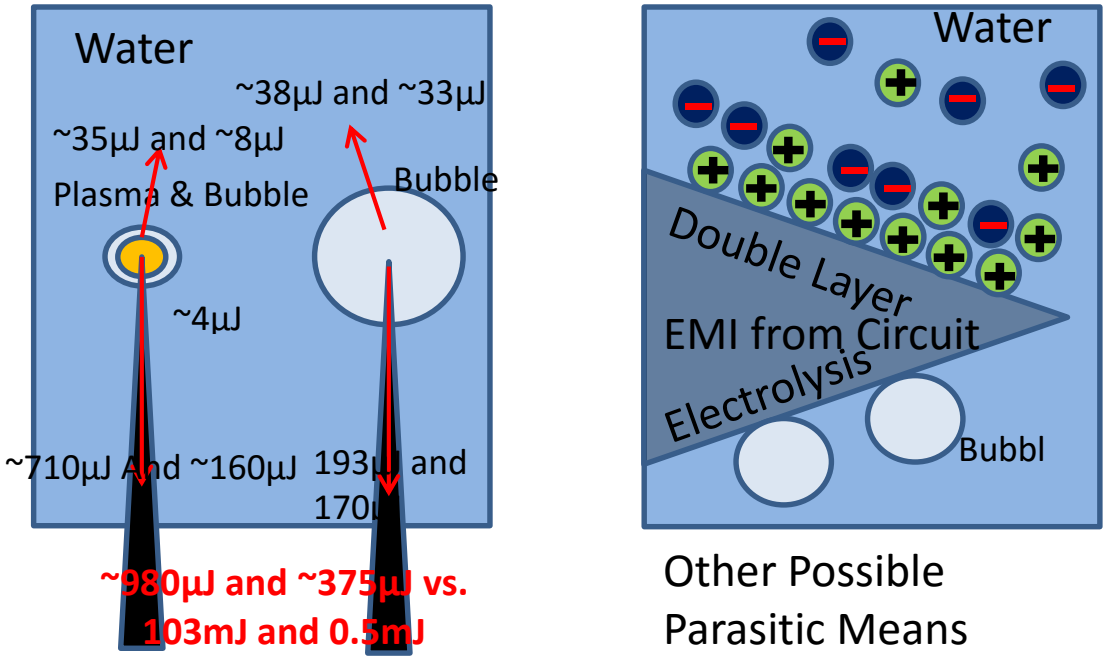

Figure 57. Possible Energy Dissipation in Liquid

Table 4. Estimated Energy Dissipations in Microplasma Discharges

Energy Path	Energy (Microsecond Dis.)	Energy (Nanosecond Dis.)
Internal Energy of Microbubble	~11nJ	4nJ
Phase Change of Water in Microbubble	~7nJ	~1.5nJ
Dissociation of Water in Microbubble ($2H_2O=2H_2+O_2$)	~0.23μJ	~0.08μJ
Kinetic Energy of Water Surrounding the Microbubble	~62nJ	~35nJ
Microtip Heating and Melting	~4μJ	~4μJ
Microelectrode Heating	0.71mJ	0.16mJ
Heat Transfer to Water Surrounding the Microbubble	~0.7μJ	~0.15μJ
Electromagnetic Interference (EMI) Caused by Wiring	~5.6μJ	~5.6μJ
Joule Heating in Liquid	0.3mJ	0.015mJ
Charging of Debye Length Capacitance	~20nJ to 20mJ	~20nJ to 20mJ
Light Emission of Na^*	~0.3nJ	0.1nJ
Electrolysis in Liquid for Microsecond	50μJ	0.4μJ

The energy dissipations from microplasma and microbubble generation are summarized and the quantities corresponding to different dissipations are calculated. In this section, details involving estimation equations and the relevant parameters are described. They are all rough estimations to present the order of each energy dissipation, by which the energy input for microplasma generation in microjoule scale is concluded.

The addition internal energy of the microbubble is estimated with temperature difference between the vapor in microbubble and the ambient liquid ΔT_1, average specific heat of vapor $C_{p-vapor}$, hydrogen C_{H_2} and oxygen C_{O_2} in the bubble and the mass of different species such as m_{vapor}, m_{H_2} and m_{o_2} from model results. The mass of bubbles are different between microsecond and nanosecond discharged microbubble, the internal energy stored is around 11 nJ and 4 nJ respectively (nanojoule scale) with Equation 20.

A component at the internal energy, estimated separately, is the energy for phase change of liquid. The vapor in the microbubble is heated from liquid to vapor at boiling temperature in the microbubble. Since the average temperature of vapor in microbubble is estimated around 373K from model, the latent heat of phase change h_{fg}, and the vapor mass m_{vapor} are chosen with an assumption that the vapor in the bubble stays at saturated temperature at 373K. The energy consumption for the phase change are around 7nJ and 1.5nJ respectively (nanojoule scale), calculated with Equation 21.

Besides the vapor in the microbubble, the dissociated incondensable gases also play important role in consuming the energy from microplasma. Dissociation of water

(electrolysis) is estimated based on the formation enthalpy of hydrogen $h^o_{H_2}$, oxygen $h^o_{O_2}$ and water $h^o_{H_2O}$ with the mass of water m_{liquid} involved in this reaction estimated in model. The energy consumption are around 0.23μJ and 0.08μJ (microjoule scale), calculated with Equation 22.

The Rayleigh-Plesset model is based on the momentum balance from microbubble's boundary to the ambient liquid. This liquid motion has kinetic energy associated with it. Due to the mass conservation of the liquid, the velocity v at radius of r in liquid can be estimated by using R_0 and V_0 from best fitting values. The kinetic energies from the microbubble interface to ambient liquid for both cases are around 62nJ and 35nJ respectively (nanojoule scale), calculated with Equation 23.

Part of the energy is used to heat up and melt the microelectrode tip. It is assumed the microtip was heated up to the melting point of tungsten. ΔT_2 is the temperature between tungsten melting point to ambient temperature, $C_{p-tungsten}$ is the specific heat for tungsten and h_{sl} is the latent heat of tungsten from solid to liquid. $m_{tungsten}$ is estimated based on the observed melting volume presented in Fig. 3. The energy for heating and melting microtip is around 4μJ (microjoule scale), calculated with Equation 24.

Thermal energy not only heats up and melts the microelectrode tip, but also conducts along the microeletrode which has radius of R_{ele}, specific heat of C_{P-W} and density of ρ_W. ΔT_3 is the temperature difference between melting point of tungsten and

ambient temperature of water at atmospheric pressure. Characteristic length of heat penetration L_1 (~18μm and ~4μm) of transient heat conduction along the microelectrode is determined with the discharge time t_1 (4μs and 200ns respectively) and tungsten thermal diffusivity α_W . The energy dissipations for both cases are around 0.71mJ and 0.16mJ respectively (microjoule scale), calculated with Equation 25.

With the same time of discharges, thermal energy also transfers from the microbubble to the ambient liquid. Characteristic length of heat penetration L_2 (~1.3μm and ~0.2μm) is determined with discharge time t_2 (4μs and 200ns respectively). ΔT_4 is the temperature difference of microbubble and ambient liquid. The energy dissipations for both cases are around 0.7μJ and 0.15μJ respectively (microjoule scale), calculated with Equation 26.

The time-varying current from the spark gap through cables emits the electromagnetic interference (EMI). The self-inductance L_{ind} of cable is 0.7μH. The time-varying currents $I(t)$ for both cases are collected. The energy emitted as EMI is around 5.6μJ (microjoule scale), calculated with Equation 27.

In addition to the microtip used for the microplasma generation, there is about 1mm of microelectrode not covered by epoxy as dielectric insulation. This area can also dissipate electrical energy through liquid to ground. The NaCl solution had a conductivity σ_{liquid} at ~5000μS. The variation of conductivity due to the change of temperature is considered and is negligible [114]. The aqueous resistance is assumed to be equivalent to a cylinder wrapped around the exposed area of microelectrode. The

length of microelectrode is L_3 (~1mm), the aqueous resistance R_{liquid} can be calculated by the integral of radius r from microelectrode surface to the gap distance between cathode and anode in the liquid, and $V(t)$ is the voltage variation of discharges. The joule heating of NaCl solution is the integral of the power of aqueous resistance. The energy dissipations for both cases are around 0.3mJ and 0.015mJ respectively (millijoule scale), calculated with Equation 28.

During the discharge, between anode to liquid, and cathode to liquid, there is Debye layer λ_D to screen charges. The potential drop across the Debye length V_{λ_D} can be treated as a capacitor [115], which stores energy from instant discharge and releases the energy into liquid later. The Debye length λ_D from the microelectrode surface is calculated based on the solution [116], A_2 is the area exposed from the microelectrode to liquid, ε_{liquid} is the permittivity of the liquid at ambient temperature with discharge frequency lower than 1GHz [114]. The energy stored in the capacitors of Debye length is provided by the potential drop across the Debye length and it is assumed it is same for both microsecond and nanosecond discharge. The energy released for both cases could be from 20nJ (nanojoule scale) to 20mJ, calculated with Equation 29. We have to admit that except the energy estimation stored in double layers, all the other energy estimations are believed to be within a 20% tolerance. The difficulties are the estimation of the thickness of the double layer, the potential drop across the double layer and the area of the double layer capacitor. Literatures we have found covered 2 to 3 V electrical potential drop, but our cases had around 3 kV to 20 kV electrical potential drop.

Plasma creates light emission by emitting photons. Light emission from electronic excited sodium species plays the main role in light emission. With sodium concentration from measurement, the mass of vapor in the microbubble estimated and the assumptions that every sodium atom in the microbubble emits one photon and Na concentration in the bubble is same as solution, parameters such as the number of sodium toms $\#_{Na^*}$, Plank's constant h, light speed c, and wavelength of sodium light emission λ_{577nm}, are used to estimate the energy dissipation. The energy consumption by light emission is at most 0.3nJ (nanojoule scale), calculated with Equation 30.

Dissociation of water in terms of electrolysis in the microbubble is described above and calculated in Equation 22. Since the whole tungsten microelectrode is immersed in water, the electrolysis along the immersing part of the microelectrode also consumes energy. By introducing Faraday's laws of electrolysis, the mole fraction of the electrons from the cathode to the generated hydrogen is calculated as two. With the time-dependent current $I(t)$ measured in Fig. 5 and Fig. 6, the energy of electrolysis along the microelectrode can be calculated with formation enthalpy of water $h^o_{H_2O}$ and Avogadro's number N_a. The energy dissipations for both cases are around 50μJ and 0.4μJ respectively (microjoule scale), calculated with Equation 31.

Table 5. Estimation Equations of Energy Dissipation

Estimation Equation	Number	Energy (Microsecond Dis.)	Energy (Nanosecond Dis.)
$E_1 = \Delta T_1 \times (C_{p-vapor} \times m_v + C_{H_2} \times m_{H_2} + C_{O_2} \times m_{O_2})$	Equation 20	~11nJ	4nJ
$E_2 = h_{fg} \times m_{vapor}$	Equation 21	~7nJ	~1.5nJ
$E_3 = (2h^o{}_{H_2} + h^o{}_{O_2} - 2h^o{}_{H_2O}) \times m_{liquid}$	Equation 22	~0.23μJ	~0.08μJ
$E_4 = \frac{1}{2} \int_{r=R_0}^{\infty} 4\pi r^2 \rho_{liquid} v^2 dr$ $v = \frac{R_0^{\,2}}{r^2} V_0$	Equation 23	~62nJ	~35nJ
$E_5 = h_{sl} \times m_W + \Delta T_2 \times C_{p-W} \times m_W$	Equation 24	~4μJ	~4μJ
$E_6 = \Delta T_3 \times \pi R_{ele}{}^2 \times L_1 \times C_{p-W} \times \rho_W$ $L_1 = \sqrt{\alpha_w \pi \times t_1}$	Equation 25	0.71mJ	0.16mJ
$E_7 = \Delta T_4 \times 4\pi R_0{}^2 \times L_2 \times C_{p-liquid} \times \rho_{liquid}$ $L_2 = \sqrt{\alpha_{liquid} \pi \times t_2}$	Equation 26	~0.7μJ	~0.15μJ
$E_8 = \int_{t=0}^{\infty} L_{ind} \frac{dI(t)}{dt} \times I(t) dt$	Equation 27	~5.6μJ	~5.6μJ
$E_9 = \int_{t=0}^{\infty} \frac{V_{drop-bulk}(t)^2}{R_{liquid}} dt$ $R_{liquid} = \int_{r=R_{ele}}^{r=cathode-anode} \frac{dr}{2\pi r L_3 \sigma_{liquid}}$	Equation 28	0.3mJ	0.015mJ
$E_{10} = \frac{1}{2} C V_{drop-\lambda_D}{}^2$ $C = \frac{\varepsilon_{liquid} A_2}{\lambda_D}$	Equation 29	~20nJ to 20mJ	~20nJ to 20mJ
$E_{11} = \#_{Na^*} \times h \frac{c}{\lambda_{577nm}}$	Equation 30	~0.3nJ	0.1nJ

Table 5 Continued

Estimation Equation	Number	Energy (Microsecond Dis.)	Energy (Nanosecond Dis.)
$4e^- + 4H_2O = 2H_2 + 4OH^-$ $E_{12} = \left[\int_{t=0}^{\infty} I(t)dt\right] / e \times \frac{4e^-}{2H_2} \times h^o_{H_2O} \times N_a$	Equation 31	50μJ	0.4μJ

The total energy involves microplasma generation is $E_1 + E_2 + E_3 + E_4 + E_5 + E_6 + E_7 + E_{11} \approx 715\mu J$ and $164\mu J$ respectively for microsecond and nanosecond discharged microbubbles.

4.6 Uncertainty Study of Best-fitting Parameter

The best-fitting parameters are calculated based on RP model presented in section 3.3. The algorithm of this best fit has been described in detail as well. The best fit in our calculation indicates a minimum of root mean square errors in a five-dimension matrix. However, whether this minimum is a local minimum or a universal minimum is still unknown. In addition, how sensitive of such minimum in our calculation needs to be carefully investigated. In this section, each of the five best fitting parameters, initial radius R_0 and initial velocity $\dot{R}_0$ as well as polytropic index n, equilibrium temperature T_{b-eq} and equilibrium radius R_{eq}, is fixed as a controlled variable, while other four best-

fitting parameters still optimize them to the minimum root mean square errors. With a varied controlled parameter, the root mean square errors are plotted in Figure 58.

In Figure 58 Rzero Sensitivity, the initial radius is used as a controlled parameter. It varies from 5 μm to 18μm with 14 steps in between. It presents that the initial radii from 6 μm to 10 μm stay at a similar root mean square error. The sensitivity is not obvious when the initial radius is from 5 μm to 12 μm. When the initial radius is set to bigger than 12 μm, the root mean square errors show significant changes. The best-fitting variables match with controlled initial radius are calculated and the results are shown in Table 6.

In Figure 58 Vzero Sensitivity, the initial velocity of a microbubble is used as a controlled parameter. It varies from 50 m/s to 130 m/s with 10 m/s as an interval. The other four parameters are used for the best fit. The root mean square errors are calculated according to different initial velocities. The initial velocity has a very single minimum in the figure and it presents that the initial velocity is pretty sensitive than the initial radius. The minimum error occurs when the initial velocity is around 110 m/s. Other than this velocity, the root mean square errors become bigger.

In Figure 58, Tb0, the equilibrium temperature in the microbubble is used as a controlled parameter. In our model, the pressure changes with the change of the temperature, and the temperature and the pressure determines the thermodynamic properties of the microbubble in liquid. The temperatures are controlled to vary from 350 K to 373.15 K as the constant for each best-fitting calculation. The upper limit for the liquid is restricted by its physics. The boiling temperature of water at one

atmospheric pressure indicates that beyond this temperature there is no liquid-vapor mixture. Without the existence of liquid and vapor, there is no boundary to form the microbubbles. From the calculation, the boiling temperature for the water at one atmospheric pressure i.e., 373.15 K presents the minimum root mean square error. When the equilibrium temperature is lower than the boiling temperature of water at one atmospheric pressure, the root means square errors increases monotonically. This results also illustrates that this boiling temperature is a very sensitive parameter, around which there only one minimum error is existing.

In Figure 58, Req Sensitivity, the equilibrium radius is used as the controlled parameter. It varies from 60 μm to 90 μm. At each equilibrium radius, the other four best-fitting parameters are calculated to get a minimum root mean square errors, just like the samples presented in above cases. The sensitivity results presented that the equilibrium radius for this case is pretty sensitive for the errors when it is smaller than 70 μm. The sensitivity becomes less sensitive when the equilibrium radius is from 70 μm to 90 μm. The results from the constant equilibrium radius actually presents that the equilibrium radius does not affect too much on the root means square errors as long as it is bigger than 70 μm. The initial radius and the equilibrium radius present similar sensitivity trends.

In Figure 58, k Sensitivity, the polytropic index is used as a controlled parameter. The physical boundary for this polytropic index has been described in previous subsection. Here the controlled parameter varies from 1.01 to 1.09. The minimum root

mean square error only occurs when the polytropic index is 1.01. It significantly changes when the polytropic index increases from 1.01 to 1.09.

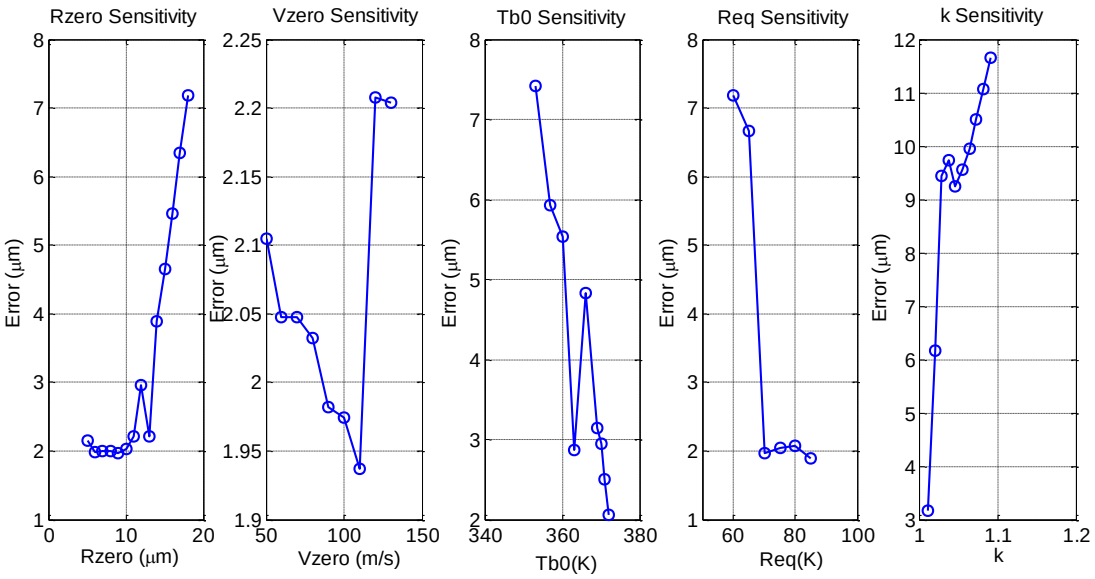

Figure 58. Sensitivity Study of Best-Fitting Parameters in RP Model

Table 6. Variation of Best-Fitting Parameters with Rzero as a Controlled Input

Req (μm)	Vzero (m/s)	Teq (K)	k	**Rzero (μm)**
71.2419	98.2877	371.6518	1.0104	**5**
69.518	99.4636	370.6047	1.0103	**6**
69.4718	99.3101	370.7103	1.0104	**7**
69.8283	99.16	371.1274	1.0113	**8**
69.4824	98.4693	371.1977	1.0111	**9**
69.5362	**98.1789**	**371.4203**	**1.0115**	**10**
70.2688	100.5244	374.8099	1.0144	**11**
70.1094	100.1563	377.4375	1.0168	**12**
69.9751	96.3771	377.977	1.0187	**13**
69.2889	97.7118	372.053	1.0142	**14**
69.02	98.2388	371.7812	1.0145	**15**
69.0886	98.9943	371.4893	1.0146	**16**
69.0772	99.6901	371.2283	1.0151	**17**
69.1886	100.0126	370.9165	1.0152	**18**

Table 7. Variation of Best-Fitting Parameters with Vzero as a Controlled Input

Req (μm)	Rzero (μm)	Teq (K)	k	**Vzero (m/s)**
71.235	9.96183	69.5555	1.0096	**50**
71.2985	10.1081	370.435	1.0108	**60**
71.2156	9.8985	370.452	1.0108	**70**
72.1245	10.0311	371.5297	1.0126	**80**
72.3407	10.1591	371.9569	1.0134	**90**
70.3145	**9.7347**	**371.8389**	**1.0122**	**100**
68.2078	9.852	372.5223	1.0123	**110**
67.9304	10.2858	372.3288	1.012	**120**
70.5924	10.0908	375.8525	1.0158	**130**

Table 8. Variation of Best-Fitting Parameters with Teq as a Controlled Input

Req (μm)	Rzero (μm)	Vzero (m/s)	k	**Teq (K)**
41.25601	3.9464	98.4385	0.98643	**350**
72.4401	10.1639	101.0067	0.9963	**353**
68.8146	10.355	102.145	0.9987	**357**
69.4983	10.0222	100.6433	1.0019	**360**
55.7239	11.3355	105.351	0.9986	**363**
72.8919	10.0355	100.5853	1.008	**366**
70.9823	10.0163	100.5323	1.0094	**369**
72.8543	9.9095	100.7954	1.0113	**370**
73.2506	9.8096	100.2666	1.0129	**371**
71.969	**9.9859**	**101.7014**	**1.0131**	**372**

Table 9. Variation of Best-Fitting Parameters with Req as a Controlled Input

Teq (K)	Rzero (μm)	Vzero (m/s)	k	**Req (μm)**
364.494	10.1672	93.7139	1.0764	**60**
377.6252	9.9938	100.157	1.0206	**65**
371.8517	**9.7222**	**99.8198**	**1.0123**	**70**
372.5585	9.7987	103.8576	1.0155	**75**
374.5785	11.0258	90.029	1.0193	**80**
374.9303	10.0993	99.5234	1.0254	**85**

Table 10. Variation of Best-Fitting Parameters with k as a Controlled Input

Teq	Rzero	Vze	Req	**k**
370.6222	**9.9121**	**100.1005**	**70.458**	**1.01**
372.5652	9.9081	99.5562	71.5241	**1.0189**
372.0734	10.5113	101.512	63.8953	**1.0278**
372.1579	10.1596	100.0841	69.7075	**1.0367**
371.7135	10.3045	100.6699	66.1755	**1.0456**
371.3906	10.3477	99.6484	68.5234	**1.0544**
371.933	10.1651	100.4792	70.3841	**1.0633**
372.0634	10.3248	99.4295	71.4804	**1.0722**
370.125	10.5313	99.6875	68.6875	**1.0811**

4.7 Summary

A single microplasma discharge is generated under water by negative (-11 kV) pulses applied to microelectrode tips. Images of discharges and generated microbubbles were captured at 10 ns exposure time with 10ns increment by the ICCD camera and at 300k fps by the CMOS video camera. Two discharges were studied in detail, a 103 mJ microsecond pulsed discharge and a 0.5 mJ nanosecond pulsed discharge. A microbubble was observed with microplasma confined in it. The shape of microbubble

and microplasma was spherical, not branches-like [73, 87] as commonly observed. The study of microplasma generated microbubble provides a path to investigate the microplasmas. The energy to support the growth of the microbubble is provided by the microplasma. After the microplasma disappears, the microbubble expands and collapse for several oscillations. Due to energy and mass transfer, the amplitude of oscillations decays to zero. Then the microbubble at equilibrium radius is visible for ~10 μs before disappears either due to leaving the field of view or dissolving. The microplasma generated microbubble by microsecond discharge had more energy to sustain more oscillations and larger maximum radius comparing to the microbubble generated by the nanosecond discharge at same applied peak voltage. The physics of oscillations are well described by Rayleight-Plesset models. A RP model with the assumption of no significant mass and energy transfer fits well with experimental results in the first cycle of oscillation for both cases. The model allows us to describe the thermodynamic state inside the microbubble e.g., pressures, temperature, mass and internal energy, based on the observed size variation. The important features of the model are that the bubble contains vapor and ideal gases mixtures. Over the range modeled, it is approximately isothermal. The energy of the microplasma is summed up roughly. Energy in the microplasma is on the order of microjoule scale. Big portion of the input energy from the spark gap can be dissipated through other parasitic means, which will be addressed in future work. Such low energy explains that the spherical stability of microbubble's interface compared to typical branched streamers. Future work will be using a RP thermal model to accurately predict the temperatures at initial stage of microplasmas.

Also it is important to determine the reasons for spherical bubbles reported in this paper and branched bubbles reported in literatures. Due to the low energy inputs, the microplasmas in this paper are believed to be non-equilibrium plasmas. It is unknown for the degree of non-equilibrium in current results. In the future work, time resolved spectroscopy involving Stark broadening will be conducted to estimate the number density of electrons in the microplasma. The number density of neutrals can be deducted from the estimation of pressure in the microbubble. With knowing the electron number density and neutral number density, the degree of non-equilibrium can be answered.

CHAPTER V

DYNAMICS OF MICRODISCHARGE GENERATED SPHERICAL MICROBUBBLE UNDER VARIOUS AMBIENT PRESSURES

5.1 Section Overview

A microplasma and a spherical microbubble can be generated simultaneously in liquid. The microbubbles' dynamics is able to give insight into the amount of energy deposited by the plasma. A DC high voltage power in combination with spark gaps were used for pulsed power input. The pulsed microsecond or nanosecond discharges were used to generate the microdischarges, and the rising time of the pulsed power was around 15 ns. The magnitudes of pulsed voltage, hereafter refer to as the applied peak voltage (APV), and the durations of discharges were varied in this research to control the energy inputs. The APVs were tuned from -3 kV to -9 kV with 2 kV as interval. The initiation of microplasma and microbubbles have been addressed in our previous research, and the hydrodynamics of microplasma generated microbubble at ambient pressure (0psig) was studied by using Rayleigh-Plesset (RP) model. With the consideration of the coexistence of the condensable and incondensable gases in the microbubble, the RP model matched well with our experimental results. In this chapter, the hydrodynamics of the microplasma generated microbubbles in a pressure controlled environment was studied parametrically. The environmental pressure was adjusted from 0psig to 80psig. DI water with two different surface tensions was prepared (71 mN/m and 35 mN/m at 25 ^{o}C) as well, since the surface tension component in RP model

contributes to the surface momentum balance. The generation and the oscillation of microbubbles were recorded by a CMOS high speed camera (300k fps). The radius change of microbubbles corresponding to time under different pressures was depicted. The RP model with different ambient pressures and surface tensions were studied and compared with our experimental results. One of the advantages of RP model, which is built up on momentum balance, is to allow the estimation of the thermodynamic states and the energy deposition of the microplasmas and microbubbles. It was observed that the pressure of the microplasma and microbubble at the initiation stage was very high and decreased significantly in first hundreds of nanoseconds. It is concluded that the moderate environmental pressure won't affect this initiation significantly, but it does affect the hydrodynamics of microplasma generated microbubble after it expands in microsecond scale.

5.2 Experimental Setup

The microplasma generation and microdischarge generated microbubbls were described in previous chapters. In order to generate microplasma in liquid, short rising time discharges (nanosecond scale) with kilovolts outputs are necessary for the plasma initiation. In Chapter II, the fabrication of micro electrode tip was introduced. A tungsten microelectrode wire was sharpened to around 2 to 3 μm using electrolysis. In this microplasma-and-microbubble-generate-in-pressure-vessel tests, a same microelectrode tip was fabricated as well. The microelectrode except the tip part was covered by Teflon coating as an electrical insulation layer. In this case, one half of the microelectrode (tip

side) was left in the pressure vessel to generate microplasma, at the same time the other half of the microelectrode was left out of the pressure vessel to connect to the power supply. The sealing and the connection will be described in detail in the later subsection.

5.2.1 Image Acquisition Toolset

Two different high speed cameras were used to capture the microplasma and microbubble generation. The ICCD camera as described in previous chapters was used to detect the microplasma generation. It was able to have a delay time and an exposure time within the nanosecond scale. The microplasma generated in our study normally lasted from the nanosecond scale to the microsecond scale, so the ICCD was fully capable of capturing the plasma's generation. The microbubble's oscillation, on the other hand, was captured and recorded using the million frame per second CMOS camera. For the microbubble generation, our concern was more on the hydrodynamic properties of microbubble, which means a continuous recording of the radius changes was very important. As for the plasma generation and the plasma light emission, this camera was not fast enough. The ICCD and the CMOS camera both were triggered by the EMI in our setup. The advantage of triggering the high speed cameras using the EMI is that the time scheme would be more accurate. The time delay after the discharge could be precisely monitored.

Choosing the right parameters for both high speed cameras could be tricky. As for the high speed CMOS camera, for instance if it works with 1 million frame per second, the exposure time will be one micro second and the frequency of the shutter

switching is 1 million Hz. One drawback of using high speed camera is that if the object of interest does not emit strong light, the environmental light needs to be bright enough to make sure that sufficient photons can be reflected from the object of interest to the CMOS camera within very limited exposure time. In addition, other than the short exposure time, the light intensity in this test were also attenuated on its path. The microplasma and microbubble generation was created in a pressure vessel. In order to make sure that the pressure be hold to 80 psig and no leaking occur, the main body of the pressure vessel was made of stainless steel and half inch thick acrylic sheets. The light was provided through a glass light pipe. The details of this light pipe and the setup of this experiment is introduced in the next subsection. The light pipe used in this test is a one foot long a quarter inch in diameter glass tube. The light through the light pipe can be projected onto the microelectrode tip, and then goes through the microscope to the observing lens. A halogen lamp was used for the alignment of microelectrode tip with the microscope objective.

Room fluorescent light or the halogen lamp in general could not provide enough light for the high speed camera due to its short exposure time. A stronger light source was necessary in this test. Laser, due to its high photon density, was used to provide a much higher light intensity. The laser used in this test was a green point laser with the wavelength of 532 nm and the laser power of 300 MW. The laser went through the light pipe, and illuminated the microelectrode and its surroundings.

For the short exposure time, the laser was used. However, the power from the laser was constant. It might be too strong for the high speed camera with long exposure

time. The intensifier in the high speed cameras could be damaged if without any protection. So neutral density filters (Edmund Optics) with 6 different attenuations were employed to control the light intensity towards the microelectrode tips. The optical density of these neutral density filers were 0.15, 0.3, 0.4, 0.6, 0.9 and 2.5 presented in Figure 59, so the transmission of the light with wavelength of 532 nm was around 70%, 50%, 40%, 25%, 12% and 1% respectively. A single neutral density filter or a combination of several neutral density filters were placed between the laser light source and the light pipe. The setup of the neutral density filter and the laser will be presented in the next subsection.

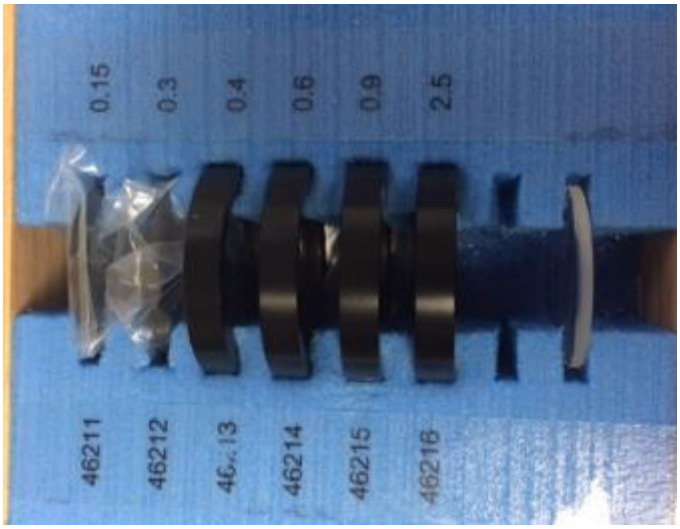

Figure 59. Neutral Density Filters

5.2.2 Experimental Layout

The experimental setup is presented in Figure 60. The pressure vessel in the center of this diagram can hole the pressure from 0 psig to 80 psig. The details of the pressure vessle will be introduced in the next subsection. Several components are critical for the pressure controlled microplasma tests. Different from the previous experiemts in open air which operated at one atmospheric pressure, the pressure vessel in this research not only needs to maintain the ambient pressure at a desirable value but also needs to assure the light, power lines and image acquisition are all sucessfully connected with the discharge wire inside of the vessel without any air leakages.

Light illumination was very important in this experiment for the observation of the microdischarge generated microbubble's hydrodynamic properties. In previous tests without using the pressure vessel, the light was placed very closed above the microelectrode tip, so the light intensity could be strong enough for the observation of nanosecond events. With the pressure vessel, the light source had to be placed around 20 cm above the microplasma discharge even without the consideration of sealing issues. The real experimental components in our tests are presented in Figure 61. Placing a LED light source with 20 cm distance from the tip was not practical, since only small portion of the light can reach the microelectrode tip and the light intensity would be attenuated during the trnasmission, not even to mention the light needed to transmit through the air in the pressure vessel and the liquid surrounding the microelectrode tip. As mentioned above, the light needed to go though a window as well no matter what design was applied eventually. The window was used on the purpose of sealing. The solution for the

light illumination was a one foot long and a quarter inch in diameter glass tube as a light pipe. The purpose of using the light pipe was to restrain the light to transmit in the light pipe and also for sealing. The light pipe was held with a wire grip on the top of the pressure vessel, and light could be transmitted into the pressure vessel towards the top of microelectrode tip. By using a wire grip connector, the sealing issue was solved sucessfully.

Single or double spark gaps were used to provide microsecond or nanosecond discharges. The discharges could be manually triggered or signally triggered by a function generator. The signal outputs from the function generator were presented on the oscilloscope together with other signals such as the time shutter opens and closes of the ICCD camera, the rising of the breakdown voltage on the discharge load and the pulsed current through the microelectrode tip to the liquid. Since all tests of electrical signals were in nanosecond scale, the signals showed on the oscilloscope could help us to determine the sequence of the different events.

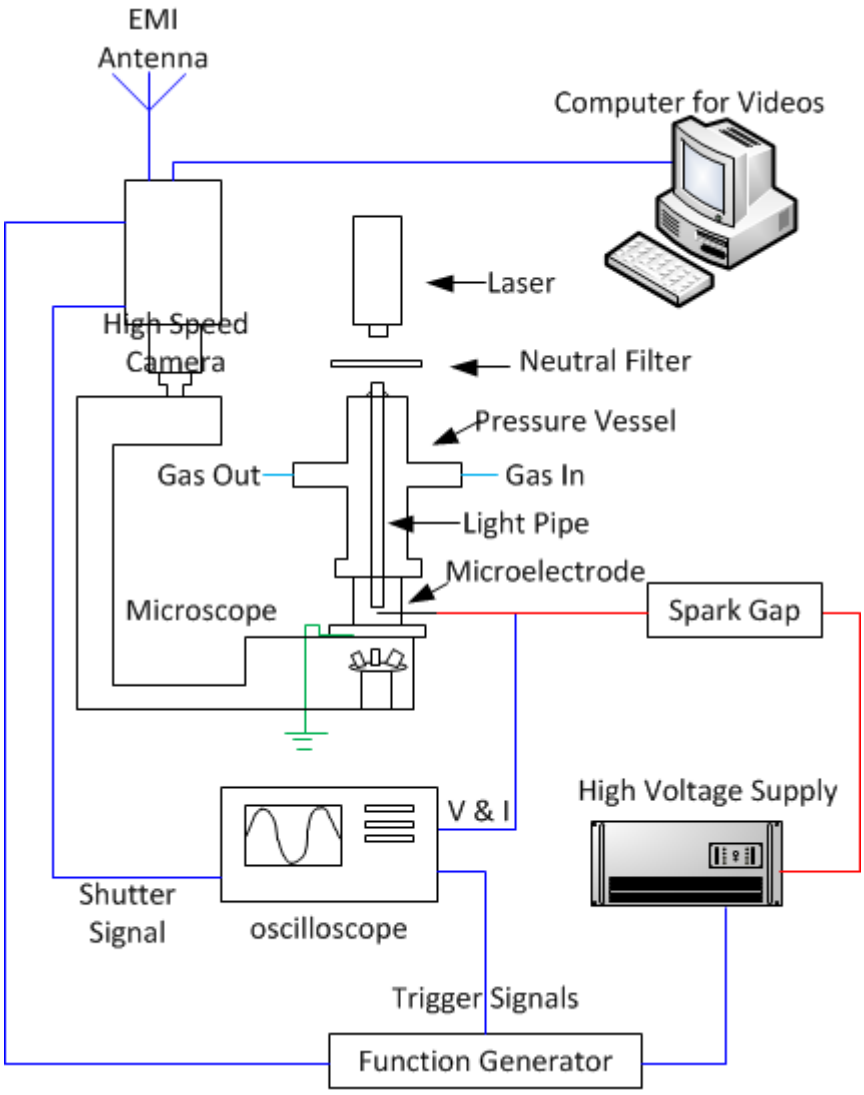

Figure 60. Schematic Diagram of Experimental Setup Using Pressure Vessel

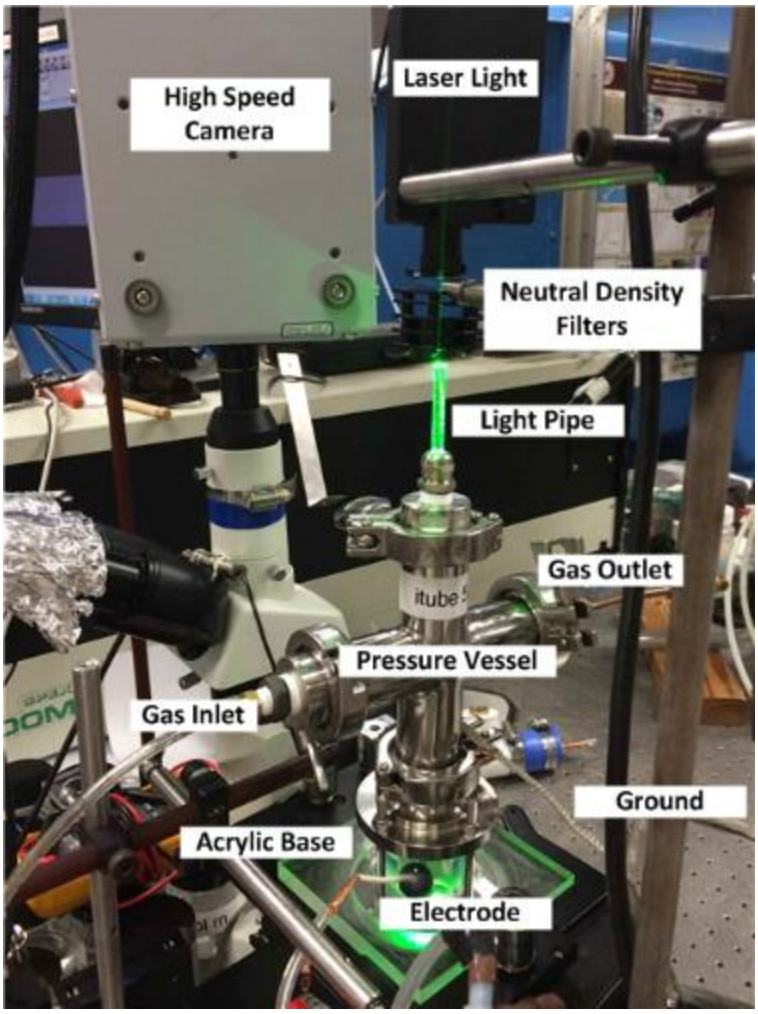

Figure 61. Experimental Setup with Different Components Corresponding to the Diagram in Figure 60

5.2.3 Fabrication of Pressure Vessel

A pressure vessel that could hold internal pressure from 0 psig to 80 psig was made in this research. The whole pressure vessel was homemade and had experienced

several different versions before successfully completed. The SolidWorks illustration is presented in Figure 62. The top part of the pressure vessel was made of a sanitary cross tube. The advantage of this tube was that it could be easily assembled with different parts using sanitary clamps to other tubes. In our experimental setup, the cross sanitary tube was connected with the “gas in” and “gas out” with its horizontal tube. Pressure gauges and valves were connected with the “gas in” and “gas out”, so the pressure in the pressure vessel could be accurately controlled and monitored. As for the vertical tube, the upper part of this vertical tube was used, as introduced in previous subsection, to seal the pressure vessel while hold the light pipe for the laser to illuminate the plasma and discharge based bubble generation. A quarter of the light pipe was left outside of the pressure vessel and the rest of the light pipe was in the pressure vessel with the inside end just above the microelectrode tip. The images illuminated with the light pipe by the laser will be presented in the following subsection.

The bottom of the pressure vessel was made of an acrylic cylinder, a piece of acrylic sheet and quartz glass. A one half inch diameter acrylic cylinder with length of 2 inches was drilled with a concentric half inch diameter hole. The drilled hole was used as the reactor chamber, while the thick wall of acrylic cylinder was used to handle the high pressure and shock wave generated during the plasma initiation. Glass beaker was used before the acrylic cylinder, and was smashed by the shockwave generated by microplasma with relatively high energy. The other reason for using thick wall acrylic was to reduce the deformation as much as possible. The liquid was contained in this acrylic cylinder and was sealed in it using compressed sealing. The pulsed high pressure

induced by a shock wave was able to deform the container if the wall was very thin, and caused leaking. Also the transparency of the acrylic was important for the microelectrode alignment later. The microelectrode tip as mentioned in the Chapter II was made of tungsten, the size of the tip was around 3 μm and the diameter of the tungsten wire before electrolysis was around 50 μm. The microelectrode tip was needed to solder to a metal wire with a bigger diameter. The microelectrode tip was needed to be placed in the acrylic container to generate microplasmas and microbubbles, and the other end of the wire was needed to stay outside of the acrylic container to connect to the high voltage supply. The sealing of this wire became very crucial in our tests. Not only the sealing but also the location of the microelectrode tip was needed to be precisely aligned. Since the whole plasma generation event needed to stay in the view of the microscope, and the depth of view of the microscope was very limited especially with higher magnification lens, the microelectrode tip needed to get closed to the bottom window as much as possible but not to touch it. The tip was also needed to stay in the center of the drilled hole in the acrylic cylinder, because the movement of the bottom plate was limited. The toughest jobs of the microelectrode tip working with the acrylic cylinder were that the tip needed to be sealed with the side hole, got closed to the bottom as much as possible but not touch the bottom, and stayed in the center of that vertical hole.

The base of the pressure vessel was also made of acrylic. It was machined into one side square and the other side round shape. In Figure 62, it shows that the 1 inch thick, 4 inch by 4 inch acrylic was machined with a sink in the center of it. The round shape at the bottom was for the purpose that the base could be mounted on the

microscope, and the center hole of the bottom round part served that the microscope objective could be inserted into it to get close to the bottom window. From the figure, we could tell that even with a 2 inch thick acrylic block, the microelectrode tip could be very close to the window. There were two rubber pads working as gaskets on and beneath the cylinder container for the purpose of sealing. And four threaded rods were placed four directions with screws to hold all parts together. The bottom central hole was drilled bigger than the microscope objective to make sure the whole base could be moved for the alignment. The four threaded rods went through the 2 inch thick portion of the acrylic base to make sure the compressed sealing was able to handle high pressure. A 1/8 inch thick with a diameter of 2 inches quartz glass was used as the window for the observation. The design goal for this window was to handle 80 psig internal pressure for several hours. The thinner the better, but a 1/16 inch quartz window cracked under 80 psig for only 10 min. Up to now, the 1/8 inch window has been working perfectly with our setup. In addition, the quartz window can also be used for light emission study in the future, since it would not block UV, visible and some IR wavelength.

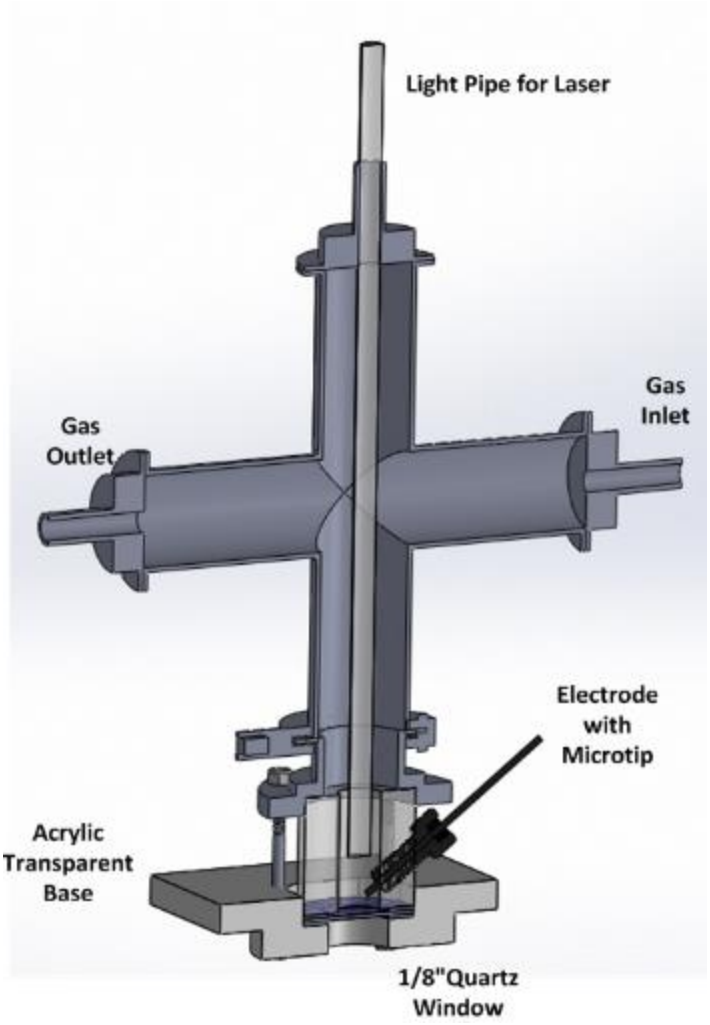

Figure 62. Cross Section View of Pressure Vessel Using SolidWorks Illustration

5.2.4 Algorithm of MATLAB for Boundary Identification

In early chapters, the microbubble radius variation versus time were plotted for a better understanding of the microbubble's hydrodynamic in liquid. Only two videos with

around 50 frames were presented. The boundary identification was rather easy since the contract between the bubble and surroundings was very clear and the number of frames was not big. In this chapter, a parametric study was pursued with microbubble generations in a pressure vessel. The energy inputs, the conductivities of liquid, the surface tensions of the liquid and the pressures of ambience were all varied experimentally. With the high energy input and low pressure, the maximum radius of microbubble could be as big as several hundreds of micron and the duration of the microbubble could be as long as several hundreds of micro seconds. Hundreds of videos with hundreds of frames for each of them made the microbubble boundary identification rather tedious. A MATLAB program was coded to solve this issue. Since the boundary identification was very important for tracing the radius change in this research, a subsection to introduce the boundary identification algorithm is necessary here.

Depending on the frame rate used in the tests, the videos for the microbubble generation could have a relatively high or low temporal resolution. In most cases, the frame rate was maintained at 300k fps. The actual time between each frame was around 3.3 μs. When the plasma was generated, the EMI accompanied with the plasma generation triggered the CMOS camera. The CMOS camera was programmed to record 50 frames after the trigger and 10 frames before the trigger. The practical problems were

- the first two photos might capture the plasma generation and the microbubble generation, it was really tough to tell the boundary of the microbubble for this case,

- the microbubble could be bigger than the microscope scope, it is hard to estimate the area of the microbubble,
- pre-existed microbubbles could confuse the program to identify the boundaries of microbubble.

The details of these problems are addressed as following. As presented in Figure 63, a very bright plasma spot can be observed in the center of the image and there is also a halo feature surrounding the microplasma in the center. This halo feature is believed to be a fast growth microbubble. Since this image needs to cover 3.3 μs and the growth speed of microbubble is very fast at the beginning stage, the image of the bubble looks very blur.

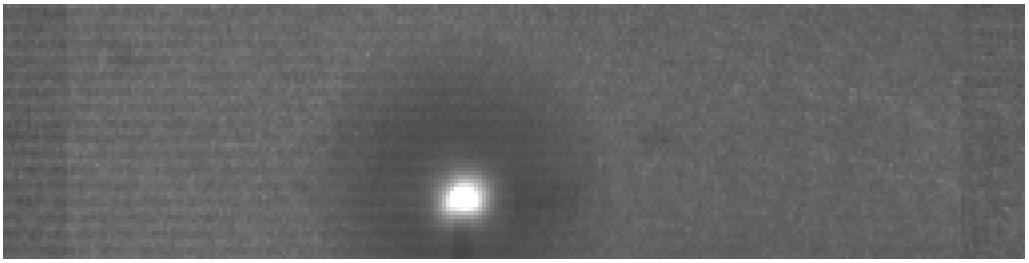

Figure 63. Microbubble Together with Microplasma Recorded by CMOS Camera

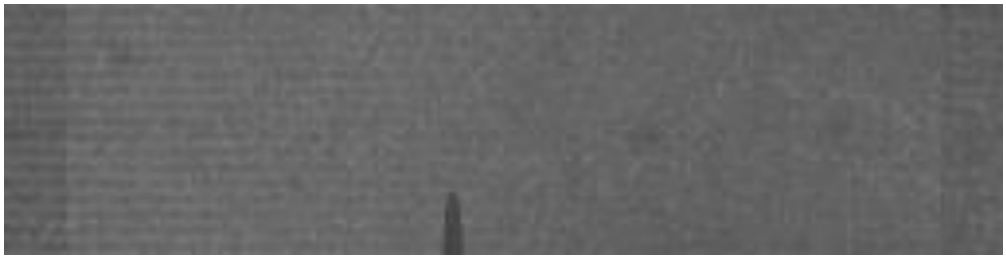

Figure 64. Microelectrode Tip in Liquid without Discharges

All the information on each pixel was first stored in a matrix. For one image, a 3 by 64 by 256 matrix was formed for the further calculation. An algorithm called ‘edge’ in MATLAB was used to identify the boundary of the microbubble. There were six different methods under this function to identify the boundary, the ‘canny’ algorithm was chosen. ‘canny’ function has both the threshold and sigma to identify complex boundary conditions. An image from the Figure 63 firstly was plotted out as presented. Then the boundary based on the transition of brightness change in the image was plotted in Figure 65. As mentioned earlier, when the plasma initiation together with the microbubble generation, there were two boundaries in the image. One of the brightness transition was from the microplasma bright spot to the environmental brightness, and the other one was from the brightness of the microbubble surface to the environmental brightness.

Figure 65. Boundary Identification Using “canny” Algorithm

The problem was not very crucial since there might be only one or two images with microplasma generation. The solution to this issue was to identify where the plasma was and where the microbubble was. The image without any discharge or microbubble was used to identify where the microelectrode tip was. The coordinate of the tip was used as the center for both of the circles. The boundary of the tip could be plotted as presented in Figure 66. Now the distance of each white point in Figure 65 to the tip was calculated and plotted in Figure 67. The circle on the microbubble could be easily distinguished from the circle of the microplasma in the center. Then the inner circle was filled with black pixel with only outside circle left there as presented in Figure 68.

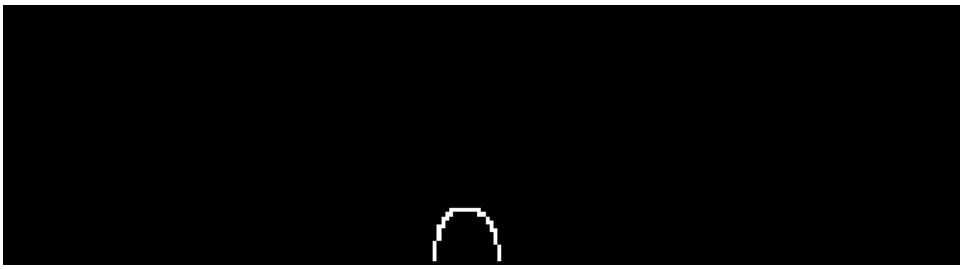

Figure 66. Boundary Identification of Microelectrode Tip

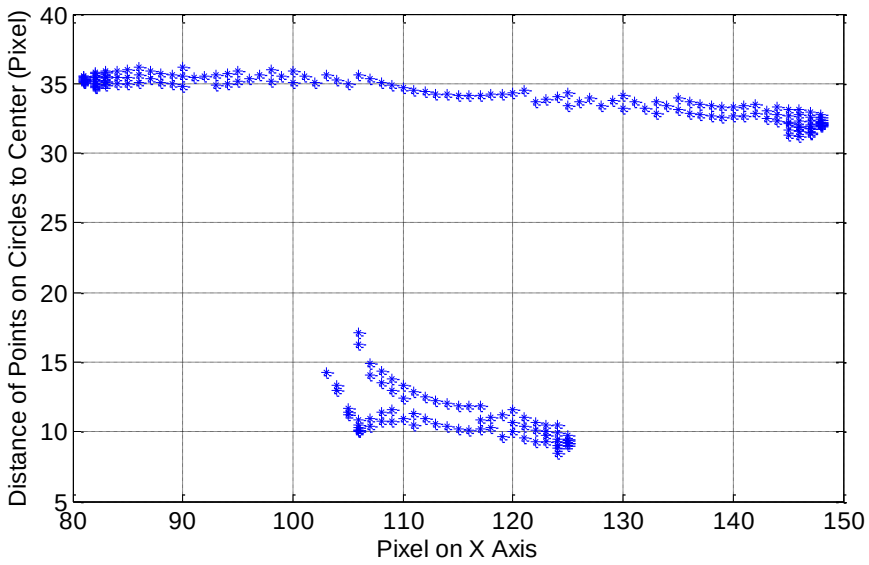

Figure 67. Distance between Each Point on Circles to Microelectrode Tip

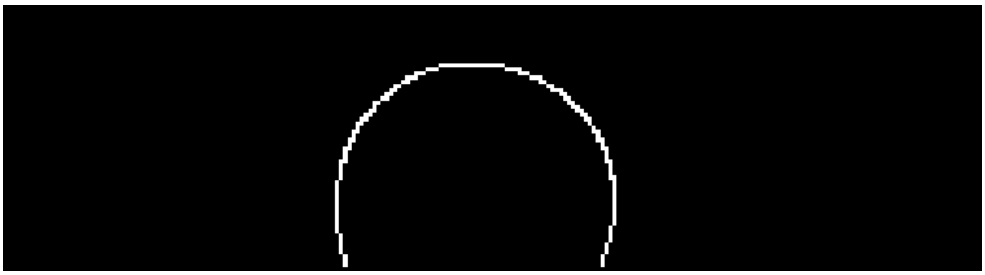

Figure 68. Microbubble Boundary after Microplasma Boundary Elimination

After the boundary of microbubble was identified and the boundary of microplasma was eliminated, a second algorithm was used to locate the center of this circle and to estimate the radius of it. The sphere was a 3D structure in the real world, but due to the limitation of observation, only 2D images could be acquired by using the microscope and the high speed cameras. It was assumed that the bubble was symmetric on 3 directions. In addition, in most cases, only some portion of a microbubble can be viewed in the image. In Figure 69 and Figure 70, the whole microbubbles were not covered in the image. It would be very inaccurate to connect a random point on the boundary to the center of the microelectrode tip.

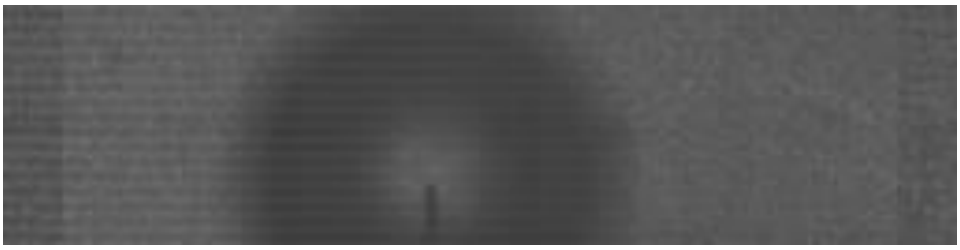

Figure 69. Big Portion of Microbubble Boundary in Image

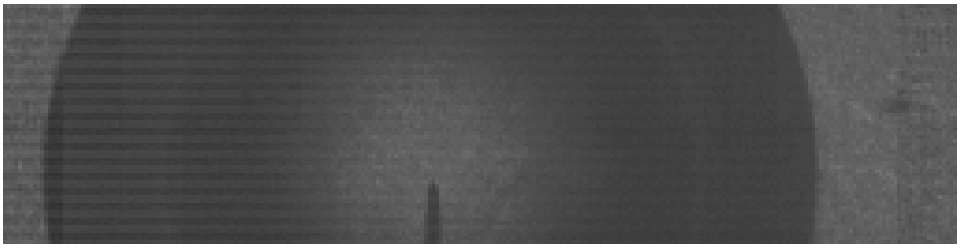

Figure 70. Small Portion of Microbubble Boundary in Image

A left curve and a right curve was then identified since in all cases the left and right side of the microbubble could always be recorded even that sometimes the upped and bottom sides were cut out from the image. In Figure 71, the left and the right side of the microbubble were both identified and marked with two different colors. Then the 'fminsearch' function in MATLAB was used to find a perfect circle with minimum difference between the radius of the perfect circle and the points on the boundary to the center of the bubble. The new perfect circle then would represent the circle of the microbubble as presented in Figure 72. Each Image were analyzed to estimate the radius,

and based on the time scale collected from the high speed camera the radius change versus time was able to be plotted as presented in Figure 73.

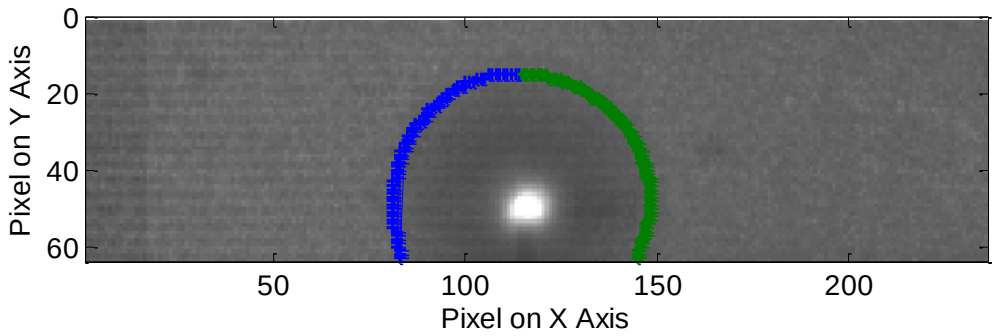

Figure 71. Identification of Left and Right Side of Microbubble

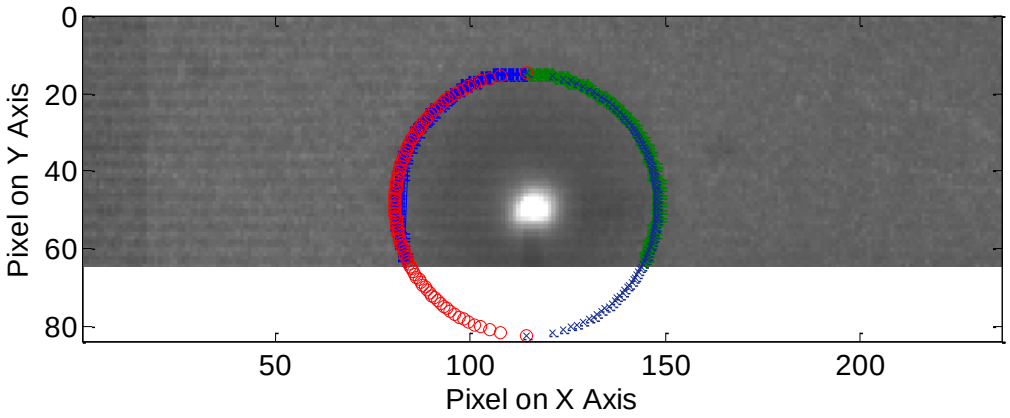

Figure 72. Perfect Circle to Represent Microbubble in Image

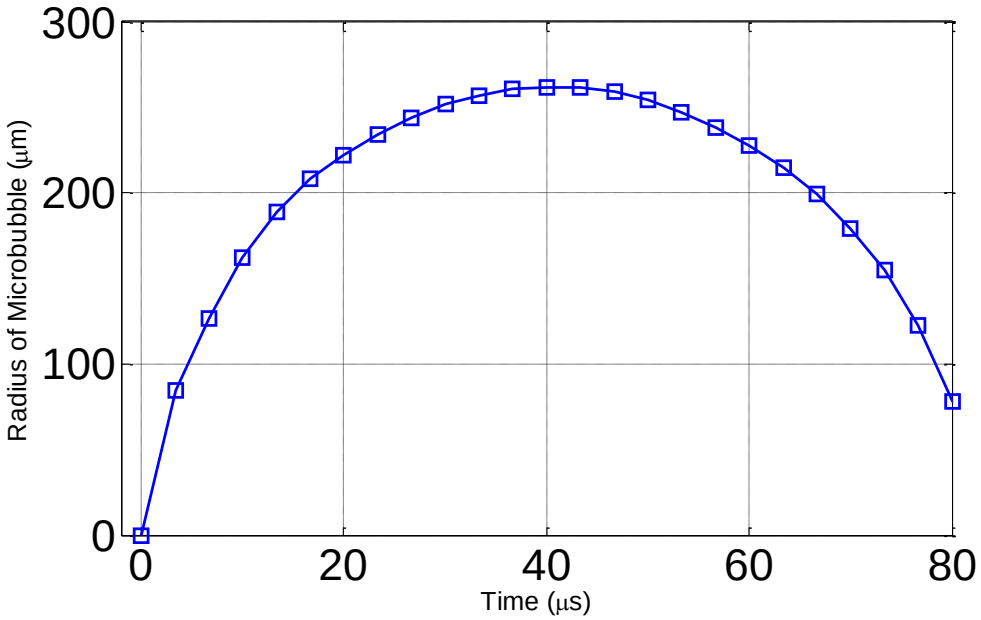

Figure 73. Radius Changes vs. Time Collected by Program

5.3 Experimental Results and Discussion

Spherical microbubbles could be generated successfully by microdischarges in liquid, which was introduced in chapter III. The microbubble's dynamics under atmospheric pressure recorded by the high speed camera and theoretically studied by the Rayleigh-Plesset model was investigated as well. The experimental results of microbubble's dynamics in pressure controlled environment are discussed in this section.

5.3.1 Parametric Design

The pressure vessel has been introduced in the experimental setup section. The pressure in the vessel could be varied from 0 psig to 80 psig. The electrical conductivity was constant at 0.2% NaCl mass concentration. The applied peak voltages could be from -2 kV to -12 kV as presented in Figure 74. They had very similar voltage rising time at round 10 ~12 ns. As mentioned in the electrode fabrication, one microelectrode tip was glued permanently through the pressure vessel, and the microelectrode tip was not replaceable. In order to protect the microelectrode tip in this test, only -3kV, -5kV, -7kV and -9kV were used for the microplasma generation.

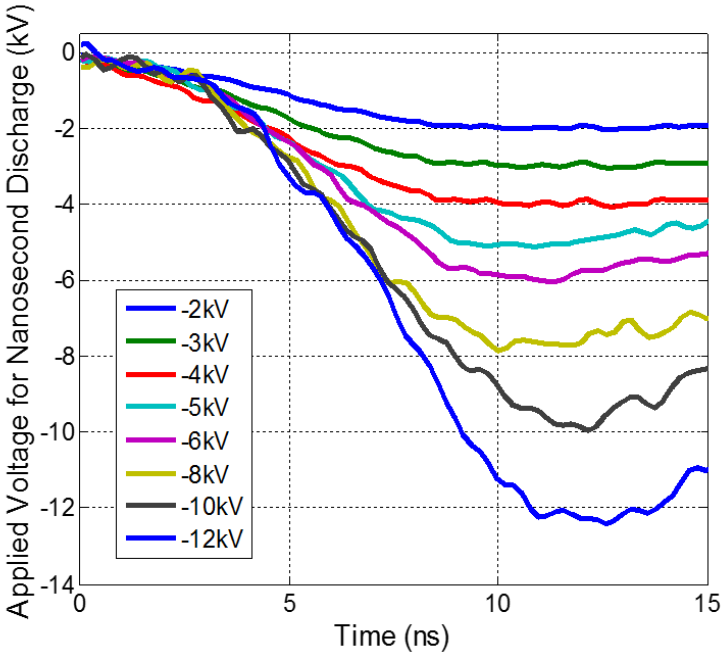

Figure 74. Voltage Rising from -2 kV to -12 kV for Microdischarges

The surface tension of the liquid was adjusted by using Sodium dodecylbenzenesulfonate (DDBSA) as a surfactant. The surface tension of DI water samples at 25 ^{o}C in this research were 35 mN/m and 71 mN/m respectively. The energy input to the liquid did not change between these two surface tensions as presented in Figure 75. It clearly presents that the energy inputs versus the applied voltages are pretty similar between nanosecond discharges and microsecond discharges with and without surfactant.

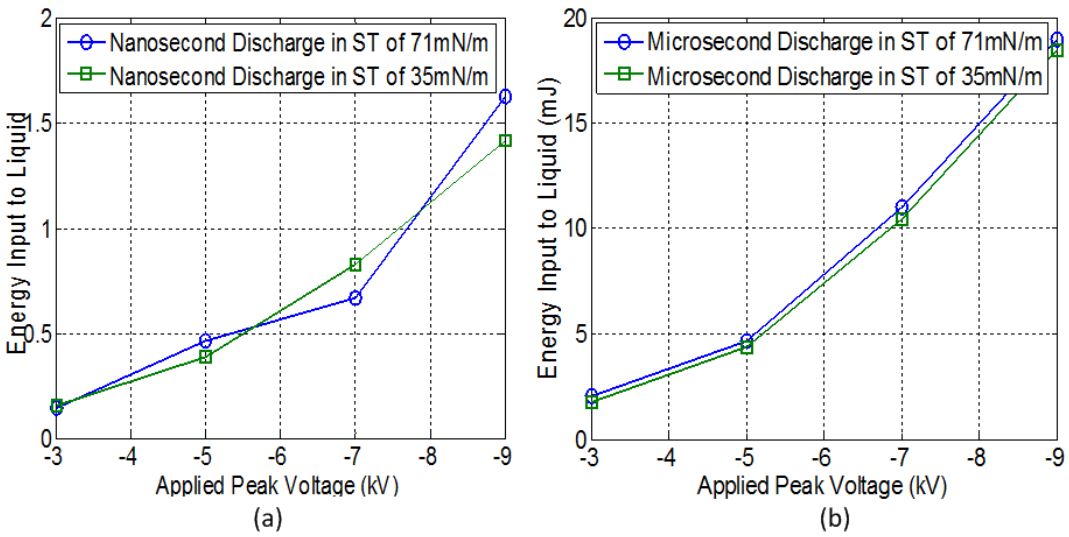

Figure 75. Energy Input to Liquid (a): Nanosecond Discharges and (b): Microsecond Discharges

5.3.2 Uncertainty of Microbubble's Dynamics under Different Parameters

The repeatability of microbubble's oscillations under atmospheric pressure was presented in the Chapter IV. The reason that the Rayleight-Plesset model could be used to compare the experimental results and the model simulation, and was believed accurately to depict the thermodynamic process with same energy inputs was because that the microbubble presented very similar dynamics. All microbubbles generated by the same breakdown voltages and discharge durations had almost same radius change trajectories on the radius versus time figure.

The Rayleight-Plesset model is based on the momentum balance across the boundary of microbubble in liquid. The pressure differences inside and outside of the microbubble wall are the driving force to expand and collapse the microbubble. The internal pressures of the microbubble had been determined by the internal energy and the mass in the microbubble in our tests. By using the same breakdown voltages and discharge durations but different ambient pressure, the input energies should be same. However, the saturation temperature of the liquid had to be changed corresponding to the ambient pressure. It was found that as the ambient pressure increased, the uncertainty of the microbubble's dynamics changed accordingly. The microbubble's expansion and collapse was very sensitive to the pressure change, and once the external pressure changed, the momentum of the microbubble boundary changed as well. In Figure 76, microdischarges generated microbubbles by microsecond discharges with the APV of -9 kV and the ambient pressures ranging from 0 psig to 80 psig is presented. As the ambient pressure went up, the duration of the first cycle of the microbubbles became

shorter and the maximum radius reduced correspondingly. The details of the change will be discussed in the next subsection. The uncertainty in this section means the differences between the durations of microbubbles' oscillation and the maximum radii of microbubbles with the exactly same parameters.

In Figure 77, the duration and the maximum radius of microbubble presents very similar patterns under the atmospheric pressures. The results from the radius change under atmospheric pressure presents the same patterns as presented in the Chapter IV. As the ambient pressure went up, however, the patterns of radius changes were not consistent any more.

The shift of the radius change curve, e.g., the radius change vs. time at 10 psig presented in Figure 76, needs to be clarified here. The shutter speed of the high speed camera used in these tests were 300k fps. The time interval between each frame was 3.3 μs. Trigger timing could be at any time between two frames one of which was the frame before the discharge and showed nothing happened in the image (the time for this image was set to 0) and the other one of which was the frame after the discharge and showed microplasma and a microbubble in the image (the time for this image was recorded as 3.3 μs). As such, so long as the time shift in the radius change figures was shorter than 3.3 μs, the temporal tolerance is acceptable.

There were some time shifts for the ambient pressure of 10 psig case, but the duration of the first oscillation and the maximum radius were fairly consistent with subtle differences there. The uncertainty became more significant with a more increasing of the ambient pressures. For the ambient pressure of 80 psig case, the variation of the

maximum radius is 25 μm (25% change) and the duration of the first oscillation is 3 μs (17.6% change). In Figure 77, the mean maximum radius with 4 different parameters versus the different ambient pressures is presented. The standard deviation of each radius are presented as well. It clearly shows that with an increasing of the ambient pressures, the uncertainty of the maximum radius becomes larger. The ambient pressure is able to affect the radius change i.e., the dynamics of microdischarge generated microbubbles. The higher breakdown voltage and lower surface tension could be used to generate bigger microbubble. The force balance has been explained in Rayleigh-Plesset model subsection. The general trend is that increasing the ambient pressure is able to increase the uncertainty of the microbubbles' radius and decrease the mean maximum radius.

The same tests were pursued with different applied peak voltage of -7 kV. In Figure 78, microdischarges generated microbubbles by microsecond discharges at -7 kV at ambient pressures ranging from 0 psig to 80 psig. The similar trend was observed to the microbubbles generated by the applied peak voltage of -9 kV. As mentioned in the Chapter IV Sensitivity Study of Best-fitting Study, the sensitivity of the radius change vs. time was pretty high. The uncertainty of the radius change affects the accuracy of the Rayleigh-Plesset estimation. This influences are discussed in the next section.

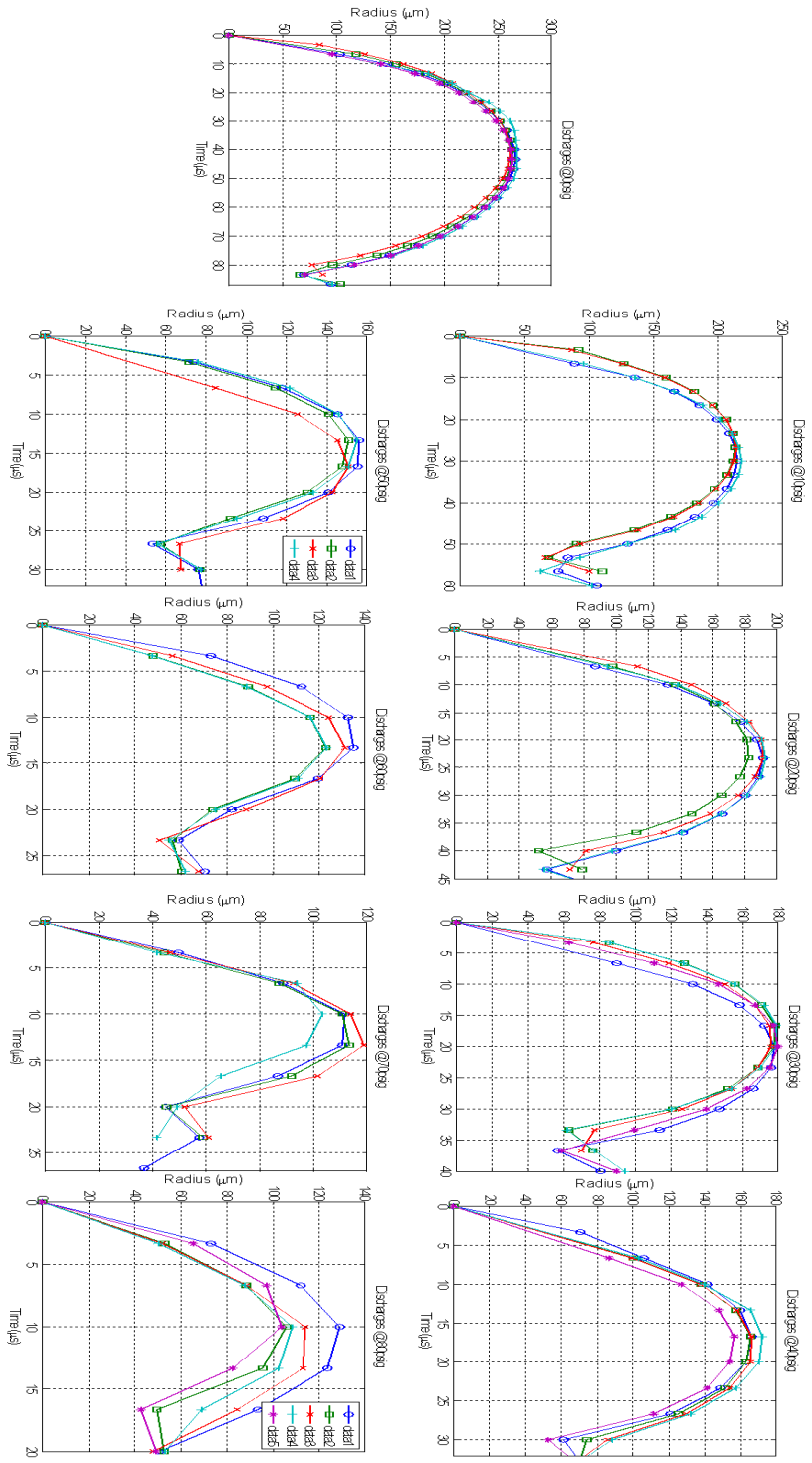

Figure 76. Microdischarges Generated Microbubbles by Microsecond Discharges at -9kV under Ambient Pressures Ranging from 0 psig to 80 psig

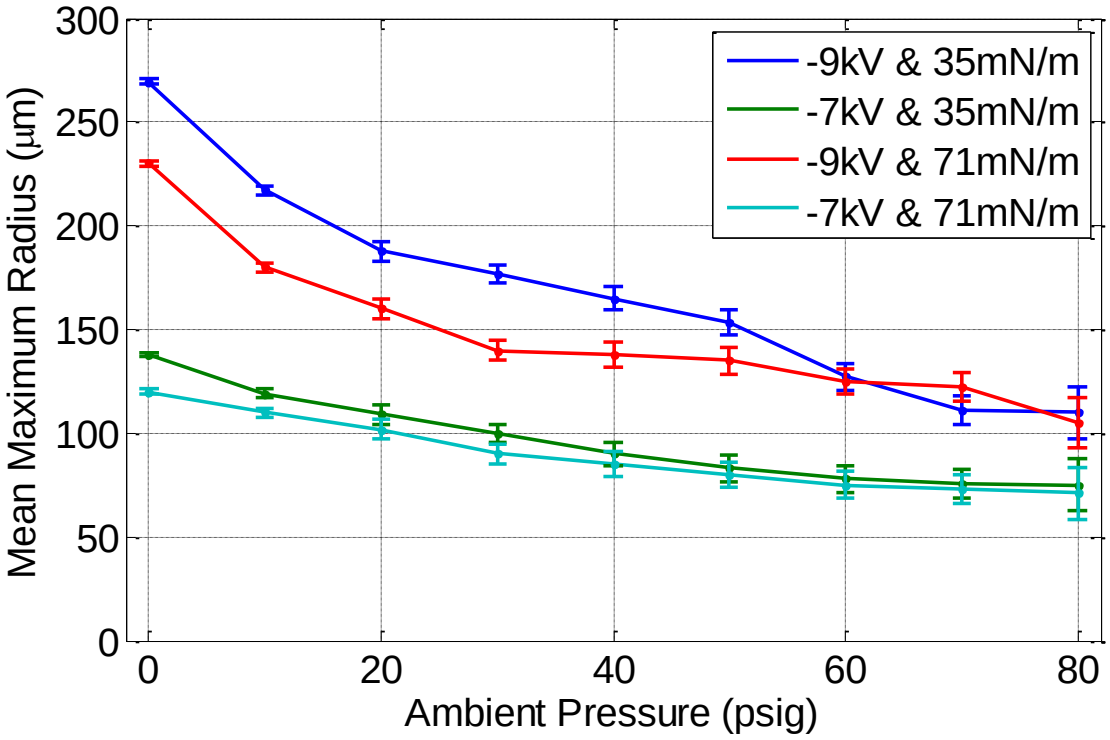

Figure 77. Mean Maximum Radius of 4 Different Conditions with Standard Deviation vs. Ambient Pressures.

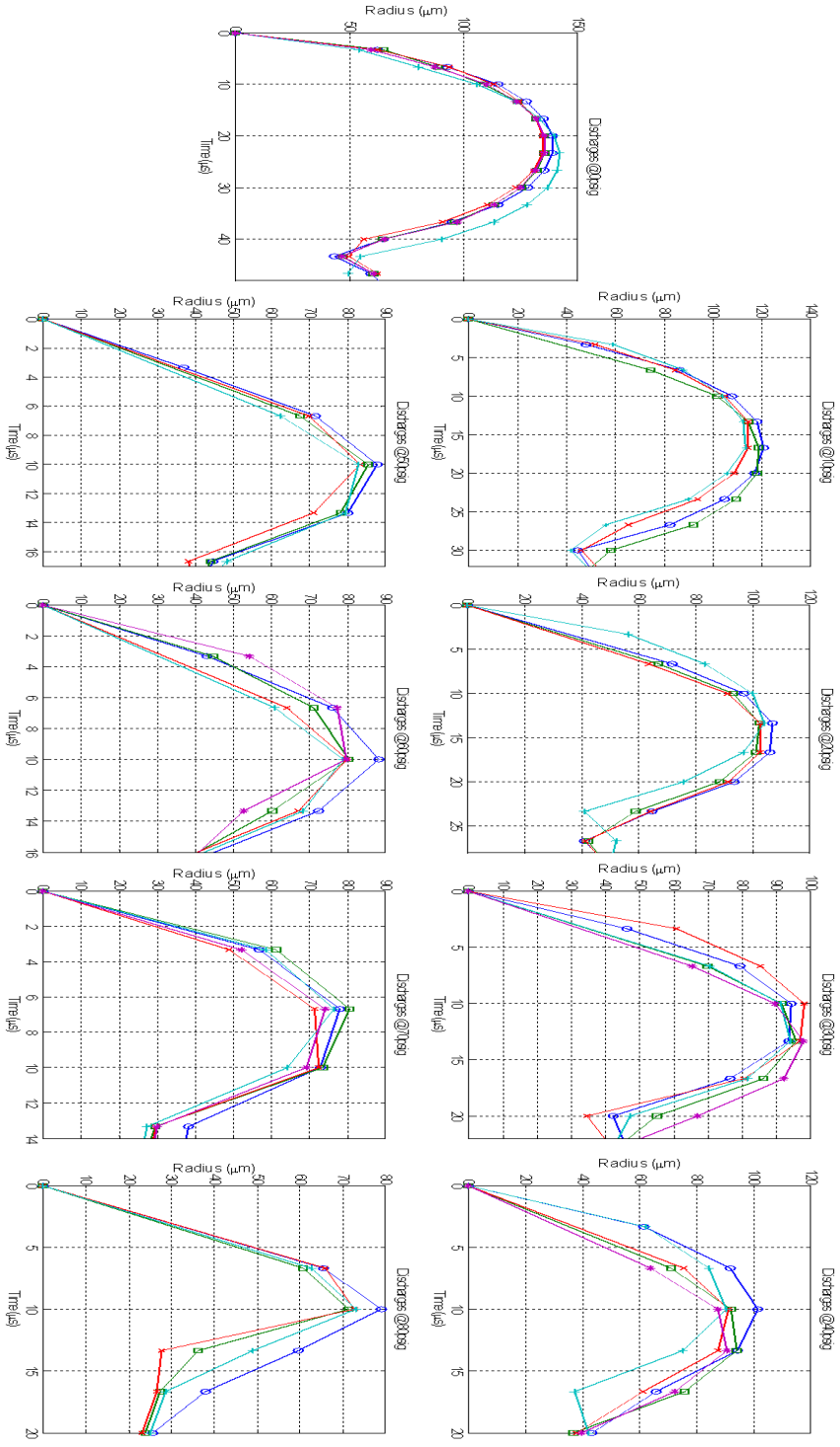

Figure 78. Microdischarges Generated Microbubbles by Microsecond Discharges at -7kV under Ambient Pressures Ranging from 0 psig to 80 psig

5.3.3 Changes of Microbubble's Dynamics

As expected, the ambient pressure affected the microbubbles' dynamics on every perspective including the maximum radius, the duration of the microbubble, the number of oscillation and the shape of the microbubble. The influence on the shape of the microbubble will be discussed in the Chapter VI. The energy inputs controlled by the applied peak voltages and the durations of the discharge were both able to influence the microbubbles' dynamics which has been described in the Chapter IV. Their influences could only affect the initiation stage of the microbubble. After the energy input for the first hundreds of nanosecond was done, the oscillation of the microbubble was on its own. On the contrary, the influence from the ambient pressure accompanied with the microbubble's oscillation until its disappearance in liquid. From the energy and momentum perspectives, the change of the energy input was to change the energy balance of the system, and the change of the ambient pressure was to change the momentum balance of the system.

Hundreds of videos were taken to record the microbubbles' dynamic with varied ambient pressures, applied peak voltages, discharge durations and surfactant addition. Some of the representative examples are shown in this dissertation. In Figure 79, the first cycle of the oscillations initiated with the same applied peak voltage of -9 kV under different ambient pressures of 0 psig, 40 psig and 80 psig is presented. The size of the microbubble and the duration of the microbubble as showed in the images were both affected significantly by the ambient pressure. Under atmospheric pressure, the

microbubble took around 83.3 μs to finish its first cycle, which was almost 4 times longer than that for the microbubble under the 80 psig ambient pressure.

The microbubble's oscillation as described in the Chapter III can be regarded as a spring damping system. Its max velocities can be observed at the minimum radii during its oscillation. In Figure 80, the relation of radius change versus time for the different ambient pressures is presented. The maximum radius and the duration of the first cycle both decreased corresponding to an increasing of the ambient pressure. The relationship between the maximum radii vs. ambient pressures have already been presented. The change was more obvious or significant when the pressure changes from 0 psig to 10 psig. As the pressure went up, the influence on the microbubbles' dynamics became less important. The radius variation of the microbubble under 70 psig and 80 psig looked already very similar. The maximum radius changed from 260 μm to 120 μm and the duration of the first cycle changed from 80 μs to 20 μs when the ambient pressure changed from 0 psig to 80 psig.

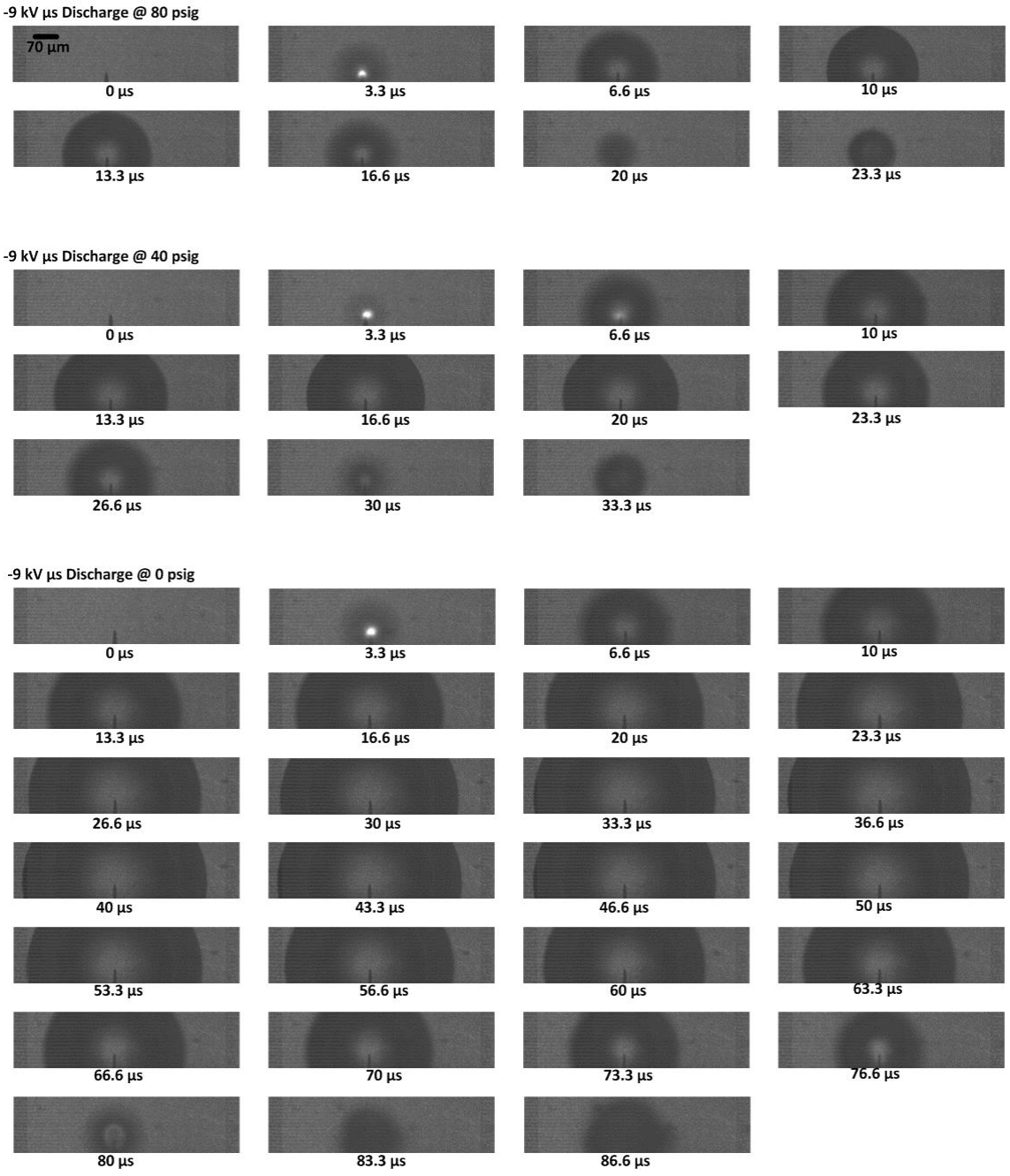

Figure 79. Images of Radius Change vs. Time for -9 kV, µs Discharge with Ambient Pressures at 0 psig, 40 psig and 80 psig

It needs to be noted that most examples covered in this chapter were discharged by using -9 kV or -7 kV microsecond discharges. The limitation of the CMOS camera has been mentioned in the Chapter II. A compromise needed to be made between the recording speed and the image resolution. The CMOS camera used in this setup was capable of taking maximum one million frame per second, but the image resolution would be so low that the boundary identification turned out to be impossible. 300k fps was eventually used to balance between the high speed and the acceptable image resolution. When the low energy inputs by using low applied peak voltages or nanosecond discharge with moderately high ambient pressure, the oscillation of microbubbles were so quick that only one or two frames recorded the appearance and disappearance of the microbubble. Those images were still very useful to firstly give some sense about how quick the microbubble could collapse, and secondly to check whether there was a microbubble generation. They cannot be used to depict the microbubbles's dynamics due to lacking of enough data points.

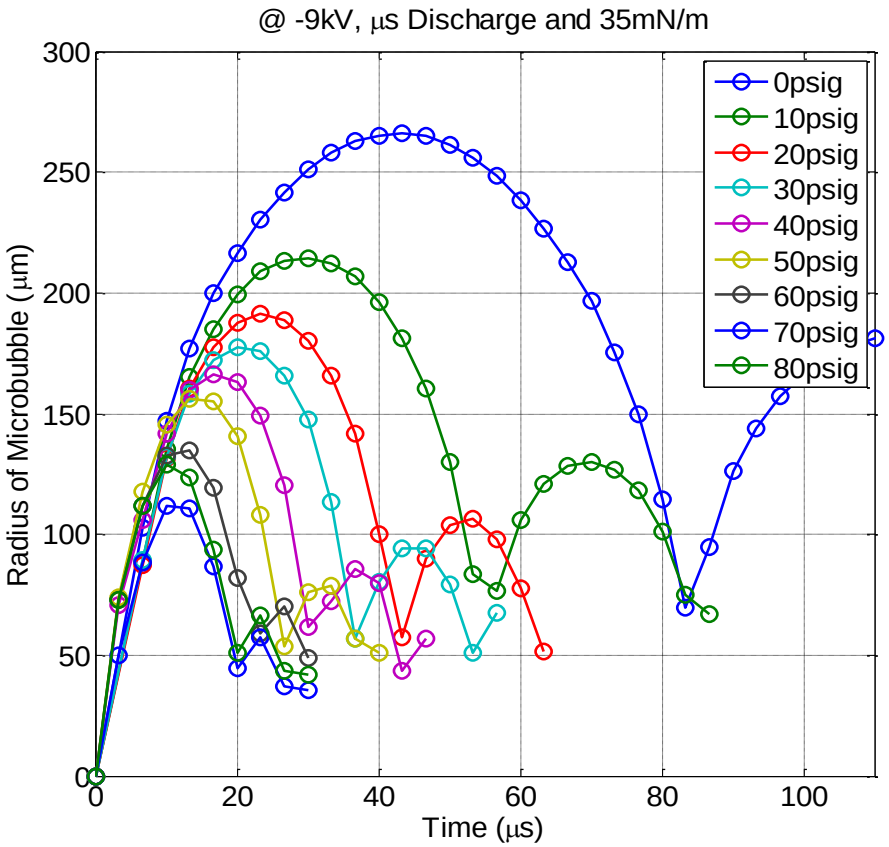

Figure 80. Radius vs. Time for -9 kV, μs Discharge in DI Water with Surface Tension of 35 mN/m and Ambient Pressure Ranging from 0 psig to 80 psig

The microbubbles' dynamics can be affected by the input energy and the surface tension as well. Since the initial energy is able to determine the initial velocity, and the damping oscillation of microbubble is a form of energy dissipation, the initial energy inputs can determine the micrbubbles' dynamics. In addition, the surface tension, one of the balance forces for the momentum balance, can affect the microbubbles' dynamics from outside. In Figure 81, the maximum radius and the duration of the first cycle both

change by only using DI water with a different surface tension. The maximum radius changed from 230 µm to 120 µm and the duration of the first cycle changed from 78 µs to 20 µs. It seems that the surfactant affected the low pressure oscillation much more significantly that the high pressure oscillation.

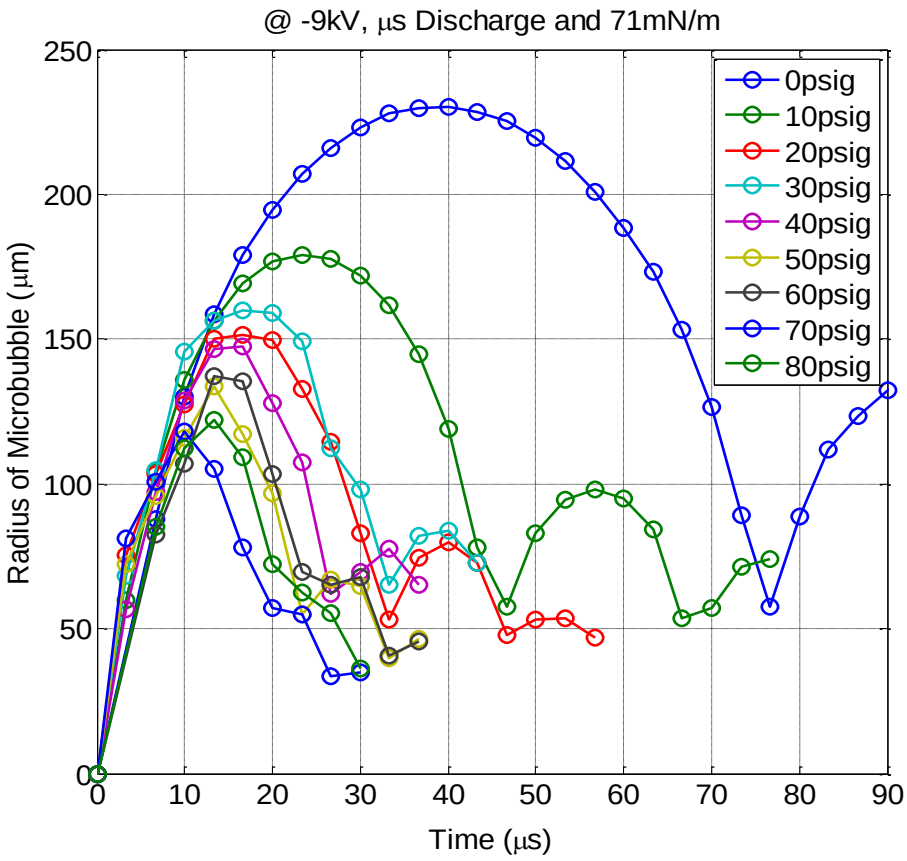

Figure 81. Discharges with Same Parameters Presented in Figure 80 except Surface Tension (Surface Tension = 71 mN/m)

The influence of microbubbles' oscillation largely depends on the energy inputs were analyzed in detail in the Chapter IV, the similar conclusion can also be drew from this part research. In Figure 82, the discharge parameters are exactly the same except the applied peak voltage as that in the Figure 80. The maximum radius and the duration of first cycle present big difference. The results from these two figures corroborated the conclusion already been drawn in the Chapter IV.

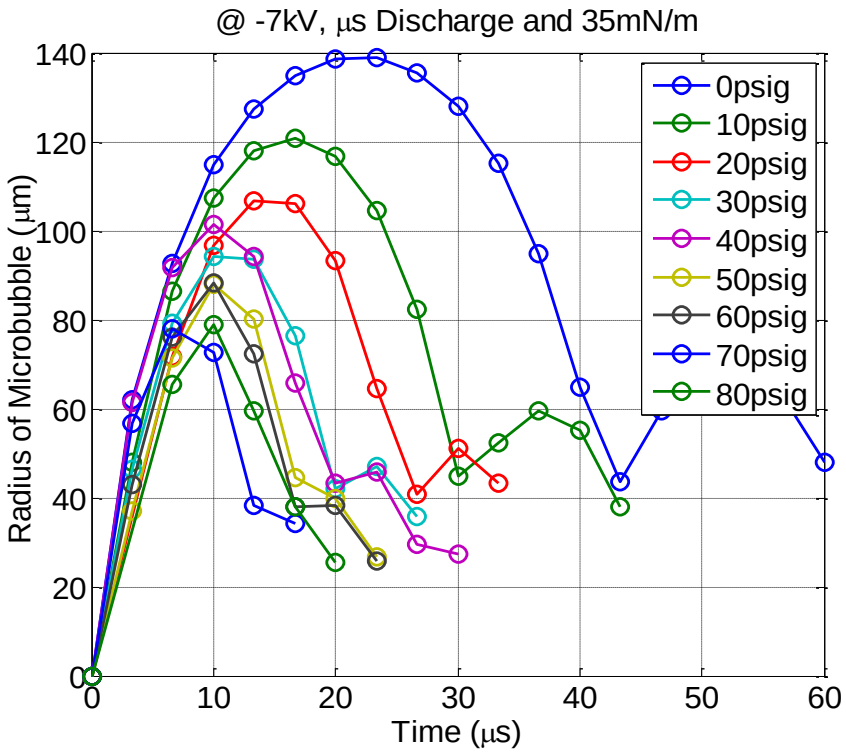

Figure 82. Discharges with Same Parameters Presented in Figure 80 except Applied Peak Voltage (Applied Peak Voltage = -7 kV)

5.4 Rayleigh-Plesset Model with Varied Ambient Pressures

The Rayleigh-Plesset model was used in the Chapter IV for the investigation of the thermodynamic properties of microdischarge generated microbubbles. The model is re-visited in this section for the microbubble generation in pressure controlled environment. Core information of the Rayleigh-Plesset model related to the pressure variation is reiterated for refreshment. The first component in bracket represents the momentum across the boundary of a microbubble. It consists of the velocity and acceleration which are expressed in terms of the first derivative and the second derivative of the radius. Comparing with the Rayleigh-Plesset Model used in the Chapter IV, the difference is the 'P_∞' component. In Chapter IV, the ambient pressure component 'P_∞' was set to be equal to one atmospheric pressure always, while initial radius R_0 and initial velocity $\dot{R}_0$ as well as n, T_{b-eq} and R_{eq} were used as fitting parameters to compare the model to experiment. In this section, the ambient pressure is still set as a constant for the best fitting calculation. However, this constant is varied from 0 psig to 80 psig in each best fitting.

$$[R\frac{d^2R}{dt^2}+\frac{3}{2}(\frac{dR}{dt})^2+4\frac{\nu_L}{R}(\frac{dR}{dt})]+[\frac{2S}{\rho_L R}]+[-\frac{P_b}{\rho_L}]+[\frac{P_\infty}{\rho_L}]=0; \qquad \text{Equation 32}$$

$$P_b = P_v + P_{gas}; \qquad \text{Equation 33}$$

$$P_{gas} = P_{g-eq}(\frac{R_{eq}}{R})^{3n}; \qquad \text{Equation 34}$$

$$R_{eq} = \frac{2S}{P_v + P_{g-eq} - P_\infty}; \qquad \text{Equation 35}$$

$$T_b = T_{b-eq}\left(\frac{P_{gas}}{P_{g-eq}}\right)^{\frac{n-1}{n}}; \qquad \text{Equation 36}$$

5.4.1 Best Fitting of Microbubble's Dynamics under Different Parameters

The ambient pressure was adjusted from 0 psig to 80 psig. The radius change versus time has been plotted in previous subsection. For the same applied peak voltage, the energy inputs to the liquid were supposed to be same no matter how the environmental parameters changed. The ambient pressure, however, was conceivably able to affect the thermodynamic properties of the liquid. The energy inputs to the microplasma and microbubble might be changed under the different ambient pressures even though the total energy into liquid which was determined by the applied peak voltage and the duration of the discharge stayed same. Rayleigh-Plesset model was first used to run the best fitting with different ambient pressures. The microdischarge with applied peak voltage of -9 kV, microsecond duration and 35 mN/m surface tension was used here as the example of detailed analysis. In Figure 83, the RP model studies accurately matched with the experimental results. The best fitting algorithm has been described in the Chapter IV and the MATLAB codes of the best fitting is attached in the APPENDIX.

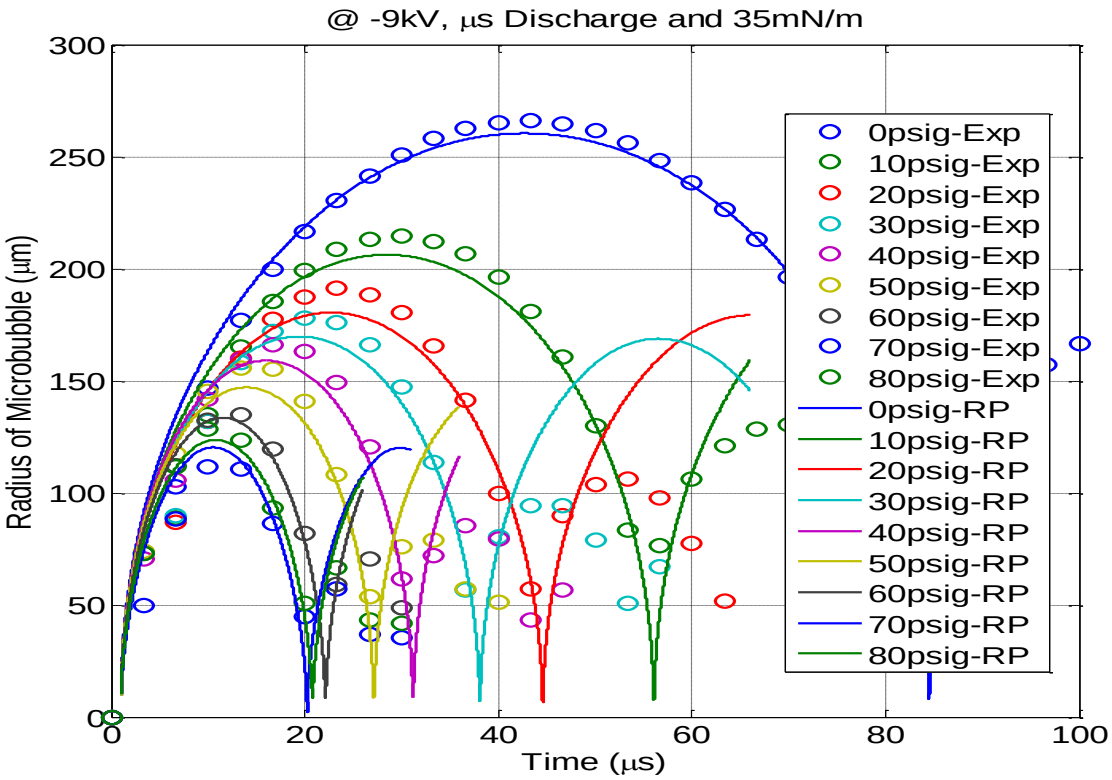

Figure 83. Comparison between Experimental Results and Rayleigh-Plesset Model Study (Discharge Condition at -9 kV APV, μs Duration and 35 mN/m Surface Tension)

As mentioned in the Chapter IV, the importance of the RP model is that it can unveil the momentum change of the whole process of a microbubble's oscillation and also present the thermodynamic properties of the microbubble during the whole process. In Figure 84, Figure 85, Figure 86, Figure 87 and Figure 88, the best fitting parameters which were used in the RP model to match the model data with experimental results are plotted. The equilibrium radius of microbubble decreases with the increasing of the ambient pressure, since a higher ambient pressure is able to restrain the growth of a

microbubble. There is a correlation between the maximum radius and the equilibrium radius. The maximum radius change is from our observation and the equilibrium radius is from the RP model calculation.

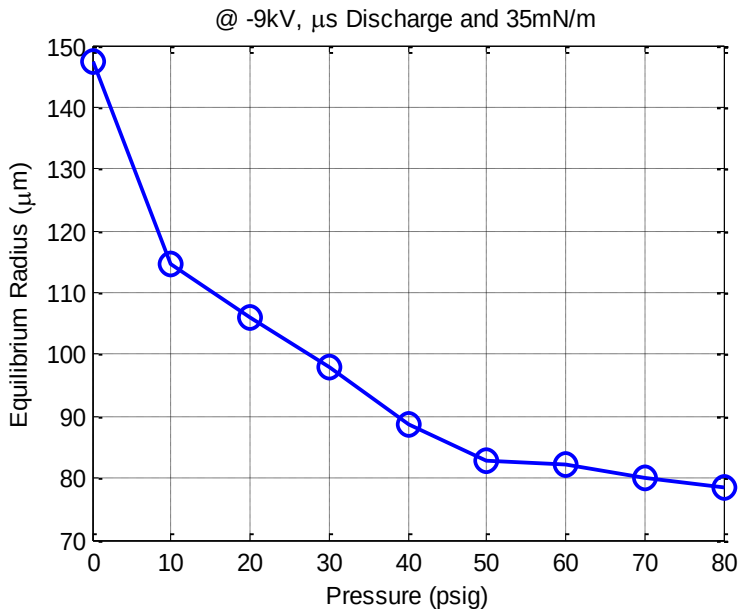

Figure 84. Equilibrium Radius vs. Ambient Pressure (Discharge Condition at -9 kV APV, µs Duration and 35 mN/m Surface Tension)

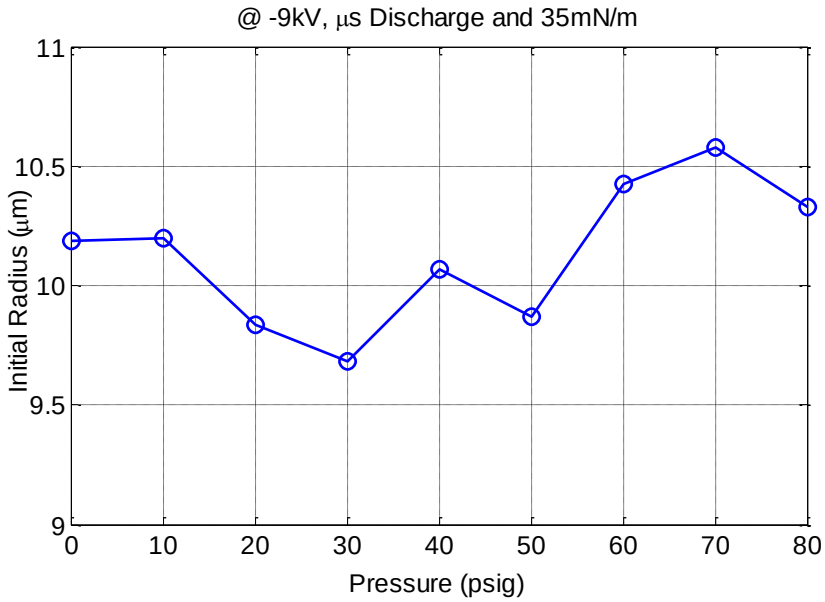

Figure 85. Initial Radius vs. Ambient Pressure (Discharge Condition at -9 kV APV, µs Duration and 35 mN/m Surface Tension)

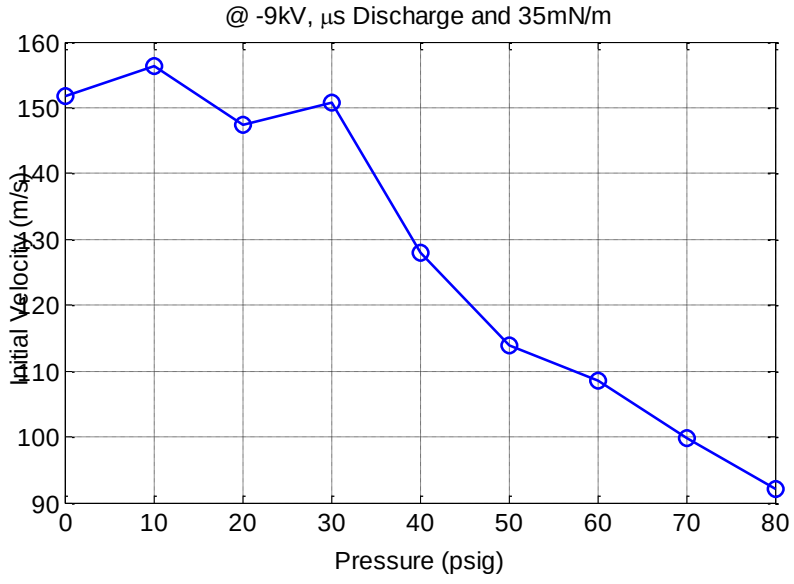

Figure 86. Initial Velocity vs. Ambient Pressure (Discharge Condition at -9 kV APV, µs Duration and 35 mN/m Surface Tension)

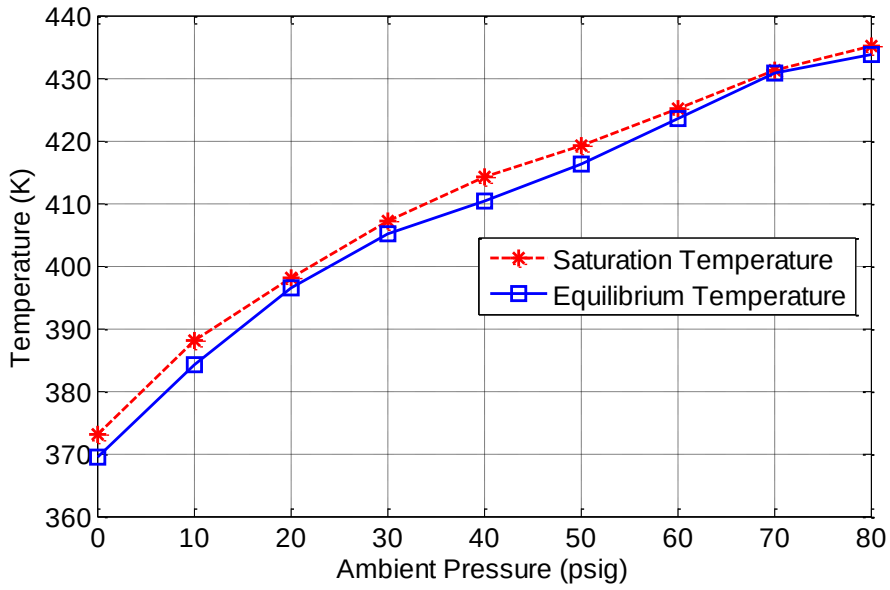

Figure 87. Saturation Temperature and Equilibrium Temperature vs. Ambient Pressure (Discharge Condition at -9 kV APV, µs Duration and 35 mN/m Surface Tension)

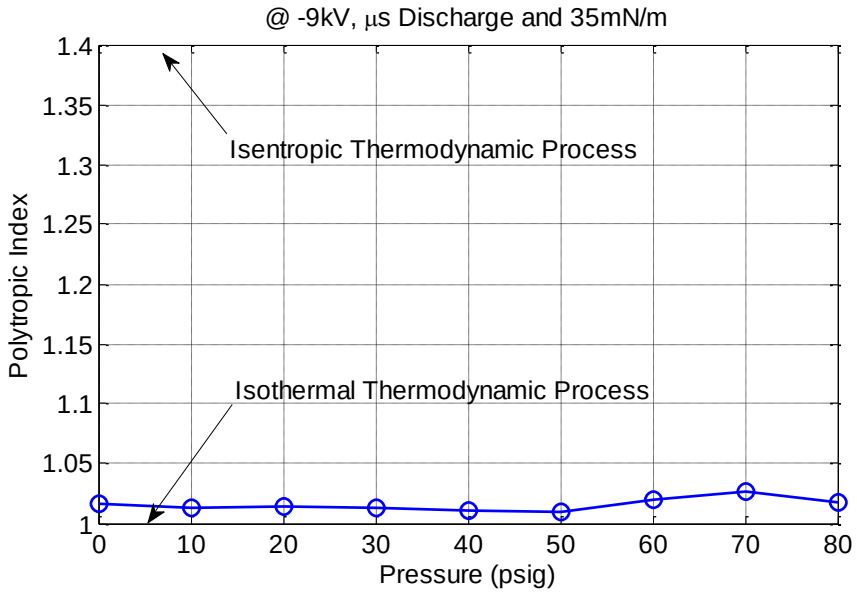

Figure 88. Polytropic Index vs. Ambient Pressure (Discharge Condition at -9 kV APV, µs Duration and 35 mN/m Surface Tension)

The initial radius and the initial velocity of microbubbles under different ambient pressures have presented fairly consistent value. They present similar conclusion that was drawn from the Chapter IV. The initial radius was around 10 μm, smaller than which required a different assumption that the mass transfer and the energy transfer both play very important roles, and the temperature difference is the main driving forces to sustain the motion of the microbubble. The important information that could be acquired from the consistent initial velocity was that the kinetic energies of the microbubbles under different ambient pressures were very similar. After this initial radius and the initial velocity of the microbubbles, the microbubbles' dynamics were heavily affected by the ambient pressures.

The equilibrium temperature of the microbubble increased dramatically with the increasing of the ambient pressure. The ambient pressure was able to determine the saturation temperature for boiling, and the increasing the ambient pressure was conceivably able to increase the equilibrium temperature in the microbubbles. For each different ambient pressure, the equilibrium temperature was very close to the saturation temperature of that pressure, which implied that during the oscillation of the microbubble the vapor inside of it oscillate around its saturation condition as well.

Polytropic index indicated the thermodynamic process the microbubbles experiences during their oscillations. Briefly speaking, the vapor in the microbubbles experienced a process possibly bouncing between isothermal process and isotropic process. The RP model results presented a consistent polytropic index of 1.01 for all

processes under different ambient pressures. From this results, it is concluded that the process of oscillation is much closer to the isothermal process than the isotropic process.

5.4.2 Thermodynamic Properties of Microbubbles under Different Ambient Pressures

The pressure variation, the temperature variation, the mass variation and the internal energy variation of the microbubbles generated by the discharges of -9 kV, microsecond discharge in water with surface tension of 35mN/m under different pressures are all plotted in Figure 89. With the increasing of the ambient pressure, the microbubbles became smaller and smaller. As the volume decreases, the mass in the microbubbles is conceivably becomes smaller as well if the density stays same. However, as the ambient pressure increases, the nucleation inception becomes harder and the density of the vapor becomes higher. So the decreasing of the volume caused by increasing ambient pressure does not necessary reduce the mass in the microbubble. The mass variation and internal energy variation are heavily contingent to the “fight” between the volume and the density of the microbubble. Even with the fight between them, as the ambient pressure changed from 0 psig to 80 psig, the general trends of the total mass and total internal energy decreased with some oscillations, as presented in Figure 90. The internal pressure estimation at 50 ns after initiation based on this case is presented in Figure 91.

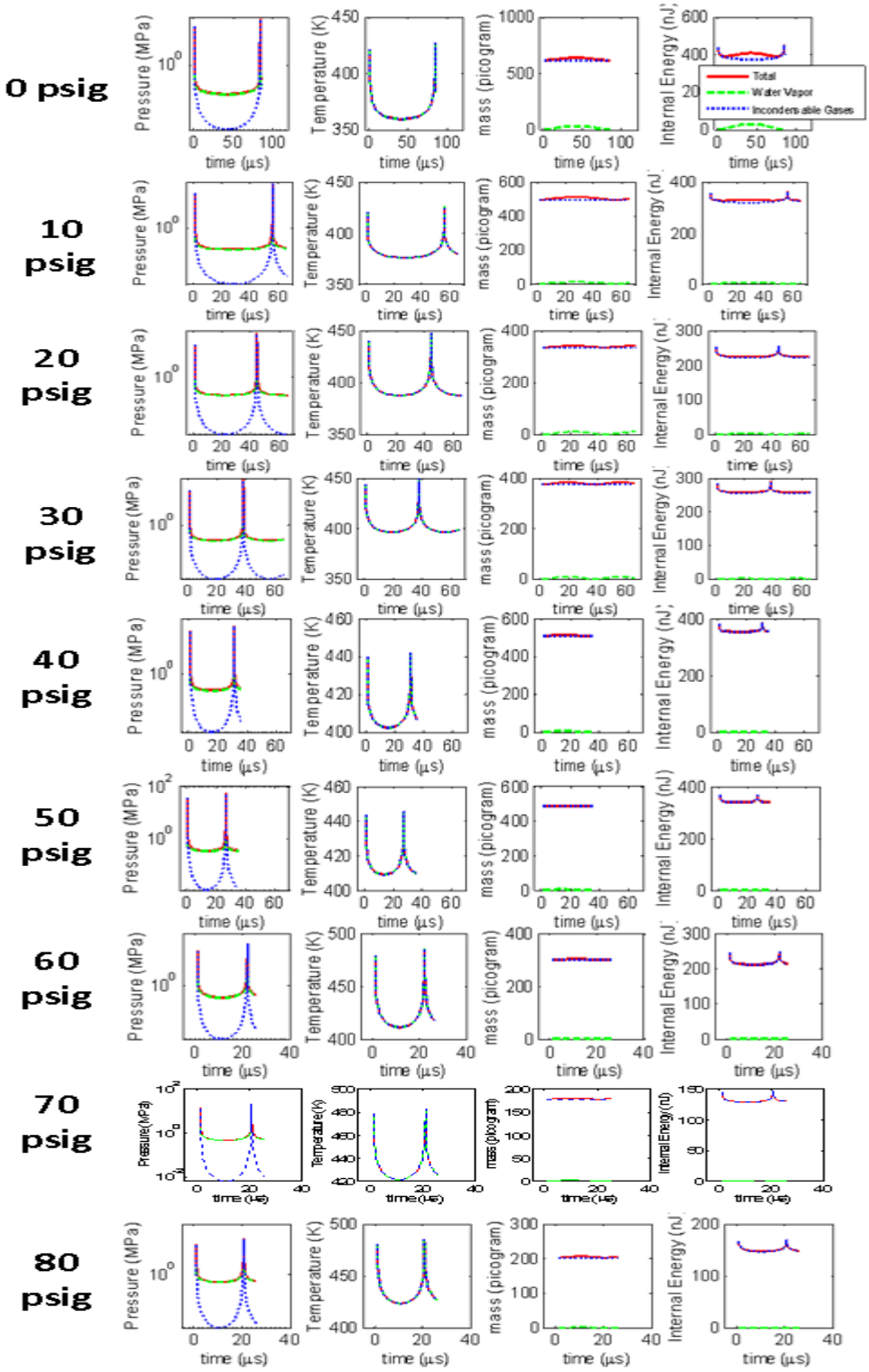

Figure 89. Thermodynamic Properties of Microbubbles under Different Pressures (Discharge Condition at -9 kV APV, μs Duration and 35 mN/m Surface Tension)

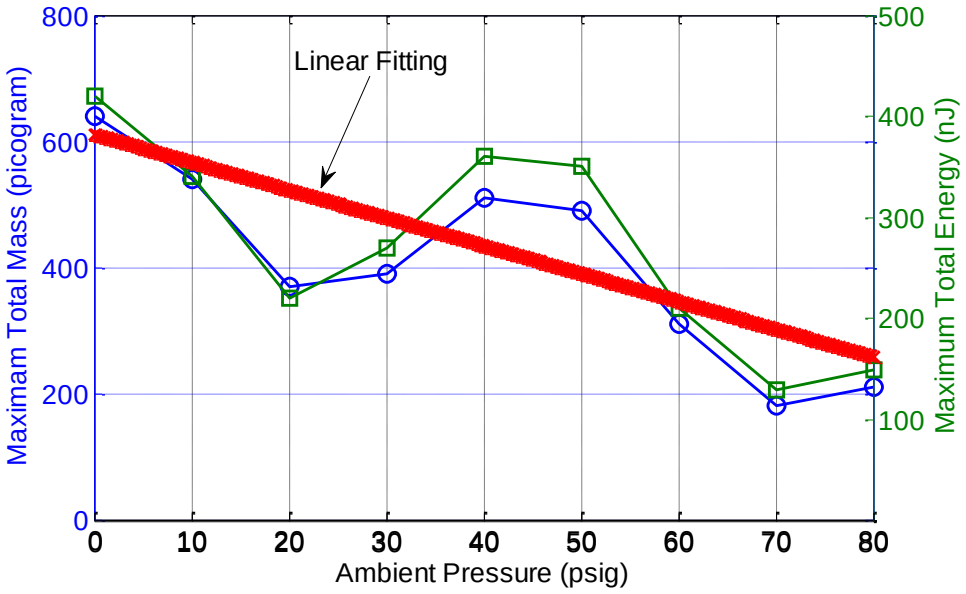

Figure 90. Variation of Maximum Total Mass and Maximum Total Energy of Microbubbles vs. Ambient Pressures (Linear Fitting Presenting General Trend)

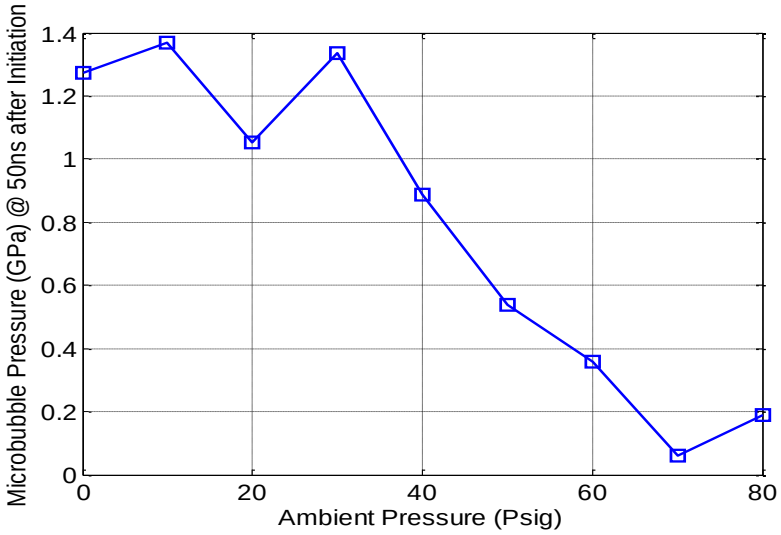

Figure 91. Internal Pressure of Microbubbles at 50 ns after Initiation under Different Ambient Pressures Based on RP model

From Figure 91, the transient pressure in the microbubble could be around Gpa scale with temperature around 400 to 500 K. This transient process is so quick that the Gpa pressure only lasted around tens of nanosecond based on our model. A bold idea is proposed here that such pressure and temperature of water label the liquid on the edge of ice VII and liquid in water phase change diagram in Figure 92.

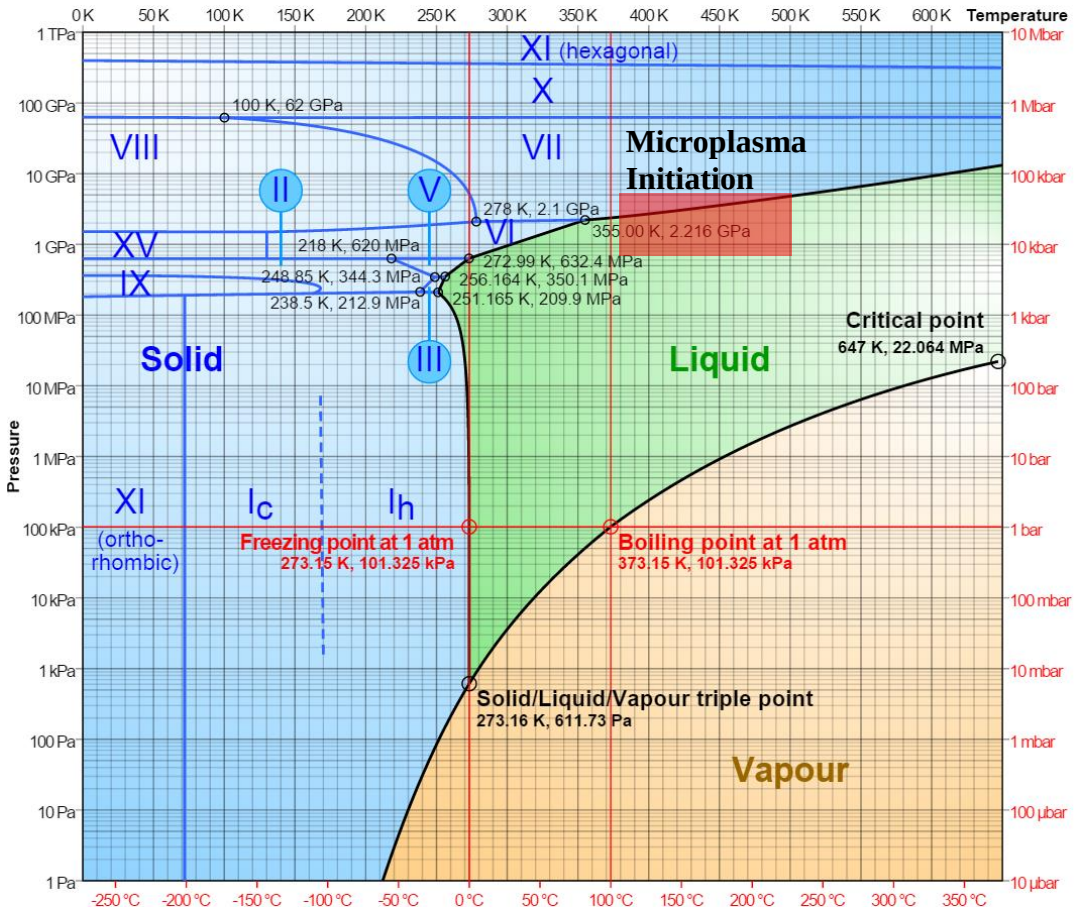

Figure 92. Water Phase Change Diagram [117] (Copyright © Wikipedia)
(Thermodynamic Properties of Microplasma Initiation in Red Box Region)

5.5 Summary

The microplasma and the microdischarge generated microbubbles were successfully generated in our homemade pressure vessel. The pressure vessel could handle 0 psig to 80 psig internal pressure. The microelectrode tips was placed at the bottom of the pressure vessel and the microplasma and the microbubble were both generated at the tip. The observation was still pursued using the high speed cameras and the microscope. Boundary identification was programed to efficiently identify the boundary of microbubbles and to estimate the radius change of them. Parametric study for the microbubble generation with various ambient pressures, liquid surface tensions, energy durations and applied peak voltages were done. It was found that the radius of microbubbles presented higher uncertainty when the ambient pressure increased. The Rayleigh-Plesset model which had been used in Chapter IV was used here to compare experimental results and the model estimation. The experimental results matched well with the model data, and the thermodynamic properties of microbubbles under different ambient pressures were calculated as well.

From the parametric experimental results,

- with the increasing of breakdown voltage while other parameters unchanged, the maximum radius of microbubbles became bigger and the duration of microbubbles became longer,
- with the decreasing of surface tension while other parameters unchanged, the maximum radius of microbubbles became bigger and the duration of microbubbles became longer,

- with the increasing of ambient pressure while other parameters unchanged, the maximum radius of microbubbles became smaller, the uncertainty of radius became bigger and the duration of microbubbles became shorter.

From the model results, the initial radius and the initial velocity did not change much with various ambient pressure, but the equilibrium temperature increased linearly corresponding to the increasing of the ambient pressure. The equilibrium temperature for each ambient pressure was very close to each of their saturation temperature. The polytropic index presented very consistent value with various ambient pressures. It implied that the thermodynamic process in the microbubble stay very similar. The polytropic index is around 1.01 which suggested during the oscillation, the vapor in the microbubble experienced an almost isothermal process. The internal energy and the mass in the microbubble did not change monotonically when the pressure linearly increased, but the general trend was that they both decreased with an increment of ambient pressure. The speculation was when the pressure increased, the volume of the microbubble became smaller but the density of the vapor in the bubble became higher, which was able to induce an oscillation of internal mass and energy change.

CHAPTER VI

MICRODISCHARGE GENERATED ASPHERICAL MICROBUBBLES IN LIQUID

6.1 Section Overview

Microbubbles with diameters from 10 ~ 300 μm were produced by micro-discharges in liquid with the discharge duration in nanosecond scale i.e., 400-700 ns. It was observed that those microbubbles could form in three different shapes at the stage of initiation. These shapes were spherical, aspherical, and branched. The microbubbles were generated using pulsed voltage with peak value from -5 to -10 kV on a tip of 3 μm in diameter. The total energy inputs for the microplasma and microbubble generation could be as low as millijoule. Bubble shapes were observed to be affected by the applied peak voltages, the solution conductivities and the ambient pressures. The stability of microdischarge initiated microbubble, i.e., the sphericity of microbubbles at the initiation, increased at higher conductivities, lower voltages and high ambient pressures. With a 0.1% mass concentration of NaCl solution (1990 μS/cm), the branched microbubbles could be easily identified, but with a 0.3% mass concentration of NaCl solution (5690 μS/cm), the spherical microbubbles were the majority of all bubbles with all other parameters same as 0.1% NaCl case. In addition, for a 0.2% mass concentration of NaCl solution (3140 μS/cm), a clear and significant transition from the spherical to the branched bubbles occurred between -7 kV and -8 kV. Furthermore, for a 0.18% mass concentration of NaCl solution (2880 μS/cm), the branches of microbubble were

observed to be suppressed by ambient pressures. The moderate ambient pressures were observed to affect the microbubble's dynamics.

6.2 Experimental Setup

The experimental setup in this chapter was very similar to the experimental setup in Chapter III, Chapter IV and chapter V. Major parts are reiterated here for a refreshment, and some minor differences are also introduced here.

6.2.1 Experimental Design

The microplasmas in these tests were generated at a microelectrode tip. The microelectrode tip was immersed in a petri dish containing water, and a grounded metal tab was placed in the water. By using a high voltage DC power supply (maximum -14 kV) and a spark gap, short rising-time and pulsed microplasmas were able to be initiated in liquid. The size of microplasma was related to the size of microelectrode tip, the applied electrical field and the input energy. A small electrode tip was used for a localized discharge and an attaining high electrical field with relatively lower applied voltages and energies. The sharp electrode tips were fabricated through electrolysis. Only corona discharges were covered in this portion of research. To prevent electrical leaking, high dielectric epoxy was used to cover the body of microelectrode except for the tip. The liquid used was a mixture of deionized water and sodium chloride (NaCl) in our tests. The water depth was about 3 mm, and the water surface was at ambient

pressure. The microbubble's dynamics were sensitive to the solution conductivity and ambient pressure.

6.2.2 Energy Input and Conductivity

A negative DC high voltage supply (Glassman Series EH), capable of -20kV and 5mA DC, provided the initial energy for the microplasma discharge. The energy from the voltage supply charged a capacitor through a resistor, and was released to the submerged microelectrode tip across a spark gap switch whose inter-electrode distance was set to give a specific voltage [118].

The microelectrode tip used for these tests ranged around 3 µm in diameter at the tip. It was fabricated from 50µm tungsten wire, which had been sharpened using electrolysis [119]. The voltage and current from the spark gap were recorded using an oscilloscope, with both a voltage probe (Lecroy S/N: 2524) and current transformer (Bergoz CT-D1.0-B) attached to the electrode. The voltage probe that was used has a maximum voltage and frequency of 20 kV and 100 MHZ. The current probe that was used had a specified rising time of 0.7ns. For the experiments conducted the spark gap circuit consisted of a 20 Mohm resistor and 1nF capacitor. The current was set such that the pulse repetition was sufficiently low that only a single discharge occurred. Prior to discharge events, no preexisting microbubbles were observed on the probe tip. Voltage was seen to rise rapidly, at approximately 500 V/ns, due to the rapidity of the spark gap switch. Currents and voltages reached their peaks within 10 ns and decayed to within 10% of the max values within 1-2 µs. The applied voltages to the electrode could be

controlled by changing the distance between the spark gap. Conductivity of the solution was measured by an electrical conductivity probe. For this experiment, 0.1%, 0.18%, 0.2% and 0.3% mass concentration of NaCl solutions were tested.

6.3 Experimental Results

Microbubbles were generated by discharges in liquid. The shapes of microbubble were recorded by the ICCD camera. With different discharge and water parameters, the microbubbles presented different forms. The reasons for such changes was thought to be caused by the instability of the microbubble in liquid. The formation and the dynamics of the microbubble were maintained by a balance between the internal and external pressure on the boundaries of microbubbles. Once the balance was broken due to a non-uniform force distribution, some spikes or branches would appear on the spherical boundary and deformed the sphericity. Spherical, aspherical, branched microbubbles are all presented in this section with different parameters. In addition, by changing the ambient pressures, the branched microbubble could be suppressed back to the spherical microbubble.

Typically spherical bubbles were unseen in microplasma based microbubbles [120]. In order to produce spherical bubbles it was necessary to use relatively low voltage, around -5 ~ -10kV, at a nanosecond scale, which in other experiments was not done because the energy levels produced by power supplies were never low enough to produce spherical microbubbles. The two main theories behind microbubble production is that they occur due to an electronic crack in the liquid, or that the high electric fields

produced lower the surface tension of the liquid by the Lipmann effect [121]. By using the negative polarity voltage source, with nanosecond scale rising time and micron scale microtip, the microbubble appeared at the cathode. This provided both electrons and high electric fields, at that point, which allows for microbubbles to form more easily at lower energies.

Understanding the way that the microbubbles formed and dissipated was multifaceted question. In order to understand what was going on in the bubble, it was necessary to take into account the variables affecting initiation of the bubble at any given time. The experimental variables important to consider were the electric field and polarity. These variables interacted influences the hydrostatic and electric forces, surface tension, charge dissipation, and streamer instabilities of the bubble.

The conductivity of the water had been found to play a significant role in the bubble growth stage, especially in determining the energy at which streamers propagate from the bubble. There were a few possible reasons why conductivity played this role. Firstly, as the conductivity of the solution increased, so did the energy that was released into the bubble. This increase in energy was possibly due to the increased conductivity of the solution affecting the amount of energy that reached the tip of the submerged electrode during the initial stages of bubble generation. The high conductivity also decreased the charge building up at the liquid interface. This was an important point because even though the energy in the system was increased, the probability of streamer instabilities occurring decreased. It was found that at lower conductivities it required less energy to created streamers.

The conductivity of the solution increased the stability of the bubbles by increasing the surface tension of the solution [122]. Because of the nanosecond time scale of the discharge, the bubbles were generated at such high rates of speed that the water solution acted as solid. By taking this view it helped to answer the questions of why streamers propagate more often in low conductivity solutions. During bubble expansion the outward force, due to the pressure gradient caused by the release of energy, was countered by the surface tension of the water resisting expansion. Past a threshold the force from the bubble became too great and the bonds that make up the water began to break. This caused "cracks" in the water that allowed the force to dissipate and eventually equalized over time, 10 ~ 20 μs, as the bubble returned to its spherical.

6.3.1 Branched Microbubble in Conductivity Controlled Liquid

Bubble formation was found to be a function of conductivities and peak voltages. In this research microbubbles were generated during the microplasma discharges for various mass concentration of NaCl and peak voltages. For a given conductivity, as the voltage increased the energy in the microplasma bubble also increased until the energy was high enough that instabilities occurred. These instabiliies, also called secondary streamers [123], were cracks that propogated from the bubble into the surrounding liquid, and we referred to them as branched bubbles. The primary range in which the transition occurred between spherical and branched bubbles was between -5 kV and -6 kV over the range of conductivities tested in this research. The images in Figure 93 were

taken approximatly one microseconds after the initial discharge occurred, and showed the electrode (coming in from the right) and bubble formed at the electrode tip. It can be seen that as the input voltage increased the bubbles increased in size correspondingly, as well as branched bubbles began to occur. Also as the conductivity of the water increased the bubbles was able to maintain the spherical shape without secondary streamers forming at higher energies. Through these voltage and current dependancies, it was possible to identify a transition in stability of the bubble's expansion.

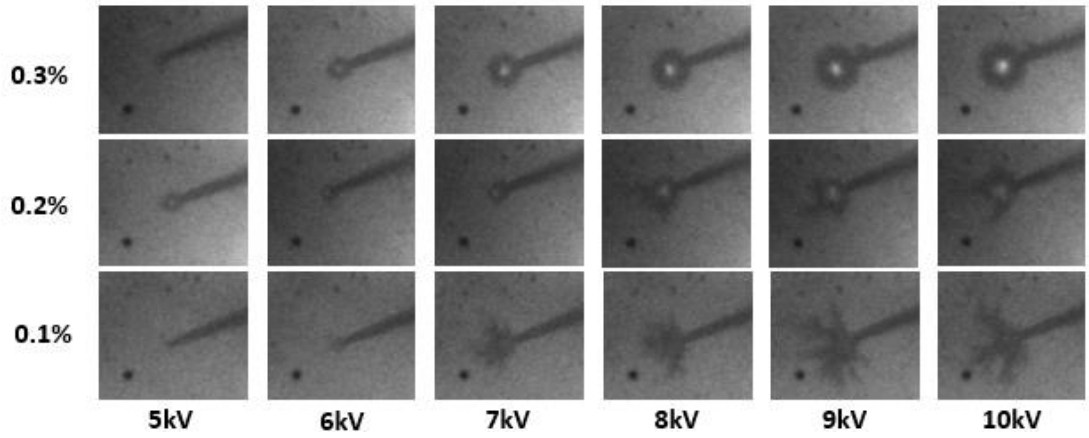

Figure 93. Microbubble Images with 0.5µs Delay, 0.5µs Exposure Time

After the discharge the microbubble lasted for approximately 10 ~ 100 µs depending on initial energy. In addition, once the microbubbles were generated there

were between 2 ~ 4 expansion and collapse oscillations before the bubble disappeared completely. The first bubble expansion lasted for 10 ~ 15 μs. It was important because during this expansion most of the energy was stored, and bubble instabilities were more likely to occur. This process of the changed in bubble shapes as it occurred over time is presented in Figure 94**.** The figure shows microbubble evolution at two different voltages as a function of time, a 0.1% mass concentration of NaCl was used. The figure shows that with all other variables held equal, it was possible to transit between bubble phases solely based upon initial voltage. The first picture in each set was taken with no background lighting, allowing for confirmation that the light emissions from the plasma are seen.

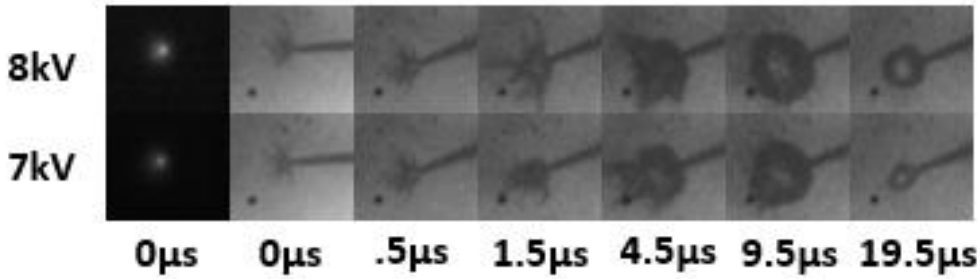

Figure 94. Bubble Images with 0.1% Mass Concentration of NaCl and Exposure Time of 0.5μs in Dark and Illuminated Environment

In Figure 95, images of the bubbles taken at increasing intervals along the bubble life show that over the first 10 microseconds any initial instability in the bubble stabilized causing a spherical bubble shape. The spherical shape could be expected because it provided the lowest energy distribution for the bubble and allowed for equilibrium force distribution along the bubble surface. The reason that microbubbles with higher initial voltages experienced an increased growth rate comparing to lower initial voltages was because as the voltage increased the energy was transferred more quickly into the bubble**.** Energy input the liquid was calculated by integrating the measured voltage and current from a discharge. After the first 500 nanoseconds microbubbles with an initial voltage of -10 kV contained a higher energy of the -5 kV generated microbubbles. This increased energy led to faster growth rates and larger sizes as the energy in the bubble forced it to expand. Increased mass percent of NaCl also caused bubble size to increase.

In order to summarize some of the trends observed. The energy released from the electrode, in the first 100ns, as it related to input voltage and NaCl concentration in water, as presented in Figure 96**.** It is seen that as the concentration of NaCl increased so did the energy transferred to the microbubble in the first 100ns. It was also seen that as the concentration of NaCl increased the microbubbles that formed were more likely to be spherical. This shows that the initial bubble formation was dependent on the conductivity of the liquid to determine the shape and stability of the bubble. The whole trends between spherical and non-spherical microbubbles are presented in Figure 97.

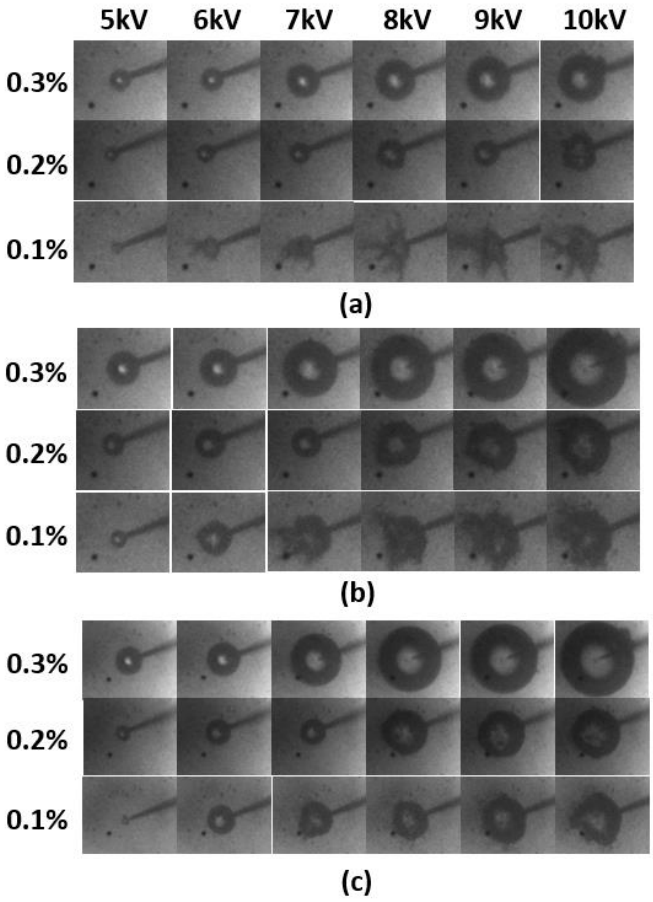

Figure 95. Bubble Images with (a) 1.5us Delay, 0.5us Exposure Time, (b) 4.5us Delay, 0.5us Exposure Time, (c) 9.5us Delay, 0.5us Exposure Time

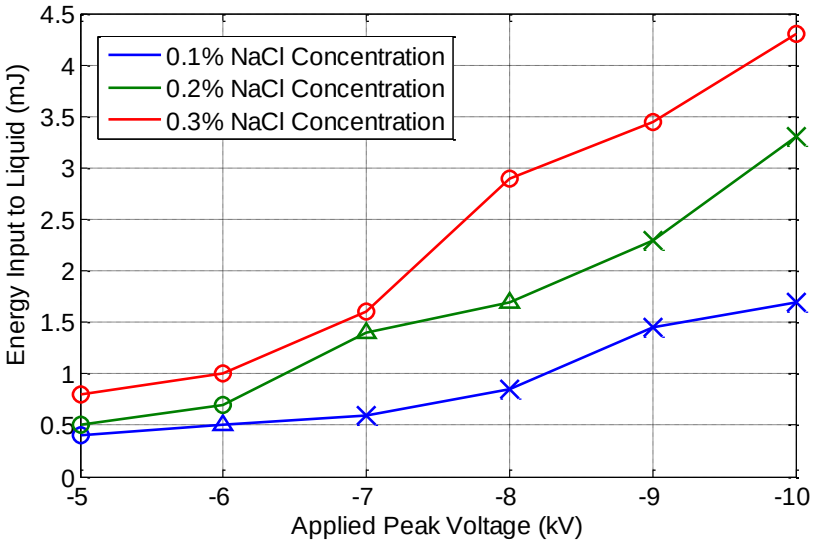

Figure 96. Integrated Energy for First 100ns vs. Input Voltage. Bubble Shape Determined from 0.5µs and Indicated by X=Branched Bubble Δ= Non-Spherical Bubble O=Spherical Bubble. Lines Connecting Conditions of Same Conductivity.

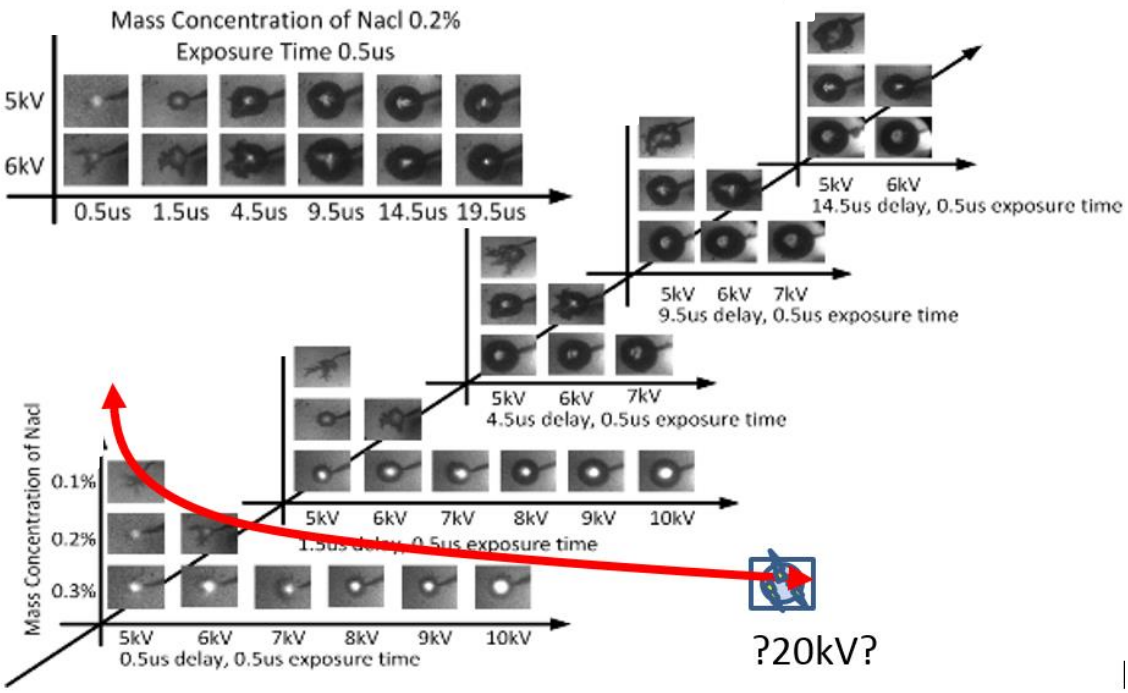

Figure 97. Development of Instabilities of Microbubble on Three Dimensions (Applied Voltages, Mass Concentration of NaCl and Time of Development)

6.3.2 Suppression of Branched Microbubble in Pressure Controlled Environment

All bubbles generated by discharges in liquid introduced in Chapter II were branch-like bubbles. Before the era of microdischarges in liquid, streamers were the most commonly discharge forms in liquid. So long as the generation of streamers, bubbles or microbubbles followed along the streamers in liquid. The shape of those bubbles were either aspherical bubbles or branched like bubbles. By using the microelectrode tip and the low energy discharges, microplasma was able to be formed

without streamer structures in liquid. The spherical form of the microplasma provided a nuclear inception site for a spherical bubble. In previous subsections, the applied peak voltage and the conductivity of liquid could both trigger the branched microbubbles. The transition from spherical bubbles to aspherical bubbles were observed. It was believed that the branches of a microbubble was caused by the unbalance force across the microbubble boundary.

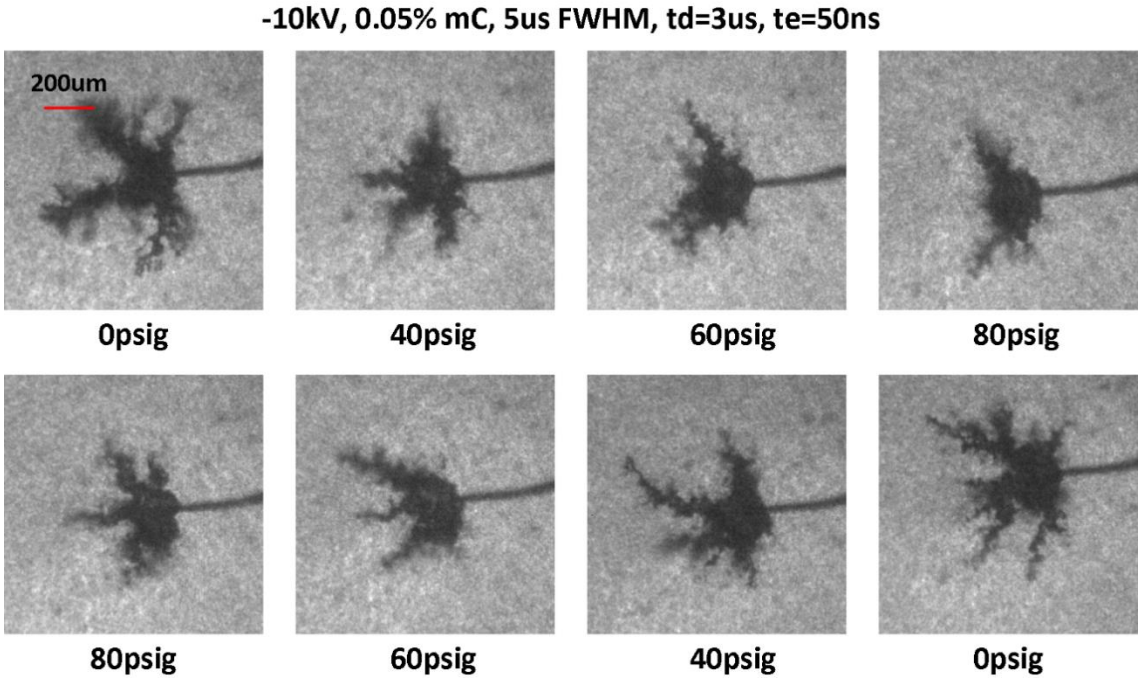

Figure 98. Branched Microbubbles with Low Conductivities (0.05% Mass Concentration of NaCl, 5 μs FWHM Discharge, td=3 μs and te=50ns) Captured by ICCD Camera

The ambient pressure was employed to balance the force across the boundary of microbubbles. Since the pressure in the pressure vessel could only be adjusted between 0 psig and 80 psig, if the internal pressure was excessively strong, the ambient pressure in the pressure vessel was impossible to suppress the branches. In Figure 98, microbubbles were generated with applied peak voltage of -10 kV. The energy from -10 kV seemed to be too strong to suppress by the external pressure. It was clearly that the whole size of the microbubble including its core and branches became smaller or shorter, but the change was not obvious. The tests were run from 0 psig to 80 psig and back to 0 psig to test the repeatability.

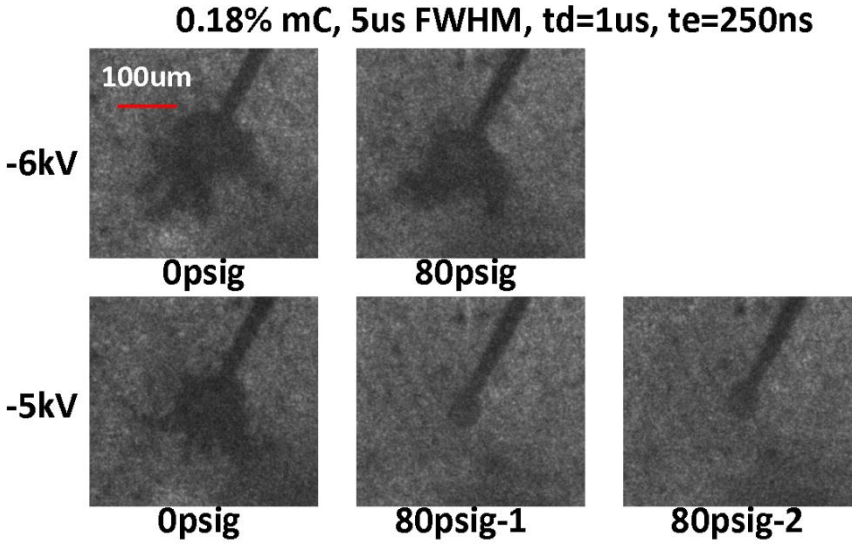

Figure 99. Branches of Microbubbles Suppressed by Ambient Pressures

With same applied peak voltages, the conductivity of the liquid was able to be used to control the energy input to the plasma and discharge generated bubbles. At the same time, a lower breakdown voltage could also be employed to control the energy input as well. In Figure 99 and Figure 99, microsecond discharges were used with the different liquid conductivities and the applied peak voltages. As introduced in Chapter III, the applied peak voltage and the conductivity could subtly influence the energy input. Microsecond discharges were hoped to provide a discharge with moderate energy, so the suppression of the branches from aspherical bubble can be observed. Nanosecond discharges were also used, but none of them was able to create a branched microbubble.

In Figure 100, branched microbubbles were generated by APV of -6 kV and -5 kV both in 0.18% mass concentration of NaCl liquid. The branches looked very clear in the images. For the APV of -6 kV case, the branches looked very clear with 0 psig ambient pressure, so did it with 80 psig ambient pressure. The maximum pressure in the pressure vessel reduced the size of the microbubble. On the other hand, for the APV of -5kV case, the branches looked pretty clear when the ambient pressure is 0psig, but a spherical bubble without any branches showed up when the ambient pressure was 80psig. In order to double confirm the result, a second discharge with exact same parameters was done, and the spherical microbubble presented again.

For spherical bubbles generated by the same parameters, the difference between each of them was subtle, and if any, the length of radius can be the only indicator. For the aspherical bubbles or branched bubbles, however, the number of branches, the length of each branch, the size of the core bubble, etc., all could be used to tell the differences

between bubbles. In Figure 100, nine discharges for each set of parameters were pursued and recorded. The ambient pressure varied from 0 psig to 80 psig with 10 psi as an interval. The length of the longest branch for each image and the core bubble which was enclosed along the roots of all branches were illustrated in Figure 101 both plotted in Figure 102. The error bars in the figure are the standard derivation of the length of the longest branch and the radius of core. The radius of core was reduced by an increasing of ambient pressure. In addition, the branches of the bubble were successfully eliminated by the ambient pressure.

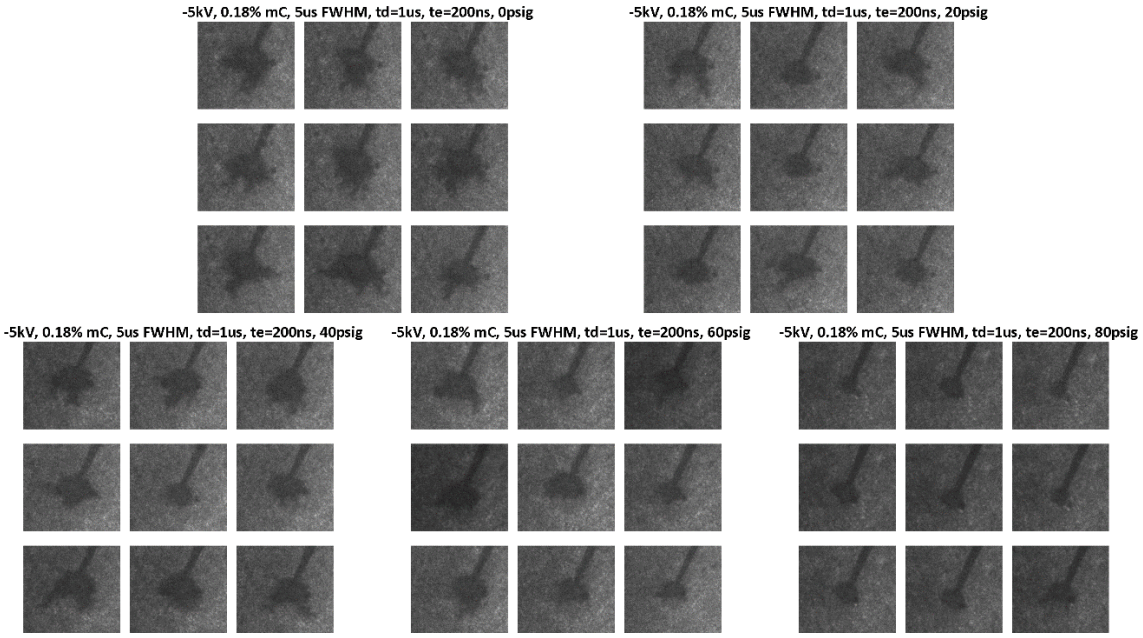

Figure 100. Statistical Study of Microbubbles with and without Branches under Different Ambient Pressures

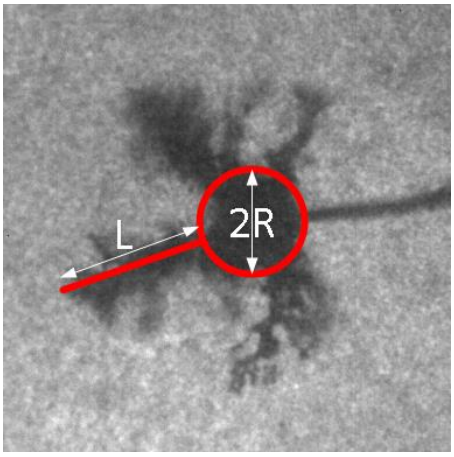

Figure 101. Length of Longest Branch and Radius of Core Bubble

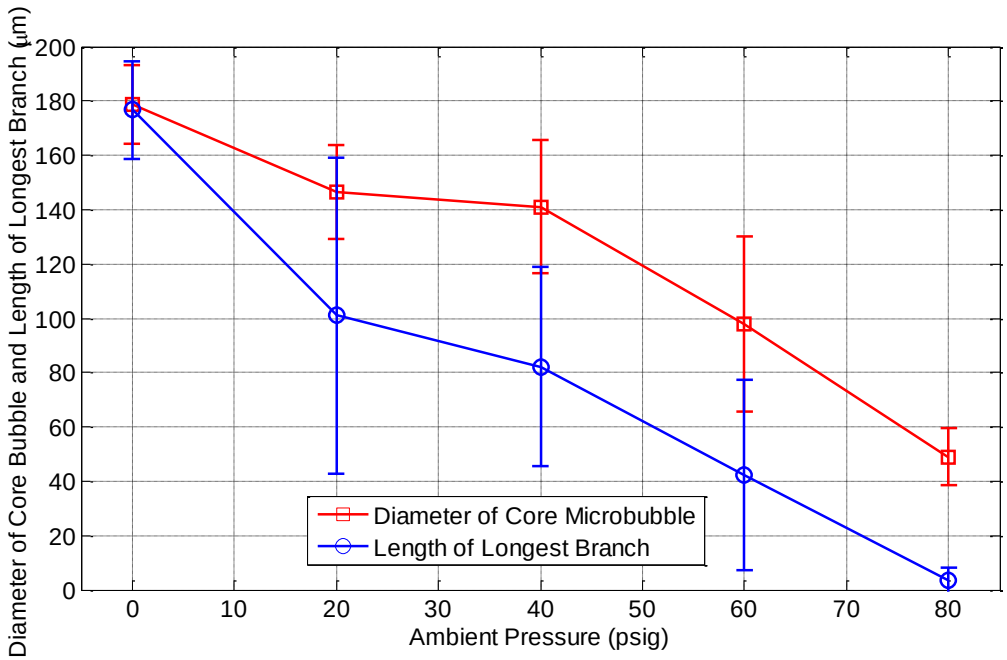

Figure 102. Radius Change of Branched Microbubble and Length of Longest Branch Change vs. Different Ambient Pressures

6.4 Summary

The shape of the microbubble is important in determining its properties and its ability to maintain a high energy density for any period of time. Spherical bubbles allow for the lowest energy distribution, maximizing the stability of the microbubble that is formed. Microplasma based microbubbles in liquids can be controlled and manipulated through the combined usage of input voltage and NaCl concentration of the liquid. Bubble shape transitions can occur by changing both voltage and concentration of NaCl, independently of one another. Increasing the NaCl concentration of the liquid is the most promising bubble stabilizer, at concentrations of 0.3 mass % NaCl spherical bubbles were able to be maintained at input voltages of -10 kV. In conclusion, bubble stability in microbubbles formed in liquids can be increased by increasing the surface tension of the liquid solution the bubble is generated in.

In addition to the transition of microbubbles from aspherical to spherical manipulated by varying the liquid conductivity and the applied peak voltage, the ambient pressure was proved to be able to suppress the branches. Different from using the liquid conductivity and the applied peak voltage which changed the discharge characteristics, the ambient pressure variation only provide external physical interference. Due to the limitation of our pressure vessel which can only handle pressure from 0 psig to 80 psig, a relatively low energy input condition was found. The branched bubbles were observed and recorded when the ambient pressure was 0 psig and all branches disappeared when the ambient pressure was 80 psig.

CHAPTER VII

CONCLUSION AND FUTURE WORK

7.1 Conclusion

Several possible physical mechanisms of bubble and plasma formation are discussed, and systematic experiments were conducted in this research. As introduced in the dissertation motivations and objectives, the general purpose of this dissertation is to explore the fundamental mechanisms of microplasma generation in liquid which has potential to create a high temperature and pressure micron scaled localized spot using low energy input. The microplasma and microbubble were both observed to be initiated in nanosecond scale by using low energy, and the thermodynamic and hydrodynamic of microdischarge generated microbubbles were estimated using Rayleigh-Plesset model (pressure of GPa scale and temperature of hundreds of K). This temperature and pressure in such a transient process together with unique characteristics of non-equilibrium plasma have presented us very promising future research in nuclear fusion, cancer therapy, analytical chemistry, material synthesis etc.

Different applied peak voltages, duration of discharges, conductivities of liquid and size of microelectrode tips were used to explore the initiation of microbubbles and microplasma light emissions. The ICCD camera was used to record the microbubble generation and detect the microplasma light emission, and the PMT was used as an indirect visualization means for the continuous detection of microplasma light emission. Their results were used to corroborate each other. The variation of light intensities

acquired from the ICCD photos matched consistently with that from the PMT. Due to the internal delay of the ICCD camera, the fact that microplasma light emission experienced a very short rising time around 40 ns to their peak values was only collected by the PMT. With the same APV, the nanosecond discharge was able to output much less energy than that from microsecond discharge. The generation of microbubble and microplasma light emission were observed together in all microsecond discharges and in nanosecond discharges with the high electrical conductivity liquid. Two thresholds of APVs were discovered by using the nanosecond discharges in the low electrical conductivity liquid. One threshold was between 1) No bubble formation and no detection of microplasma light emission and 2) Bubble formation but no detection of microplasma light emission. And the other one was between 2) Bubble formation but no detection of microplasma light emission and 3) Bubble formation and the detection of microplasma light emission. The three phenomenon suggest that a certain energy input be able to initiate a phase change in liquid without causing plasma generations. Under the same conditions, e.g., same APV, conductivity of liquid and energy input, the size of microelectrode tips shifted the thresholds from our observations. After the microplasma light emissions were initiated, their intensities showed similar linear trends as the energy input to liquid. The lower energy not only shifted the thresholds of APV for the microplasma initiation, but also reduced the light intensity. At the same APV, the light intensity from the small tip was stronger than the big tip. As the microbubble was created using the lower APV than the microplasma in each case, it seemed that phase change needs lower energy to initiate than the microplasmas. When there existed

thresholds, the electrical field for microbubble generation was around 1.1 GV/m and for microplasma light emission was around 1.3-1.4 GV/m for both microelectrode tips. From energy perspective, the criteria for the initiation of microbubble seems lower than that for the initiation of microplasma.

Images of discharges generated microbubbles were captured at 10 ns exposure time with 10ns increment by the ICCD camera and at 300k fps by the CMOS video camera. Two discharges were studied in detail, a 103 mJ microsecond pulsed discharge and a 0.5 mJ nanosecond pulsed discharge. A microbubble was observed with microplasma confined in it. The study of microplasma generated microbubble provides a path to investigate the microplasmas. The energy to support the growth of the microbubble is provided by the microplasma. After the microplasma disappears, the microbubble expands and collapse for several oscillations. Due to energy and mass transfer, the amplitude of oscillations decays to zero. Then the microbubble at equilibrium radius is visible for ~10 μs before disappears either due to leaving the field of view or dissolving. The microplasma generated microbubble by microsecond discharge had more energy to sustain more oscillations and larger maximum radius comparing to the microbubble generated by the nanosecond discharge at same applied peak voltage. The physics of oscillations are well described by Rayleight-Plesset models. A RP model with the assumption of no significant mass and energy transfer fits well with experimental results in the first cycle of oscillation for both cases. The model allows us to describe the thermodynamic state inside the microbubble e.g., pressures, temperature, mass and internal energy, based on the observed size variation. The

important features of the model are that the bubble contains vapor and ideal gases mixtures. Over the range modeled, it is approximately isothermal. The energy of the microplasma is summed up roughly. Energy in the microplasma is on the order of microjoule scale. Such low energy explains that the spherical stability of microbubble's interface compared to typical branched streamers.

The microplasma and the microdischarge generated microbubbles were successfully generated in our homemade pressure vessel. The pressure vessel could handle 0 psig to 80 psig internal pressure. The microelectrode tips was placed at the bottom of the pressure vessel and the microplasma and the microbubble were both generated at the tip. The observation was still pursued using the high speed cameras and the microscope. Boundary identification was programed to efficiently identify the boundary of microbubbles and to estimate the radius of them. Parametric study for the microbubble generation with various ambient pressure, liquid surface tension, energy duration and applied peak voltage were done. It was found that the radius of microbubbles presented higher uncertainty when the ambient pressure increased. The Rayleigh-Plesset model which has been used in Chapter IV was used here to compare experimental results and the model estimation. The experimental results matched well with the model data, and the thermodynamic properties of microbubbles under different ambient pressures were calculated as well. From the model results, the initial radius and the initial velocity did not change much with various ambient pressure, but the equilibrium temperature increased linearly corresponding to the increasing of the ambient pressure. The equilibrium temperature for each ambient pressure was very close

to each of their saturation temperature. The polytropic index presented very consistent value with various ambient pressures. It implied that the thermodynamic process in the microbubble stay very similar. The polytropic index is around 1.01 which suggested during the oscillation, the vapor in the microbubble experienced an almost isothermal process. The internal energy and the mass in the microbubble did not change monotonically when the pressure linearly increased. The speculation was when the pressure increased, the volume of the microbubble became smaller but the density of the vapor in the bubble became higher. By adding up these two effects, the internal energy and the mass contained in the microbubble did not change monotonically.

The generation of spherical bubbles by discharges assists our model study for the thermodynamic properties of microdischarges, since the Rayleigh-Plesset model can only apply for the thermodynamic property estimation of spherical bubbles in liquid. Besides that, spherical bubbles allow for the low energy input and high energy density. Microplasma based microbubbles in liquids can be controlled by adjusting the input voltage, NaCl concentration of the liquid and ambient pressures. Increasing the NaCl concentration of the liquid is the most effective bubble stabilizer, at concentrations of 0.3 mass % NaCl spherical bubbles were able to be maintained at input voltages of -10 kV. Different from using the liquid conductivity and the applied peak voltage which changed the discharge characteristics, the ambient pressure variation only provide external physical interference. Due to the limitation of our pressure vessel which can only handle pressure from 0 psig to 80 psig, a relatively low energy input condition was found. The

branched bubbles were observed and recorded when the ambient pressure was 0 psig and all branches disappeared when the ambient pressure was 80 psig.

7.2 Future Work

The nanosecond micron scale microplasma and the microsecond micron scale microbubbles have been successfully generated in liquid with different experimental conditions. Their thermodynamic properties have been studied experimentally and theoretically. Based on the objectives, motivations and current results of this research, some future work in terms of short term plans and long term plans can be done.

7.2.1 Short Term Plans

The maximum radius of the microbubble in this research was around 300 μm. A bigger capacitor can be used in the spark gap circuit in the future. A much higher energy input from the bigger capacitor is believed to be able to generate a bigger microbubble. As suggested from sonoluminescence bubbles, it is worthwhile to investigate if a second microplasma can be generated from the collapse of a gas bubble in liquid. Mechanical means to generate plasma will be a very interesting and new area.

The Rayleigh-Plesset model used in this research was a momentum balance based RP model. As mentioned in the Chapter IV, when the diameter of the microbubble is smaller than 10 μm, the mass transfer and heat transfer caused by the temperature

difference dominate the motion of the microbubble. An energy balance based RP model needs to be developed for the microbubbles with diameters smaller than 10 μm.

In analysis of the energy balance between the energy input from the circuit and the energy used for the plasma generation and the bubble generation, the energy stored in double layer formed on the electrode is still unknown. The double layer can function as an effective capacitor and hold a big portion of the energy. The research on double layer in high electrical field will be useful for a better understanding of the energy dissipation during discharges.

The 65 ns delay of the ICCD was the problem which prevented us from taking image in that period of time. PMT successfully helped us indirectly acquired light signal, but the images will still be useful for the bubble detection. A pre-trigger system can be built in the future, so the high speed camera can receive the shutter open command 65 ns before the discharge event. With this 65 ns pre-trigger system, the internal delay of the ICCD camera can be compensated.

The whole research covered in this dissertation focused on fundamental research. The microplasma discharge in liquid was also designed to be used as an industrial product. The spectroscopic analysis using microplasma discharge in liquid or gas was designed to replace laser induced breakdown system. It is still in this very early preliminary stage, and R&D work needs to be continued.

7.2.2 Long Term Plans

As introduced in Chapter I, one of the objectives and motivations is to push the research boundary of the classical plasmas which in general stay in gaseous phase to an uncharted area where the liquid and solid phases dominate the existence. The energy input in our research is low and the initiation site is in liquid, which are the reasons the plasma can be small and spherical. Thanks to the confinement of the liquid, the energy density (energy in plasma/volume of plasma) can be extremely high. From initiation rate and energy density perspective, there are many similarities between the microplasma initiations in liquid and the nuclear fusion. One of the long term plans is to explore plasmas with as-high-as-possible energy density which can be comparable to a nuclear fusion. The maximum power density in our case is around 7.4e20 W/m^3.

The high energy density is one of the magnificent advantages that microplasma generation in liquid has. Furthermore, the localized transient chemical process plus mechanical process in the scale of cells has attracted our attention. The idea here is to use the microplasma to get as close as possible to lysed cells e.g., lysed cancer cells. So a localized plasma can target specific cells without causing big collateral damages. The microplasma generation in liquid has solved a big problem that not only doesn't the microplasma need to be created in a vacuum environment but an aqueous environment for microplasma generation is more close to the real environment where the cells live.

REFERENCES

[1] A. L. Peratt, *Physics of the plasma universe*, 2nd ed. New York: Springer, 2015.

[2] I. Langmuir, "Oscillations in ionized gases," *Proceedings of the National Academy of Sciences of the United States of America*, vol. 14, pp. 627-637, 1928.

[3] Contemporary Physics Education Project, "Different forms of plasma in universe," NASA, 1996.

[4] P. Xiao and D. Staack, "Microbubble generation by microplasma in water," *Journal of Physics D-Applied Physics*, vol. 47, 2014.

[5] P. Xiao and D. Staack, "Microbubble generation by microplasma in water," *Journal of Physics D: Applied Physics*, vol. 47, p. 355203, 2014.

[6] P. Xiao and D. Staack, "PMT and ICCD investigation of light emission from microplasma generated in liquid," in *Pulsed Power Conference (PPC), IEEE*, 2013, pp. 1-6.

[7] P. Xiao and D. Staack, "Experimental and modeling analysis of the single micro bubble generation by micro plasma in water," in *APS Meeting Abstracts*, 2012, p. 4006.

[8] R. Toumi, J. D. Haigh, and K. S. Law, "A tropospheric ozone-lightning climate feedback," *Geophysical Research Letters*, vol. 23, pp. 1037-1040, 1996.

[9] K. Miyazaki, H. J. Eskes, K. Sudo, and C. Zhang, "Global lightning NOx production estimated by an assimilation of multiple satellite data sets," *Atmospheric Chemistry and Physics*, vol. 14, pp. 3277-3305, 2014.

[10] X. X. Tie, R. Y. Zhang, G. Brasseur, and W. F. Lei, "Global NOx production by lightning," *Journal of Atmospheric Chemistry*, vol. 43, pp. 61-74, 2002.

[11] T. Tsubota, K. Kuratsu, N. Murakami, and T. Ohno, "Attempt of deposition of Ag-doped amorphous carbon film by Ag-cathode DC plasma with CH4 flow," *Journal of Nanoscience and Nanotechnology*, vol. 15, pp. 4619-4631, 2015.

[12] Y. Zhang, M. Creatore, Q. B. Ma, A. El Boukili, L. Gao, M. A. Verheijen, *et al.*, "Nitrogen-doping of bulk and nanotubular TiO2 photocatalysts by plasma-assisted atomic layer deposition," *Applied Surface Science*, vol. 330, pp. 476-486, 2015.

[13] J. Yoon, J. G. Song, H. Kim, and H. B. R. Lee, "Plasma-enhanced atomic layer deposition of Co on metal surfaces," *Surface & Coatings Technology*, vol. 264, pp. 60-65, 2015.

[14] N. Kumar, S. A. Barve, S. S. Chopade, R. Kar, N. Chand, S. Dash, *et al.*, "Scratch resistance and tribological properties of SiOx incorporated diamond-like carbon films deposited by r.f. plasma assisted chemical vapor deposition," *Tribology International*, vol. 84, pp. 124-131, 2015.

[15] A. W. Zia, Y. Q. Wang, and S. Lee, "Effect of physical and chemical plasma etching on surface wettability of carbon fiber-reinforced polymer composites for bone plate applications," *Advances in Polymer Technology*, vol. 34, 2015.

[16] V. V. Felmetsger, M. K. Mikhov, and P. N. Laptev, "Effect of pre-deposition rf plasma etching on wafer surface morphology and crystal orientation of

piezoelectric aln thin films," *IEEE Transactions on Ultrasonics Ferroelectrics and Frequency Control,* vol. 62, pp. 387-391, 2015.

[17] M. Ekielski, M. Juchniewicz, M. Pluska, M. Wzorek, E. Kaminska, and A. Piotrowska, "Nanometer scale patterning of GaN using nanoimprint lithography and inductively coupled plasma etching," *Microelectronic Engineering,* vol. 133, pp. 129-133, 2015.

[18] K. C. Wright, H. S. Kim, D. J. Cho, A. Rabinovich, A. Fridman, and Y. I. Cho, "New fouling prevention method using a plasma gliding arc for produced water treatment," *Desalination,* vol. 345, pp. 64-71, 2014.

[19] R. Wascher, N. Schulze, G. Avramidis, H. Militz, and W. Viol, "Increasing the water uptake of wood veneers through plasma treatment at atmospheric pressure," *European Journal of Wood and Wood Products,* vol. 72, pp. 685-687, 2014.

[20] P. M. K. Reddy, S. Mahammadunnisa, and C. Subrahmanyam, "Catalytic non-thermal plasma reactor for mineralization of endosulfan in aqueous medium: A green approach for the treatment of pesticide contaminated water," *Chemical Engineering Journal,* vol. 238, pp. 157-163, 2014.

[21] M. Holub, R. Brandenburg, H. Grosch, S. Weinmann, and B. Hansel, "Plasma supported odour removal from waste air in water treatment plants: an industrial case study," *Aerosol and Air Quality Research,* vol. 14, pp. 697-707, 2014.

[22] European Fusion Development Agreement (EFDA) - The Joint European Torus (JET), "Inside View of JET Tokamak,"

[23] Plasma Engineering and Diagnostic Laboratory (PEDL), 2009.

[24] C. F. Gallo, "Coronas and gas discharges in electrophotography: a review," *Industry Applications, IEEE Transactions on,* vol. IA-11, pp. 739-748, 1975.

[25] F. Paschen, "Ueber die zum Funkenübergang in Luft, Wasserstoff und Kohlensäure bei verschiedenen Drucken erforderliche Potentialdifferenz," *Annalen der Physik,* vol. 273, pp. 69-96, 1889.

[26] Y. P. Raizer, *Gas discharge physics*. Berlin: Springer, 1997.

[27] J. Li, M. Sato, and T. Ohshima, "Degradation of phenol in water using a gas–liquid phase pulsed discharge plasma reactor," *Thin Solid Films,* vol. 515, pp. 4283-4288, 2007.

[28] B. R. Locke, M. Sato, P. Sunka, M. R. Hoffmann, and J. S. Chang, "Electrohydraulic discharge and nonthermal plasma for water treatment," *Industrial & Engineering Chemistry Research,* vol. 45, pp. 882-905, 2006.

[29] H. Akiyama, "Streamer discharges in liquids and their applications," *Dielectrics and Electrical Insulation, IEEE Transactions on,* vol. 7, pp. 646-653, 2000.

[30] C. Richmonds and R. M. Sankaran, "Plasma-liquid electrochemistry: Rapid synthesis of colloidal metal nanoparticles by microplasma reduction of aqueous cations," *Applied Physics Letters,* vol. 93, p. 131501, 2008.

[31] M. Vittori Antisari, R. Marazzi, and R. Krsmanovic, "Synthesis of multiwall carbon nanotubes by electric arc discharge in liquid environments," *Carbon,* vol. 41, pp. 2393-2401, 2003.

[32] R. Burlica, M. J. Kirkpatrick, and B. R. Locke, "Formation of reactive species in gliding arc discharges with liquid water," *Journal of Electrostatics,* vol. 64, pp. 35-43, 2006.

[33] J.-S. Chang, "Recent development of plasma pollution control technology: a critical review," *Science and Technology of Advanced Materials,* vol. 2, pp. 571-576, 2001.

[34] J. Woloszko, K. R. Stalder, and I. G. Brown, "Plasma characteristics of repetitively-pulsed electrical discharges in saline solutions used for surgical procedures," *Plasma Science, IEEE Transactions on,* vol. 30, pp. 1376-1383, 2002.

[35] A. Vogel, N. Linz, S. Freidank, and G. Paltauf, "Femtosecond-laser-induced nanocavitation in water: implications for optical breakdown threshold and cell surgery," *Physical Review Letters,* vol. 100, p. 038102, 2008.

[36] G. Fridman, A. Shereshevsky, M. Jost, A. Brooks, A. Fridman, A. Gutsol, *et al.*, "Floating electrode dielectric barrier discharge plasma in air promoting apoptotic behavior in melanoma skin cancer cell lines," *Plasma Chemistry and Plasma Processing,* vol. 27, pp. 163-176, 2007.

[37] T. C. Montie, K. Kelly-Wintenberg, and J. Reece Roth, "An overview of research using the one atmosphere uniform glow discharge plasma (OAUGDP) for sterilization of surfaces and materials," *Plasma Science, IEEE Transactions on,* vol. 28, pp. 41-50, 2000.

[38] A. T. Sugiarto and M. Sato, "Pulsed plasma processing of organic compounds in aqueous solution," *Thin solid films*, vol. 386, pp. 295-299, 2001.

[39] A. T. Sugiarto, S. Ito, T. Ohshima, M. Sato, and J. D. Skalny, "Oxidative decoloration of dyes by pulsed discharge plasma in water," *Journal of Electrostatics*, vol. 58, pp. 135-145, 2003.

[40] A. Starikovskiy, Y. Yang, Y. I. Cho, and A. Fridman, "Non-equilibrium plasma in liquid water: dynamics of generation and quenching," *Plasma Sources Science & Technology*, vol. 20, 2011.

[41] C. H. A. Juvan, "Separation of dissolved and undissolved substances from liquids using high energy discharge initiated shock waves," ed: Google Patents, 1990.

[42] D. V. Palanker, "Method and apparatus for pulsed plasma-mediated electrosurgery in liquid media," ed: Google Patents, 2000.

[43] V. Y. Ushakov, N. M. Torbin and Foreign Technology Div Wright-Patterson AFB Ohio, "Concerning the development of a discharge in solid dielectrics." *Ft. Belvoir: Defense Technical Information Center*, 1967.

[44] W. Douyan, A. Hidenori, and N. Takao, *Pulsed Discharge Plasma for Pollution Control*: INTECH Open Access Publisher, 2010.

[45] T. Sakugawa, T. Yamaguchi, K. Yamamoto, T. Kiyan, T. Namihira, S. Katsuki, *et al.*, "All solid state pulsed power system for water discharge," in *Pulsed Power Conference, 2005 IEEE*, 2005, pp. 1057-1060.

[46] O. Lesaint and G. Massala, "Positive streamer propagation in large oil gaps: experimental characterization of propagation modes," *Dielectrics and Electrical Insulation, IEEE Transactions on*, vol. 5, pp. 360-370, 1998.

[47] M. A. Malik, A. Ghaffar, and S. A. Malik, "Water purification by electrical discharges," *Plasma Sources Science & Technology*, vol. 10, pp. 82-91, 2001.

[48] Institute of Plasma Physics Academy of Sciences of the Czech Republic, 2006.

[49] Photron and Stanford Computer Optics, USA.

[50] Hamamatsh Photonics, Japan.

[51] M. Sato, M. Saito, and T. Hatori, "Emulsification and size control of insulating and/or viscous liquids in liquid-liquid systems by electrostatic dispersion," *Journal of Colloid and Interface Science*, vol. 156, pp. 504-507, 1993.

[52] M. Sato, T. Hatori, and M. Saito, "Experimental investigation of droplet formation mechanisms by electrostatic dispersion in a liquid-liquid system," *Industry Applications, IEEE Transactions on*, vol. 33, pp. 1527-1534, 1997.

[53] P. Šunka, "Pulse electrical discharges in water and their applications," *Physics of Plasmas (1994-present)*, vol. 8, pp. 2587-2594, 2001.

[54] W. An, K. Baumung, and H. Bluhm, "Underwater streamer propagation analyzed from detailed measurements of pressure release," *Journal of Applied Physics*, vol. 101, p. 053302, 2007.

[55] K. Schoenbach, J. Kolb, S. Xiao, S. Katsuki, Y. Minamitani, and R. Joshi, "Electrical breakdown of water in microgaps," *Plasma Sources Science and Technology*, vol. 17, p. 024010, 2008.

[56] P. Bruggeman and C. Leys, "Non-thermal plasmas in and in contact with liquids," *Journal of Physics D: Applied Physics,* vol. 42, p. 053001, 2009.

[57] M. Sato, T. Ohgiyama, and J. S. Clements, "Formation of chemical species and their effects on microorganisms using a pulsed high-voltage discharge in water," *Industry Applications, IEEE Transactions on,* vol. 32, pp. 106-112, 1996.

[58] P. Bruggeman, J. Degroote, J. Vierendeels, and C. Leys, "DC-excited discharges in vapour bubbles in capillaries," *Plasma Sources Science and Technology,* vol. 17, p. 025008, 2008.

[59] K. Sato and K. Yasuoka, "Pulsed discharge development in oxygen, argon, and helium bubbles in water," *Plasma Science, IEEE Transactions on,* vol. 36, pp. 1144-1145, 2008.

[60] Y.-S. Chen, X.-S. Zhang, Y.-C. Dai, and W.-K. Yuan, "Pulsed high-voltage discharge plasma for degradation of phenol in aqueous solution," *Separation and Purification Technology,* vol. 34, pp. 5-12, 2004.

[61] W.-T. Shin, S. Yiacoumi, C. Tsouris, and S. Dai, "A pulseless corona-discharge process for the oxidation of organic compounds in water," *Industrial & Engineering Chemistry Research,* vol. 39, pp. 4408-4414, 2000.

[62] T. Miichi, S. Ihara, S. Satoh, and C. Yamabe, "Spectroscopic measurements of discharges inside bubbles in water," *Vacuum,* vol. 59, pp. 236-243, 10// 2000.

[63] C. Yamabe, F. Takeshita, T. Miichi, N. Hayashi, and S. Ihara, "Water treatment using discharge on the surface of a bubble in water," *Plasma Processes and Polymers,* vol. 2, pp. 246-251, 2005.

[64] P. J. Bruggeman, C. A. Leys, and J. A. Vierendeels, "Electrical breakdown of a bubble in a water-filled capillary," *Journal of Applied Physics,* vol. 99, p. 116101, 2006.

[65] P. Bruggeman, C. Leys, and J. Vierendeels, "Experimental investigation of dc electrical breakdown of long vapour bubbles in capillaries," *Journal of Physics D: Applied Physics,* vol. 40, p. 1937, 2007.

[66] P. Bruggeman, J. Degroote, C. Leys, and J. Vierendeels, "Electrical discharges in the vapour phase in liquid-filled capillaries," *Journal of Physics D: Applied Physics,* vol. 41, p. 194007, 2008.

[67] J. K. Evju, P. B. Howell, L. E. Locascio, M. J. Tarlov, and J. J. Hickman, "Atmospheric pressure microplasmas for modifying sealed microfluidic devices," *Applied Physics Letters,* vol. 84, pp. 1668-1670, 2004.

[68] Y. Akishev, M. Grushin, V. Karalnik, A. Monich, A. Petryakov, and N. Trushkin, "Self-pulsing regime of dc electric discharge in dielectric tube filled with water containing gas bubble," *Plasma Science, IEEE Transactions on,* vol. 36, pp. 1142-1143, 2008.

[69] E. A. Azizov, A. I. Emelyanov, and V. A. Yagnov, "Underwater electrical discharge with a large surface of radiation," *Dielectrics and Electrical Insulation, IEEE Transactions on,* vol. 14, pp. 1291-1294, 2007.

[70] I. Prysiazhnevych, V. Yukhymenko, V. Chernyak, S. Olshevskiy, V. Naumov, J. Skalny, *et al.*, "Discharge in the gas channel with liquid walls as generator of

non-thermal plasma at atmospheric pressure," in *28th ICPIG, Prague, Czech Republic*, ed, 2007.

[71] J. Janca, S. Kuzmin, A. Maximov, J. Titova, and A. Czernichowski, "Investigation of the chemical action of the gliding and “point” arcs between the metallic electrode and aqueous solution," *Plasma Chemistry and Plasma Processing,* vol. 19, pp. 53-67, 1999.

[72] P. Lukes and B. R. Locke, "Degradation of substituted phenols in a hybrid gas-liquid electrical discharge reactor," *Industrial & engineering chemistry research,* vol. 44, pp. 2921-2930, 2005.

[73] T. J. Lewis, "Breakdown initiating mechanisms at electrode interfaces in liquids," *IEEE Transactions on Dielectrics and Electrical Insulation,* vol. 10, pp. 948-955, Dec 2003.

[74] S. Bhattacharyya, D. Staack, E. A. Vitol, R. Singhal, A. Fridman, G. Friedman, *et al.*, "Localized synthesis of metal nanoparticles using nanoscale corona discharge in aqueous solutions," *Advanced Materials,* vol. 21, pp. 4039-4044, 2009.

[75] D. Staack, A. Fridman, A. Gutsol, Y. Gogotsi, and G. Friedman, "Nanoscale corona discharge in liquids, enabling nanosecond optical emission spectroscopy," *Angewandte Chemie International Edition,* vol. 47, pp. 8020-8024, 2008.

[76] A. Starikovskiy, "Pulsed nanosecond discharge development in liquids with various dielectric permittivity constants," *Plasma Sources Science and Technology*, vol. 22, p. 012001, 2013.

[77] W. G. Graham and K. R. Stalder, "Plasmas in liquids and some of their applications in nanoscience," *Journal of Physics D-Applied Physics*, vol. 44, 2011.

[78] P. Bruggeman, T. Verreycken, M. A. Gonzalez, J. L. Walsh, M. G. Kong, C. Leys, *et al.*, "Optical emission spectroscopy as a diagnostic for plasmas in liquids: opportunities and pitfalls," *Journal of Physics D-Applied Physics*, vol. 43, Mar 31 2010.

[79] M. Laroussi, D. A. Mendis, and M. Rosenberg, "Plasma interaction with microbes," *New Journal of Physics*, vol. 5, 2003.

[80] S. Rupf, A. Lehmann, M. Hannig, B. Schafer, A. Schubert, U. Feldmann, *et al.*, "Killing of adherent oral microbes by a non-thermal atmospheric plasma jet," *Journal of Medical Microbiology*, vol. 59, pp. 206-212, 2010.

[81] K. R. Stalder, G. Nersisyan, and W. G. Graham, "Spatial and temporal variation of repetitive plasma discharges in saline solutions," *Journal of Physics D: Applied Physics*, vol. 39, pp. 3457-3460, 2006.

[82] K. R. Stalder, J. Woloszko, I. G. Brown, and C. D. Smith, "Repetitive plasma discharges in saline solutions," *Applied Physics Letters*, vol. 79, pp. 4503-4505, 2001.

[83] F. Iza, G. J. Kim, S. M. Lee, J. K. Lee, J. L. Walsh, Y. T. Zhang, *et al.*, "Microplasmas: Sources, particle kinetics, and biomedical applications," *Plasma Processes and Polymers*, vol. 5, pp. 322-344, 2008.

[84] K. H. Becker, K. H. Schoenbach, and J. G. Eden, "Microplasmas and applications," *Journal of Physics D-Applied Physics*, vol. 39, pp. R55-R70, 2006.

[85] K. Becker, A. Koutsospyros, S. M. Yin, C. Christodoulatos, N. Abramzon, J. C. Joaquin, *et al.*, "Environmental and biological applications of microplasmas," *Plasma Physics and Controlled Fusion*, vol. 47, pp. B513-B523, 2005.

[86] J. A. C. Broekaert, "Analytical chemistry - Plasma bubbles detect elements," *Nature*, vol. 455, pp. 1185-1186, 2008.

[87] W. An, K. Baumung, and H. Bluhm, "Underwater streamer propagation analyzed from detailed measurements of pressure release," *Journal of Applied Physics*, vol. 101, pp. 053302-053302-10, 2007.

[88] B. S. Sommers and J. E. Foster, "Plasma formation in underwater gas bubbles," *Plasma Sources Science & Technology*, vol. 23, 2014.

[89] B. S. Sommers, J. E. Foster, N. Y. Babaeva, and M. J. Kushner, "Observations of electric discharge streamer propagation and capillary oscillations on the surface of air bubbles in water," *Journal of Physics D-Applied Physics*, vol. 44, 2011.

[90] W. Tian, K. Tachibana, and M. J. Kushner, "Plasmas sustained in bubbles in water: optical emission and excitation mechanisms," *Journal of Physics D: Applied Physics*, vol. 47, 2014.

[91] Y. P. Raizer, *Gas discharge physics*. Berlin ; New York: Springer-Verlag, 1991.

[92] M. Pekker, Y. Seepersad, M. N. Shneider, A. Fridman, and D. Dobrynin, "Initiation stage of nanosecond breakdown in liquid," *Journal of Physics D: Applied Physics*, vol. 47, 2014.

[93] D. Dobrynin, Y. Seepersad, M. Pekker, M. Shneider, G. Friedman, and A. Fridman, "Non-equilibrium nanosecond-pulsed plasma generation in the liquid phase (water, PDMS) without bubbles: fast imaging, spectroscopy and leader-type model," *Journal of Physics D-Applied Physics,* vol. 46, 2013.

[94] P. H. Ceccato, O. Guaitella, M. R. Le Gloahec, and A. Rousseau, "Time-resolved nanosecond imaging of the propagation of a corona-like plasma discharge in water at positive applied voltage polarity," *Journal of Physics D: Applied Physics,* vol. 43, 2010.

[95] M. Klas, S. Matejcik, M. Radmilovic-Radjenovic, and B. Radjenovic, "Electrical breakdown and volt-ampere characteristics in water vapor in microgaps," *Epl,* vol. 99, 2012.

[96] N. Skoro, D. Maric, G. Malovic, W. G. Graham, and Z. L. Petrovic, "Electrical Breakdown in Water Vapor," *Physical Review E,* vol. 84, 2011.

[97] R. P. Joshi, J. Qian, G. Zhao, J. Kolb, K. H. Schoenbach, E. Schamiloglu, *et al.*, "Are microbubbles necessary for the breakdown of liquid water subjected to a submicrosecond pulse?," *Journal of Applied Physics,* vol. 96, pp. 5129-5139, 2004.

[98] C. E. Brennen, *Cavitation and bubble dynamics*. New York: Oxford University Press, 1995.

[99] "Plasma conditions measured in bubbles imploded by extreme sonoluminescence," *Mrs Bulletin,* vol. 35, pp. 642-642, 2010.

[100] T. J. Lewis, "Breakdown initiating mechanisms at electrode interfaces in liquids," *Dielectrics and Electrical Insulation, IEEE Transactions on,* vol. 10, pp. 948-955, 2003.

[101] T. J. Lewis, "The electrode-liquid interface under high fields," in *Dielectric Liquids, 2002. ICDL 2002. Proceedings of 2002 IEEE 14th International Conference on*, 2002, pp. 91-94.

[102] H. M. Jones and E. E. Kunhardt, "Development of pulsed dielectric breakdown in liquids," *Journal of Physics D: Applied Physics,* vol. 28, p. 178, 1995.

[103] Q. Jun, R. P. Joshi, K. H. Schoenbach, J. R. Woodworth, and G. S. Sarkisov, "Model analysis of self- and laser-triggered electrical breakdown of liquid water for pulsed-power applications," *Plasma Science, IEEE Transactions on,* vol. 34, pp. 1680-1691, 2006.

[104] N. F. Bunkin, N. V. Suyazov, and D. Y. Tsipenyuk, "Small-angle scattering of laser radiation by stable micron particles in twice-distilled water," *Quantum Electronics,* vol. 35, p. 180, 2005.

[105] N. F. Bunkin and A. V. Lobeyev, "Influence of dissolved gas on optical breakdown and small-angle scattering of light in liquids," *Physics Letters A,* vol. 229, pp. 327-333, 1997.

[106] Y. Seepersad, M. Pekker, M. N. Shneider, D. Dobrynin, and A. Fridman, "On the electrostrictive mechanism of nanosecond-pulsed breakdown in liquid phase," *Journal of Physics D: Applied Physics,* vol. 46, p. 162001, 2013.

[107] F.-T. Weng and C.-T. Ho, "Manufacturing of a micro-tungsten carbide electrode using a supersonic-aided electrolysis process," *Journal of Micromechanics and Microengineering,* vol. 18, p. 037001, 2008.

[108] L. Rayleigh, "VIII. On the pressure developed in a liquid during the collapse of a spherical cavity," *Philosophical Magazine Series 6,* vol. 34, pp. 94-98, 1917.

[109] M. S. Plesset and A. Prosperetti, "Bubble Dynamics and Cavitation," *Annual Review of Fluid Mechanics,* vol. 9, pp. 145-185, 1977.

[110] S. J. Putterman, "Sonoluminescence - Sound into Light," *Scientific American,* vol. 272, pp. 46-51, 1995.

[111] S. J. Putterman and K. R. Weninger, "Sonoluminescence: How bubbles turn sound into light (vol 32, pg 445, 2000)," *Annual Review of Fluid Mechanics,* vol. 34, pp. Ix-Ix, 2002.

[112] M. P. Brenner, S. Hilgenfeldt, and D. Lohse, "Single-bubble sonoluminescence," *Reviews of Modern Physics,* vol. 74, pp. 425-484, 2002.

[113] R. P. Joshi, J. F. Kolb, S. Xiao, and K. H. Schoenbach, "Aspects of Plasma in Water: Streamer Physics and Applications," *Plasma Processes and Polymers,* vol. 6, pp. 763-777, 2009.

[114] A. I. Gerasimov, "Water as an insulator in pulsed facilities - (Review)," *Instruments and Experimental Techniques,* vol. 48, pp. 141-167, 2005.

[115] G. S. Kulkarni and Z. H. Zhong, "Detection beyond the Debye Screening Length in a High-Frequency Nanoelectronic Biosensor," *Nano Letters,* vol. 12, pp. 719-723, Feb 2012.

[116] F. Ziebert and D. Lacoste, "A Poisson–Boltzmann approach for a lipid membrane in an electric field," *New Journal of Physics*, vol. 12, p. 095002, 2010.

[117] Cmglee, "Phase diagram of water," Open Link

[118] Bruce R. Locke and Selma Mededovic Thagard "Analysis and review of chemical reactions and transport processes in pulsed electrical discharge plasma formed directly in liquid water," *Plasma Chemistry and Plasma Processing*, 2012.

[119] Y. K. Jeong, C. H. Jeon, and Y. J. Chang, "Evaluation of the equivalence ratio of the reacting mixture using intensity ratio of chemiluminescence in laminar partially premixed CH4-air flames," *Experimental Thermal and Fluid Science*, vol. 30, pp. 663-673, 2006.

[120] J. M. Van Doren, J. F. Friedman, T. M. Miller, A. A. Viggiano, S. Denifl, P. Scheier, *et al.*, "Electron attachment to POCl3: Measurement and theoretical analysis of rate constants and branching ratios as a function of gas pressure and temperature, electron temperature, and electron energy," *Journal of Chemical Physics*, vol. 124, 2006.

[121] W. H. Tao and H. K. Yasuda, "Measurement of spatial distributions of electron density and electron temperature in direct current glow discharge by double langmuir probes," *Plasma Chemistry and Plasma Processing*, vol. 22, pp. 297-311, 2002.

[122] Wetz, D.A., Truman, K.P., Mankowski, J.J. and Kristiansen, M. "The Impact of Surface Conditioning and Area on the Pulsed Breakdown Strength of Water," *Ieee Transactions on Plasma Science,* vol. 33, p. 1161, 2005.

[123] Wladimir An1, Kurt Baumung1 and Hansjoachim Bluhm, "Underwater streamer propagation analyzed from detailed measurements of pressure release," *Journal of Applied Physics,* vol. 101, p. 053302, 2007.

APPENDIX

MATLAB codes concerning the video processing, boundary identification, Rayleigh-Plesset model are presented in appendix. There are many other programs for data processing, but only above three categories are recorded in this dissertation.

Video Processing

Conversion from Videos to Frames

```
clear
clc
close all
dir
FilesName =  '20x_100000fps_26nsrise_10kV_C001H001S0001.avi'
FPS = 300000;
% specify frames to load
InitialFrame = 1;
FinalFrame = 71;
m_px = 24e-6/5;%% m/pixel % need more accurate value
A_px = m_px^2; % pixel area m^2
% specify region of interest (ROI)
%ROIcol = [55:300];
%ROIrow = [81:160];
% specify theshold fraction of max brightness to use for finding ball
% center
FractionThreshold = 0;
% load frames
c = mmreader(FilesName);
vidFrames = read(c,[InitialFrame,FinalFrame]);
vidFrames_ROI = double(squeeze(vidFrames(:,:,1,:))); % grey scale so only one of the RGB indexes is required.
clear vidFrames %% significant memory burden so clear unneeded data
ss = size(vidFrames_ROI);
FullSize = get(c,'NumberOfFrames');
X = [1:ss(2)]*m_px ;
Y = [1:ss(1)]*m_px ;
[Xm,Ym] = meshgrid(X,Y); % matrix values of x and y for easy indexing with matrices
PLOTIT = 1; %% a boolean to see if plot the frames and images during analysis % plotting is very very slow but a good check of the algorithm
```

```
Xcen = 0*ones(1,ss(3)); % initialize arrays for faster calculation
Ycen = 0*ones(1,ss(3));
Time = (1:ss(3))/FPS;
%f1 = figure;
%figure(f1);
%set(gcf,'position',[142   89   990   833]);% set the figure position, it is not important in
this program
NominalPics = vidFrames_ROI(:,:,1:5);
BG = mean(NominalPics,3);
MX = max(max(max(vidFrames_ROI)));
MN = min(min(min(vidFrames_ROI)));
DELTA = MX-MN;
%Xcen = 0*Time;
%Ycen = 0*Time;
%NumChanged = 0*Time;
%Radius = Xcen;
%Radius2 = Xcen;
for i=14%i = 1:FinalFrame-InitialFrame
   %pctdone = 100*i/ss(3);
   CF = vidFrames_ROI(:,:,i); % current frame
   CF2 = CF-BG;
   %Threshold = FractionThreshold*DELTA;
   %IsChange = abs(CF2)>Threshold;
   %IndIsChange = find(IsChange);
   %A = IsChange; %
   %B = A.*Xm;
   %C = A.*Ym;
   %Xcen(i) = sum(B(IndIsChange))./sum(A(IndIsChange));
   %Ycen(i) = sum(C(IndIsChange))./sum(A(IndIsChange)); % centriods of the changed
areas by a brightness weighted average
   %NumChanged(i) = length(IndIsChange);
   %Area(i) = A_px*NumChanged(i);
   %Radius(i) =sqrt(Area(i)/pi);
   %[junk,indc] =min(abs(X-Xcen(i)));
   %if  Radius(i)>0
   %    Radius2(i)=Ycen(i)- Y(min(find(A(:,indc)>0)));
   %end
   %if PLOTIT|i==ss(3)|(round(pctdone/5)==pctdone/5)
      %subplot(2,1,1)
      imagesc(X,Y,CF);
      %saveas (gcf,'Bubble(i)','bmp');
      colormap gray
      CF_gray = mat2gray(CF);
      imwrite(CF_gray,['Bubble',num2str(i),'.bmp'])
```

```
        hold on
        % if Radius(i)>0
        %       R1 = rectangle('Curvature', [1 1], 'position',[Xcen(i)-Radius(i),Ycen(i)-
Radius(i),2*Radius(i),2*Radius(i)]);
        %       set(R1,'EdgeColor','r')
        %end
        %p1=plot(Xcen(i),Ycen(i),'r.');
        %set(p1,'MarkerFaceColor','r')
        %plot(Xm(IndIsChange),Ym(IndIsChange),'.k')
        axis equal
        hold off
        %subplot(2,1,2)
        %plot(Time,Radius,'.b-')%, Time,Radius2,'r')
        %xlabel('time (s)')
        %ylabel('Radius (m)')
        pause(0.1)
    %end
end
```

Combination of Frames to Videos

```
clc;
clear all;
FileName='10x_video3_C001H001S0001.avi';
A=VideoReader(FileName);
Front=100;
Back=200;
vidFrames=read(A,[Front,    Back]);

% aviobj=avifile('test.avi','fps',10);
% fig=figure;
% for ii=1: Back-Front
%     image(vidFrames(:,:,:,ii));
%     F = getframe(fig);
%     aviobj = addframe(aviobj,F);
%     pause(0.1);
% end
% close(fig);
% aviobj = close(aviobj);
% for ii=1:Back-Front+1
%     image(vidFrames(:,:,:,ii));
%     F(ii)=getframe;
% end
vidObj=VideoWriter('test.avi');
open(vidObj);
writeVideo(vidObj,vidFrames);
close(vidObj);
```

Load Images into Maxtrix

```
clear
clc
close all
a = dir('*.bmp');
%////// need this number every time
for ii = 1:25
   nm = b{ii};
   ind(ii) = str2num(nm(findstr(nm,'Bubble')+6:findstr(nm,'.')-1));
   A = imread(nm);
   ss = size(A);
   if length(ss)== 3
      Mat(ind(ii),1:ss(1),1:ss(2),1:3) = A(:,:,1:3);
   else
      Mat(ind(ii),1:ss(1),1:ss(2)) = A;
      Mat(ind(ii),1:ss(1),1:ss(2),2) = A;
      Mat(ind(ii),1:ss(1),1:ss(2),3) = A;
   end
end
%save AllImages.mat Mat

 %for jj=1:length(b)
    %imagesc(squeeze(Mat(jj,:,:,1:3)));
    %colormap gray
    %pause(0.2)
 %end
```

Boundary Identification

Canny Algorithm and Radius Trace

```
clear all
clc
load AllImages.mat;
vidObj = VideoWriter('Single-300k-9kv-0psi-30mNperm-0p2per-5cycle-10X.avi');
vidObj.FrameRate = 5;
open(vidObj);
fig = figure;
for i=2:42
   M=squeeze(Mat(i,:,:,:));
   I=squeeze(M(:,:,1));
   if max(max(I))<200
      BW = edge(I,'canny',[0.67],8); %original version is 0.67 8
      a0=0;
      a=45;
      b=115;
   else
      [row0, col0]=find(I>130);
      a=mean(row0);
      b=mean(col0);
      for ii=1:size(row0)
         I(row0(ii),col0(ii))=130;
      end
      BW = edge(I,'canny',[0.67], 12);
      a0=1;
   end
   [row00, col00]=find(BW);
   Z=sqrt((row00-a).^2+(col00-b).^2);
   if i==22 ||i==23
      zz=40;
   elseif i==24
      zz=30;
   else
      zz=24;
   end
   c=find(Z<zz);
   %else
   %c=find(Z<100);
   %end
   BW(row00(c),col00(c))=0;
   subplot(2,1,1)
```

```
imshow(BW);
imagesc(M);
title('Micro Plasma based Micro Bubble');
xlabel('Pixel on X axis');
ylabel('Pixel on Y axis');
hold on
[row, col]=find(BW);
%     plot(col,row,'g.')
%     axis equal
% identify left and right curve
s=size(col);
m=1;
n=1;
k=1;
for j=1:s
   if mean(col)<140
      if col(j)<mean(col)
         colL(m)=col(j);
         rowL(m)=row(j);
         m=m+1;
      else
         colR(n)=col(j);
         rowR(n)=row(j);
         n=n+1;
      end
      a1=0;
   else
      if col(j)>140
         colR(k)=col(j);
         %colL(j)=col(j);
         rowR(k)=row(j);
         %rowL(j)=row(j);
         k=k+1;
      end
      a1=1;
   end
end
% best fit for the radius
if mean(col)<140
   r=30;
   x0=mean(col);
   y0=mean(row);
   x(1) = r;
   x(2) = x0;
```

```
    x(3)= y0;
    params{1}=colL ;
    params{2}=rowL ;
    params{3} =colR;
    params{4}=rowR;
    err = circlefiterror(x,params);
    Xnew = fminsearch('circlefiterror',x,[]12,params);
    r = Xnew(1);
    x0 = Xnew(2);
    y0 = Xnew(3);
    cp = circlefunction(r,x0,y0,rowL,rowR);
    ynew = linspace(y0-r,y0+r,100);
    cp = circlefunction(r,x0,y0,ynew,ynew);
    xf_fit = cp{1};
    xb_fit = cp{2};
    plot(colL,rowL,colR,rowR,xf_fit,ynew,xb_fit,ynew)
    a2=0;
    clear colL rowL colR rowR xf_fit ynew xb_fit ynew
else
    r=35;
    x0=110;
    y0=40;

    x(1) = r;
    x(2) = x0;
    x(3)= y0;
    params{1}=colR ;
    params{2}=rowR ;
    err = circlefiterrorXX(x,params);
    Xnew = fminsearch('circlefiterrorXX',x,[],params);
    r = Xnew(1);
    x0 = Xnew(2);
    y0 = Xnew(3);
    cp = circlefunctionXX(r,x0,y0,rowR);
    ynew = linspace(y0-r,y0+r,100);
    cp = circlefunctionXX(r,x0,y0,ynew);
    xb_fit = cp{1};
    plot(colR,rowR,xb_fit,ynew)
    a2=1;
    clear colL rowL colR rowR xf_fit ynew xb_fit ynew
end
axis equal
hold off;
subplot(2,1,2)
```

```
    RR(1)=0;
    RR(i)=r;
    FPS=300000;
    deltaT=1/FPS*1e6;
    t(1)=0;
    t(i)=(i)*deltaT;
    Radius=RR*2.5;
    plot(t,Radius,'*-')
    title('Micro Plasma based Micro Bubble');
    xlabel('Time(us)');
    ylabel('Radius(um)');
    grid on;
    pause(0.3)
    F=getframe(fig);
    writeVideo(vidObj,F);
end
%close(fig);
close(vidObj);
savefile='S9kV0pS2C.mat'; % single+-7kV+10psi+surfactant+0.2conductivity
save(savefile,'t','Radius');
```

```
function err =circlefiterror(x,params)
r = x(1);
x0 = x(2);
y0 = x(3);
xf = params{1};
yf = params{2};
xb = params{3};
yb = params{4};
cp = circlefunction(r,x0,y0,yf,yb);
xf_fit = cp{1};
xb_fit = cp{2};
err = sqrt(sum((xf-xf_fit).^2) +sum((xb-xb_fit).^2));
```

```
function circlepoints=circlefunction(r,x0,y0,yf,yb)
xf = real(x0-sqrt(r^2-(yf-y0).^2));
```

```
xb = real(x0+sqrt(r^2-(yb-y0).^2));
circlepoints = {xf,xb};
```

Rayleigh-Plesset Partial Differential Equation
Best Fitting for ‘fminsearch’

```
clear
clc
close all
PlotIt = 1;
load S9kV70pS2C.mat;
Time=t(2:7);
Rad=Radius(2:7);
Params{1} = Time;
Params{2} = Rad;
Params{3} = PlotIt ;
% x = [Req*1e6,Rzero*1e6,Vzero,TimeOffset*1e6,k,pinf/1e5];
% x = [103.7015,101.8816,-5.0877,0.9856,1.1008,1.0001];
Req = 85e-6;
% pinf = 1.7e5; % external pressure
k = 1.014; % ideally could be time varying (should be 1 for large slow bubble and >1 but
<gamma for fater bubble
% h=1.012e-8;
% gamma=35e-3;
Rzero = 10e-6; % intiall bubble radius
Vzero =100; % intiall bubble wall velcotiy
%TimeOffset = 1e-6; % time of initial bubble should be < 1/fps
%Tb=300;
%PvTb2=0.7e5;
%Pgas0=2*gamma/Req-PvTb2+pinf;
Tb0=420.38;
%x = [Req*1e6,Rzero*1e6,Vzero,TimeOffset*1e6,k,pinf/1e5,Tb,Pgas,PvTb2];
x = [Req*1e6, Rzero*1e6,Vzero,Tb0, k]; %Pgas/1e5,PvTb2/1e5, Req*1e6,
Params{3} = 1;
figure
x1=BubbleSolveError(x,Params);
opts = optimset('fminsearch');
opts.TolFun = 1;
opts.TolX = 1;
x2 = fminsearch(@BubbleSolveError,x,opts,Params);
% params{3} = 2;
x3=BubbleSolveError(x2,Params);
```

```
Minimum Error
function RMSEBubble = BubbleSolveError(x,Params)
Time = Params{1};
Rad = Params{2};
PlotIt = Params{3};
f1 = gcf;
%f2 = figure;
%% Things to Consider Changing
%x = [Req*1e6, Rzero*1e6,Vzero,Tb0, k]; from best fitting codes
Req = x(1)/1e6;
%pinf = x(2); % external pressure
Pinf=5.9e5;
%k = x(3); % ideally could be time varying (should be 1 for large slow bubble and >1
but <gamma for fater bubble
Rzero = x(2)/1e6; % intiall bubble radius
Vzero = x(3); % intiall bubble wall velcotiy
%TimeOffset = x(4)/1e6; % time of initial bubble should be < 1/fps
TimeOffset=1e-6;
%Req = 36.5e-6;
h=1.012e-8;
gamma=35e-3;
%pinf = x(6)*1e5; % external pressure
%k=1.02;
k = x(5); % ideally could be time varying (should be 1 for large slow bubble and >1 but
<gamma for fater bubble
%Rzero = 1e-6; % intiall bubble radius
%Vzero = 1e3; % intiall bubble wall velcotiy
%TimeOffset = x(7)/1e8; % time of initial bubble should be < 1/fps
%Tb=x(5);
Tb0=x(4);
%Pgas0=x(7)*1e5;
%PvTb2=x(4)*1e5;
%%
TP_sats = [
6.04E-01        2.73E+02
9.34E-01        2.79E+02
1.41E+00        2.85E+02
2.09E+00        2.91E+02
3.05E+00        2.97E+02
4.36E+00        3.04E+02
6.14E+00        3.10E+02
8.52E+00        3.16E+02
1.16E+01        3.22E+02
1.57E+01        3.28E+02
```

2.09E+01 3.34E+02
2.76E+01 3.40E+02
3.59E+01 3.46E+02
4.63E+01 3.53E+02
5.91E+01 3.59E+02
7.47E+01 3.65E+02
9.37E+01 3.71E+02
1.16E+02 3.77E+02
1.43E+02 3.83E+02
1.76E+02 3.89E+02
2.13E+02 3.95E+02
2.58E+02 4.02E+02
3.09E+02 4.08E+02
3.68E+02 4.14E+02
4.36E+02 4.20E+02
5.14E+02 4.26E+02
6.03E+02 4.32E+02
7.03E+02 4.38E+02
8.16E+02 4.44E+02
9.43E+02 4.51E+02
1.09E+03 4.57E+02
1.24E+03 4.63E+02
1.42E+03 4.69E+02
1.62E+03 4.75E+02
1.83E+03 4.81E+02
2.07E+03 4.87E+02
2.33E+03 4.93E+02
2.61E+03 5.00E+02
2.93E+03 5.06E+02
3.26E+03 5.12E+02
3.63E+03 5.18E+02
4.03E+03 5.24E+02
4.46E+03 5.30E+02
4.93E+03 5.36E+02
5.43E+03 5.42E+02
5.98E+03 5.49E+02
6.56E+03 5.55E+02
7.18E+03 5.61E+02
7.85E+03 5.67E+02
8.57E+03 5.73E+02
9.20e3 578
9.8e3 583
10.547e3 588
11.274e3 593

```
12.845e3    603
14.586e3    613
16.51e3     623
18.651e3    636
21.03e3     643
22.09e3     647.14
];% kPa, K
T_sat = TP_sats(:,2);
P_sat = TP_sats(:,1)*1e3;
PvTb0=interp1(T_sat,P_sat,Tb0);
Pgas0=2*gamma/Req-PvTb0+Pinf;
params = [Req,Pinf,h,k,gamma,Pgas0,PvTb0,Tb0];
y0 = [Rzero,Vzero]; % initial guesses
ts = linspace(0,25e-6,1e5);
[t,y]=ode23t(@myodefun,ts,y0,[],params);
t = t + TimeOffset;
% if PlotIt
%     [yp,Res] = myodefun2(t,y,params);
% end
radius = y(:,1);
[Rmax,indm] = max(radius*1e6);
period = 2*min(t(radius>0.95*(Rmax/1e6)));

% if PlotIt
%     figure(f1)
%     subplot(2,2,3)
%     plot(t*1e6,y(:,2))
%     xlabel('time (\mus)')
%     ylabel('velocity (\mum/s^2)')
%     grid on;
%
%     subplot(2,2,4)
%     semilogy(t*1e6,abs(yp(:,2)))
%     xlabel('time (\mus)')
%     ylabel('accel (\mum/s^2)')
%     grid on;
% end
Rmod = Rmax;
Tmod = period;
%figure(f2)
% ExRmax = max(Rad);
% ExPer = 2.7957*1e-6;
% Error1 = sqrt((Rmod-ExRmax).^2+(1e6*(Tmod-ExPer)).^2);
```

```
IndToFit = find(Rad>0&Time>0);
InterpModelRadius = interp1(t*1e6,radius*1e6,Time(IndToFit));
Error2 = sqrt(sum((InterpModelRadius-Rad(IndToFit)).^2));
RMSEBubble  = Error2;
if k>1.4|k<1.0
   RMSEBubble=100*RMSEBubble;
end
%
% if  pinf>1.1e5|pinf<0.9e5;
%     RMSEBubble=100*RMSEBubble;
% end
if PlotIt
   figure(f1)
   subplot(2,1,1)
   plot(Time,Rad,'o')
   hold on
   xlabel('time (\mus)')
   ylabel('radius (\mum)')
   grid on;
   x
end

if PlotIt
   %subplot(2,1,1)
   p1 = plot(t*1e6,radius*1e6);
   set(p1,'color','k')
   subplot(2,1,1)
   plot(Time(IndToFit),InterpModelRadius,'x')
   hold off
   grid on;
end
```

Function for Boundary Velocity and Acceleration

```
function yp = myodefun(t,y,params)
t;
% params = [Req,pinf,h,k,gamma,Tb,Pgas];
%params = [Req,pinf,h,k,gamma,Tb,Pgas,PvTb2];
rho = 1000; % kg/m^3
Tinf=300;
mu = 8.9e-4; % 8.9e-4 pa-s -- Not very sensitive to this
Pinf = params(2); % 1e5 Pa
Pt = 0*t; % Pressure as a function of time
gamma = params(5); % N/m
%Pg = 1e4; % Pa
%Req = 10e-6; % m equlibrium bubble diameter
h = params(3); % volume taken up by neucleii
%k=1.3; % 1 is isothermal 5/3 for adiabatic
Req = params(1);
k = params(4);
%Tb =params(6);
Pgas0 = params(6);
% Pressure in Gas
% Pg = (Pinf+2.*gamma./Req).*((Req.^3-h.^3).^k)./((y(1).^3-h.^3).^k);
PvTb2=params(7);
Tb0=params(8);
Pgas=Pgas0*(Req/y(1))^(3*k);
Tb=(Pgas/Pgas0)^((k-1)/k)*Tb0;
TP_sats = [
6.04E-01        2.73E+02
9.34E-01        2.79E+02
1.41E+00        2.85E+02
2.09E+00        2.91E+02
3.05E+00        2.97E+02
4.36E+00        3.04E+02
6.14E+00        3.10E+02
8.52E+00        3.16E+02
1.16E+01        3.22E+02
1.57E+01        3.28E+02
2.09E+01        3.34E+02
2.76E+01        3.40E+02
3.59E+01        3.46E+02
4.63E+01        3.53E+02
5.91E+01        3.59E+02
7.47E+01        3.65E+02
9.37E+01        3.71E+02
```

```
1.16E+02        3.77E+02
1.43E+02        3.83E+02
1.76E+02        3.89E+02
2.13E+02        3.95E+02
2.58E+02        4.02E+02
3.09E+02        4.08E+02
3.68E+02        4.14E+02
4.36E+02        4.20E+02
5.14E+02        4.26E+02
6.03E+02        4.32E+02
7.03E+02        4.38E+02
8.16E+02        4.44E+02
9.43E+02        4.51E+02
1.09E+03        4.57E+02
1.24E+03        4.63E+02
1.42E+03        4.69E+02
1.62E+03        4.75E+02
1.83E+03        4.81E+02
2.07E+03        4.87E+02
2.33E+03        4.93E+02
2.61E+03        5.00E+02
2.93E+03        5.06E+02
3.26E+03        5.12E+02
3.63E+03        5.18E+02
4.03E+03        5.24E+02
4.46E+03        5.30E+02
4.93E+03        5.36E+02
5.43E+03        5.42E+02
5.98E+03        5.49E+02
6.56E+03        5.55E+02
7.18E+03        5.61E+02
7.85E+03        5.67E+02
8.57E+03        5.73E+02
9.20e3      578
9.8e3       583
10.547e3    588
11.274e3    593
12.845e3    603
14.586e3    613
16.51e3     623
18.651e3    636
21.03e3     643
22.09e3     647.14
];% kPa, K
```

```
P_sat = TP_sats(:,1)*1e3;
T_sat = TP_sats(:,2);
PvTb=interp1(T_sat,P_sat,Tb);
Pg2=PvTb+Pgas;
yp(1) = y(2);
term1 = Pg2-Pinf;
term2 = -4.*mu.*y(2)./y(1);
term3 = -2.*gamma./y(1);
term123 =1./rho.*(term1+term2+term3);
term4 = -3./2.*y(2).^2;
yp(2) = (term123+term4)./y(1);
yp = yp';
```